



**Transition metal nitrides and oxynitrides as  
catalysts for N<sub>2</sub> electroreduction to NH<sub>3</sub> –  
from theory to experiments**

Fatemeh Hanifpour



**Faculty of Industrial Engineering, Mechanical  
Engineering and Computer Science  
University of Iceland**



# **Transition metal nitrides and oxynitrides as catalysts for N<sub>2</sub> electroreduction to NH<sub>3</sub> – from theory to experiments**

Fatemeh Hanifpour

Dissertation submitted in partial fulfillment of a  
*Philosophiae Doctor* degree in Chemical Engineering

## Advisors

Prof. Egill Skúlason  
Dr. Helga Dögg Flosadóttir

## PhD Committee

Prof. Egill Skúlason  
Dr. Helga Dögg Flosadóttir  
Dr. Kristján Leósson

## Opponents

Prof. Douglas R. MacFarlane  
Prof. Plamen Atanassov

Faculty of Industrial Engineering, Mechanical Engineering  
and Computer Science  
University of Iceland  
Reykjavik, Oct 2021

Transition metal nitrides and oxynitrides as catalysts for  $N_2$  electroreduction to  $NH_3$  – from theory to experiments  
Dissertation submitted in partial fulfillment of a *Philosophiae Doctor* degree in Chemical Engineering

Copyright © 2021 Fatemeh Hanifpour  
All rights reserved

Faculty of Industrial Engineering, Mechanical Engineering  
and Computer Science  
School of Engineering and Natural Sciences  
University of Iceland  
Tæknigarði, Dunhaga 5  
107, Reykjavík  
Iceland

Telephone: 525 4000

**Bibliographic information:**

Fatemeh Hanifpour, 2021, *Transition metal nitrides and oxynitrides as catalysts for  $N_2$  electroreduction to  $NH_3$  – from theory to experiments*, PhD dissertation, Faculty of Industrial Engineering, Mechanical Engineering and Computer Science, University of Iceland, 177 pp.

Author ORCID: 0000-0003-3844-5219

Printing: Háskolaprent, Fálkagata 2, 107  
Reykjavík, Iceland, Oct 2021

# Abstract

Our world is struggling with the negative impacts of greenhouse gases, with CO<sub>2</sub> constituting more than  $\frac{3}{4}$  of them. The ammonia production through the Haber-Bosch process which is vital for the sustain of human beings by ensuring food security, accounts for 1% of the CO<sub>2</sub> emissions and is, unfortunately, the only economically viable option as of today. Therefore, a global endeavor towards finding sustainable and carbon-free alternative pathways for ammonia synthesis initiated and peaked during the past decade.

The present thesis is one step forward in this path reporting experimental results for electrosynthesis of ammonia via the nitrogen reduction reaction at ambient conditions in aqueous electrolytes. The first and the foremost important factor in these studies is to be able to reliably report data from experiments. This is because the adventitious ammonia from the atmosphere, human breath, laboratory equipment, gas supplies, etc. can emerge as false positives in samples that are hoped to contain ammonia from an electrocatalytic reaction. Due to this fact, a great deal of the endeavors in this work is focused on securing reliable data. The electrochemical cell, ammonia measurement method, and experimental procedures are all chosen and optimized carefully for this aim.

The previous theoretical studies in our group have narrowed down the possible choices of electrocatalysts among transition metal nitrides and transition metal oxides. The candidates that are tested in the experiments include CrN, VN, NbN, ZrN, NbO<sub>2</sub>, and NbON, all in the form of thin-film polycrystalline surfaces. In the electrochemical experiments, various techniques are employed to study the behaviors of the surfaces in the absence and the presence of the reactive gas that is Ar(g) and N<sub>2</sub>(g), respectively. Ammonia production in all cases is measured at various applied potentials and compared between the two gas environments. The combined data from electrochemical studies, ammonia measurements, surface analysis before and after experiments, and isotope labeling experiments proves the catalytic/non-catalytic nature of the processes.

The results of the studies are presented in the form of one published paper, one submitted paper, and one article draft attached at the end of this thesis.



# Útdráttur

Á heimsvísu berst mannkynið við neikvæð áhrif gróðurhúsalofttegunda, þá aðallega CO<sub>2</sub> sem fyllir um þrjá fjórðunga af heildar gróðurhúsalofttegundunum losuðum af mannavöldum. Framleiðsla ammóníaks með Haber-Bosch aðferðinni er lífsnauðsynleg fyrir heimsbyggðina þar sem hún tryggir fæðuöryggi. Hins vegar veldur það ferli losun 1% af allri losun CO<sub>2</sub> af mannavöldum og er því miður eina þekkta ferlið til framleiðslu ammóníaks. Þess vegna hefur samfélag vísindamanna hafið þróun á sjálfbærri ferli til framleiðslu ammóníaks undanfarinn áratuginn.

Þessi ritgerð færir okkur eitt skref áfram í þessari þróun. Hér birti ég niðurstöður tilrauna í rafefnafræðilegum smíðum ammóníaks með afoxun niturs við herbergis hita og þrýsting í raflausn úr vatni. Í þessum rannsóknum er allra mikilvægast að hanna tilraunir á þann hátt að þær tryggja áreiðanlegar niðurstöður. Þetta er sérstaklega flókið í ljósi þess að ammóníak er til staðar í andrúmsloftinu, andardrætti, búnaði á tilraunastofu og einnig sem snefill í gastegunum sem eru notaðar í tilraunum osfrv. Það er því mjög auðvelt að fá falskar jákvæðar niðurstöður í tilraunum ef ekki er vel gætt að. Vegna þessa er stór hluti af vinnunni sem er birt hér einsett á að tryggja áreiðanleg gögn. Rafefnafræði sellan, ammóníaks magngreiningar og allir tilraunaferlar eru hannaðir og bestaðir nákvæmlega í þessum tilgangi.

Rannsóknarhópur prófessors Egils Skúlasonar hafði áður þrengt leitina að góðum hvata til afoxunar köfnunarefnis úr hópi hliðarmálm oxíða og hliðarmálm nítíða. Mest lofandi hvatarnir eru prófaðir hér í tilraunum, CrN, VN, NbN, ZrN, NbO<sub>2</sub> og NbON, sem þunnar húðir á fjölkristölluðum yfirborðum. Í rafefnafræði tilraununum eru ýmsar nálganir nýttar til þess að rannsaka hegðun yfirborðanna með og án hvarfefnisins, niturs. Framleiðsla ammóníaks er í öllum tilfellum magngreind við mismunandi spennugildi og borin saman á milli hvarfaðstæðna (N<sub>2</sub>) og bakgrunns (Ar). Magngreiningar ammóníaks, greiningar á yfirborðum fyrir og eftir tilraunir og samsætumerking hvarfefnisins (<sup>15</sup>N<sub>2</sub>) eru svo nýtt til þess að gera grein fyrir hvort hvötun afoxunar niturs eigi sér stað eða ekki.

Niðurstöðurnar eru settar fram sem ein birt grein í ritrýndu tímariti, ein innsendar grein og eitt uppkast að grein, sem eru festar við enda ritgerðarinnar.



*This dissertation is sincerely dedicated to  
my lovely parents who dedicated their lives to me.*

*I hope this makes up for at least a small portion of your sacrifices.*



# Preface

This thesis is submitted in candidacy for a Ph.D. degree in Chemical Engineering from the Faculty of Industrial Engineering, Mechanical Engineering and Computer Science at the University of Iceland. The laboratory work was conducted between October 2016 and February 2021 at the Atmonia laboratory under the supervision of Prof. Egill Skúlason and Dr. Helga Dögg Flosadóttir.

The financial support of the work was as follows:

October 2016 – December 2017: Grant of Excellence from Icelandic Research Fund (grant no. 152619-051, grant recipient: Prof. Egill Skúlason)

January 2018 – December 2020: PhD grant from Icelandic Research Fund (grant no. 185404-051, grant recipient: Fatemeh Hanifpour)

January 2021 – June 2021: Grant of Excellence from Icelandic Research Fund (grant no. 196437-051, grant recipient: Prof. Egill Skúlason)

Fatemeh Hanifpour

July 2021

# Table of Contents

List of Figures .....	xii
List of Tables.....	xiv
List of Papers .....	xv
Abbreviations.....	xvii
Acknowledgements.....	xix
<b>1 Introduction .....</b>	<b>1</b>
1.1 Ammonia; the savior .....	1
1.2 Current industrial ammonia production .....	1
1.3 Alternative pathways for ammonia synthesis .....	3
1.3.1 Electrocatalysis .....	3
1.3.2 Photocatalysis .....	4
1.3.3 Plasma catalysis .....	5
1.3.4 Plasma electrolysis .....	6
1.3.5 Homogeneous catalysis .....	6
1.3.6 Electrochemical lithium cycling .....	7
1.3.7 Summary of alternative pathways for ammonia synthesis .....	8
1.4 Thesis objectives and outline .....	8
1.4.1 Research objectives/questions .....	9
1.4.2 Research outline .....	9
<b>2 Electrocatalysis .....</b>	<b>11</b>
2.1 Electrocatalyst/electrolyte design .....	11
2.1.1 Electrolytes .....	11
2.1.2 Electrocatalysts .....	17
2.2 State of the art .....	21
<b>3 Electrochemical techniques .....</b>	<b>25</b>
3.1 Linear sweep voltammetry .....	25
3.2 Cyclic voltammetry .....	26
3.3 Chronoamperometry .....	27
3.4 Differential pulse voltammetry .....	29
3.5 Electrochemical impedance spectroscopy .....	30
<b>4 Summary of papers .....</b>	<b>33</b>
4.1 Paper I .....	33
4.2 Paper II.....	34
4.3 Paper III.....	35
<b>5 Conclusion and outlook.....</b>	<b>37</b>
5.1 Conclusion .....	37

5.2 Outlook.....	39
<b>References.....</b>	<b>41</b>
<b>Paper I .....</b>	<b>51</b>
<b>Paper II.....</b>	<b>69</b>
<b>Paper III .....</b>	<b>117</b>

# List of Figures

Figure 1. An overview of the world's population growth from 1700 up to now and projection until 2100, adapted from [1].....	2
Figure 2. A simple schematic of an electrochemical cell for ammonia synthesis, reprinted with permission from [10]. .....	4
Figure 3. Schematic illustration of photocatalytic NRR process, reprinted with permission from [10]. .....	5
Figure 4. An N <sub>2</sub> -H <sub>2</sub> plasma catalytic reactor for ammonia synthesis using a tungsten surface, reprinted from [14].....	5
Figure 5. A simple plasma electrolytic cell for ammonia synthesis. The species contained in the plasma and their role in the reactions giving rise to the final product is also shown. Reprinted with permission from [15]. .....	6
Figure 6. Ammonia synthesis cycle via homogeneous catalysis using Mo(PNP), Adapted from [17]. .....	7
Figure 7. Ammonia synthesis via electrochemical lithium cycling, Adapted from [18]. .....	7
Figure 8. Solid-state electrochemical ammonia synthesis using (a) proton-conducting electrolyte, and (b) oxide-conductive electrolyte. Reprinted with permission from [22]. .....	12
Figure 9. Double-chamber reactor cell utilizing proton-conducting solid-state electrolyte. Reprinted with permission from [23]. .....	13
Figure 10. Single-compartment reaction cell utilizing molten salt electrolyte. Reprinted with permission from [27]. .....	14
Figure 11. Membrane electrode assembly for ammonia synthesis at low temperatures. Reprinted with permission from [29]. .....	15
Figure 12. Schematic and apparatus for anion-exchange membrane electrode assembly. Reprinted from [33]. .....	16
Figure 13. Mechanisms governing the heterogenous nitrogen reduction to ammonia. Reprinted with permission from [35]. .....	17
Figure 14. Ammonia formation on a metal nitride surface via. the Mars-van Krevelen mechanism. Reprinted with permission from [41]. .....	19
Figure 15. Number of published articles in the field of NRR in the past decade, derived from the database of "Web of Science". The data was collected on May 3, 2021. ....	21

Figure 16. Linear sweep voltammetry (LSV). (a) Linear potential step from E1 to E2 as a function of time. Potential scan rate is higher in the case shown as a blue line compared to the red one. (b) the corresponding current response as a function of the applied potential. The maximum reduction current achieved at EP increases with the increase in the potential scan rate.....	26
Figure 17. Cyclic voltammetry (CV). (a) Linear potential step from E1 to E2 and back to E1 again as a function of time. The potential cycling is shown for two cycles. (b) the corresponding current response as a function of the applied potential. Here the current response is only shown for one cycle. ....	27
Figure 18. Chronoamperometry with a double potential step. (a) Potential (E) step as a function of time, and (b) the corresponding current response as a function of time. Adapted from [94] with slight modifications.....	28
Figure 19. Illustration of the differential pulse voltammetry (DPV) technique. Typical parameters values are: 5 mV for step size, 25 mV for pulse size, 50 ms for pulse time, and 0.5 s for sample period. ....	29
Figure 20. Current response as a function of applied potential in two techniques of LSV (black line) and DPV (red line) recorded using a TiN surface in K <sub>2</sub> SO <sub>4</sub> electrolyte saturated with N <sub>2</sub> gas in a three-electrode H-cell setup. ....	30
Figure 21. (a) A typical Nyquist plot showing two semi-circles at higher frequencies and an oblique line at the lower frequency region. (b) the corresponding Bode plot demonstrating the total impedance (green solid line) and the phase angle (blue dashed line) as a function of applied frequency. The elements of the equivalent circuit are marked on the Bode plot.....	31
Figure 22. Equivalent circuit for the data in Figure 20. The model circuit consists of three resistors (describing the electrolyte resistance and two charge transfer resistances), two constant phase elements (describing the capacitance associated with the two resistors), and a Warburg element describing the diffusion-controlled region.....	31

# List of Tables

Table 1. General overview of the alternative methods for ammonia synthesis. ....	8
Table 2. State of the art on experimental NRR results.....	22

# List of Papers

## Included in this thesis:

- I.** Hanifpour, F., Sveinbjörnsson, A., Canales, C. P., Skúlason, E., & Flosadóttir, H. D. (2020). Preparation of Nafion Membranes for Reproducible Ammonia Quantification in Nitrogen Reduction Reaction Experiments. *Angewandte Chemie*, 132, 23138-23142.

**My contribution to this publication:** I performed all the experiments. I did all the data analysis. I wrote the first draft of the manuscript.

- II.** Hanifpour, F., Canales, C. P., Fridriksson, E. G., Sveinbjörnsson, A., Tryggvason, T. K., Yang, J., von Fieandt, K., Arthur, C., Jónsdóttir, S., Garden, A. L., Ólafsson S., Leósson, K., Árnadóttir, L., Lewin, E., Abghoui, Y., Ingason, Á. S., Magnus. F., Flosadóttir, H. D., & Skúlason, E. In-line quantification of ammonia produced from theoretically derived transition metal nitrides electro-catalysts.

### **In preparation**

**My contribution to this manuscript:** I performed most of the electrochemical experiments. I did all the data analysis related to the electrochemical experiments. I wrote the first draft of the manuscript.

- III.** Hanifpour, F., Canales, C. P., Fridriksson, E. G., Sveinbjörnsson, A., Tryggvason, T. K., Lewin, E., Magnus. F., Ingason, Á. S., Skúlason, E., & Flosadóttir, H. D. Investigation into the mechanism of electrochemical nitrogen reduction reaction to ammonia using niobium oxynitride thin-film catalysts.

### **Submitted**

**My contribution to this manuscript:** I performed all the electrochemical experiments. I did all the data analysis related to the electrochemical experiments. I wrote the first draft of the manuscript.

**Not included in this thesis:**

- IV.** Hanifpour, F., Sveinbjörnsson, A., Abghoui, Y., Magnus, F., Tryggvason, T.K., Ingason, Á.S., Flosadóttir, H.D., & Skúlason, E. Electrochemical nitrogen reduction to ammonia on polycrystalline and single crystal ZrN catalysts

**In preparation**

**My contribution to this manuscript:** I performed all the electrochemical experiments. I did all the data analysis related to the electrochemical experiments. I wrote the first draft of the manuscript.

# Abbreviations

ATP	adenosine triphosphate
NRR	nitrogen reduction reaction
HER	hydrogen evolution reaction
BDD	boron-doped diamond
AAEMs	alkali anion exchange membranes
CCMs	catalyst-coated membranes
MEA	membrane electrode assembly
PEMEL	proton-exchange membrane electrolyzer
AEMEL	anion-exchange membrane electrolyzer
SDC	samaria-doped ceria
RHE	reversible hydrogen electrode
DFT	density functional theory
TMs	transition metals
TMNs	transition metal nitrides
MvK	Mars Van Krevelen
RS	rocksalt
ZB	zincblende
TMOs	transition metal oxides
TMCs	transition metal carbides
TMSs	transition metal sulfides
TMBs	transition metal borides
SACs	single-atom catalysts
PCN	polymeric carbon nitride
TMONs	transition metal oxynitrides
TMCNs	transition metal carbonitrides
VON	vanadium oxynitride

DEIS	dynamic electrochemical impedance spectroscopy
FIA	flow injection analysis
SIA	sequential injection analysis
LOD	limit of detection
LUMO	lowest unoccupied molecular orbital
HOMO	highest occupied molecular orbital
LSV	linear sweep voltammetry
EDL	electrical double layer
OP	onset potential
RDS	rate-determining step
CV	cyclic voltammetry
OCP	open circuit potential
DPV	differential pulse voltammetry
EIS	electrochemical impedance spectroscopy
DC	direct current
AC	alternative current
R <sub>ct</sub>	charge transfer resistance
DEIS	dynamic electrochemical impedance spectroscopy
FTO	fluorine doped tin oxide
SS	stainless steel
NF	nickel foam
SSC	stainless steel cloth
SERS	surface enhanced Raman spectroscopy

# Acknowledgements

My special thanks go to my supervisor, Prof. Egill Skúlason, for his non-stop support throughout my studies. His patience in explaining the underlying theories behind my experimental world, and his brilliant ideas to push forward the experiments were exemplary. He is the most fantastic supervisor by every definition, and it has been an honor for me to work with him since 2016. Next, I would like to thank my co-supervisor, friend, and mentor, Dr. Helga Dögg Flosadóttir, who helped me unconditionally during my studies. Without her knowledge, constructive ideas, patience, and amazing positivism, I could have not gone this far into defending my PhD thesis, today. I would also like to thank Dr. Kristján Leósson for serving as a committee member for my PhD dissertation. It is an honour to have him on board.

I would like to specifically thank Prof. Douglas R. MacFarlane from School of Chemistry at Monash University, and Chancellor's Prof. Plamen Atanassov from School of Engineering at the University of California, Irvine for accepting to be the opponents in my Ph.D. defence despite their unimaginably busy schedules. They are both globally noticed and leading scientists in the field.

Many thanks to my talented colleague and friend, Arnar Sveinbjörnsson (the Saviour). It would, certainly, have not been easy to go through the everyday challenges in the lab without him being there and helping to solve some of the problems.

I, sincerely, appreciate all the efforts that the Grein Research team, Dr. Friðrik Magnus, Dr. Árni S. Ingason, Tryggvi Kr. Tryggvason, and Emil G. Friðriksson, put into providing the electrocatalysts and surface analysis for this big project. They are simply and undoubtedly the best at what they do. I would like to specifically thank Dr. Erik Lewin from Uppsala University who provided this research with the XPS analysis with his deep insights.

I have been privileged to have a supporting group of people around me in Atmonia, our small company with big ambitions. Thanks to all my team-mates for taking the time to proof-read my thesis and shaping the final work with their constructive comments. I would like to specifically thank Guðbjörg Rist, the CEO, for her unconditional support and inspirations, plus organizing seasonal seminars with the aim of coordinating and keeping the group focused (and of course the frequent fun events to keep the group lively). Thanks to Magnús Már Guðnason for the helpful discussions and upgrading our lab into a more standardized, professional, and user-friendly environment. My special thanks to my dear colleague, Dr. Camila Pía Canales for her helpful insights into the electrochemical discussions. Helga Dögg Flosadóttir, Arnar Sveinbjörnsson, Hákon Örn Birgisson, Dr. Amanda Luther, James Edward McDaniel, Naseeb Nisar Pookkat, and Jinchao Wang, thank you for all the nice moments at work. I am so proud to have officially started a career path among these wonderful people in Atmonia, moving forward our research towards our common goal stronger than ever.

I would like to thank Dr. Younes Abghoui and Dr. Ebrahim Tayyebi, research assistants at the University of Iceland, for our valuable discussions and their theoretical insights that assisted the experiments. A special thanks to Associate Professor Líney Árnadóttir from Oregon State University and Sveinn Ólafsson from University of Iceland who helped the project, mostly in its initial stages, with their constructive and “outside of the box” ideas.

Many thanks to my dear friend, Sahar, who was always a helping hand, making my new life in Iceland much easier. I am, also, grateful to all my friends at the University of Iceland and Reykjavík University with whom we shared unforgettable moments during the past years.

I would like to show my deepest appreciation to my lovely parents, Effat Bozorgi and Hasan Hanifpour, who have always had faith in me, helping me to endure through the long years of being apart. And last, but not least, I am wholeheartedly thankful to my life companion, Mehdi Maghsoudi, who equally deserves to get this degree as he has also gone through all the hardships with me, encouraged me, empowered me, admired me, and on top of all tolerated me.

# 1 Introduction

The world's population has increased from around 1 billion in the year 1800 to 7.8 billion today. Although the rate of the population growth is now not as drastic as it was up to 1970 and even projected to fall to 0.1% per year by the year 2100, as seen in Figure 1, the existing global population will still need substantial amount of food to survive<sup>1</sup>.

In this chapter we will look briefly into the importance of ammonia as the main source of nitrogen in fertilizers. After that, the current industrial ammonia production process and the limitations associated with it will be discussed. Next, alternative ammonia production methods devised so far to address the drawbacks of current practices will be briefly reviewed. Finally, the thesis outline will be highlighted.

## 1.1 Ammonia; the savior

Ammonia (NH<sub>3</sub>) is one of the most highly produced chemicals in the world and an important commodity. It has widespread application in nitrogen fertilizers, pharmaceutical products, cleaning products, and as an energy carrier, refrigerant, etc. Of the total ammonia produced annually, more than 85% is consumed in the manufacturing of fertilizers to feed and sustain the world's growing population<sup>2</sup>. Without synthetic ammonia in fertilizers, the naturally available sources can only support half of this population<sup>3</sup>. The production process of ammonia from its elements, nitrogen gas (N<sub>2</sub>) and hydrogen (H<sub>2</sub>), is rather challenging as the cleavage of the extremely strong triple bond of nitrogen requires a large energy input of 941 kJ mol<sup>-1</sup>. In nature, the N<sub>2</sub> fixation process is catalyzed at ambient conditions by an enzyme called nitrogenase. The active site in this enzyme which is the CFe<sub>7</sub>MoS<sub>9</sub> cluster converts N<sub>2</sub> to NH<sub>3</sub> together with the reduction of protons to H<sub>2</sub>:



This biological process is inefficient since it requires 16 mol adenosine triphosphate (ATP) per mol N<sub>2</sub> reduced, equivalent to an energy expense of nearly 5 eV per turnover of one N<sub>2</sub> molecule (ca. 500 kJ/mol of N<sub>2</sub>)<sup>4,5</sup>. In industry, however, the story is different.

## 1.2 Current industrial ammonia production

To date, the only economically feasible ammonia production process is via the Haber-Bosch method which could be categorized as one of the most important and revolutionary industrial chemical processes ever developed. Thanks to this great invention, humankind has been fed over the past century.

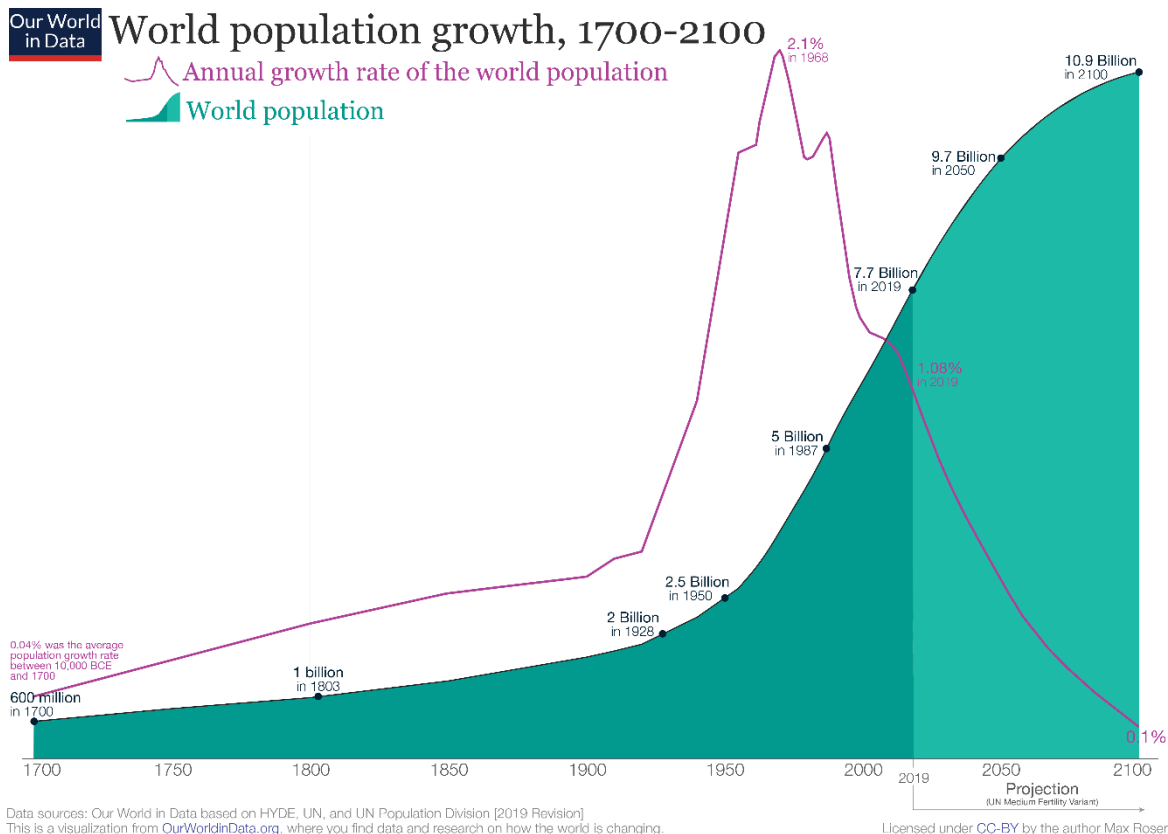
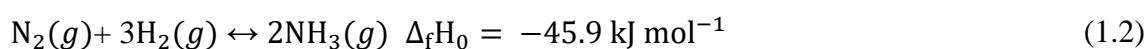


**Figure 1. An overview of the world’s population growth from 1700 up to now and projection until 2100, adapted from [1].**

The Haber-Bosch process is an example of heterogeneous catalysis. This means that the reaction occurs at the interface between two phases. Here, the reactants, which are hydrogen and nitrogen gas are passed over an Fe-based catalyst promoted with  $K_2O$ ,  $CaO$ ,  $SiO_2$ , and  $Al_2O_3$ , at 300-500 °C to facilitate the kinetics and 150-200 atm to shift the equilibrium of the exothermic reaction in favor of the products<sup>6</sup>:



The source of nitrogen for this process is air, while hydrogen is commonly produced on-site via methane reforming reactors using steam at 700-1000 °C:



followed by a water-gas shift reactor<sup>7</sup>:



Although the Haber-Bosch process was a revolutionary contribution to the human progress, there are many limitations associated with it. To start with, the operating conditions are harsh, that is high temperatures and pressures in the ammonia production reactor, and high temperatures in the hydrogen production reactor. These conditions require expensive infrastructure which is only economically viable at a very large scale. Secondly, the process itself is complex, owing to the fact that it has to be integrated with the hydrogen production

process and a gas recycler to improve the low equilibrium single-pass conversion of ammonia from around 15% to 98%. Moreover, the whole process is highly energy-intensive and emits up to 2 tons of CO<sub>2</sub> per ton of NH<sub>3</sub>, making the worldwide manufacturing of ammonia account for 1% of CO<sub>2</sub> emissions<sup>8</sup>. Finally, the proximity to methane source limits the plant locations to only to a few places around the globe, thus, necessitating the distribution of product to the points of use by means of transportation which again adds to the overall CO<sub>2</sub> emissions. Although, electrolysis was shown to be a green and viable option for hydrogen production and has been implemented for a long time in few countries in their Haber-Bosch plants, no major ammonia manufacturing plants are currently using this method as it is more expensive than the conventional steam methane reforming<sup>9</sup>.

These limitations drive scientists to look for more environmentally friendly means of ammonia synthesis. In the next chapter, we will look into the most important alternative pathways devised so far to overcome the Haber-Bosch process limitations.

## 1.3 Alternative pathways for ammonia synthesis

The urge to mitigate CO<sub>2</sub> emissions and decrease the cost of ammonia production have motivated researchers to look for other low cost and low-carbon alternatives. To date, multiple options have been sought after and studied. These alternatives have made it possible for the reactions to be performed under milder conditions; that is intermediate temperature/pressure, intermediate temperature/atmospheric pressure, and room temperature/atmospheric pressure (ambient conditions). In this section these options will be briefly looked into.

### 1.3.1 Electrocatalysis

In this process, two electrodes are placed inside an electrolyte. A power supply provides the electrodes with negative charge (cathode) and positive charge (anode). The general process of electrocatalytic nitrogen reduction reaction (NRR) consists of: (i) formation of protons at the anode/electrolyte interface, (ii) transport of protons through the electrolyte, (iii) reduction of N<sub>2</sub> at the catalyst (cathode) active sites by up-take of electrons, and (iv) ammonia formation by protonation of N. Figure 2 shows the electrocatalysis process using a simple schematic.

**Catalyst materials:** metals; metal nitrides/oxides/carbides/sulfides/borides; metal-free catalysts; metal compounds.

**Pros:** Sustainable; Carbon-free; Ambient operating conditions

**Cons:** Low yield; Low current efficiency

This process will be discussed in more details in Chapter 2.

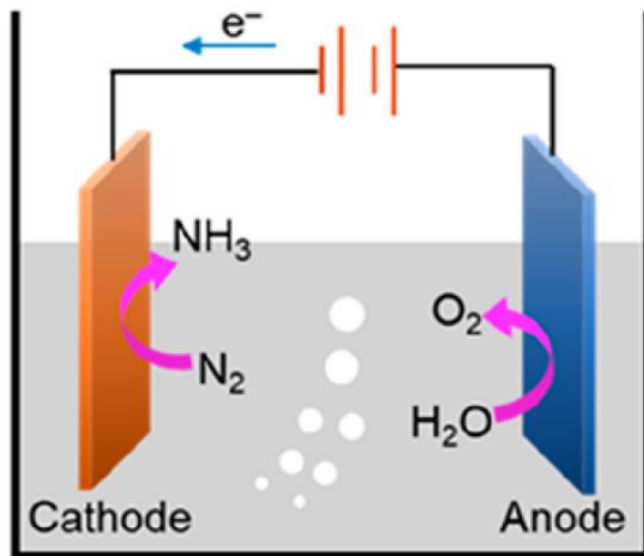


Figure 2. A simple schematic of an electrochemical cell for ammonia synthesis, reprinted with permission from [10].

### 1.3.2 Photocatalysis

The photocatalytic production process of ammonia takes advantage of an external light source to excite a photocatalyst. The excitation step generates electrons and holes in the conduction band and valence band, respectively. These electrons and holes, then, migrate to the photocatalyst's active sites where the reduction process takes place once nitrogen is adsorbed to the surface<sup>10</sup>. Figure 3 shows a simple schematic of the photocatalytic NRR process.

**Catalyst materials:** bio-species/inorganic hybrids; biomimetic photocatalysts; pure inorganic photocatalysts; functional diamond and silicon

**Pros:** Sustainable; Carbon-free; Ambient operating conditions

**Cons:** Low yield; Low efficiency; limited choice of catalyst; limited effective active sites on the catalysts; inadequate light absorption; poor separation of photo-generated charge; challenges regarding nitrogen adsorption to the surface<sup>11</sup>.

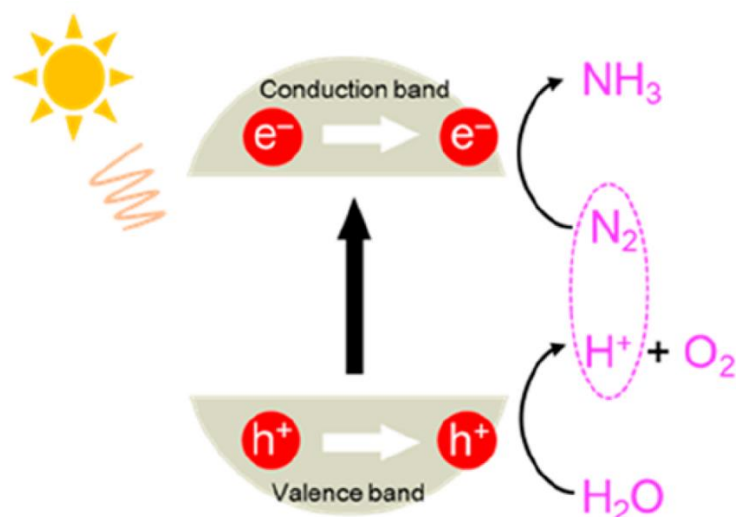


Figure 3. Schematic illustration of photocatalytic NRR process, reprinted with permission from [10].

### 1.3.3 Plasma catalysis

Plasma is created by applying a strong electric field in the gas phase. As a result of a discharge in the partially ionized gas molecules in the plasma, a high density of electrons, neutral species, and highly excited atomic, molecular, ionic, and radical species is generated which greatly enhances the reaction kinetics<sup>12,13</sup>. Figure 4 depicts a plasma catalysis reactor for ammonia synthesis used by Benyaala et al. in 2019.

**Catalyst materials:** Metals, metal oxides

**Pros:** Synergistic effect of surface and gas reactions; high throughput of ammonia

**Cons:** Energy intensive

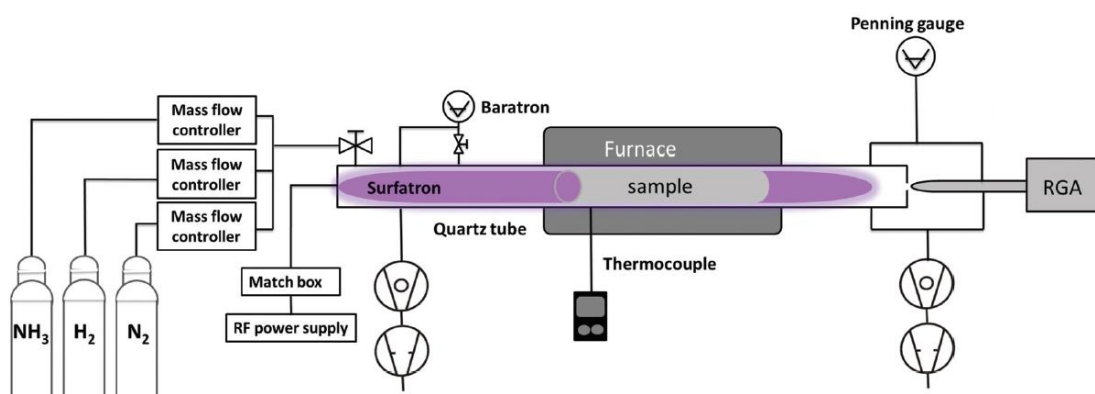


Figure 4. An N<sub>2</sub>-H<sub>2</sub> plasma catalytic reactor for ammonia synthesis using a tungsten surface, reprinted from [14].

### 1.3.4 Plasma electrolysis

A plasma catalysis system is a hybrid electrolytic cell supported by a gaseous plasma electrode which catalyzes NRR in the absence of any catalyst material. The process takes advantage of electricity to form solvated electrons at the  $N_2(g)$ -liquid interface which thereby reduce  $N_2$  to form ammonia. As there is no catalyst used in this method, the kinetic barrier for adsorption of species to a surface is removed, and thus the rate of the reaction only depends on the concentration and transport of protons<sup>15</sup>.

**Catalyst materials:** Catalyst-free

**Pros:** Up to 100% current efficiency

**Cons:** Extremely energy intensive

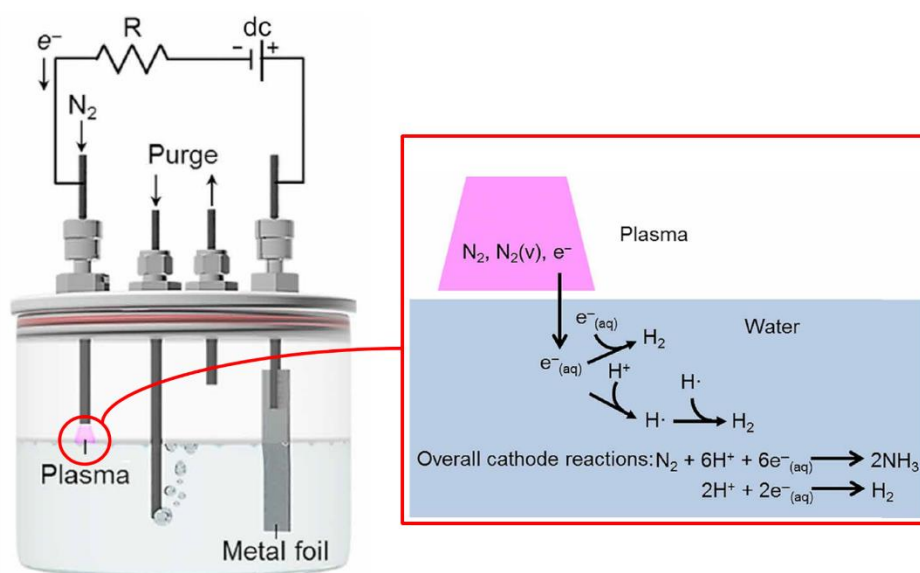


Figure 5. A simple plasma electrolytic cell for ammonia synthesis. The species contained in the plasma and their role in the reactions giving rise to the final product is also shown. Reprinted with permission from [15].

### 1.3.5 Homogeneous catalysis

Homogeneous catalysis involves catalysts that are in the same phase as the electrolyte. In this route, electrons are provided from a metal complex and protons are supported from an acid media<sup>16</sup>. Figure 6 shows a homogeneous catalytic cycle for ammonia synthesis using Mo(2,6-bis(di-tert-butyl phosphinomethyl) pyridine) or Mo(PNP) as catalyst.

**Catalyst materials:** Iron and molybdenum complexes as in Nitrogenase enzyme

**Pros:** Mild operating conditions

**Cons:** Poor selectivity

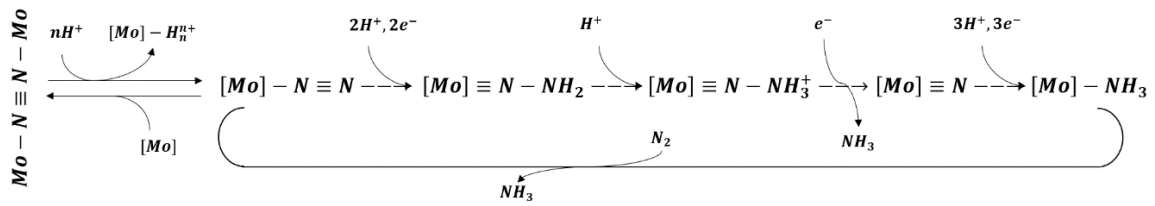


Figure 6. Ammonia synthesis cycle via homogeneous catalysis using Mo(PNP), Adapted from [17].

### 1.3.6 Electrochemical lithium cycling

This innovative strategy takes advantage of a stepwise approach to separate the reduction of  $N_2$  from its protonation step to produce ammonia. The steps include: (i) electrolysis of LiOH to produce Li, (ii) Li nitridation to produce solid  $Li_3N$ , and (iii) reaction of  $Li_3N$  with  $H_2O$  to produce  $NH_3$  and LiOH regeneration. This method was first introduced in 2017 by McEnaney et al.<sup>18</sup>. Figure 7 shows this ammonia synthesis cycle.

**Catalyst materials:** Steel as cathode and graphite as anode for LiOH electrolysis

**Pros:** Circumventing HER; high selectivity

**Cons:** High temperatures up to 450 °C needed for LiOH electrolysis; energy intensive

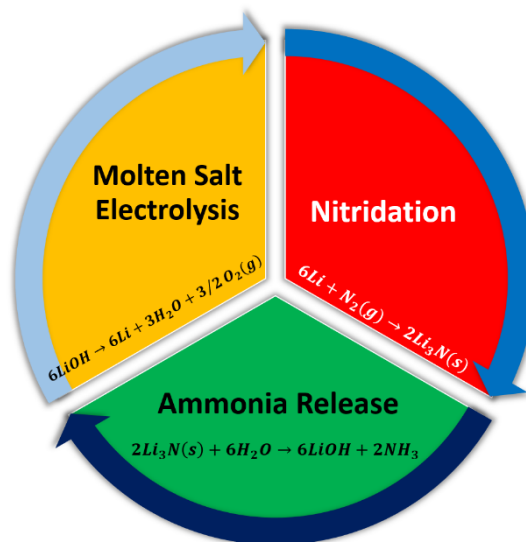


Figure 7. Ammonia synthesis via electrochemical lithium cycling, Adapted from [18].

### 1.3.7 Summary of alternative pathways for ammonia synthesis

The alternative methods of ammonia synthesis, discussed above, are summarized in Table 1.

**Table 1. General overview of the alternative methods for ammonia synthesis.**

Methods	Catalyst Material	General Process	Pros.	Cons.
<b>Electrocatalysis</b>	Metals, Metal nitrides/oxides/carbides/sulfides/borides, Metal-free catalysts, Metal compounds	(1) Formation of protons in the anode/electrolyte interface (2) Transport of protons through the electrolyte (3) Reaction of protons with N <sub>2</sub> at the catalyst active sites (4) Ammonia formation by up-taking electrons	Sustainable, Carbon-free, Ambient operating conditions	Low yield, Low current efficiency
<b>Photocatalysis</b>	Bio-species/inorganic hybrids, Biomimetic photocatalysts, Pure inorganic photocatalysts, Functional diamond and silicon	(1) Absorption of light to generate photo-excited electrons and holes (2) Migration of photo-excited electrons to the catalyst active sites for NRR (3) Migration of photo-induced holes to the counter electrode for water oxidation	Sustainable, Carbon-free, Ambient operating conditions	Low yield, Low selectivity, Limited choices of catalyst
<b>Plasma catalysis</b>	Metals/metal oxides	Highly reactive ions, electrons, and molecular species in the plasma enhance the kinetics	Synergistic effect of surface and gas reactions	Energy intensive
<b>Plasma electrolysis</b>	Catalyst-free	Cathodic plasma electrolytic cell	Up to 100% Current efficiency	Energy intensive
<b>Homogenous catalysis</b>	Iron and molybdenum complexes as in Nitrogenase enzyme	Electrons come from the metal complex and protons from an acid media	Mild conditions,	Poor selectivity
<b>Chemical looping</b>	Steel cathode and graphite anode for LiOH electrolysis	A cycle of: (1) LiOH electrolysis (2) Li Nitridation (3) Reaction of LiN with H <sub>2</sub> O, ammonia release and LiOH regeneration	High selectivity	450 °C needed for LiOH electrolysis, Energy intensive

## 1.4 Thesis objectives and outline

So far, the importance of ammonia in sustaining of human life has been briefly introduced. Given the limitations associated with the current industrial production of this commodity, and the discussion around the viable alternative methods of ammonia synthesis and their pros and cons, electrocatalysis seems to be the most appealing alternative to the Haber-Bosch process. Therefore, the aim of this thesis is to develop more insights into the electrocatalytic synthesis of ammonia, and address solutions to the challenges that the researchers in this field might encounter in their endeavors. In a broader scope, the goal of the electrochemical NRR studies is to design small-scale and decentralized ammonia synthesis units to be run by farmers directly at the point of use. Right now, there is a common global endeavor to realize this goal. The present research is one of those many trying to elucidate some aspects of the whole picture. Therefore, within the chapters of this thesis, I will try to answer the following research questions:

### **1.4.1 Research objectives/questions**

1. Right now, that the majority of researchers in this field utilize H-cell reactors for ammonia synthesis, is there a possibility to use flow-cell reactors with the added benefit of automatic sample collection and higher surface to volume ratio?
2. Since almost all the methods of NRR samples analysis commonly used by researchers include manual sample preparation, how is it possible to integrate an automated ammonia analysis method to the electrochemical setup?
3. What are the NRR experimental protocols that are often ignored by researchers and therefore question their reported results?
4. How do electrochemical techniques describe the catalysts performances and how do the combined results from multiple techniques help to understand the mechanism of NRR?
5. How does the combined results from catalyst characterization analysis and ammonia production align with the results from the electrochemical characterizations?
6. Based on the detailed methodologies devised throughout the project, are transition metal nitrides, that had previously been selected by theoretical computations, promising candidates for electrochemical NRR under ambient conditions?
7. Does the presence of oxygen in the lattice structure of the transition metal nitrides affect the activity and stability of the catalysts?

### **1.4.2 Research outline**

In Chapter 2 of this thesis, the focus is on electrocatalysis and the principles of electrocatalyst/electrolyte design. Different types of electrolytes and electrocatalyst used so far in electrocatalytic synthesis of ammonia are discussed. Protocols for conducting reliable NRR experiments are highlighted and based on those the state-of-the-art only considers the studies that have managed to fulfill the necessary criteria. Chapter 3 gives a brief discussion around the electrochemical techniques and their application in the study of ammonia synthesis. In Chapter 4, the papers which are included at the end of this thesis are summarized. Finally, in Chapter 5, conclusions are drawn on the whole study and a discussion of the general outlook is given.



## 2 Electrocatalysis

Having learnt a lesson from nature on the requirement of proton-electron transfer in the natural N<sub>2</sub> fixation process (reaction 1.1), scientists started to investigate electrochemical pathways to catalyze the nitrogen reduction reaction (NRR) or in other words to produce NH<sub>3</sub> electrocatalytically.

Electrocatalysis reactions take place at a polarized catalyst-solution interface and involve at least one step of charge transfer<sup>19</sup>. The source of protons is the proton-donor electrolyte, and electrons are provided to the catalyst surface through application of an overpotential. There are several advantages to this process which include but are not limited to: (1) simple control of voltage/current (on/off control); (2) integrating renewable energy sources to power the process; (3) operation in ambient conditions which enables a variety of materials to be used for reactor design; (4) minimum separation of products from reactants; (5) facile scale-up of the process by stacking single-cells to increase the throughput; and (6) reduction of CO<sub>2</sub> emissions to the environment provided that the source of electricity is from renewable sources<sup>20,21</sup>. The process of NH<sub>3</sub> synthesis electrocatalytically under ambient conditions with the abovementioned advantages is highly challenging but extremely beneficial for a sustainable future, once realized. Such a process is worth more in-depth investigations into the choice of catalysts, types of electrolytes, reactor design, and a great deal of optimization to be finally economically feasible.

### 2.1 Electrocatalyst/electrolyte design

Electrocatalysts facilitate electron transfer to the reactants in the electrolyte and in this way, enable chemical reactions through direct use of electrons<sup>21</sup>. For such electron transfer reactions to take place, reactants need to be either adsorbed on or in the proximity of the electrode surface. In NRR, N<sub>2</sub> molecules need to be adsorbed on electrodes, reduced by the electrons that are supplied from the external circuit and simultaneously react with protons to form ammonia. Thus, the medium which is the bulk of the electrolyte containing electroactive species, needs to fulfill certain criteria regarding mass and ion transport and at the same time the catalyst should be correctly engineered to favor NRR rather than the competing hydrogen evolution reaction (HER):



#### 2.1.1 Electrolytes

Electrolytes used in NRR are generally divided into three groups based on the operating temperature: (i) electrolytes for high temperature purposes which are proton-conducting solid electrolytes applied in temperatures above 500 °C, (ii) electrolytes used at medium temperature, which are mainly molten salts of chlorides, bromides, hydroxides, etc. used as eutectic mixtures and applied at a temperature range of 200-500 °C, (iii) electrolytes such as

ion-conductive membranes, which are designed for operation under low temperatures (below 100 °C), and (iv) electrolytes for room temperature use, which can be classified as aqueous (water-based) or non-aqueous (organic, ionic liquids).

### Solid-state electrolytes

This electrolyte type is used at high temperatures and atmospheric pressures with the best results usually achieved at temperatures above 500 °C. Solid-state ammonia synthesis makes use of a dense solid electrolyte as a media to conduct either protons or oxide ions and to serve as a barrier to gas diffusion. Figure 8 shows a schematic of these two types of systems<sup>22</sup>.

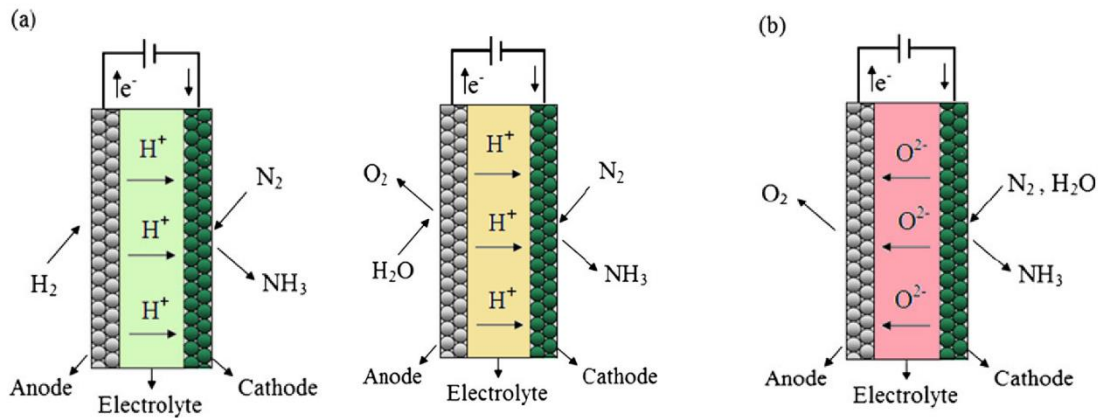


**Figure 8. Solid-state electrochemical ammonia synthesis using (a) proton-conducting electrolyte, and (b) oxide-conducting electrolyte. Reprinted with permission from [22].**

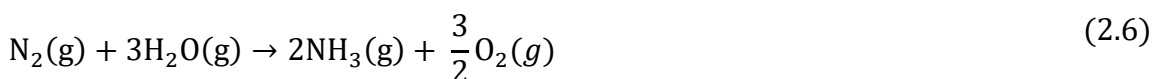
In the case of proton-conductive solid electrolytes, gaseous H<sub>2</sub> or steam is passed over the anode and converted to protons:



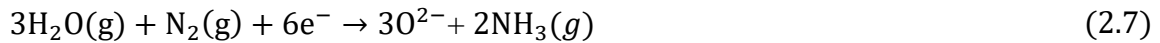
N<sub>2</sub> gas is passed over the cathode and reacts with the protons that are transported through the solid electrolyte to form ammonia:



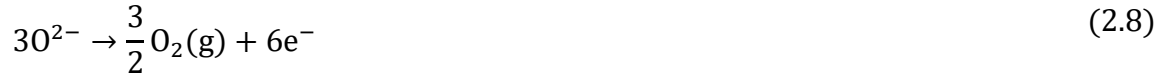
Thus, the overall reaction would be either of the following:



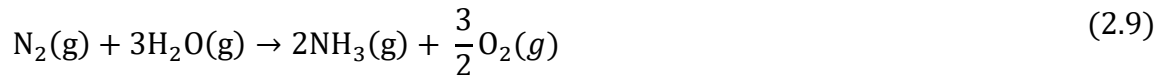
In the case of oxide-conductive solid electrolytes, on the cathode side:



And on the anode:



The overall reaction is then:



Solid electrolytes include mainly perovskites-type oxides due to their exceptional chemical and mechanical stability, along with their high proton conductivity, but some polymers and composites have also been used for this purpose. Figure 9 is a schematic diagram of a double chamber reactor cell used by Marnellos et al. The electrolyte of choice in this case is strontia–ceria–ytterbia (SCY) perovskite of the form  $\text{SrCe}_{0.95}\text{Yb}_{0.05}\text{O}_3$ . Porous palladium (Pd) is used both as the cathode and the anode in the electrochemical cell<sup>23</sup>.

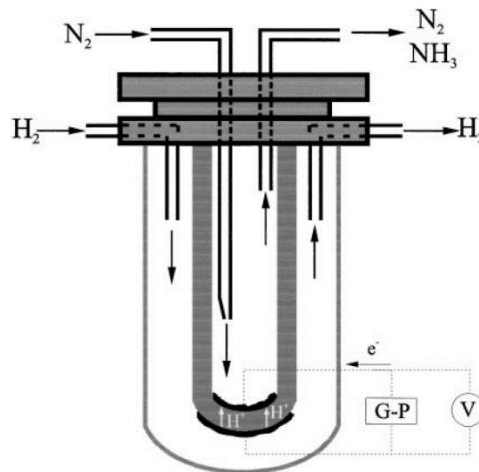


**Figure 9. Double-chamber reactor cell utilizing proton-conducting solid-state electrolyte. Reprinted with permission from [23].**

Ammonia yield in such systems depends on the operating temperature, applied potential, the thickness and the structure of the solid electrolyte or in other words its proton conductivity, and the pore size of the electrodes which affects the surface area and catalytic activity<sup>22</sup>. To date, the highest rate of ammonia production using this method has been achieved in a study done by Wang et al. A composite of 80 wt%  $\text{Ce}_{0.8}\text{Y}_{0.2}\text{O}_{1.9}$  and 20 wt% binary phosphates ( $\text{Ca}_3(\text{PO}_4)_2\text{-K}_3\text{PO}_4$ ) as proton conductor was used as the electrolyte, Ag-Pd both as anode and cathode, and  $\text{N}_2$  and  $\text{H}_2$  as feed gases. At a temperature of 650 °C a maximum rate of  $9.5 \times 10^{-9} \text{ mol cm}^{-2} \text{ s}^{-1}$  was reported<sup>24</sup>. The highest faradaic efficiency thus far is 80 % and was achieved by Marnellos et al. at 570 °C<sup>23</sup>.

NH<sub>3</sub> synthesis in solid-state electrolytes benefits from high yields of ammonia production. Elevated temperatures help the kinetics of the reaction and the conductivity of the electrolyte. However, the exothermic reaction in the case of N<sub>2</sub> and H<sub>2</sub> feed gasses is not thermodynamically favorable. The H<sub>2</sub> gas source is the steam reforming of natural gas, thus, not environmentally friendly. NH<sub>3</sub> synthesis via N<sub>2</sub> and H<sub>2</sub>O is exothermic and carbon-free, however, the reducing power is not as strong as in the case of N<sub>2</sub>/H<sub>2</sub>, and weaker conductivity of O<sup>2-</sup> limits NH<sub>3</sub> yield substantially<sup>25</sup>.

### Molten salt electrolytes

Molten salts are usually applied at intermediate temperatures (200-500 °C). The mechanism of ammonia synthesis in these systems is based on the conversion of the nitrogen gas to nitride ions at the cathode and the reaction of the nitride ions with hydrogen or steam at the anode to form ammonia<sup>26,27</sup>.



Figure 10 shows the apparatus used by Murakami et al. who were among the first to study these systems. The electrolyte in this case was a molten salt mixture of LiCl, KCl, and CsCl (0.5% Li<sub>3</sub>N added). Porous Ni was used as anode and boron-doped diamond (BDD) as cathode. At 300 °C, this study reports a rather high ammonia production efficiency of 80% and a rate of  $5.8 \times 10^{-9} \text{ mol cm}^{-2} \text{ s}^{-1}$  [27].

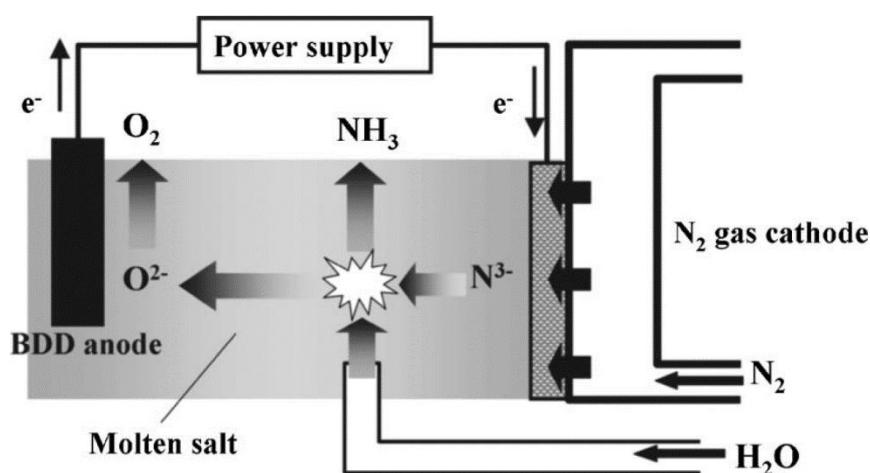


**Figure 10.** Single-compartment reaction cell utilizing molten salt electrolyte. Reprinted with permission from [27].

The ionic conductivity of the electrolyte for the transport of nitride ion is a critical factor in the yield of the system. In a similar set-up with Ni as anode and Ni-Monel mesh as cathode, Li et al. electrolyzed nitrogen and water vapor by means of a molten hydroxide

(NaOH/KOH) electrolyte containing suspended  $\text{Fe}_2\text{O}_3$  nanoparticles and reached an ammonia yield of  $1.0 \times 10^{-8} \text{ mol cm}^{-2} \text{ s}^{-1}$  at  $200 \text{ }^\circ\text{C}$ <sup>28</sup>.

Molten salt electrolytes decrease the competing HER greatly since they are free of protic solvents. However, the limitations associated with the solid-state electrolytes hold in this case as well (hydrogen feed and thermal requirements).

### Ion-conductive electrolytes

At low temperatures (below  $100 \text{ }^\circ\text{C}$ ), proton-conductive and alkali anion-conductive membranes come into practice. Proton exchange membranes (PEMs) are applied more frequently and include Nafion and sulfonated polysulfone (SPSF)<sup>24</sup>. Alkali anion exchange membranes (AAEMs) are less frequently used and are of the hydroxide-exchange membrane type. In either case, the electrodes are heat-pressed to the membrane and these catalyst-coated membranes (CCMs) are assembled in a stack along with a gas-diffusion layer for each electrode. The complete electrolyzer is called a membrane electrode assembly (MEA). Depending on the type of membrane, MEA is either a proton-exchange membrane electrolyzer (PEMEL) or an anion-exchange membrane electrolyzer (AEMEL)<sup>29</sup>. MEA design takes advantage of a large triple-phase boundary which boosts the performance of the electrochemical nitrogen reduction reaction (ENRR). Figure 11 shows a simple schematic of a MEA electrolyzer.

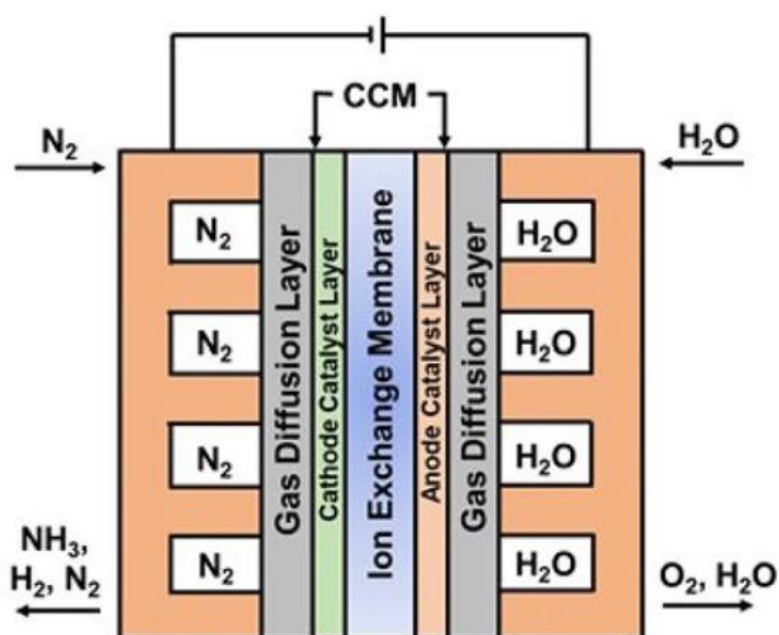


**Figure 11. Membrane electrode assembly for ammonia synthesis at low temperatures. Reprinted with permission from [29].**

Kordali et al. Were the first to synthesize ammonia at atmospheric pressure and low temperature ( $90 \text{ }^\circ\text{C}$ ) using a Nafion electrolyte in  $2 \text{ M KOH}$ . By introducing  $\text{N}_2$  to the Ru cathode and water to the Pt anode and applying a potential of  $-1.02 \text{ V vs. Ag/AgCl}$ ,  $1.30 \mu\text{g h}^{-1} \text{ cm}^{-2}$  of ammonia was detected and a maximum current efficiency of  $0.92\%$  was achieved at an applied potential of  $-0.96 \text{ V}$ <sup>30</sup>. It is likewise possible to feed a stream of  $\text{H}_2$  gas in place of water to the anode side. Xu et al. used  $\text{SmFe}_{0.7}\text{Cu}_{0.3-x}\text{Ni}_x\text{O}_3$  as the cathode and samaria-

doped ceria  $\text{Ce}_{0.8}\text{Sm}_{0.2}\text{O}_{2-\delta}$  (SDC) as the anode in their MEA. Using a Nafion electrolyte in the cell at a temperature of  $80\text{ }^\circ\text{C}$ , they reached a maximum ammonia synthesis rate of  $1.13 \times 10^{-8}\text{ mol cm}^{-2}\text{ s}^{-1}$  and a current efficiency of  $90.4\%$ <sup>31</sup>. The reliability of this report with such high rate and efficiency at a rather low temperature is, however, under question since no proof of catalysis has been provided by the authors. I encourage the reader to refer to section 2.2 for more information in this regard.

Renner et al. were among the first to study AEMEL and found that with Fe and Ni catalysts, up to 2% and 3.5% ammonia synthesis efficiency could be achieved, respectively, and tested the combination of these two with varying particle surface area. These researchers argue that AEM technology is capable of reaching the performance necessary to replace the current Haber-Bosch process provided that the membranes and catalyst materials are improved<sup>32</sup>. Kong et al used an AEMEL with 0.5 M KOH to synthesize ammonia at temperatures below  $65\text{ }^\circ\text{C}$  using  $\gamma\text{-Fe}_2\text{O}_3$  as cathode and Ti as anode. Figure 12 is adapted from their published report and shows the schematic of the process and the apparatus. A  $14.8\text{ nmol h}^{-1}\text{ cm}^{-2}_{\text{geo}}$  (where “geo” refers to the geometric surface area) ammonia production rate and a very low ammonia current efficiency of 0.0014% were reported. The authors believe the low activity and selectivity is due to ammonia adsorption on the electrolyte membrane and reactor surfaces<sup>33</sup>. Nash et al. studied the performance of several noble metal catalysts (Pt/C, Ir/C, Pd/C, Ru/C, and Au/C) in both proton-exchange and hydroxide-exchange membrane electrolyzers at  $-0.2\text{ V}$  and  $-0.4\text{ V}$  vs. reversible hydrogen electrode (RHE). The authors report higher ammonia reaction rates in PEMEL but higher ammonia current efficiencies in AEMEL. Higher current efficiency in AEMEL is attributed to the relatively slow kinetics of HER in alkaline media<sup>34</sup>.

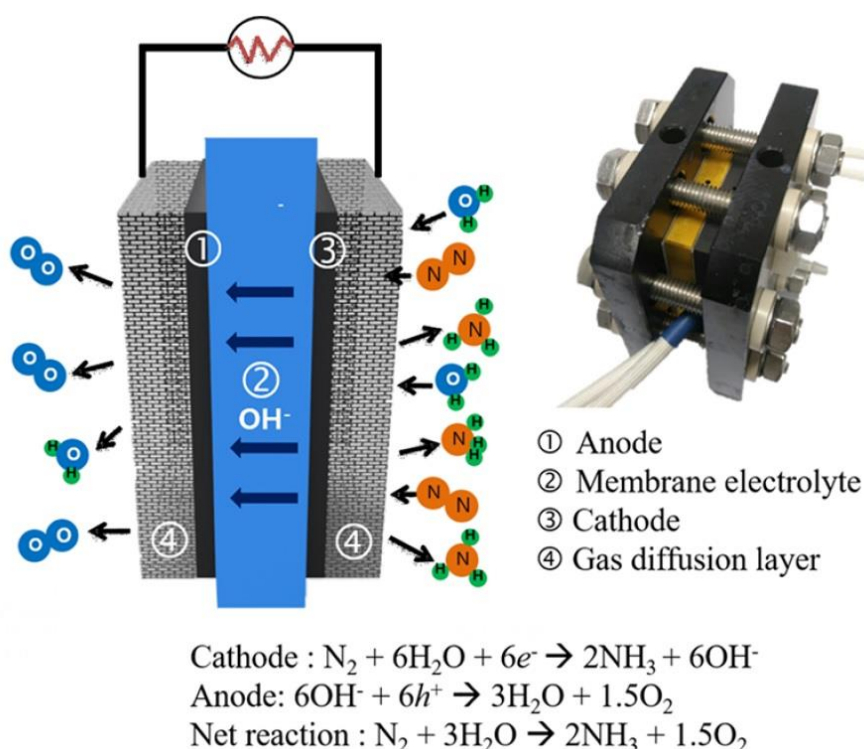


Figure 12. Schematic and apparatus for anion-exchange membrane electrode assembly. Reprinted from [33].

As mentioned, there are pros and cons associated with each electrolyte option. On the one hand, working at high temperatures is not favorable since it adds to the complexity of the systems. Molten salts are corrosive and finding electrode materials stable at these conditions is an issue. Also, the design and optimization of reactors based on MEA and solid electrolytes is difficult and challenging. These options, thus, seem obsolete for small-scale and decentralized units that are meant to be operated by farmers on their lands. On the other hand, reaction rates are much lower at ambient conditions due to slower reaction kinetics. However, it does not disqualify this option because reaction rate can in principle be modified by the correct design of the other key factors in the system such as the electrocatalyst. The two remaining options for electrolytes at ambient conditions i.e., aqueous, and non-aqueous electrolytes again have pros and cons. Aqueous electrolytes have high water contents and low  $N_2$  solubilities. But non-aqueous electrolytes take advantage of the high  $N_2$  solubility and low water content, thus, suppressing the competing HER substantially. Nevertheless, as the final goal of these studies is to synthesize ammonia from air and water, this study will be focused only on aqueous electrolytes.

## 2.1.2 Electrocatalysts

The correct design of catalysts for the electrolyte of choice is critical in achieving the desired reactions. For this aim, one needs to understand the underlying theoretical mechanisms for nitrogen reduction to ammonia on heterogeneous surfaces. These are categorized into two main mechanisms: Associative and Dissociative (Figure 13)<sup>35</sup>.

In a dissociative mechanism, first, the triple bond of  $N_2$  is broken, and then protonation takes place on the individual N-atoms on the surface. It is believed that the Haber-Bosch process operates through this mechanism. The high temperatures and pressures in this process provide the ground for the strong  $N\equiv N$  bonds to split before protonation occurs<sup>36</sup>.

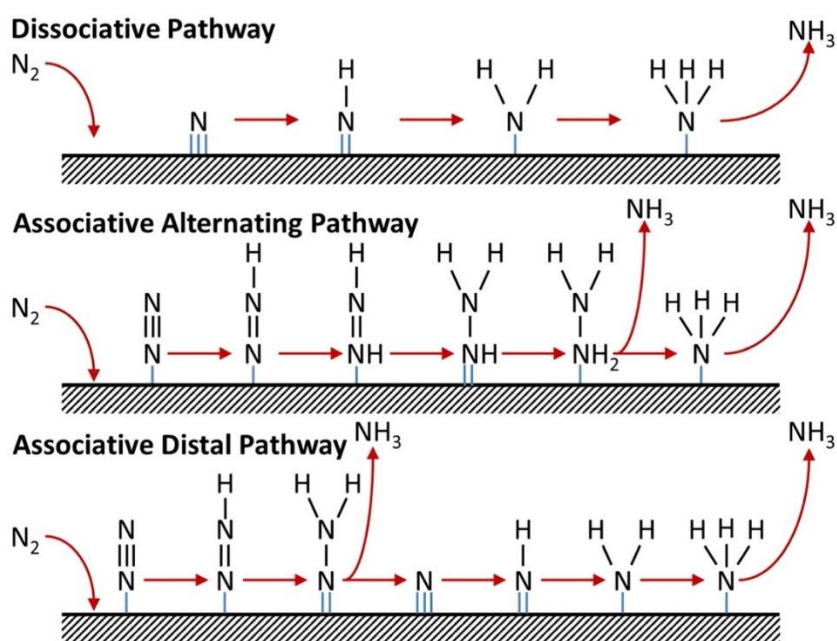


Figure 13. Mechanisms governing the heterogeneous nitrogen reduction to ammonia. Reprinted with permission from [35].

In an associative mechanism, protonation of nitrogen atoms takes place only after nitrogen molecule is adsorbed on the surface. Protonation itself can occur through two possible pathways: Alternating and Distal. In the alternating pathway, protonation of both N atoms in the nitrogen molecule takes place alternatively until one of the N atoms is converted into  $\text{NH}_3$ . At this point, the N-N bond breaks and the first ammonia is released. The second ammonia will thereafter be released after another step of protonation. In the distal pathway, the furthest nitrogen away from the surface is hydrogenated until the first ammonia molecule is released. This leaves behind an N atom bound to the metal ( $\text{M}\equiv\text{N}$ ), which in turn is hydrogenated to release the second ammonia molecule<sup>35</sup>.

The feasibility of ammonia synthesis and the mechanism through which it is realized depends on the catalyst surface and its structure. Thanks to the advances in computational methods, it is now possible to predict the catalysts behavior, and in this way, screen through a pool of options to narrow down the field to a few promising ones to test in practice. Density functional theory (DFT) calculations provide invaluable understandings in this regard. So far, various surfaces have been studied via DFT calculations which include pure transition metals, transition metal nitrides/oxides/carbides/sulfides/borides, single-atom catalysts, and metal-free catalysts.

### Transition metals (TMs)

The DFT calculations done by Skúlason et al. on stepped TMs have shown W, Mo, Fe, Rh, and Ru to be active towards ammonia synthesis, however, not selective. In other words, these surfaces favor HER over NRR. On the other hand, defect-free surfaces of the early TMs like Sc, Y, Ti, and Zr tend to bind N-atoms more strongly than the H-atoms and thus, favoring ammonia production when an overpotential of -1 V to -1.5 V vs. standard hydrogen electrode (SHE) was applied<sup>37</sup>. More in-depth investigations were carried out over Ru(0001) surfaces to study the mechanism of nitrogen reduction, and to identify the rate and potential limiting steps.<sup>38</sup> The authors found that the initial activation of  $\text{N}_2(\text{g})$  was the rate-determining step (RDS). They further predicted a combination of associative (up to the second proton-electron transfer) and dissociative ( $\text{NH}_2\text{-NH}_2$  bond breakage) mechanisms of NRR towards ammonia formation. A robust experimental study was conducted to test the ammonia formation in a cell comprising of Ru as the working electrode, Ir as the counter electrode, and 0.1 M KOH as the electrolyte.<sup>39</sup> The authors did not detect any ammonia more than the background level and thus reported no ammonia activity.

### Transition metal nitrides (TMNs)

TMNs can outperform pure TMs in favoring NRR over HER by stabilizing surface N-vacancies and destabilizing H or O surface species. The role of N-vacancies in these surfaces which push forward the reaction through the Mars-van Krevelen (MvK) mechanism instead of associative or dissociative mechanisms, makes these surfaces unique in their application<sup>40</sup>. In this scheme which is illustrated in Figure 14, a surface nitrogen goes through three consecutive steps of proton and electron transfer, resulting in the formation and desorption of one molecule of ammonia, and formation of an N-vacancy.  $\text{N}_2$  is next adsorbed on the surface and reduced either via a dissociative (solid arrows) or an associative (dashed arrows) mechanism<sup>41</sup>. Abghoui et al. conducted comprehensive DFT calculations on a wide range of TMNs in their rocksalt (RS) and zincblende (ZB) structures and studied their behavior regarding catalytic activity, stability of surface N-vacancies, stability against poisoning, and decomposition potentials. They found VN, CrN, NbN, and ZrN in the RS (100) structure to

be promising in these regards. Among these, VN was shown to be able to catalyze NRR with a relatively low overpotential of -0.5 V, thereby avoiding decomposition<sup>42,43</sup>.

### Transition metal oxides (TMOs)

TMOs were first studied using DFT calculations by Nguyen et al. who predicted an associative mechanism on hematite (0001) surfaces. However, the surface needed a large bias to make the reaction steps downhill in free energy and thus, thermodynamically favorable<sup>44</sup>. Later, Höskuldsson et al. investigated the stability and the catalytic activity of the (110) facet of 11 TMOs in their rutile structure. They found that  $\text{ReO}_2$  and  $\text{TaO}_2$  favored NNH adsorption over hydrogen, resulting in high ammonia synthesis yields.  $\text{NbO}_2$  was also among the promising candidates on the volcano diagram<sup>45</sup>.  $\text{Nb}_2\text{O}_5$  (001) in another DFT study showed high activation of  $\text{N}\equiv\text{N}$  bond due to back transfer of charges from the surface to the adsorbed  $\text{N}_2$  molecule. The study predicts the associative distal pathway for the reduction mechanism<sup>46</sup>.

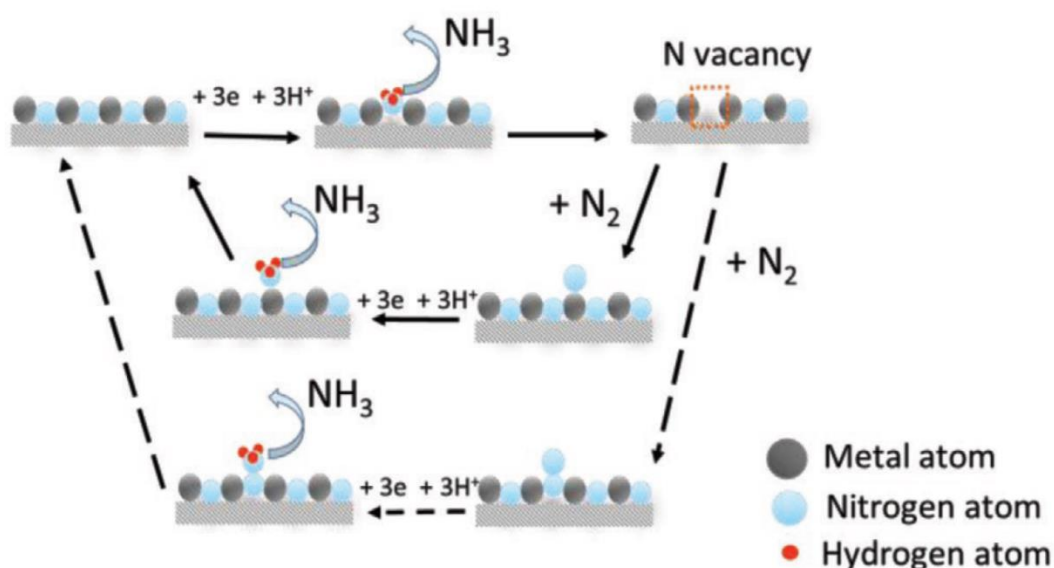


Figure 14. Ammonia formation on a metal nitride surface via the Mars-van Krevelen mechanism. Reprinted with permission from [41].

### Transition metal carbides (TMCs)

TMCs are believed to ease the desorption of the ammonia product from the catalyst surface by weakening the metal- $\text{N}_2$  interaction through their strong electronegative non-metal bond. This was shown by Li et al. on  $\text{Mo}_2\text{C}$  (100) surfaces; however, H-coverage was shown to disrupt NRR activity<sup>47</sup>. In another work,  $\text{Mo}_2\text{C}$  and  $\text{W}_2\text{C}$  were predicted to have the best catalytic performances due to their exothermic reaction steps<sup>48,49</sup>. The DFT calculations by Matanovic et al. predicted  $\text{MoC}$  (111) to be stable in a wide range of potentials and active towards NRR through an associative mechanism, while suppressing HER<sup>50</sup>. In an experimental study, Roy et al modified the surface of  $\text{Mo}_2\text{C}$  with Co, and due to the strong electron-donating property of the catalyst to dissociate nitrogen molecules, achieved high yields of ammonia<sup>51</sup>.

## Transition metal sulfides (TMSs)

TMSs are found in the active sites of the nitrogenase enzyme that produces ammonia via an associative mechanism. This inspired researchers to study surfaces containing similar elements. Zhang et al. initially investigated the energy profile of NRR on MoS<sub>2</sub> and found out that the positively charged Mo-edge would polarize and activate the N<sub>2</sub> molecule<sup>52</sup>. Chen et al. took advantage of the interfacial engineering strategy and the coupling effect between CoS<sub>2</sub> nanoparticles and graphene to make a strong bridging bonds of Co–N/S–C. These bonds are believed to facilitate electron transport and, in this way, accelerate reaction kinetics<sup>53</sup>. Abghoui et al. did a thorough investigation on 18 TMSs regarding their selectivity, activity, and the overpotential required for electrochemical ammonia formation. They found RuS<sub>2</sub> to be the most active candidate catalyzing NRR via the associative mechanism. NbS, CrS, TiS, and VS were also promising catalysts that were predicted to undergo both associative and dissociative mechanisms<sup>54</sup>.

## Transition metal borides (TMBs)

TMBs take advantage of boron as a p-block catalyst and a transition metal to improve N<sub>2</sub> adsorption and fixation. It is believed that the synergistic effect of boron and the metal works towards lowering the maximum energy required in the elementary steps<sup>55,56</sup>. This has been shown in a theoretical study by Li et al. on FeB<sub>6</sub>(β)<sup>55</sup>. Qi et al. investigated into ten candidates of TMBs and found out that TiB, YB, ZrB, and WB needed low overpotentials and followed the direct dissociative mechanism for NRR<sup>57</sup>. Furthermore, Liu et al. have calculated relatively low limiting potentials for Fe<sub>2</sub>B, MO<sub>2</sub>B, and CO<sub>2</sub>B as -0.75 V, -0.82 V, and -0.84 V vs. RHE<sup>58</sup>.

## Single-atom catalysts (SACs)

SACs are another category of catalyst material that gained attention in the field of NRR quite recently. SACs are isolated metal atoms anchored on a support which are believed to gain their excellent performance towards NRR due to the ability of the substrate to provide electrons to the anchored sites that adsorb the N<sub>2</sub> molecules<sup>59</sup>. Some examples of SACs whose mechanisms have so far been studied include Ru<sub>1</sub>@γ-graphyne<sup>60</sup>, Ti and V@N<sub>4</sub><sup>[61]</sup>, Mo<sub>1</sub>-N<sub>1</sub>C<sub>2</sub><sup>[62]</sup>, Mo@MoS<sub>2</sub> nanosheet<sup>63</sup>, Mo and Ru@CeO<sub>2</sub><sup>[64]</sup>, Fe@N doped carbon<sup>65</sup>, and Cu@N doped carbon<sup>66</sup>.

## Metal-free catalysts

Polymeric carbon nitride (PCN), as one of the examples of this class of catalysts, was reported by Lv et al. to catalyze the NRR by chemisorption of N<sub>2</sub> molecules on the as-engineered N-vacancies<sup>67</sup>. In another study, boron-interstitial (B<sub>int</sub>)-doped C<sub>2</sub>N layer was studied using DFT computations and reported as efficient metal-free catalyst that triggers NRR via an enzymatic mechanism with relatively low overpotentials (-0.15 V)<sup>68</sup>. Other promising metal-free catalyst studied by DFT include N-heterocyclic carbene<sup>69</sup> and O-doped graphdyne<sup>70</sup> which operate through enzymatic and associative mechanisms, respectively.

## Hybrid systems

This class of catalysts which include mixed metals, alloys, metal doped TMOs, transition metal oxynitrides (TMONs), transition metal carbonitrides (TMCNs), etc. have been studied to a great deal as these systems take advantage of the synergistic effect of their components towards the common goal of electrochemical ammonia synthesis<sup>71-77</sup>. A recent theoretical

study by Pan et al<sup>73</sup>. investigated various oxygen contents in vanadium oxynitride (VON) and reported the effect of specific low and high oxygen contents on enhanced selectivity and improved nitrogen adsorption and dissociation, respectively.

## 2.2 State of the art

In the past few years, the scientific society has faced a rapid growth in the number of published articles in the field of NRR. Figure 15 is derived from the “Web of Science” database using the keywords: “nitrogen reduction” AND “ammonia” AND “electrochemical” OR “electro-synthesis of ammonia” OR “electrochemical ammonia synthesis”.

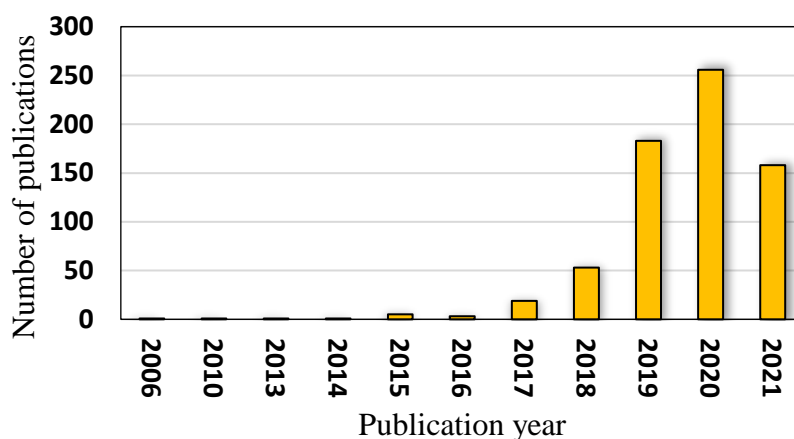


**Figure 15. Number of published articles in the field of NRR in the past decade, derived from the database of “Web of Science”. The data was collected on July 26, 2021.**

This search result might not cover all publications on this topic; however, the trend conveys an increasing number of published articles with time which is due to an intensely competitive environment, where the aim is merely to report maximized ammonia reaction rates and current efficiencies for various catalysts and electrolytes. Unfortunately, the majority of reports are being published with only preliminary results, without proper controls or adequate proof of the source of the nitrogen in the measured ammonia product.

The importance of conducting accurate control experiments with Ar(g) and  $^{15}\text{N}_2(\text{g})$  for NRR experiments was first stressed by Chen et al<sup>78</sup>. Later, Andersen et al. proposed a thorough protocol for electrochemical ammonia synthesis experiments<sup>39</sup>. In this scheme, when ammonia is formed using a catalyst, researchers need to follow several steps to verify catalysis before publishing their results. The first step is to run control experiments in Ar media under the same exact conditions as with  $\text{N}_2$ , and with  $\text{N}_2$  gas with no applied potential. If ammonia is detected in these controls at comparable quantities to the experiment with  $\text{N}_2$  and applied potential, then researchers need to carefully examine the source of adventitious ammonia from atmosphere, equipment, chemicals and gases, membrane, and the nitrogen-containing catalyst or support. If ammonia is detected in quantities of an order of magnitude lower than the experiment with  $\text{N}_2$  and applied potential, then the next step would be to conduct an isotope labeling experiment after having assured that no contaminants are present in the gas. If labeled ammonia is detected in comparable amounts to that detected using  $^{14}\text{N}_2$

gas, then the reproducibility needs to be checked and it is safe to report the results. It is worth noting that the importance of following strict experimental procedures for NRR has also been addressed by a few other research groups<sup>79-81</sup>.

In this section, I decided not to report any results from those studies which have failed to fulfill the NRR protocols described above as the data is considered unreliable. Table 2 summarizes the experimental conditions and the results from those studies that meet the essential NRR experimental criteria. It is worth noting that some of these studies still fail to report quantitative data from their isotope labeling experiments.

**Table 2. State of the art on experimental NRR results.**

Catalyst	Electrolyte	T, P	Reaction rate	Current efficiency	Ref.
Mo foil	0.2 M LiClO <sub>4</sub> in 1% ethanol, 99% THF	ambient	11.9 μg h <sup>-1</sup> cm <sup>-2</sup>	7.5	39*
Nb <sub>3</sub> O <sub>7</sub> (OH)/CFC	0.1 M Na <sub>2</sub> SO <sub>4</sub>	ambient	622 μg h <sup>-1</sup> mg <sup>-1</sup>	39.9	82*
N-doped nanocarbon/Fe <sub>3</sub> C	0.1 M KOH	ambient	0.88‡ μg h <sup>-1</sup> mg <sup>-1</sup>	2.72	83
1) Fe/FTO, 2) Fe/NF, 3) Fe/SS	a) [C4mpyr][eFAP] <sup>†</sup> b) [P6,6,6,14][eFAP] <sup>†</sup>	ambient	3,a) 2.22‡ μg h <sup>-1</sup> mg <sup>-1</sup>	1,b) 60	84*
Cu disk	0.2 M LiBF <sub>4</sub> + 0.1 M [P6,6,6,14][eFAP] in THF	ambient T, 20 bar	3249.3 μg h <sup>-1</sup> cm <sup>-2</sup>	69	85*
Li plated on SSC	1 M LiBF <sub>4</sub> , 0.1 M ethanol	ambient	620.16‡ μg h <sup>-1</sup> mg <sup>-1</sup>	35.3	86
Single atom Fe on MoS <sub>2</sub> nanosheet	0.1 M KCl	ambient	97.5 μg h <sup>-1</sup> mg <sup>-1</sup>	31.6	87
FeSnO <sub>2</sub>	0.1 M HCl	ambient	82.7 μg h <sup>-1</sup> mg <sup>-1</sup>	20.4	88
Single atom Yt on carbon coated TiO <sub>2</sub>	0.1 M HCl	ambient	6.3 μg h <sup>-1</sup> mg <sup>-1</sup>	11	89
Pd nanoparticles	0.1 M Li <sub>2</sub> SO <sub>4</sub>	ambient	24.3 μg h <sup>-1</sup> mg <sup>-1</sup>	36.6	90
VN nanodots in graphite	0.1 M HCl	ambient	20.5 μg h <sup>-1</sup> mg <sup>-1</sup>	8.6	91*
Zirconia nanofiber	0.1 M Na <sub>2</sub> SO <sub>4</sub>	ambient	9.63 μg h <sup>-1</sup> mg <sup>-1</sup>	12.1	92
Mo foil	0.3 M LiClO <sub>4</sub> in 99% THF, 1% ethanol	ambient T, 10 bar	Not specified	37	93*
Ru on carbon black	0.1 M phosphate buffer solution	ambient	60.7 μg h <sup>-1</sup> cm <sup>-2</sup>	64.8	94
CuAu@Cu	0.1 M HCl	ambient	33.9 μg h <sup>-1</sup> mg <sup>-1</sup>	24.1	95*
Carbon-based catalyst in Proton-filtering covalent organic framework	0.1 M HCl	ambient	287.2 μg h <sup>-1</sup> mg <sup>-1</sup>	54.5	96*
Pd icosahedron	0.1 M Li <sub>2</sub> SO <sub>4</sub>	ambient	43.9 μg h <sup>-1</sup> mg <sup>-1</sup>	31.98	97*

<sup>†</sup> Ionic liquid

<sup>‡</sup> Converted to this unit based on the data provided in the paper

\* Quantitative isotope labeling is done.

The experiments done within this PhD thesis are not only in thorough fulfilment of the experimental NRR protocols, but also one step forward and beyond the state-of-the-art methodologies. In this research, TMN and TMON thin-film catalysts are applied in an electrochemical micro-reactor flow-cell which is connected in-line to an ammonia detection and measurement unit. The direct connection of these two units minimizes the external contaminations to a great deal as the samples are at all times confined in clean gas-tight tubes and never taken out and gone through manual treatments and thus, never in contact with the surrounding environment, human breath, nitril gloves, and unnecessary extra glassware. Another advantage of this in-line synthesis and measurement system is the fast acquirement of results after few minutes of electrochemical reactions. This immediately gives researchers ideas about how to optimize and continue with the electrochemical methods applications in much shorter time and of course with much less labor work. The ammonia measurement itself is done using flow injection analysis (FIA)/ sequential injection analysis (SIA) whose method is by far the most sensitive ammonia detection method with as low as 1 ppb limit of detection (LOD), outperforming other common ammonia measurement techniques used by researchers in this field such as the Nessler reagent, and Bromothymol Blue methods.

Furthermore, using the electrochemical data for guiding the way towards an active and stable catalyst has not been performed before to the extend as within this thesis. Optimization of chronoamperometry technique and voltammetry methods throughout the duration of NRR experiments provide deep learning on the behavior of the systems as the reactions progress. The distinct differences between Ar and N<sub>2</sub> environments, that are usually not recognized well using voltammetry methods, are demonstrated using dynamic electrochemical impedance spectroscopy (DEIS), showing different values/numbers of resistances and capacitances at specific potential ranges between the two media, suggesting the adsorption and reduction process of N<sub>2</sub> on the electrode surface. These electrochemical techniques and their applications are briefly discussed in Chapter 3.



## 3 Electrochemical techniques

Various techniques are devised to study electrochemical reactions; that is chemical reactions that involve the transfer of electrons. Electron transfer from an electrode surface to the species in the electrolyte (reduction process of the species at the cathode) occurs when the lowest unoccupied molecular orbital (LUMO) of the species is at a lower energy level than the electrons in the electrode. Conversely, electron transfer from the species in the electrolyte to an electrode surface (oxidation process of the species at the anode) takes place when the highest occupied molecular orbital (HOMO) of the species is at a higher energy level than the electrons in the electrode<sup>98</sup>. Therefore, the energy level of electrons (Fermi level) defines the way in which electrochemical reactions proceed. This energy level is modulated in various ways through different electrochemical techniques by an external power source or a potentiostat to enable electrochemical reactions, study the behavior of the electrochemical systems, and to measure the thermodynamic and kinetic parameters<sup>99</sup>. In this chapter the electrochemical techniques that were utilized in this study are briefly discussed.

### 3.1 Linear sweep voltammetry

In linear sweep voltammetry (LSV), the applied potential is linearly stepped from an upper limit (E1; no faradaic processes) to a lower limit (E2; faradaic processes), as seen in Figure 16, and the resulting current response is plotted as a function of the applied potential. Note that faradaic processes that give rise to faradaic currents are those that involve the transfer of electrons while non-faradaic (capacitive) processes are those that involve the rearrangement of ions in the electrical double layer (EDL) and thereby give rise to capacitive or charging currents<sup>99</sup>.

At E1 no faradaic processes take place as this potential does not provide enough energy to alter the Fermi level of the electrons to the extent that makes electron transfer possible. The current response is then only that of the charging current. As the potential is scanned to more negative values, electron transfer at the electrode-electrolyte interface becomes possible and the species at the interface are reduced. The resulting current is termed as faradaic current. The potential at which this process is enabled is called the onset potential (OP).

The slope of the plot of E vs. t is the potential scan rate which directly affects the magnitude of the peak current. At lower scan rates, the sweep from E1 to E2 takes longer time and thus, the diffusion layer grows much further from the electrode. This causes a decline in the flux of the species to the electrode surface and therefore, lower reduction current compared to the case with higher potential scan rate, as explained by the Fick's laws<sup>100</sup>. For those reactions with fast electron transfer kinetics, the potential at which the maximum reduction current is achieved ( $E_p$ ) stays unchanged with varying scan rates.

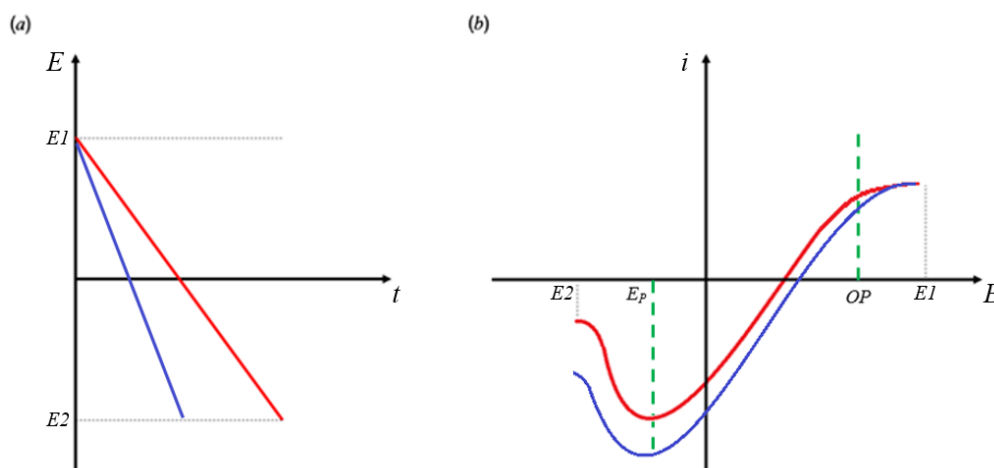


**Figure 16. Linear sweep voltammetry (LSV).** (a) Linear potential step from  $E1$  to  $E2$  as a function of time. Potential scan rate is higher in the case shown as a blue line compared to the red one. (b) the corresponding current response as a function of the applied potential. The maximum reduction current achieved at  $EP$  increases with the increase in the potential scan rate.

An important parameter derived from the LSV curves at very low scan rates is the Tafel slope. Tafel slope conveys the energy required to increase the current by a factor of 10 and initiate the faradaic processes in a system that it is almost unaltered<sup>101</sup>. To calculate the Tafel slope, first we need to consider the Butler-Volmer equation that describes simple redox reactions:

$$j = j_0 \left\{ \exp\left(-\alpha \frac{F}{RT} \eta\right) - \exp\left[\left(1 - \alpha\right) \frac{F}{RT} \eta\right] \right\} \quad (3.1)$$

where  $\alpha$  is the transfer coefficient,  $\eta$  defines the overpotential which is the difference between the electrode and standard potentials ( $E - E^\circ$ ),  $F$  is the Faraday's constant,  $R$  is the universal gas constant,  $T$  is the temperature,  $j_0$  is the exchange current density, and  $j$  is the total current densities from both reduction and oxidation reactions with opposite signs. Now, if we just consider the reduction process, the following equation can be derived from equation 3.1:

$$\eta = \frac{RT}{\alpha F} \ln(j_0) - \frac{RT}{\alpha F} \ln(j) \quad (3.2)$$

Therefore,  $\eta$  vs.  $\ln(j)$  is a linear plot whose slope and intercept define the Tafel Slope and the exchange current density, respectively. These two parameters give insight about the reaction mechanism, by knowing the RDS, and the catalytic activity<sup>102,103</sup> which is discussed in detail for NRR experiments in Paper II attached to this thesis.

## 3.2 Cyclic voltammetry

Cyclic voltammetry (CV) is a popular technique that is used in almost all electrochemical studies. As the name suggests, it is performed by cycling the potential of the catalyst

(working electrode) in a specific window and measuring the resulting current. In another sense, it is an extension of the LSV by adding a reverse scan from the final potential ( $E_2$ ) back to the initial potential ( $E_1$ ) as seen in Figure 17(a). The outcome of this technique is a plot (Figure 17(b)) in which the parameter that is imposed on the system ( $E$ ; applied potential) is put on the x-axis while the y-axis is the system response ( $i$ ; current).

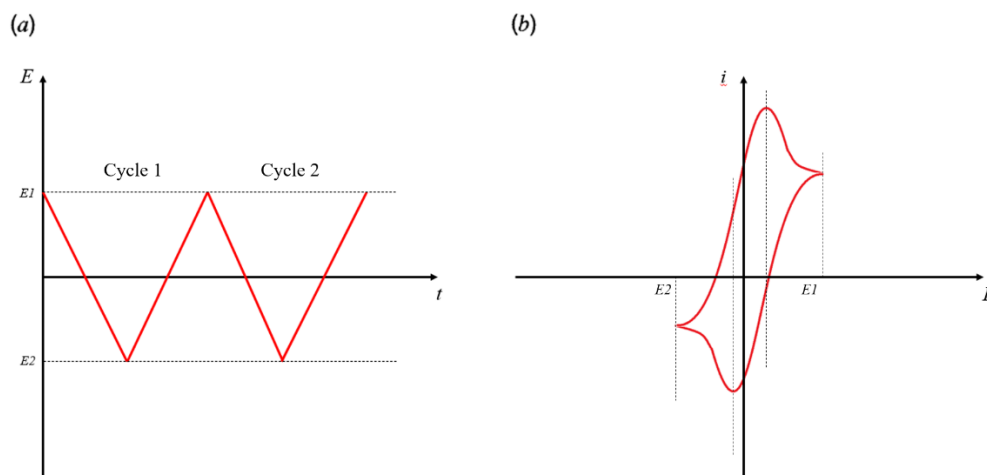


**Figure 17. Cyclic voltammetry (CV). (a) Linear potential step from  $E_1$  to  $E_2$  and back to  $E_1$  again as a function of time. The potential cycling is shown for two cycles. (b) the corresponding current response as a function of the applied potential. Here the current response is only shown for one cycle.**

This plot provides both qualitative and quantitative information about the system under study. Qualitatively, it is possible to observe the presence of intermediates, by following the number of redox peaks, as well as the reversibility of the redox reactions by observing an oxidation peak corresponding to a reduction peak (with a difference of no more than 60 mV)<sup>103</sup>. Quantitatively, it is possible to obtain the catalysts' active surface area and specific capacitance from cyclic voltammograms, however, these quantitative analyses were not practiced as a part of this thesis.

It is also possible to run multiple cycles of CV and track down the changes in the current density, position of peaks, and the onset potential. This gives an insight about the stability of the catalyst. In the studies done within this thesis, this technique is used as one of the methods to track the stability of the surfaces throughout the whole duration of the experiments. Additionally, in NRR experiments, CV is recorded under  $N_{2(g)}$  and  $Ar_{(g)}$  media where any shift in the current response and onset potential in  $N_{2(g)}$  vs.  $Ar_{(g)}$  are taken as the positive effect of the presence of  $N_2$  molecules in the environment which leads to its adsorption and reduction on the catalyst's active sites.

### 3.3 Chronoamperometry

Chronoamperometry is a technique in which the current response to a potential step ( $\Delta E$ ) is recorded as a function of time ( $t$ ). This technique is used to study the kinetics of chemical reactions, diffusion processes, and adsorption<sup>99,104</sup>. Figure 18(a) shows a potential step, as a consequence of which a current response is generated (Figure 18(b)), with  $\tau$  being the time of the potential step. The current response yields useful information about the system under study.

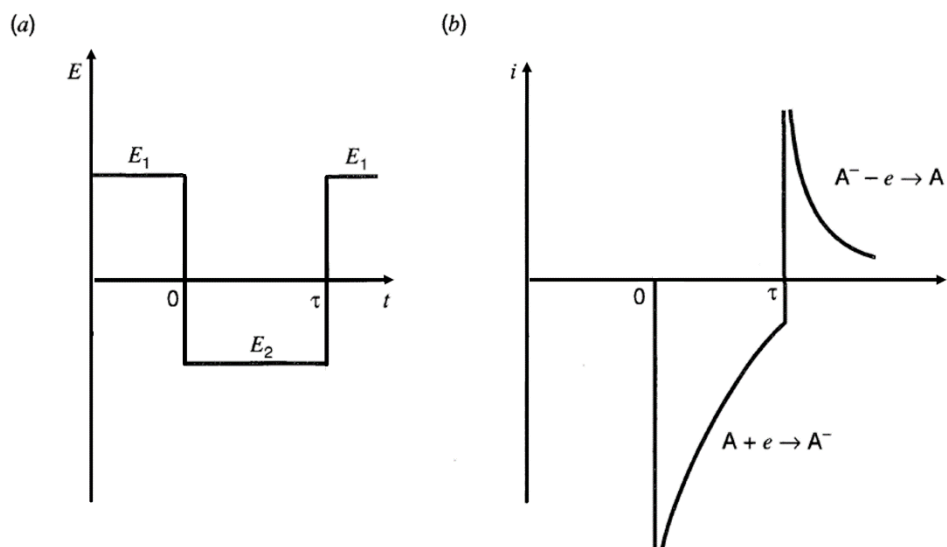


**Figure 18. Chronoamperometry with a double potential step. (a) Potential (E) step as a function of time, and (b) the corresponding current response as a function of time. Adapted from [94] with slight modifications.**

$E_1$  in Figure 18 is a potential at which no faradaic processes occur. Stepping the potential to  $E_2$  results in a current response, whose shape suggests that (i) reduction of specie A at the electrode surface is instant; and (ii) from 0 to  $\tau$ , reduction reaction is diffusion-controlled that is the rate of the reduction reaction is limited by the diffusion of specie A towards the electrode; (iii) from 0 to  $\tau$ , there is a buildup of  $A^-$  near the electrode; (iv) at time  $\tau$ , oxidation of  $A^-$  is instant; and (v) after  $\tau$ , the oxidation reaction is diffusion-controlled. In such a system which is unstirred and diffusion-controlled, current decays with  $t^{1/2}$  and the current response obeys the Cottrell equation:

$$i = \frac{nFAD_0^{1/2}C_0}{\pi^{1/2}t^{1/2}} \quad (3.3)$$

where  $n$  is the number of electrons in the redox process,  $F$  is the Faraday constant,  $A$  is electrode area,  $D_0$  is the diffusion coefficient of the redox species,  $C_0$  is the bulk concentration of the redox species, and  $t$  is time. By conducting the chronoamperometry technique, it is possible to define either the electrode area, diffusion coefficient, or sample concentration provided that two of these variables are known and as long as the adsorption is negligible<sup>104,105</sup>.

In the NRR experiments performed in this thesis, chronoamperometry at different potentials is used mainly for ammonia synthesis, and the calculations of reaction rates and current efficiencies. However, the way this technique is implemented is to repeat a cycle of applied potential and open circuit potential (OCP) measurement for ca. 30 minutes for the ammonia synthesis purpose. Recording the OCP in between the applied potentials is done to free the catalyst's active sites that might have been blocked by other species in the electrolyte and to allow  $N_{2(g)}$  to have access the vacancies. On the importance of  $N_{2(g)}$  access to the catalyst, it is worth to note that the electrochemical cell used in our studies is a two-compartment three-electrode micro-reactor flow-cell that allows the direct gas flow inside the working compartment (refer to Papers II and III, supporting information, Section 2).

### 3.4 Differential pulse voltammetry

Differential pulse voltammetry (DPV) is a sensitive technique in which amplitude potential pulses are applied on a linear ramp potential<sup>99</sup>. The base potential ( $E_1$ ) is where no faradaic processes take place. This base potential is then increased by equal increment pulses until reaching  $E_2$  as seen in Figure 19. Note that we refer to the increase in potential when its value tends to more negative values. The resulting currents before and after the pulse application are recorded and the difference in current is plotted as a function of the base potential. This pulse technique is sensitive as it minimizes the capacitive current and thus, enables the observation of possible reduction peaks in the capacitive zone that would otherwise not be recognized in the other voltametric studies described above<sup>99</sup>.

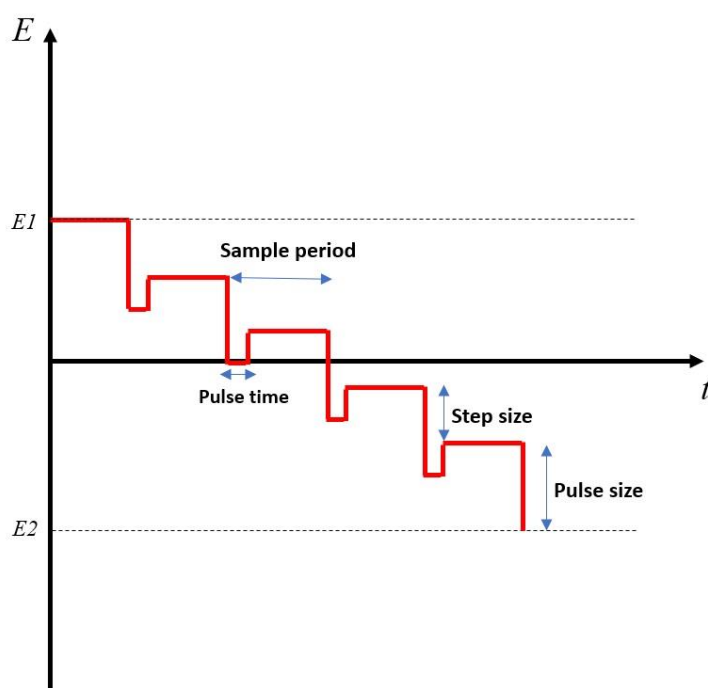


**Figure 19. Illustration of the differential pulse voltammetry (DPV) technique. Typical parameters values are: 5 mV for step size, 25 mV for pulse size, 50 ms for pulse time, and 0.5 s for sample period.**

Figure 20 shows an overlay of two LSV and DPV curves recorded using a TiN surface in  $K_2SO_4$  electrolyte in  $N_2$  environment. No reduction peak is observed in the LSV curve in the capacitive zone up to the onset potential at around -1 V vs. Ag/AgCl. However, using DPV, it is possible to observe a clear reduction peak at around -0.8 V vs. Ag/AgCl. This technique thus helps to identify the potentials that need to be studied for catalysis studies.

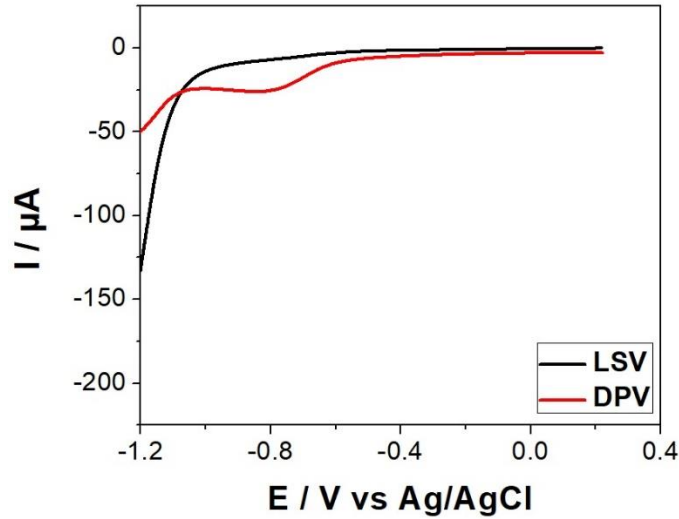


Figure 20. Current response as a function of applied potential in two techniques of LSV (black line) and DPV (red line) recorded using a TiN surface in  $K_2SO_4$  electrolyte saturated with  $N_2$  gas in a three-electrode H-cell setup.

### 3.5 Electrochemical impedance spectroscopy

The electrical behavior of an electrochemical system is best described by the analysis of electrochemical impedance spectroscopy (EIS). This technique focuses on the electrolyte side of the interface between electrode and electrolyte and develops models based on the frequency response of the electrochemical system. The parameters that are finally identified and determined from the developed models, help to understand the behavior of the system under study<sup>99</sup>.

Unlike the so far mentioned electrochemical techniques in which direct current (DC) potentials are applied to the electrodes, in the EIS technique a time-independent DC potential is applied with a time harmonic oscillating electric or alternative current (AC) potential most commonly with a frequency range of  $10^5 - 10^{-2}$  Hz<sup>106</sup>. The input potential is in the form of a sinusoidal signal,  $E = E_0 \sin(\omega t = 2\pi f t)$ , and the resulting current is also in the form of a sinusoidal wave with a phase shift,  $I = I_0 \sin(\omega t + \varphi)$ . Following Ohm's law, the impedance is thus:

$$Z = \frac{E}{I} = \frac{E_0}{I_0} \frac{\sin(\omega t)}{\sin(\omega t + \varphi)} = Z_0 \exp(j\varphi) = Z_0 (\cos\varphi + j\sin(\varphi)) \quad (3.4)$$

Where  $E_0$ , and  $I_0$ , are the amplitude of the potential, and the current signals, respectively,  $\omega$  is the radial frequency,  $\varphi$  is the phase shift, and  $Z_0$  is the magnitude of the impedance following Ohm's law when  $E$  and  $I$  are in the same phase. Therefore, impedance is a complex value consisting of a real and an imaginary component. The plot of the imaginary component ( $Z'' = Z_0 \sin\varphi$ ) as a function of the real component ( $Z' = Z_0 \cos\varphi$ ) in all the frequency range results in the Nyquist plot, while the plots of the total impedance ( $|Z|$  or the impedance modulus) as well as the phase angle as a function of the applied frequency ( $f$ ) result in the Bode plot. These plots describe the whole electrochemical system in terms of electrical

parameters such as charge transfer resistivities ( $R_{ct}$ ), capacitances ( $C_{dl}$ ), inductances ( $L$ ), etc.<sup>107</sup>.

Nyquist plot, an example of which is shown in Figure 21(a), usually consists of one or two semi-circles at high frequency regions, representing the electrolyte and the charge transfer resistance, respectively. In the systems with limitation of mass transport, a non-vertical line is also present at low frequency regions.

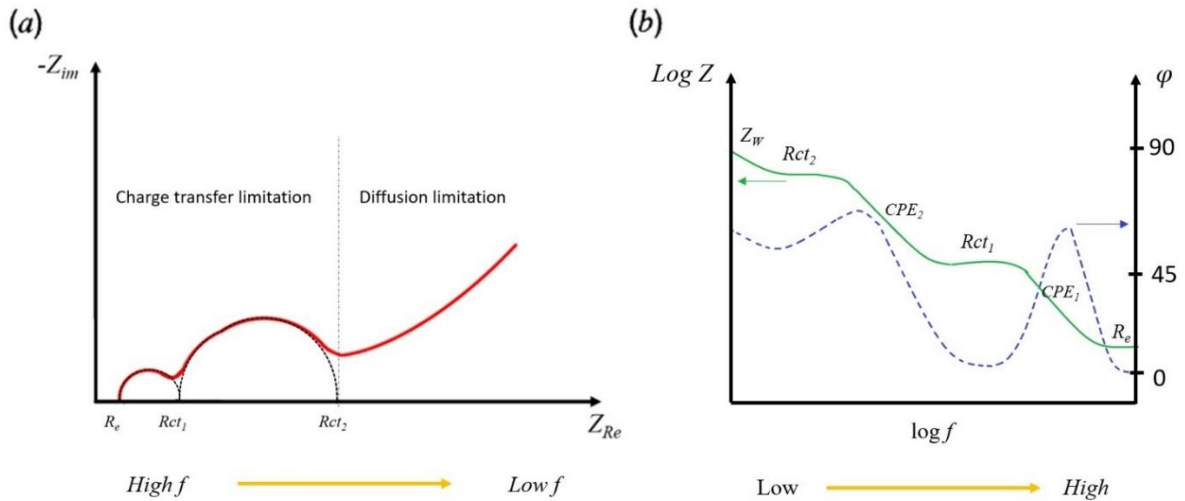


**Figure 21. (a) A typical Nyquist plot showing two semi-circles at higher frequencies and an oblique line at the lower frequency region. (b) the corresponding Bode plot demonstrating the total impedance (green solid line) and the phase angle (blue dashed line) as a function of applied frequency. The elements of the equivalent circuit are marked on the Bode plot.**

The Nyquist and the Bode plots are analyzed using the Z-view software (Scribner Associates ®) where different models of an electrical circuit are fitted to the curves until reaching a model that gives the best goodness of fit ( $\chi^2$ ). Equivalent circuits consist of different elements such as resistors, capacitors (or constant phase elements), inductors, Warburg elements, etc. Figure 22 demonstrates the circuit equivalent to the plots shown in Figure 21.

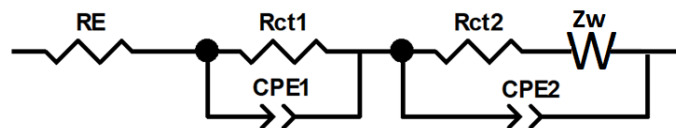


**Figure 22. Equivalent circuit for the data in Figure 21. The model circuit consists of three resistors (describing the electrolyte resistance and two charge transfer resistances), two constant phase elements (describing the capacitance associated with the two resistors), and a Warburg element describing the diffusion-controlled region.**

In this thesis, dynamic electrochemical impedance spectroscopy (DEIS) was implemented for NRR studies (Papers II and III). This means that EIS was carried out at various DC potentials based on the requirements of the experiments. These potentials were selected such that they would cover the open circuit potential, the capacitive zone, onset potential, and the faradaic zone. The changes observed in the EIS plots give insights about the dynamic change of the electrical double layer and electron transfer, as applied potentials tend to more negative values.



## 4 Summary of papers

### 4.1 Paper I

The first paper was sheerly the outcome of a keen observation while working on the NRR experiments. In these experiments, a two-chamber micro-reactor flow-cell was used as the reactor, and the working and the counter electrode chambers were separated by means of a proton exchange membrane, which in our case was always Nafion 211. The common pretreatment procedure of Nafion as practiced today is to use  $\text{H}_2\text{O}_2$  (3–5)% at 80 °C for 1 h to remove organic impurities, next rinsing in 0.1–1 M  $\text{H}_2\text{SO}_4$  at 80 °C for 3 h to eliminate metallic impurities and to protonate the membrane, and finally leaving the membrane in ultrapure water at 80 °C for over 6 hours to rinse the excess acid and reach the maximum expansion. After applying the same methodology, I found out that this procedure was leaving Nafion with a significant amount of ammonia which would have inevitably found its way to the reactor and measured as catalysis product, while being a false positive in essence. The importance of preventing false positives from NRR experiments had previously been stressed enough in a few publications, however, the correct pretreatment of Nafion, the most used membrane in this field, had never been discussed. This made me, dig deeper into the issue, and design more experiments to see how environmental conditions were affecting the degree of contamination.

I started with one of the commonly practiced methods of treatment denoted in the paper as “short treatment” and prepared same-size Nafion pieces (Nafion 211 and 117) in two different containers; polypropylene with screw cap and borosilicate glass beaker covered with Al foil. The same treatment process left the pretreated Nafion in the polypropylene container with randomly and drastically higher ammonia contaminations which was attributed to the containers’ caps popping up at 80 °C throughout the process leaving the Nafion soaking the external contamination which varies on a timely basis. This container was, therefore, not used anymore in our tests. Next, I tried “long treatment” process using glass beakers only. I tested the same glass beaker throughout the whole treatment process vs. using a fresh acid-washed beaker at each step of the process. In both cases, Nafion (211 and 117) pieces were left with noticeable amount of ammonia. The replicates of the same tests yielding various results proved that these contamination levels were dependent on the  $\text{NH}_3$  concentrations in local atmosphere (in Iceland, close to a geothermal drill hole, in direct relationship with environmental  $\text{H}_2\text{S}$  level) that could vary quite drastically between locations world-wide and on daily basis. Finally, I proposed a modification to this process which consisted of four steps of ultrasonic cleaning of Nafion at room temperature, each for a duration of 20 min. The steps included using (i) 5%  $\text{H}_2\text{O}_2$ , (ii) ultrapure water, (iii) 0.5 M  $\text{H}_2\text{SO}_4$ , and (iv) ultrapure water. The membrane was then left for 12 h in ultrapure water at 80 °C. Right before application in the electrochemical setup, the membrane was sonicated in 0.05 M  $\text{H}_2\text{SO}_4$  and ultrapure water. The modified method is not only more practical than commonly used methods, but also rules out the chance of Nafion being a source for ammonia detected in NRR experiments.

## 4.2 Paper II

After spending a great deal of time on setup and method optimizations and having established a robust basis on how to conduct electrochemical NRR as reliably as possible, I started to test some of the catalysts that had previously been predicted by DFT calculations as promising candidates for this reaction. In this manuscript the performance of four TMN catalysts towards nitrogen reduction reaction and ammonia synthesis was investigated. These catalysts included CrN, VN, NbN, and ZrN grown as polycrystalline thin-films and were compared regarding activity, selectivity, and stability. A three-electrode, two-compartment micro-reactor setup was used in all experiments wherein the electrolyte and gas were directly introduced over the working electrode and the working and the counter compartments were separated by a correctly pretreated Nafion 211 membrane. All gas streams in the experiments were purified and deprived of ammonia and NO<sub>x</sub> traces prior to entering the electrochemical setup using two gas washing bottles containing 0.05 M H<sub>2</sub>SO<sub>4</sub> and ultrapure water. Ammonia synthesis was done by means of chronoamperometry loops and accurate measurement of the product was realized in an in-line connection of the electrochemical setup to the ammonia detection unit without manual handling of the samples. Electrochemical impedance spectroscopy was carried out to study the electrical behavior of the system, and cyclic voltammetry technique was implemented at fixed intervals to track the surface changes throughout the experiments. All experiments were done in N<sub>2</sub> and Ar as the reactive and the blank medium, respectively. Surfaces were characterized by means of XRD, XRR, and XPS both before starting the experiments on the pristine samples and after all the experiments.

Results of this study indicate that **ZrN** fulfills all the criteria for an electrochemical NRR catalyst at a certain potential range (-0.6 to -0.8 V vs. RHE). At these two potentials, ammonia is produced when there is access to N<sub>2</sub>(g) but not in its absence i.e., in Ar(g). The highest current efficiency is 1.30% ± 0.59% which is achieved at -0.6 V vs. RHE. In more negative applied potentials, ZrN surface decomposes as increasing amounts of ammonia are detected in an Ar(g) medium. Larger Tafel slopes in Ar vs. N<sub>2</sub> environments which are calculated from linear sweep voltammograms also suggest that an added reaction other than HER is in process in N<sub>2</sub> medium which could be attributed to the NRR. Dynamic EIS studies reveal more capacitance in N<sub>2</sub> vs. Ar which could mean that nitrogen is adsorbed on the surface. The stability of this surface is fairly good throughout the tests in both N<sub>2</sub> and Ar gas and the films experience minimal changes compared to their pristine forms. Ammonia production at -0.6 V and -0.8 V vs. RHE is, unfortunately, not sufficient and falls below the LOD of the <sup>1</sup>H-NMR method (~ 30 ppb). Therefore, the isotope labeling experiment on ZrN is not conducted. Based on previous predictions from DFT calculations on three facets of RS(100), (110), and (111) of ZrN, it seems that the polycrystalline film under experimental conditions predominantly releases ammonia from its (100) facet since there is a close agreement between the theoretical and experimental onset potentials. **CrN** surface does not produce ammonia higher than the limit of detection at any stage of the electrochemical characterization and chronoamperometry studies although it shows significant current density responses. Out of the DFT calculation analysis it was confirmed that this surface is always adsorbing more stable species like H<sup>+</sup>, OH<sup>-</sup>, and O<sup>2-</sup> in all the potential ranges and there is no potential window in which none of these species are adsorbed to the surface. This is believed to be the reason that N<sub>2</sub> can never be adsorbed to the surface and reduced. **VN** and **NbN** surfaces both produce ammonia by releasing their inherent N atoms in the beginning of electrochemical experiments. Based on theoretical onset potential

determinations from DFT data, it is believed that ammonia production on NbN is dominantly from the RS(100) facet while VN has all its three facets actively involved. Both these surfaces become inactive upon reacting their N atoms of the topmost layers and thus, no further ammonia is produced.

### 4.3 Paper III

NbO<sub>2</sub> was reported by theoretical computations to be among the promising TMO candidates to catalyze NRR. Extensive electrochemical tests on thin films of NbO<sub>2</sub> proved their complete inactivity towards NRR. However, the hybrid class of catalysts mentioned in section 2.1.2 of this thesis seemed to have promising features enhancing the performance of the NRR catalysts. As a result, four niobium oxynitride (NbO<sub>x</sub>N<sub>y</sub>) surfaces with various stoichiometries of non-metals to metal were grown by adjusting the flowrates of O<sub>2</sub> and N<sub>2</sub> during the growth procedure in a magnetron sputtering chamber. We named these surfaces: NbON#1, NbON#2, NbON#3, and NbON#4 and their exact stoichiometries were found by the X-ray photoelectron spectroscopy (XPS) analysis as NbON#1: NbO<sub>0.80</sub>N<sub>0.42</sub>, NbON#2: NbO<sub>0.86</sub>N<sub>0.42</sub>, NbON#3: NbO<sub>1.20</sub>N<sub>0.23</sub>, and NbON#4: NbO<sub>1.28</sub>N<sub>0.24</sub>. The combined stoichiometry of non-metal vs. metal (x+y) were 1.22, 1.28, 1.43, and 1.52, respectively. These surfaces were investigated for the effect of their stoichiometries on the electrochemical behavior of catalyzing the nitrogen reduction reaction at ambient conditions. All experimental preparations, electrochemical setup, the in-line ammonia detection, and the electrochemical methods were as mentioned in the summary of Paper II above.

The differences in the stoichiometries gave rise to different onset potentials and current density responses recorded in cyclic voltammograms in Ar vs. N<sub>2</sub> on each surface as well as in N<sub>2</sub> or Ar on all the surfaces. Ammonia quantification experiments using chronoamperometry technique applied between various negative and positive potentials revealed that the first two surfaces were decomposing in an Ar environment, releasing more ammonia with higher current efficiencies compared to that in an N<sub>2</sub> environment. NbON#3 showed the least activity and selectivity towards NRR compared to the rest. However, NbON#4 which had the highest x+y in the series (1.52), demonstrated higher ammonia production and current efficiency in N<sub>2</sub> vs. Ar at some chronoamperometry potential combinations. Two chronoamperometry loops of A = OCP+0.2 V and B = -0.2 V, and A = OCP+0.2 V and B = -0.4 V yield the highest current efficiency and reaction rate for this surface;  $1.5 \times 10^{-12} \pm 7.9 \times 10^{-14} \text{ mol cm}^{-2} \text{ s}^{-1}$ ,  $8.47 \pm 0.45\%$  and  $2.3 \times 10^{-12} \pm 3.5 \times 10^{-13} \text{ mol cm}^{-2} \text{ s}^{-1}$ ,  $5.57 \pm 0.82\%$ , respectively. Electrochemical impedance spectroscopy in N<sub>2</sub> medium at the onset potential demonstrated two charge transfers for NbON#1 and NbON#2 while there were three charge transfers visible on NbON#3 and NbON#4. In Ar medium, all the surfaces showed only two charge transfers. The two charge transfers were attributed to hydrogen evolution reaction (HER) and lattice oxide reduction reaction (ORR). However, the extra third charge transfer in N<sub>2</sub> environment was attributed to the only extra reaction that was possible in this environment which was NRR. Based on these observations plus the fact that these surfaces released ammonia at open circuit potential (OCP), a mechanism for NRR was proposed wherein three protons were adsorbed to the lattice N producing the first ammonia and forming an N vacancy on the surface. Nitrogen was next adsorbed on the N vacancy and reduced. Next, three protons were adsorbed to the surface N atom. Finally, the second ammonia was desorbed, and surface was replenished. Although, these observations were quite promising in demonstrating the catalytic behavior of the surfaces, <sup>15</sup>N<sub>2</sub> isotope labelling

yielded only  $^{14}\text{N}$  ammonia, meaning that the catalytic system was not stable enough to maintain the MvK mechanism and produce detectable  $^{15}\text{NH}_3$  with the GC-MS methodology.

# 5 Conclusion and outlook

## 5.1 Conclusion

When I started my Ph.D. studies in 2016, the NRR field was a lot different from how I find it today. The keen reader would realize this simply by looking at Figure 15 in this thesis. At that time, the scientific society was rather a “quiet place”. But soon this peaceful world was bombarded by massive number of publications claiming to excel previous works by reporting high records of ammonia reaction rates and current efficiencies, fighting over the first place in simple terms. This is not all bad in a sense, but sadly enough, most scientists publishing these articles, were not cautious about the very many sources of external contaminations that would jeopardize their research, and (either aware or unaware) contributed to this chaos. Interestingly, those times coincided with my NRR studies yielding promising preliminary results, however, before any attempt to publish, I was insightfully instructed to study all the possible sources of false positives in my studies and that was the time when the exciting results turned unattractive. At that time, we built our self-protocols, which is schematically described in Paper III, and always stucked to it. A couple of years after that, the importance of NRR protocols were stressed by few research groups in the form of published papers which were truly noticed. However, it is only recently that researchers are beginning to realize the importance of following strict NRR protocols and implementing them in their studies. I grew up in these five years as did the whole NRR field and I can say for sure that the *electrosynthesis of ammonia at ambient conditions in the laboratory scale is challenging but not impossible*. These challenges mainly root in the correct performance of experiments which should consequently lead to correct and reliable data reported from the experiments. Therefore, I have done my best in this research and focused a great deal of attention on securing reliable data and therefore, my reported results are not subjected to any uncertainty (to the best of my knowledge). Referring to Table 2 in this thesis and comparing the results in Papers II and III with these reports, it is clear to the reader that I have not, so far, accomplished to reach higher ammonia reaction rates and current efficiencies. However, this project is not coming into a halt at this point and more research based on the lessons learned is on the plan. I am, overall, happy and satisfied that the methodologies presented in this thesis can be elucidating guidelines for researchers, improving the quality of future reports in this field.

This project goes beyond the state of the art in the following manner:

- a) **Addressing research question 1: (Right now, that the majority of researchers in this field utilize H-cell reactors for ammonia synthesis, is there a possibility to use flow-cell reactors with the added benefit of automatic sample collection and higher surface to volume ratio?)** An electrochemical micro-reactor flow-cell with the possibility of creating a three-phase contact takes advantage of small volumes of electrolyte continuously fed to the system with optimized flowrates. This is while the majority of the NRR research is done in H-cell type reactors where larger volumes of electrolytes are fed initially to the system. The benefit of using a micro-reactor

over a H-cell reactor is the faster achievement of detectable amounts of ammonia higher than the LOD values, and its facile connection to in-line product quantification units. The design of our modified micro-reactor flow-cell is described in detail in the supplementary information of Papers II and III.

- b) **Addressing research question 2: (Since almost all the methods of NRR samples analysis commonly used by researchers include manual sample preparation, how is it possible to integrate an automated ammonia analysis method to the electrochemical setup?)** A direct connection of the electrochemical system to an in-line ammonia quantification system not only reduces the possibility of introducing external contamination to the experimental samples, but also reduces the labor work associated with sample preparation and analysis. The usual practiced method in most of the laboratories, however, is to manually take samples from the H-cell reactor and prepare the sample for analysis by manual treatment. This increases the chance of contamination from adventitious ammonia in the surroundings and the equipment and thus, not repeatable and reliable results may be obtained. The in-line ammonia quantification setup was used in all electrochemical experiments and reported in detail in the supplementary information of Papers II and III.
- c) **Addressing research question 2:** The ammonia measurement method developed by FIALab and modified in this research, has so far, the most sensitive LOD (~ 1 ppb) which is over 10 and 20 times lower than that of the commonly used indophenol blue and Nessler reagent quantification methods, respectively. FIA method was used throughout this thesis for ammonia quantification and the details of the process are elaborated in the supplementary information of Papers I, II, and III.
- d) **Addressing research question 3: (What are the NRR experimental protocols that are often ignored by researchers and therefore question their reported results?)** Here in this thesis and in more details in Paper I, I demonstrate how the commonly used Nafion membrane in the NRR experiments can be a random source of ammonia contamination to the electrochemical environment if not pretreated correctly. An improved pretreatment method is presented, as well, that guarantees ammonia-free membranes before starting NRR experiments.
- e) **Addressing research question 4: (Application of various electrochemical techniques)** Within this project and in more details in Paper II and III, I demonstrate the importance of utilizing various electrochemical measurements to understand the system responses in the presence and the absence of nitrogen, and the possible underlying reaction mechanism by analyzing the agreement/disagreement of one technique vs. the others.
- f) **Addressing research question 5: (How does the combined results from catalyst characterization analysis and ammonia production align with the results from the electrochemical characterizations?)** Integrating surface analysis into quantitative ammonia analysis as employed in Paper II is based on XRR analysis. The method relies on our knowledge of the number of N atoms initially and finally present in the catalyst i.e., before and after each experiment. The difference between the initial and the final state yields the “N atoms of the catalyst consumed” in the experiment. On the other hand, the total produced ammonia in the experiments can also be easily converted to equivalent “N atoms/ NH<sub>3</sub> molecules produced”. The

comparison of these two gives a clearer image of the source of the produced ammonia.

- g) **Addressing research question 6: (Are transition metal nitrides, that had previously been selected by theoretical computations, promising candidates for electrochemical NRR under ambient conditions?)** The results of Paper II show that polycrystalline ZrN, previously identified by DFT as promising candidate for NRR, demonstrates catalytic responses within certain potential windows. ZrN is stable and produces ammonia catalytically with a low reaction rate and current efficiency at -0.6 V to -0.8 V vs. RHE. This production is, unfortunately, not sufficient and falls below the LOD of the  $^1\text{H-NMR}$  method ( $\sim 30$  ppb). Therefore, the isotope labeling experiment on ZrN appear to be a waste of time and precious  $^{15}\text{N}_2$  gas. We are currently working on improving our electrodes and cell design to overcome this challenge.
- h) **Addressing research question 7: (Does the presence of oxygen in the lattice structure of the transition metal nitrides affect the activity and stability of the catalysts?)** What is concluded from Paper III is that niobium oxynitride thin films demonstrate catalytic responses within certain potential windows.  $\text{NbO}_{1.28}\text{N}_{0.24}$  shows distinct electrochemical responses in  $\text{N}_2$  vs. Ar environment suggesting an electrocatalytic process; however, the catalyst is not stable enough and decomposes. This is proved by conducting isotope labeling experiment and sample analysis using GC-MS. For this aim a method to concentrate ammonia in samples and its derivatization in the form of benzenesulfonamide was devised and optimized. This study did not prove catalysis since the isotope-labeled form of the derivatized product was not measured in any of the samples. The promising behavior of this surface, however, can benefit from an improved electrode and cell design; the first steps towards which have already been taken.

## 5.2 Outlook

Currently, numerous NRR studies are being conducted globally, a large proportion of which still fail to follow the required protocols. It is hoped that this proportion increases in the future. The electrochemical NRR field is still in its infancy and there are still many opportunities for optimization, and research and development before commercialization becomes feasible. For an NRR process to become economically feasible, the reaction rate must surpass a value of  $10^{-9}$  mol  $\text{cm}^{-2}$   $\text{s}^{-1}$ . So far, researchers have tried to make use of high surface area catalysts, thin-film, or spiral wound type electrode configurations, as well as optimizing catalysts' thickness to overcome this issue to some extent.<sup>[84]</sup> Engineering the catalyst/substrates to provide more reactants for the active reaction sites is another strategy that has gained a lot of attention recently. Most of these strategies bear serious mass transport problems and is still in the stage of development.

Another factor that is of paramount importance is the long-term stability of the catalysts. Catalysts performing under ambient conditions have limited life cycle which is in most cases less than 1 h. This is an obstacle on the way to industrial application where years of life cycle is demanded. This stems from a great lack of fundamental understandings in reaction mechanisms, intermediate species generation and consumptions, rate determining steps, etc.

in real experimental conditions. Under such conditions, catalysts can readily undergo poisoning and deactivation if not treated correctly. Adsorption of reactants and desorption of products are the two main steps that need accurate control while applying electrochemical techniques. Therefore, this gap between theoretical computations and experimental applications needs to become narrower and eventually lifted which inevitably demands much longer and more expensive computations. The constant interplay between experiment and theory should then boost the performance of the catalysts.

## References

- [1] Roser, M. (2019). Future Population Growth. Published online at OurWorldInData.org. Retrieved from: '<https://ourworldindata.org/future-population-growth>'.
- [2] Liu X, Elgowainy A, Wang M. Life cycle energy use and greenhouse gas emissions of ammonia production from renewable resources and industrial by-products. *Green Chemistry*. **2020**;22(17):5751-61.
- [3] Smil V. Detonator of the population explosion. *Nature*. **1999** Jul;400(6743):415-.
- [4] Dance I. A molecular pathway for the egress of ammonia produced by nitrogenase. *Scientific reports*. **2013** Nov 18;3(1):1-9.
- [5] Burgess BK, Lowe DJ. Mechanism of molybdenum nitrogenase. *Chemical reviews*. **1996** Nov 7;96(7):2983-3012.
- [6] Foster SL, Bakovic SI, Duda RD, Maheshwari S, Milton RD, Minter SD, Janik MJ, Renner JN, Greenlee LF. Catalysts for nitrogen reduction to ammonia. *Nature Catalysis*. **2018** Jul;1(7):490-500.
- [7] Capdevila-Cortada M. Electrifying the Haber–Bosch. *Nature Catalysis*. **2019** Dec;2(12):1055-.
- [8] Smith C, Hill AK, Torrente-Murciano L. Current and future role of Haber–Bosch ammonia in a carbon-free energy landscape. *Energy & Environmental Science*. **2020**;13(2):331-44.
- [9] Brown, T. (2017). The Future of Ammonia: Improvement of Haber-Bosch ... or Electrochemical Synthesis? Published online at Ammonia Industry.com. Retrieved from: '<https://ammoniaindustry.com/the-future-of-ammonia-improvement-of-haber-bosch-or-electrochemical-synthesis>'.
- [10] Wang Z, Hu X, Liu Z, Zou G, Wang G, Zhang K. Recent developments in polymeric carbon nitride-derived photocatalysts and electrocatalysts for nitrogen fixation. *ACS Catalysis*. **2019** Oct 2;9(11):10260-78.
- [11] Ithisuphalap K, Zhang H, Guo L, Yang Q, Yang H, Wu G. Photocatalysis and photoelectrocatalysis methods of nitrogen reduction for sustainable ammonia synthesis. *Small Methods*. **2019** Jun;3(6):1800352.
- [12] Patil BS, Wang Q, Hessel V, Lang J. Plasma N<sub>2</sub>-fixation: 1900–2014. *Catalysis today*. **2015** Nov 1;256:49-66.

- [13] Hong J, Praver S, Murphy AB. Plasma catalysis as an alternative route for ammonia production: status, mechanisms, and prospects for progress. *ACS Sustainable Chemistry & Engineering*. **2018** Jan 2;6(1):15-31.
- [14] Yaala MB, Saeedi A, Scherrer DF, Moser L, Steiner R, Zutter M, Oberkofler M, De Temmerman G, Marot L, Meyer E. Plasma-assisted catalytic formation of ammonia in N<sub>2</sub>-H<sub>2</sub> plasma on a tungsten surface. *Physical Chemistry Chemical Physics*. **2019**;21(30):16623-33.
- [15] Hawtof R, Ghosh S, Guarr E, Xu C, Sankaran RM, Renner JN. Catalyst-free, highly selective synthesis of ammonia from nitrogen and water by a plasma electrolytic system. *Science advances*. **2019** Jan 1;5(1):eaat5778.
- [16] MacLeod KC, Holland PL. Recent developments in the homogeneous reduction of dinitrogen by molybdenum and iron. *Nature chemistry*. **2013** Jul;5(7):559-65.
- [17] Jia HP, Quadrelli EA. Mechanistic aspects of dinitrogen cleavage and hydrogenation to produce ammonia in catalysis and organometallic chemistry: relevance of metal hydride bonds and dihydrogen. *Chemical Society Reviews*. **2014**;43(2):547-64.
- [18] McEnaney JM, Singh AR, Schwalbe JA, Kibsgaard J, Lin JC, Cargnello M, Jaramillo TF, Nørskov JK. Ammonia synthesis from N<sub>2</sub> and H<sub>2</sub>O using a lithium cycling electrification strategy at atmospheric pressure. *Energy & Environmental Science*. **2017**;10(7):1621-30.
- [19] Rosca V, Duca M, de Groot MT, Koper MT. Nitrogen cycle electrocatalysis. *Chemical Reviews*. **2009** Jun 10;109(6):2209-44.
- [20] Kibria MG, Edwards JP, Gabardo CM, Dinh CT, Seifitokaldani A, Sinton D, Sargent EH. Electrochemical CO<sub>2</sub> reduction into chemical feedstocks: from mechanistic electrocatalysis models to system design. *Advanced Materials*. **2019** Aug;31(31):1807166.
- [21] Yazdani A, Botte GG. Perspectives of electrocatalysis in the chemical industry: a platform for energy storage. *Current Opinion in Chemical Engineering*. **2020** Sep 1;29:89-95.
- [22] Amar IA, Lan R, Petit CT, Tao S. Solid-state electrochemical synthesis of ammonia: a review. *Journal of Solid State Electrochemistry*. **2011** Sep 1;15(9):1845.
- [23] Marnellos G, Zisekas S, Stoukides M. Synthesis of ammonia at atmospheric pressure with the use of solid state proton conductors. *Journal of Catalysis*. **2000** Jul 1;193(1):80-7.
- [24] Kyriakou V, Garagounis I, Vasileiou E, Vourros A, Stoukides M. Progress in the electrochemical synthesis of ammonia. *Catalysis Today*. **2017** May 15;286:2-13.
- [25] Li C, Wang T, Gong J. Alternative strategies toward sustainable ammonia synthesis. *Transactions of Tianjin University*. **2020** Apr;26(2):67-91.
- [26] Murakami T, Nishikiori T, Nohira T, Ito Y. Electrolytic synthesis of ammonia in molten salts under atmospheric pressure. *Journal of the American Chemical Society*. **2003** Jan 15;125(2):334-5.

- [27] Murakami T, Nohira T, Araki Y, Goto T, Hagiwara R, Ogata YH. Electrolytic synthesis of ammonia from water and nitrogen under atmospheric pressure using a boron-doped diamond electrode as a nonconsumable anode. *Electrochemical and Solid State Letters*. **2007** Feb 7;10(4):E4.
- [28] Li FF, Licht S. Advances in understanding the mechanism and improved stability of the synthesis of ammonia from air and water in hydroxide suspensions of nanoscale Fe<sub>2</sub>O<sub>3</sub>. *Inorganic chemistry*. **2014** Oct 6;53(19):10042-4.
- [29] Yao Y, Wang J, Shahid UB, Gu M, Wang H, Li H, Shao M. Electrochemical synthesis of ammonia from nitrogen under mild conditions: current status and challenges. *Electrochemical Energy Reviews*. **2020** Jun;3(2):239-70.
- [30] Kordali V, Kyriacou G, Lambrou C. Electrochemical synthesis of ammonia at atmospheric pressure and low temperature in a solid polymer electrolyte cell. *Chemical Communications*. **2000**(17):1673-4.
- [31] Xu G, Liu R, Wang J. Electrochemical synthesis of ammonia using a cell with a Nafion membrane and SmFe<sub>0.7</sub>Cu<sub>0.3-x</sub>Ni<sub>x</sub>O<sub>3</sub> (x= 0– 0.3) cathode at atmospheric pressure and lower temperature. *Science in China Series B: Chemistry*. **2009** Aug 1;52(8):1171-5.
- [32] Renner JN, Greenlee LF, Ayres KE, Herring AM. Electrochemical synthesis of ammonia: a low pressure, low temperature approach. *The Electrochemical Society Interface*. **2015** Jan;24(2):51.
- [33] Kong J, Lim A, Yoon C, Jang JH, Ham HC, Han J, Nam S, Kim D, Sung YE, Choi J, Park HS. Electrochemical synthesis of NH<sub>3</sub> at low temperature and atmospheric pressure using a  $\gamma$ -Fe<sub>2</sub>O<sub>3</sub> catalyst. *ACS Sustainable Chemistry & Engineering*. **2017** Nov 6;5(11):10986-95.
- [34] Nash J, Yang X, Anibal J, Wang J, Yan Y, Xu B. Electrochemical nitrogen reduction reaction on noble metal catalysts in proton and hydroxide exchange membrane electrolyzers. *Journal of The Electrochemical Society*. **2017** Dec 29;164(14):F1712.
- [35] Shipman MA, Symes MD. Recent progress towards the electrosynthesis of ammonia from sustainable resources. *Catalysis Today*. **2017** May 15;286:57-68.
- [36] Van der Ham CJ, Koper MT, Hettterscheid DG. Challenges in reduction of dinitrogen by proton and electron transfer. *Chemical Society Reviews*. **2014**;43(15):5183-91.
- [37] Skulason E, Bligaard T, Gudmundsdóttir S, Studt F, Rossmeisl J, Abild-Pedersen F, Vegge T, Jónsson H, Nørskov JK. A theoretical evaluation of possible transition metal electro-catalysts for N<sub>2</sub> reduction. *Physical Chemistry Chemical Physics*. **2012**;14(3):1235-45.
- [38] Tayyebi E, Abghoui Y, Skulason E. Elucidating the mechanism of electrochemical N<sub>2</sub> reduction at the Ru (0001) electrode. *ACS Catalysis*. **2019** Oct 25;9(12):11137-45.
- [39] Andersen SZ, Čolić V, Yang S, Schwalbe JA, Nielander AC, McEnaney JM, Enemark-Rasmussen K, Baker JG, Singh AR, Rohr BA, Statt MJ. A rigorous

electrochemical ammonia synthesis protocol with quantitative isotope measurements. *Nature*. **2019** Jun;570(7762):504-8.

[40] Ceballos BM, Pilania G, Ramaiyan KP, Banerjee A, Kreller C, Mukundan R. Roads Less Traveled: Nitrogen Reduction Reaction (NRR) Catalyst Design Strategies for Improved Selectivity. *Current Opinion in Electrochemistry*. **2021** Feb 27:100723.

[41] Yao Y, Feng Q, Zhu S, Li J, Yao Y, Wang Y, Wang Q, Gu M, Wang H, Li H, Yuan XZ. Chromium oxynitride electrocatalysts for electrochemical synthesis of ammonia under ambient conditions. *Small Methods*. **2019** Jun;3(6):1800324.

[42] Abghoui Y, Garden AL, Hlynsson VF, Björgvinsdóttir S, Ólafsdóttir H, Skúlason E. Enabling electrochemical reduction of nitrogen to ammonia at ambient conditions through rational catalyst design. *Physical Chemistry Chemical Physics*. **2015**;17(7):4909-18.

[43] Abghoui Y, Garden AL, Howalt JG, Vegge T, Skúlason E. Electroreduction of N<sub>2</sub> to ammonia at ambient conditions on mononitrides of Zr, Nb, Cr, and V: A DFT guide for experiments. *ACS Catalysis*. **2016** Feb 5;6(2):635-46.

[44] Nguyen MT, Seriani N, Gebauer R. Nitrogen electrochemically reduced to ammonia with hematite: density-functional insights. *Physical Chemistry Chemical Physics*. **2015**;17(22):14317-22.

[45] Höskuldsson AB, Abghoui Y, Gunnarsdóttir AB, Skúlason E. Computational screening of rutile oxides for electrochemical ammonia formation. *ACS Sustainable Chemistry & Engineering*. **2017** Nov 6;5(11):10327-33.

[46] Kong W, Liu Z, Han J, Xia L, Wang Y, Liu Q, Shi X, Wu Y, Xu Y, Sun X. Ambient electrochemical N<sub>2</sub>-to-NH<sub>3</sub> fixation enabled by Nb<sub>2</sub>O<sub>5</sub> nanowire array. *Inorganic Chemistry Frontiers*. **2019**;6(2):423-7.

[47] Li Q, Qiu S, He L, Zhang X, Sun C. Impact of H-termination on the nitrogen reduction reaction of molybdenum carbide as an electrochemical catalyst. *Physical Chemistry Chemical Physics*. **2018**;20(36):23338-43.

[48] Shao M, Shao Y, Chen W, Ao KL, Tong R, Zhu Q, Chan IN, Ip WF, Shi X, Pan H. Efficient nitrogen fixation to ammonia on MXenes. *Physical Chemistry Chemical Physics*. **2018**;20(21):14504-12.

[49] Zhang B, Zhou J, Elliott SR, Sun Z. Two-dimensional molybdenum carbides: active electrocatalysts for the nitrogen reduction reaction. *Journal of Materials Chemistry A*. **2020**;8(45):23947-54.

[50] Matanovic I, Garzon FH. Nitrogen electroreduction and hydrogen evolution on cubic molybdenum carbide: a density functional study. *Physical Chemistry Chemical Physics*. **2018**;20(21):14679-87.

[51] Roy PK, Kumar S. Strong Interfacial Electronic Interaction in the Transition-Metal/Mo<sub>2</sub>C Catalyst for Enhanced Ammonia Synthesis at Ambient Pressure: Shift of the Rate Determining Step. *ACS Applied Energy Materials*. **2020** Jul 1;3(7):7167-79.

- [52] Zhang L, Ji X, Ren X, Ma Y, Shi X, Tian Z, Asiri AM, Chen L, Tang B, Sun X. Electrochemical ammonia synthesis via nitrogen reduction reaction on a MoS<sub>2</sub> catalyst: theoretical and experimental studies. *Advanced Materials*. **2018** Jul;30(28):1800191.
- [53] Chen P, Zhang N, Wang S, Zhou T, Tong Y, Ao C, Yan W, Zhang L, Chu W, Wu C, Xie Y. Interfacial engineering of cobalt sulfide/graphene hybrids for highly efficient ammonia electrosynthesis. *Proceedings of the National Academy of Sciences*. **2019** Apr 2;116(14):6635-40.
- [54] Abghoui Y, Sigtryggsson SB, Skúlason E. Biomimetic nitrogen fixation catalyzed by transition metal sulfide surfaces in an electrolytic cell. *ChemSusChem*. **2019** Sep 20;12(18):4265-73.
- [55] Li Q, Liu C, Qiu S, Zhou F, He L, Zhang X, Sun C. Exploration of iron borides as electrochemical catalysts for the nitrogen reduction reaction. *Journal of Materials Chemistry A*. **2019**;7(37):21507-13.
- [56] Yang X, Shang C, Zhou S, Zhao J. MBenes: emerging 2D materials as efficient electrocatalysts for the nitrogen reduction reaction. *Nanoscale Horizons*. **2020**;5(7):1106-15.
- [57] Qi S, Fan Y, Zhao L, Li W, Zhao M. Two-dimensional transition metal borides as highly efficient N<sub>2</sub> fixation catalysts. *Applied Surface Science*. **2021** Jan;536:147742.
- [58] Liu X, Jiao Y, Zheng Y, Qiao SZ. Isolated boron sites for electroreduction of dinitrogen to ammonia. *ACS Catalysis*. **2020** Jan 2;10(3):1847-54.
- [59] Li XF, Li QK, Cheng J, Liu L, Yan Q, Wu Y, Zhang XH, Wang ZY, Qiu Q, Luo Y. Conversion of dinitrogen to ammonia by FeN<sub>3</sub>-embedded graphene. *Journal of the American Chemical Society*. **2016** Jul 20;138(28):8706-9.
- [60] Cao Y, Gao Y, Zhou H, Chen X, Hu H, Deng S, Zhong X, Zhuang G, Wang J. Highly efficient ammonia synthesis electrocatalyst: single Ru atom on naturally nanoporous carbon materials. *Advanced Theory and Simulations*. **2018** May;1(5):1800018.
- [61] Choi C, Back S, Kim NY, Lim J, Kim YH, Jung Y. Suppression of hydrogen evolution reaction in electrochemical N<sub>2</sub> reduction using single-atom catalysts: a computational guideline. *ACS Catalysis*. **2018** Jul 3;8(8):7517-25.
- [62] Ling C, Bai X, Ouyang Y, Du A, Wang J. Single molybdenum atom anchored on N-doped carbon as a promising electrocatalyst for nitrogen reduction into ammonia at ambient conditions. *The Journal of Physical Chemistry C*. **2018** Jul 9;122(29):16842-7.
- [63] Zhao J, Zhao J, Cai Q. Single transition metal atom embedded into a MoS<sub>2</sub> nanosheet as a promising catalyst for electrochemical ammonia synthesis. *Physical Chemistry Chemical Physics*. **2018**;20(14):9248-55.
- [64] Qi J, Gao L, Wei F, Wan Q, Lin S. Design of a high-performance electrocatalyst for N<sub>2</sub> conversion to NH<sub>3</sub> by trapping single metal atoms on stepped CeO<sub>2</sub>. *ACS applied materials & interfaces*. **2019** Nov 26;11(50):47525-34.

- [65] Zhang R, Jiao L, Yang W, Wan G, Jiang HL. Single-atom catalysts templated by metal–organic frameworks for electrochemical nitrogen reduction. *Journal of Materials Chemistry A*. **2019**;7(46):26371-7.
- [66] Zang W, Yang T, Zou H, Xi S, Zhang H, Liu X, Kou Z, Du Y, Feng YP, Shen L, Duan L. Copper single atoms anchored in porous nitrogen-doped carbon as efficient pH-universal catalysts for the nitrogen reduction reaction. *ACS Catalysis*. **2019** Sep 30;9(11):10166-73.
- [67] Lv C, Qian Y, Yan C, Ding Y, Liu Y, Chen G, Yu G. Defect engineering metal-free polymeric carbon nitride electrocatalyst for effective nitrogen fixation under ambient conditions. *Angewandte Chemie*. **2018** Aug 6;130(32):10403-7.
- [68] Ji S, Wang Z, Zhao J. A boron-interstitial doped C<sub>2</sub>N layer as a metal-free electrocatalyst for N<sub>2</sub> fixation: a computational study. *Journal of Materials Chemistry A*. **2019**;7(5):2392-9.
- [69] Li H, Yang L, Wang Z, Jin P, Zhao J, Chen Z. N-heterocyclic carbene as a promising metal-free electrocatalyst with high efficiency for nitrogen reduction to ammonia. *Journal of Energy Chemistry*. **2020** Jul 1;46:78-86.
- [70] Feng Z, Tang Y, Chen W, Wei D, Ma Y, Dai X. O-doped graphdiyne as metal-free catalysts for nitrogen reduction reaction. *Molecular Catalysis*. **2020** Mar 1;483:110705.
- [71] Ma X, Hu J, Zheng M, Li D, Lv H, He H, Huang C. N<sub>2</sub> reduction using single transition-metal atom supported on defective WS<sub>2</sub> monolayer as promising catalysts: a DFT study. *Applied Surface Science*. **2019** Sep 30;489:684-92.
- [72] Li L, Wang X, Guo H, Yao G, Yu H, Tian Z, Li B, Chen L. Theoretical screening of single transition metal atoms embedded in MXene defects as superior electrocatalyst of nitrogen reduction reaction. *Small Methods*. **2019** Nov;3(11):1900337.
- [73] Pan J, Hansen HA, Vegge T. Vanadium oxynitrides as stable catalysts for electrochemical reduction of nitrogen to ammonia: the role of oxygen. *Journal of Materials Chemistry A*. **2020**;8(45):24098-107.
- [74] Lv XW, Liu Y, Hao R, Tian W, Yuan ZY. Urchin-like Al-doped Co<sub>3</sub>O<sub>4</sub> nanospheres rich in surface oxygen vacancies enable efficient ammonia electrosynthesis. *ACS applied materials & interfaces*. **2020** Mar 20;12(15):17502-8.
- [75] Chen X, Li K, Yang X, Lv J, Sun S, Li S, Cheng D, Li B, Li YG, Zang HY. Oxygen vacancy engineering of calcium cobaltate: A nitrogen fixation electrocatalyst at ambient condition in neutral electrolyte. *Nano Research*. **2021** Feb;14(2):501-6.
- [76] Fu Y, Richardson P, Li K, Yu H, Yu B, Donne S, Kisi E, Ma T. Transition Metal Aluminum Boride as a New Candidate for Ambient-Condition Electrochemical Ammonia Synthesis. *Nano-Micro Letters*. **2020** Feb;12(1):1-3.
- [77] Wang Z, Shen J, Fu W, Liao J, Dong J, Zhuang P, Cao Z, Ye Z, Shi J, Ye M. Controlled oxygen vacancy engineering on In<sub>2</sub>O<sub>3-x</sub>/CeO<sub>2-y</sub> nanotubes for highly selective

and efficient electrocatalytic nitrogen reduction. *Inorganic Chemistry Frontiers*. **2020**;7(19):3609-19.

[78] Chen GF, Ren S, Zhang L, Cheng H, Luo Y, Zhu K, Ding LX, Wang H. Advances in electrocatalytic N<sub>2</sub> reduction—strategies to tackle the selectivity challenge. *Small Methods*. **2019** Jun;3(6):1800337.

[79] Tang C, Qiao SZ. How to explore ambient electrocatalytic nitrogen reduction reliably and insightfully. *Chemical Society Reviews*. **2019**;48(12):3166-80.

[80] Suryanto BH, Du HL, Wang D, Chen J, Simonov AN, MacFarlane DR. Challenges and prospects in the catalysis of electroreduction of nitrogen to ammonia. *Nature Catalysis*. **2019** Apr;2(4):290-6.

[81] Choi J, Suryanto BH, Wang D, Du HL, Hodgetts RY, Vallana FM, MacFarlane DR, Simonov AN. Identification and elimination of false positives in electrochemical nitrogen reduction studies. *Nature communications*. **2020** Nov 3;11(1):1-0.

[82] Wu T, Han M, Zhu X, Wang G, Zhang Y, Zhang H, Zhao H. Experimental and theoretical understanding on electrochemical activation and inactivation processes of Nb<sub>3</sub>O<sub>7</sub>(OH) for ambient electrosynthesis of NH<sub>3</sub>. *Journal of Materials Chemistry A*. **2019**;7(28):16969-78.

[83] Cong L, Yu Z, Liu F, Huang W. Electrochemical synthesis of ammonia from N<sub>2</sub> and H<sub>2</sub>O using a typical non-noble metal carbon-based catalyst under ambient conditions. *Catalysis Science & Technology*. **2019**;9(5):1208-14.

[84] Zhou F, Azofra LM, Ali M, Kar M, Simonov AN, McDonnell-Worth C, Sun C, Zhang X, MacFarlane DR. Electro-synthesis of ammonia from nitrogen at ambient temperature and pressure in ionic liquids. *Energy & Environmental Science*. **2017**;10(12):2516-20.

[85] Suryanto BH, Matuszek K, Choi J, Hodgetts RY, Du HL, Bakker JM, Kang CS, Cherepanov PV, Simonov AN, MacFarlane DR. Nitrogen reduction to ammonia at high efficiency and rates based on a phosphonium proton shuttle. *Science*. **2021** Jun 11;372(6547):1187-91.

[86] Lazouski N, Chung M, Williams K, Gala ML, Manthiram K. Non-aqueous gas diffusion electrodes for rapid ammonia synthesis from nitrogen and water-splitting-derived hydrogen. *Nature Catalysis*. **2020** May;3(5):463-9.

[87] Li J, Chen S, Quan F, Zhan G, Jia F, Ai Z, Zhang L. Accelerated dinitrogen electroreduction to ammonia via interfacial polarization triggered by single-atom protrusions. *Chem*. **2020** Apr 9;6(4):885-901.

[88] Zhang L, Cong M, Ding X, Jin Y, Xu F, Wang Y, Chen L, Zhang L. A Janus Fe-SnO<sub>2</sub> Catalyst that Enables Bifunctional Electrochemical Nitrogen Fixation. *Angewandte Chemie*. **2020** Jun 26;132(27):10980-5.

[89] Yang L, Choi C, Hong S, Liu Z, Zhao Z, Yang M, Shen H, Robertson AW, Zhang H, Lo TW, Jung Y. Single yttrium sites on carbon-coated TiO<sub>2</sub> for efficient electrocatalytic N<sub>2</sub> reduction. *Chemical Communications*. **2020**;56(74):10910-3.

- [90] Zhao H, Zhang D, Li H, Qi W, Wu X, Han Y, Cai W, Wang Z, Lai J, Wang L. Exposure of Definite Palladium Facets Boosts Electrocatalytic Nitrogen Fixation at Low Overpotential. *Advanced Energy Materials*. **2020** Oct;10(37):2002131.
- [91] Lv XW, Liu Y, Wang YS, Liu XL, Yuan ZY. Encapsulating vanadium nitride nanodots into N, S-codoped graphitized carbon for synergistic electrocatalytic nitrogen reduction and aqueous Zn-N<sub>2</sub> battery. *Applied Catalysis B: Environmental*. **2021** Jan;280:119434.
- [92] Xia J, Guo H, Cheng M, Chen C, Wang M, Xiang Y, Li T, Traversa E. Electrospun zirconia nanofibers for enhancing the electrochemical synthesis of ammonia by artificial nitrogen fixation. *Journal of Materials Chemistry A*. **2020** Nov 16.
- [93] Andersen SZ, Statt MJ, Bukas VJ, Shapel SG, Pedersen JB, Krempel K, Saccoccio M, Chakraborty D, Kibsgaard J, Vesborg PC, Nørskov J. Increasing stability, efficiency, and fundamental understanding of lithium-mediated electrochemical nitrogen reduction. *Energy & Environmental Science*. **2020**;13(11):4291-300.
- [94] Wei X, Pu M, Jin Y, Wessling M. Efficient Electrocatalytic N<sub>2</sub> Reduction on Three-Phase Interface Coupled in a Three-Compartment Flow Reactor for the Ambient NH<sub>3</sub> Synthesis. *ACS Applied Materials & Interfaces*. **2021** Apr 28;13(18):21411-25.
- [95] Wang P, Nong W, Li Y, Cui H, Wang C. Strengthening nitrogen affinity on CuAu@Cu core-shell nanoparticles with ultrathin Cu skin via strain engineering and ligand effect for boosting nitrogen reduction reaction. *Applied Catalysis B: Environmental*. **2021** Jul 5;288:119999.
- [96] Liu S, Qian T, Wang M, Ji H, Shen X, Wang C, Yan C. Proton-filtering covalent organic frameworks with superior nitrogen penetration flux promote ambient ammonia synthesis. *Nature Catalysis*. **2021** Apr;4(4):322-31.
- [97] Cai W, Han Y, Pan Y, Zhang X, Xu J, Zhang Y, Sun Y, Li S, Lai J, Wang L. The twinned Pd nanocatalyst exhibits sustainable NRR electrocatalytic performance by promoting the desorption of NH<sub>3</sub>. *Journal of Materials Chemistry A*. **2021**;9(23):13483-9.
- [98] González FJ, Frontana C, Gómez M, González I. General Aspects of Redox Chemistry. *Encyclopedia of Physical Organic Chemistry*. **2016** Oct 21:1-9.
- [99] Allen JB, Larry RF. Electrochemical methods fundamentals and applications. John Wiley & Sons; **2001**.
- [100] Ruiz Y, Baeza JA, Montpart N, Moral-Vico J, Baeza M, Guisasola A. Repeatability of low scan rate cyclic voltammetry in bioelectrochemical systems and effects on their performance. *Journal of Chemical Technology & Biotechnology*. **2020** May;95(5):1533-41.
- [101] Fletcher S. Tafel slopes from first principles. *Journal of Solid State Electrochemistry*. **2009** Apr;13(4):537-49.
- [102] Fang YH, Liu ZP. Tafel kinetics of electrocatalytic reactions: from experiment to first-principles. *ACS Catalysis*. **2014** Dec 5;4(12):4364-76.

- [103] Elgrishi N, Rountree KJ, McCarthy BD, Rountree ES, Eisenhart TT, Dempsey JL. A practical beginner's guide to cyclic voltammetry. *Journal of chemical education*. **2018** Feb 13;95(2):197-206.
- [104] Kamat A, Huth A, Klein O, Scholl S. Chronoamperometric investigations of the electrode–electrolyte interface of a commercial high temperature PEM fuel cell. *Fuel Cells*. **2010** Dec;10(6):983-92.
- [105] Ikeuchi H, Sato GP. Determination of diffusion coefficients by means of chronoamperometric methods. *Analytical sciences*. **1991**;7(Supple):631-4.
- [106] Mei BA, Lau J, Lin T, Tolbert SH, Dunn BS, Pilon L. Physical interpretations of electrochemical impedance spectroscopy of redox active electrodes for electrical energy storage. *The Journal of Physical Chemistry C*. **2018** Oct 2;122(43):24499-511.
- [107] Choi W, Shin HC, Kim JM, Choi JY, Yoon WS. Modeling and applications of electrochemical impedance spectroscopy (EIS) for lithium-ion batteries. *Journal of Electrochemical Science and Technology*. **2020** 11(1):1-3.



# Paper I

## **Preparation of Nafion Membranes for Reproducible Ammonia Quantification in Nitrogen Reduction Reaction Experiments**

Hanifpour, F., Sveinbjörnsson, A., Canales, C. P., Skúlason, E., & Flosadóttir, H. D.

**Angewandte Chemie.** 2020, 132(51): 23138-23142.



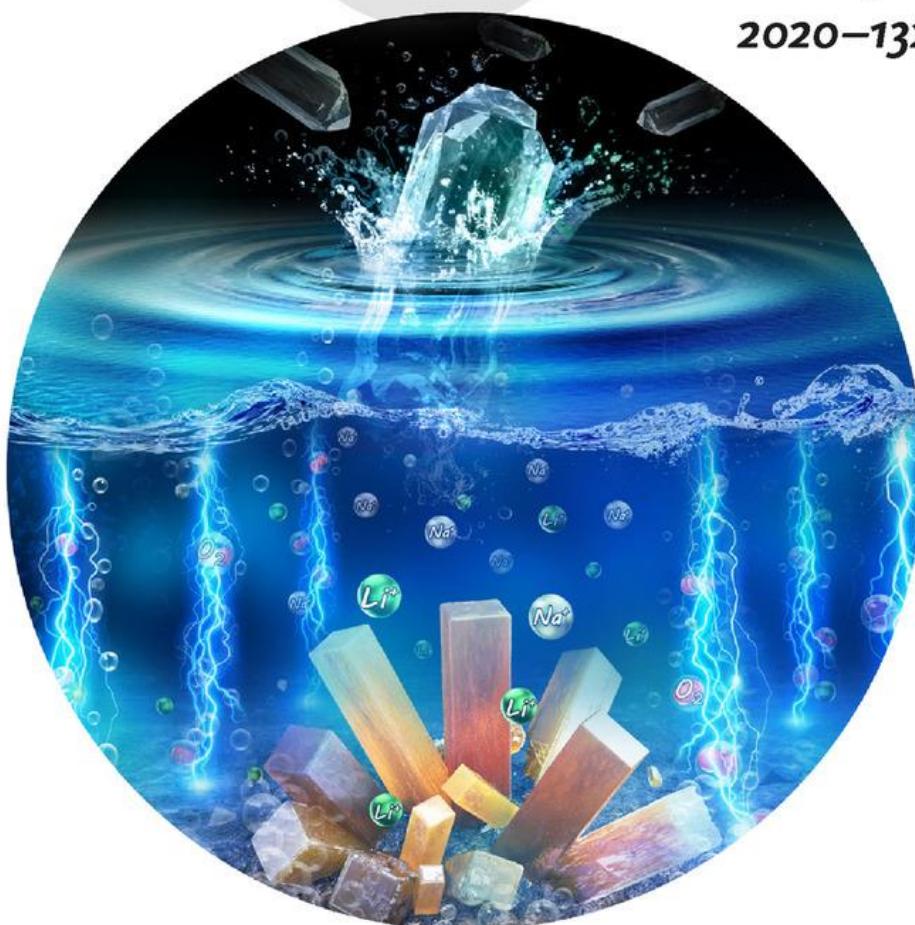
# Angewandte Chemie

GDCh

Eine Zeitschrift der Gesellschaft Deutscher Chemiker

[www.angewandte.de](http://www.angewandte.de)

2020–132/51



## Titelbild

*J. Lu, K. Amine et al.*

Cation Additive Enabled Rechargeable LiOH-Based  
Lithium–Oxygen Batteries

ANCEAD 132 (51) 22993–23548 (2020) · ISSN 0044–8249 · Vol. 132 · No. 51

WILEY-VCH



**Nitrogen Reduction**

# Preparation of Nafion Membranes for Reproducible Ammonia Quantification in Nitrogen Reduction Reaction Experiments

Fatemeh Hanifpour, Arnar Sveinbjörnsson, Camila Pía Canales, Egill Skúlason, and Helga Dögg Flosadóttir\*

**Abstract:** This study highlights the importance of following a strict protocol for Nafion membrane pretreatment for electrochemical nitrogen reduction reaction experiments. Atmospheric ammonia pollution can be introduced to the experimental setup through membranes and interpreted falsely as catalysis product from  $N_2$ . The sources of ammonia contamination vary drastically between locations worldwide and even within the same location between days depending on temperature, wind direction, fertilizer use, and manure accumulation in its vicinity. The study shows that significant amounts of ammonium is accumulated in the membranes after commonly practiced pretreatment methods, where the amount depends on the ammonia concentration in the surrounding of the experiment. Therefore, we introduce a new pretreatment method which removes all the ammonium in the membrane. The membranes can be stored for several days but a short final step in the method needs to be carried out right before NRR experiments.

The development of a sustainable and efficient process for ammonia ( $NH_3$ ) production from nitrogen ( $N_2$ ) is now a significant research and development objective. Many researchers are focusing on  $NH_3$  synthesis at ambient conditions by means of  $N_2$  reduction reaction (NRR) using heterogeneous catalysts as an alternative for the conventional Haber–Bosch process. This interesting new field is at the same time quite challenging as there are numerous possible sources of contamination introduced to the experiments, causing false positive results, that is, the produced  $NH_3$  may not in fact be the result of a catalytic reaction but come from different sources of contamination. In this sense, several researchers have recently published articles stressing the importance of rigorous and efficient experimental protocols to conduct NRR as reliable as possible to minimize the external sources of contamination. These sources include, but are not limited to, the inherent contamination in the setup, the reactant gas ( $^{14}N_2$  and  $^{15}N_2$ ) and electrolyte, human breath, and nitrile

rubber gloves.<sup>[1–5]</sup> For this reason, as reported by Chorcken-dorff and co-workers, it is important to consider a systematic benchmarking protocol to eliminate the false and retain the true results in NRR.<sup>[5]</sup>

However, environmental effects on NRR experiments have not yet been seriously considered. Atmospheric  $NH_3$  pollution commonly exists as a point source from industry or agriculture, and its concentration at each location can therefore vary quite drastically between days and seasons within the exact same location depending on temperature, wind direction, fertilizer use, and manure accumulation and use.<sup>[6]</sup> These variations can cause false positives in NRR experiments. A study on ammonia concentrations in the atmosphere in Taiwan shows that  $NH_3$  levels can reach as high as 100 ppb in such a highly populated and polluted location.<sup>[7]</sup> Atmospheric contamination of such levels could interfere with the ammonia quantification in NRR experiments done worldwide today. The ventilation system together with the fume hood in laboratories should be capable of providing indoor air quality according to acceptable standards. For such ventilation to be effective, large volumes of external atmosphere are pumped through the laboratory during the day, in most cases not considering purifying gaseous atmospheric pollution from the inlet air. Poor ventilation and infiltration are found to be the major sources of laboratory indoor air pollution.<sup>[8]</sup>

To minimize the variable effects of environmental pollutants, it is necessary to start the NRR experiments as clean as possible and maintain that throughout the experiment by minimizing handling of samples. A typical setup for NRR experiments includes a double compartment electrochemical cell utilizing a proton exchange membrane (PEM) to separate the two compartments. The role of the PEM in aqueous-acidic electrolyte is to crossover protons from the anodic chamber to the cathodic chamber and, at the same time, to prevent diffusion of  $O_2$  and the decomposition of the  $NH_4^+$  product on the counter electrode. However, PEMs, with Nafion 211 and Nafion 117 being the most common membranes in such applications, can accumulate and partially crossover  $NH_4^+$  ions resulting in gradual decrease of membrane conductivity during experiments.<sup>[1,2,9]</sup> Ren and co-workers have concluded that the use of Nafion membranes in NRR experiments may be inappropriate, as ammonium can pass through the membrane, be adsorbed on the membrane or, even, interact with it, which is unfavorable for reliable and reproducible quantification of the product.<sup>[10]</sup> Although long-term application of Nafion (7–10 days) is not suitable owing to loss of conductivity, Nafion membranes are nevertheless widely used in short term (ca. 2 h) NRR experiments today and deserve

[\*] F. Hanifpour, Dr. C. P. Canales, Prof. E. Skúlason  
Science Institute & Faculty of Industrial Engineering, Mechanical Engineering and Computer Science, University of Iceland  
VR-III, Hjardarhaga 2, 107 Reykjavík (Iceland)  
E-mail: helgadogg@atmonia.com

A. Sveinbjörnsson, Dr. H. D. Flosadóttir  
Innovation Center Iceland  
Árleyni 2–8, 112 Reykjavík (Iceland)

 Supporting information and the ORCID identification number(s) for the author(s) of this article can be found under:  
<https://doi.org/10.1002/anie.202007998>

further investigation on pretreatment protocols to obtain as reliable data as possible.

In this work, we report measurements on ammonium contamination in pretreated Nafion membranes using the common pretreatment methods reported in the literature and recommend a modification to this process. Two of the most common Nafion membranes (117 and 211) are used as an example. It is observed that the accumulation of  $\text{NH}_4^+$  in the membrane highly depends on the local atmospheric levels of  $\text{NH}_{3(\text{g})}$  on the specific day when the pretreatment process takes place or when the membranes are used. As atmospheric levels of ammonia vary between locations, this can be an important factor to consider when doing NRR experiments in highly populated and polluted cities, or close to industries or agriculture. This study is performed in the outskirts of Reykjavík, Iceland, a city where atmospheric pollutants are usually very low.<sup>[11]</sup> The main repeating sources of atmospheric  $\text{NH}_3$  pollution are from the geothermal wells in Hengill area and a few agricultural activities such as a pig farm in a 25 km distance from the research site.

Measurements of atmospheric  $\text{NH}_{3(\text{g})}$  are not commonly performed in Iceland where the experiments reported here are conducted. Geothermal wells, however, have been shown to emit  $\text{NH}_3$  to some extent along with many other gases such as  $\text{H}_2\text{S}$ ,  $\text{CO}_2$ ,  $\text{H}_2$ , and  $\text{CH}_4$ .<sup>[12,13]</sup> Air pollution stations in Reykjavík commonly monitor  $\text{H}_2\text{S}$  as the main pollutant. The studies presented here are performed at the Innovation Center Iceland, which is within 1 km distance from the nearest monitoring station, Lambhagi. In this study, we use environmental data of atmospheric  $\text{H}_2\text{S}$  for the purpose of estimating the change in the local, proportional atmospheric level of  $\text{NH}_3$ , as these two tend to co-exist and correlate in atmosphere as emissions from geothermal wells. The geothermal well at Nesjavellir is estimated to be the main source of atmospheric  $\text{NH}_3$  pollution, but there may also be other temporary sources. The source of atmospheric  $\text{NH}_{3(\text{g})}$  can vary between locations and the level of concentration can vary within location between seasons and days. It should be noted that the levels of  $\text{H}_2\text{S}$  and  $\text{NH}_3$  can vary significantly between days in Iceland, depending on wind direction and location with regards to the geothermal areas, but these levels are commonly very low compared to most cities.<sup>[7]</sup> This study is in all cases performed at the same location but different days. We observe a great variation in repeated experiments depending on the day. These results can in principle be extrapolated to different locations world-wide where a large variation of ammonia concentration may exist in atmosphere depending on both the date and location of the experiment.

Therefore, there is a need for a standard procedure for Nafion pretreatment to ensure that the membrane is not a source for ammonia. This study introduces a method for expansion and purification of Nafion membranes that provides ammonium-free membranes to conduct NRR experiments with.

The commercial expansion method for Nafion membranes is to use water (room temperature or up to 90 °C) or dilute acids (0.2% to 0.5%  $\text{HNO}_3$  or  $\text{HCl}$ ), depending on application.<sup>[14]</sup> The common Nafion pretreatment method as practiced in most of the published reports in the NRR field,

however, is to treat Nafion first using  $\text{H}_2\text{O}_2$  (3–5%) at 80 °C to remove organic impurities, next using 0.1–1 M  $\text{H}_2\text{SO}_4$  at 80 °C to eliminate metallic impurities and to protonate the membrane, and finally leave Nafion in ultrapure water at 80 °C to rinse the excess acid and reach the maximum expansion.<sup>[15]</sup> The commonly used pretreatment process could leave the membrane polluted with significant amounts of ammonium because atmospheric and gaseous ammonia is dissolved in any aqueous solution open to air, and protonated to form ammonium. A piece of Nafion submerged in the aqueous solution is then exposed to ammonium ions, that are then exchanged with the acid sites of the membrane, in equilibrium with the  $\text{NH}_4^+$  concentration in the solution. Following the ion exchange, the Nafion adsorbed ammonium ions self-diffuse into and through the membrane.<sup>[16]</sup> This brings forth doubts in the actual quantification of the NRR product.

In this study, multiple versions of pretreatment methods are performed to account for many possible variations within laboratories carrying out NRR experiments to date. These are referred to as Methods 1–4 within this text. These different procedures are shown in detail in Table 1 and compared with a modified procedure (Method 5) we introduce here to minimize the amount of ammonium ions in Nafion membranes before they are used in NRR experiments.

Dry Nafion sheets of size 4.5 cm<sup>2</sup> are used in all cases. All containers are acid washed with 20%  $\text{HCl}$  at least for 12 h before the experiments. The effect of container type (Method 1 vs. 2) and the use of fresh container in each step vs. using same container all through the pretreatment procedure (Method 3 vs. 4) are studied. Ammonia uptake by Nafion is measured at the end of the pretreatment processes by sonicating the membrane in 5 mL of fresh 0.05 M  $\text{H}_2\text{SO}_4$  for 10 minutes and measuring the ammonia

**Table 1:** Variations in Nafion pretreatments tested in this study.<sup>[a]</sup>

Method no.	Method name	Container	Procedure <sup>[b]</sup>
1		polypropylene w/screw cap	1. 80 °C, 1 h, 5% $\text{H}_2\text{O}_2$
2	short treatment	glass, Al foil	2. 80 °C, 1 h, milliQ water 3. 80 °C, 1 h, 0.5 M $\text{H}_2\text{SO}_4$ 4. 80 °C, 1 h, milliQ water
3	long treatment (fresh)	glass, Al foil (fresh)	1. 80 °C, 1 h, 5% $\text{H}_2\text{O}_2$ 2. 80 °C, 1 h, milliQ water
4	(common practice)	glass, Al foil (same)	3. 80 °C, 3 h, 0.5 M $\text{H}_2\text{SO}_4$ 4. 80 °C, 6 h, milliQ water
5	modified method	glass, Al foil (same)	In ultrasonic bath: 1. RT, 20 min, 5% $\text{H}_2\text{O}_2$ 2. RT, 20 min, milliQ water 3. RT, 20 min, 0.5 M $\text{H}_2\text{SO}_4$ 4. RT, 20 min, milliQ water 5. 80 °C, > 12 h, milliQ water 6. RT, Sonication in 0.05 M $\text{H}_2\text{SO}_4$ and milliQ water directly before use

[a] Polypropylene beaker with screw cap is used in Method 1 but glass beakers covered with Al foil are used in Methods 2–5. In Method 3 a fresh beaker is used in each step of the procedure, while Methods 4 and 5 use the same beaker in all steps. [b] RT = room temperature.

content in the acidic solution by means of flow injection analysis, a selective quantification method of aqueous ammonium ions as low as 1 ppb (see the full description in the Supporting Information). In all experiments, blanks were collected by sonicating 5 mL of 0.05 M sulfuric acid for 10 minutes under the same condition as the samples. In all cases the ammonia detected in the blanks was lower than the limit of detection.

Methods 1 and 2 used the same procedure but different containers; plastic beakers with screw caps (Method 1) and glass beakers covered with Al foil (Method 2). The study showed that plastic beakers with screw caps were not suitable containers for this high temperature method, as the caps popped up randomly owing to high pressure inside, and the contents were, on such occasions, totally exposed to the surrounding environment. Thus, plastic beakers were disregarded in later experiments.

Methods 3 and 4 were performed according to the common method practiced for Nafion pretreatment as described in Table 1. There, the comparison was made between using a new and clean beaker for every new preparation step (Method 3) and using only one and single beaker for all preparation steps (Method 4).

Ammonia contents of pretreated Nafion 211 and 117 undergoing these methods are shown in Figure 1. Apparently, the use of pretreatment Methods 1–4 does not remove ammonium from the membranes in any of the 18 tests performed. The ammonia content is measured from around 0.1–2  $\mu\text{g}$  whereas the limit of detection in this study is much lower, or 5 ng. This external ammonium contamination would therefore significantly affect the results obtained in NRR experiments. There is no clear difference between Methods 1–4 tested here when it comes to ammonium removal. However, fluctuations between replicates of the same tests could only be attributed to the atmospheric concentrations of ammonia (estimated from the  $\text{H}_2\text{S}$  atmospheric level in this study) or other external contamination factors. This underpins the demand for a reliable method for contaminant-free preparation of Nafion membrane.

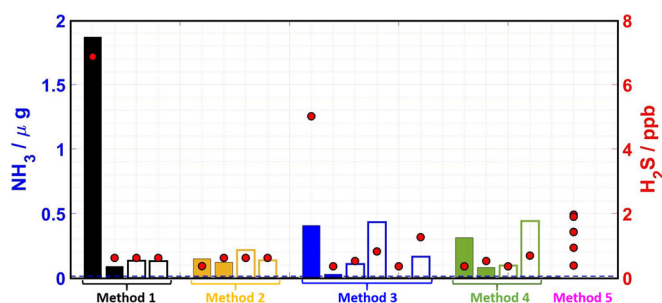


**Figure 1.** Ammonia content in Nafion membranes after pretreatment methods listed in Table 1. Solid columns in each method represent  $\text{NH}_3$  data on Nafion 211 and empty columns represent the data on Nafion 117.  $\text{H}_2\text{S}$  data is shown as dots. Limit of Detection (LOD) of the method for ammonia analysis is typically between 5–15 ng (dashed line at 5 ng). Method 5 was repeated 7 times on different days for both Nafion types where atmospheric  $\text{H}_2\text{S}$  levels were varying but the ammonia content was always under the LOD.

To reach the maximum expansion and remove ammonium from Nafion membrane before applying it in the electrochemical cell, we suggest a pretreatment process referred to Method 5 in Table 1. Nafion is first sonicated for 20 minutes at room temperature (RT) in 5%  $\text{H}_2\text{O}_2$ . The analysis of total organic content (TOC) in Vario TOC cube (Elementar Analysensysteme GmbH, 63505 Langenselbold, Germany) shows that this step can remove all the possible organic impurities in the membrane (see the Supporting Information, Table S1). Next, Nafion is sonicated for 20 minutes at RT in ultrapure water (milliQ Quantum TEX) before undergoing the same sonication step in 0.5 M  $\text{H}_2\text{SO}_4$ . Inductively coupled plasma (ICP) analysis (Agilent Technologies 7800 ICP-MS) confirms that this step can remove metallic impurities inside the membrane (Supporting Information, Table S2). Nafion is next sonicated again for 20 minutes at RT in ultrapure water to rinse the excessive acid from the previous step. To reach the maximum expansion, Nafion needs to be kept in ultrapure water at 80 °C for a minimum of 12 h. In this step, Nafion membrane is expanded and protonated and may be kept at room temperature in water inside an amber glass until its application. However, directly prior to use, the membrane needs to be sonicated in 0.05 M  $\text{H}_2\text{SO}_4$  and ultrapure water. Immersing Nafion in  $\text{H}_2\text{SO}_4$  solution provides excessive access to protons, reversing the cation exchange and extracting  $\text{NH}_4^+$  from Nafion into the solution and thus, fully protonating the membrane prior to use in experiments. Ammonia content of Nafion prepared using this procedure was measured several times (either using one beaker or different beakers in the pretreatment procedure) and the resulting amount was always lower than the limit of detection of the method (5 ng  $\text{NH}_3$ ). As shown in Figure 1,  $\text{H}_2\text{S}$  contaminant was present in the atmosphere during all the tests that were performed using Method 5, and in many cases the levels were even higher than those of the tests done using Methods 1–4, yet no ammonia contamination was found in the membrane after such pretreatment. It is worth to note that all measurements of each sample were repeated at least twice in a row. The measurements were in all cases reproducible within measurement error. For a detailed description of the ammonia measurement method, see the Supporting Information.

It is common laboratory practice to pretreat several Nafion membranes simultaneously for a use-period of the following 5–7 days. Nafion is then stored in ultrapure water until use, during which time it may accumulate  $\text{NH}_3$  to higher contamination levels. This highly depends on the storage solution which is constantly in dynamic equilibrium with the surrounding atmosphere. An experiment to demonstrate the effect of atmospheric  $\text{NH}_3(\text{g})$  concentration on extended storage of Nafion in ultrapure water, was performed with Nafion 211 (as no distinct difference was observed between Nafion 211 and 117 in previous experiments). Here, a 10-day study was performed where a fully prepared membrane (4.5  $\text{cm}^2$  of Nafion 211 pretreated initially using Method 5) was kept in ultrapure water and analyzed for  $\text{NH}_3$  concentration on various days (Figure 2a). Six samples were taken: the first one, right after pretreatment which as expected did not contain any ammonia contamination, and the rest of the

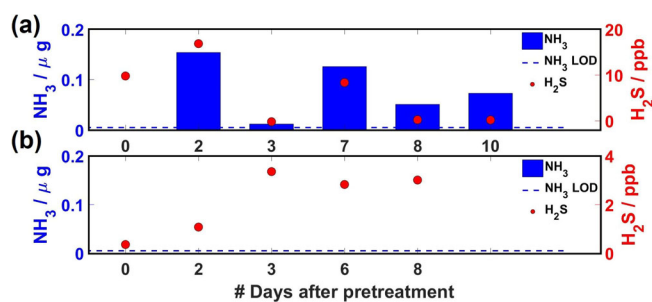


**Figure 2.** Ammonia content in Nafion 211 (4.5 cm<sup>2</sup>) as a function of days after pretreatment and atmospheric H<sub>2</sub>S levels. Membranes were pretreated initially using the modified method and kept in ultrapure water in a glass beaker covered with Al foil. a) Significant amount of ammonia was measured, except at day zero, right after pretreatment, when step 6 in Method 5 was not carried out directly before ammonia measurements whereas b) the ammonia content was always lower than the LOD when step 6 in Method 5 was carried out directly before ammonia measurements. LOD of the method for ammonia analysis is typically between 5–15 ng (dashed line at 5 ng).

samples were taken after 2, 3, 7, 8, and 10 days after the initial pretreatment. The results demonstrated a high variation of NH<sub>3</sub> concentration in membranes on the specified days. The ammonia concentration in the membrane is plotted against the number of days passed initial pretreatment. The results appear to follow the local atmospheric concentration of NH<sub>3</sub> (estimated from the H<sub>2</sub>S atmospheric level). It should be noted that here the ammonia content was measured in the membranes after storing them in ultrapure water for a few days without performing the final step of Method 5 directly before analysis.

Considering the above, similar sets of tests were repeated, but sample collection and analysis were done after performing the final step of Method 5 (sonication in 0.05 M H<sub>2</sub>SO<sub>4</sub> and ultrapure water) directly before sample collection; see Figure 2b. Despite the various H<sub>2</sub>S levels on various days within this test, the results showed ammonia concentrations below limit of detection in all the samples.

Note in Figure 2a that although the average of H<sub>2</sub>S level on the pretreatment day (day 0) was significant, there was no ammonia detected in the sample, demonstrating the methods reproducibility and the need for this pretreatment. Figure 2b also demonstrates that pretreatment can be done several days before experiments if the final step of the method is performed directly before use. Furthermore, the variable concentrations observed depending upon the local and short-term atmospheric levels of NH<sub>3</sub> implies that the comparison of an NRR experiment and its associate blank test done on different days may not represent the true results without ensuring a clean and closed experimental environment.

Further comparison between Nafion 211 pretreatment using Method 4 and Method 5 was done in a double-compartment H-cell. Two cells were used for each pretreatment method; 1) blank cell filled with 20.0 mL of 0.05 M H<sub>2</sub>SO<sub>4</sub> in both cathodic and anodic chambers and 2) sample cell filled with 20.0 mL of 0.05 M H<sub>2</sub>SO<sub>4</sub> containing 0.3 ppm of ammonia (60 μg) in the cathodic chamber and no concentration of

ammonia in the anodic chamber. N<sub>2</sub> was bubbled through the cathodic chambers for 2 h. The Nafion membranes were collected and sonicated in 5.0 mL of 0.05 M H<sub>2</sub>SO<sub>4</sub>. The ammonia contained in Nafion after the test is shown in Table 2. Similar results as shown before in Figure 1 were obtained for the blank tests; Nafion pretreated using Method 4 included significant amount of ammonium whereas with Method 5 this amount was under detection limit. For the sample tests it is clear that in both cases (Methods 4 and 5) more ammonia was adsorbed into the Nafion compared with the blank tests, demonstrating the fast equilibrium between electrolyte and membrane. Similar amount of ammonium was absorbed into the membranes with both methods (65–78 ng), which is around 0.001 % of the ammonia in the electrolyte (60 μg) during the 2 hour experiments. This simulated NRR experiments shows that our proposed method can be used for the pretreatment process and then ammonia from the membrane can be accounted for in the end of the experiment if needed.

The sources of atmospheric H<sub>2</sub>S in Iceland are geothermal wells and drill holes. Ammonia emissions from geothermal wells in Iceland have not been widely studied. One study performed in Iceland observed NH<sub>3</sub> in geothermal steam condensate of Hellisheiði.<sup>[17]</sup> On the other hand, H<sub>2</sub>S, a well-known geothermal emission gas, is extensively monitored.<sup>[18]</sup> Furthermore, a study on geothermal wells in Cerro Prieto IV in Mexico measured CO<sub>2</sub>, H<sub>2</sub>S, H<sub>2</sub>, CH<sub>4</sub>, and NH<sub>3</sub> from geothermal wells, which demonstrates the co-existence of NH<sub>3</sub> and H<sub>2</sub>S.<sup>[12]</sup> Intermittent and short-term increase in local atmospheric levels of H<sub>2</sub>S and NH<sub>3</sub>, therefore, simultaneously implies the short-term increase of geothermal well pollution often observed in specific wind direction. The direct relation between H<sub>2</sub>S and NH<sub>3</sub> concentration levels in atmosphere has also been reported in a study by Blunden *et al.* where they monitor the diurnal variations for H<sub>2</sub>S and NH<sub>3</sub> emission rates from the ventilation exhaust of a pig barn in North Carolina.<sup>[13]</sup> The geothermal wells are the main source of atmospheric NH<sub>3</sub> in Reykjavík, Iceland, but there are many other possible sources elsewhere causing much higher atmospheric concentrations.

It is important to notice that the concentration of ammonium in Nafion reported here are significant, yet not very high. We show that the concentration of ammonium in the membrane highly depends on atmospheric levels of NH<sub>3</sub>, which we observe by performing the experiments on different days using commonly utilized pretreatment methods and compare it with pollutant data for those days. Since the atmospheric levels of ammonia can vary greatly between locations world-wide,<sup>[19]</sup> the ammonium content in the membrane will highly depend on the location of the experi-

**Table 2:** Ammonia content in Nafion 211 undergone common and modified pretreatment methods in a simulated NRR experiment.

Method no.	Ammonia in Nafion in blank cell [ng]	Ammonia in Nafion in sample cell [ng]
4	150 ± 8	228 ± 13
5	< 18	65 ± 1

ment. The atmospheric concentration of ammonia also highly depends upon temperature and season (fertilizer application).<sup>[20]</sup> Measurements of aerosol NH<sub>3</sub> in Heimaey, an active volcano island south of Iceland, demonstrated 0.05–0.12 ppb NH<sub>3</sub> in air.<sup>[21]</sup> Atmospheric concentrations have been measured in various cities worldwide and reported between 3 ppb and 100 ppb (up to 800 times the reported concentration in Heimaey) depending on location and time.<sup>[7]</sup> These variations further support the demand to ensure that Nafion used for each experiment is not a source of ammonia. The very low atmospheric concentrations of NH<sub>3</sub> in Iceland can still cause observable concentrations of NH<sub>3</sub> in the membranes, unless the proposed method in this study is used. Variations of atmospheric NH<sub>3</sub> may in many cases cause differences in NH<sub>3</sub> concentrations that can be falsely attributed to catalysis.

In conclusion, this study reports an observation of ammonium contamination in expanded and protonated Nafion membranes ready for application, as one of the sources of false positive results in NRR experiments. An improved pretreatment procedure is suggested to ensure ammonium-free membranes prior to use. The contamination levels are demonstrated to be dependent upon the NH<sub>3</sub> concentrations in local atmosphere that can vary quite drastically between locations world-wide and on daily basis. The modified method of Nafion pretreatment is both more practical than previous methods and rules out the chance of Nafion being a source for ammonia detected in NRR experiments.

### Acknowledgements

This work was supported by the Icelandic Research Fund (grant nos. 196437-051 and 185404-051) and the Icelandic Technology Development Fund (grant no. 175350-0611). We wish to thank the Icelandic environmental agency for providing us with the H<sub>2</sub>S data.

### Conflict of interest

The authors declare no conflict of interest.

**Keywords:** ammonia · contamination · Nafion · nitrogen reduction reaction · pretreatment methods

[1] G. F. Chen, S. Ren, L. Zhang, H. Cheng, Y. Luo, K. Zhu, L. X. Ding, H. Wang, *Small Methods* **2019**, *3*, 1800337.

- [2] C. Tang, S.-Z. Qiao, *Chem. Soc. Rev.* **2019**, *48*, 3166–3180.  
 [3] B. H. Suryanto, H.-L. Du, D. Wang, J. Chen, A. N. Simonov, D. R. MacFarlane, *Nat. Catal.* **2019**, *2*, 290–296.  
 [4] S. L. Foster, S. I. P. Bakovic, R. D. Duda, S. Maheshwari, R. D. Milton, S. D. Minter, M. J. Janik, J. N. Renner, L. F. Greenlee, *Nat. Catal.* **2018**, *1*, 490–500.  
 [5] S. Z. Andersen, V. Čolić, S. Yang, J. A. Schwalbe, A. C. Nie-lander, J. M. McEnaney, K. Enemark-Rasmussen, J. G. Baker, A. R. Singh, B. A. Rohr, M. J. Statt, S. J. Blair, S. Mezzavilla, J. Kibsgaard, P. C. K. Vesborg, M. Cargnello, S. F. Bent, T. F. Jaramillo, I. E. L. Stephens, J. K. Nørskov, I. Chorkendorff, *Nature* **2019**, *570*, 504–508.  
 [6] C. Krauter, D. Goorahoo, C. Potter, S. Klooster, *Emission Inventories-Partnering for the Future* **2002**, *11*, 15–18.  
 [7] S. Wang, J. Nan, C. Shi, Q. Fu, S. Gao, D. Wang, H. Cui, A. Saiz-Lopez, B. Zhou, *Sci. Rep.* **2015**, *5*, 15842.  
 [8] T. Ugranli, E. Gungormus, A. Sofuoglu, S. C. Sofuoglu, *Compr. Anal. Chem.* **2016**, *73*, 859–878.  
 [9] K. Hongsirikarn, J. G. Goodwin, Jr., S. Greenway, S. Creager, *J. Power Sources* **2010**, *195*, 30–38.  
 [10] Y. Ren, C. Yu, X. Tan, X. Han, H. Huang, H. Huang, J. Qiu, *Small Methods* **2019**, *3*, 1900474.  
 [11] K. Steinecke, *Atmos. Environ.* **1999**, *33*, 4157–4162.  
 [12] R. M. Barragán, V. M. Arellano, M. H. Rodríguez, A. Pérez, N. Segovia, *Geofluids* **2010**, *10*, 511–524.  
 [13] J. Blunden, V. P. Aneja, P. W. Westerman, *Atmos. Environ.* **2008**, *42*, 3315–3331.  
 [14] Fuel Cell Store, “NAFION Hydrogen-Form Membrane Expansion Technical Information Bulletin 93-01”, **2019**.  
 [15] R. Kuwertz, C. Kirstein, T. Turek, U. Kunz, *J. Membr. Sci.* **2016**, *500*, 225–235.  
 [16] R. M. Jung, H. S. Cho, S. Park, J. W. Van Zee, *J. Power Sources* **2015**, *275*, 14–21.  
 [17] A. I. Remoroza, Calcite Mineral Scaling Potentials of High-Temperature Geothermal Wells (Unpublished MSc Thesis), University of Iceland, Reykjavik, **2010**.  
 [18] Measurements on air quality in Iceland, Environmental agency, <https://loftgaedi.is/?zoomLevel=7&lat=64.894972&lng=-18.675028>.  
 [19] M. Crippa, D. Guizzardi, M. Muntean, E. Schaaf, F. Dentener, J. A. van Aardenne, S. Monni, U. Doering, J. G. Olivier, V. Pagliari, *Earth Syst. Sci. Data* **2018**, *10*, 1987–2013.  
 [20] A. D. Larios, S. Godbout, S. K. Brar, J. H. Palacios, D. Zegan, A. Avalos-Ramírez, F. Sandoval-Salas, *Biosyst. Eng.* **2018**, *169*, 165–174.  
 [21] J. M. Prospero, D. L. Savoie, R. Arimoto, H. Olafsson, H. Hjartarson, *Sci. Total Environ.* **1995**, *160*, 181–191.

Manuscript received: June 4, 2020

Revised manuscript received: August 21, 2020

Accepted manuscript online: August 28, 2020

Version of record online: ■■■■■, ■■■■■

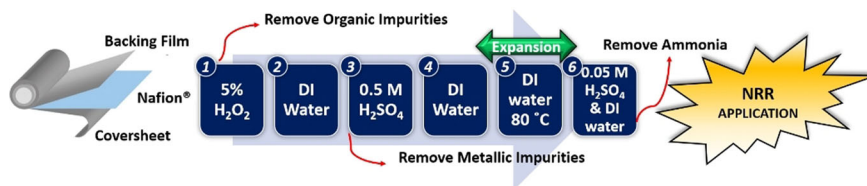
## Zuschriften



## Nitrogen Reduction

F. Hanifpour, A. Sveinbjörnsson,  
C. P. Canales, E. Skúlason,  
H. D. Flosadóttir\*                                                                                                                                                                                                                                            

Preparation of Nafion Membranes for  
Reproducible Ammonia Quantification in  
Nitrogen Reduction Reaction  
Experiments



A utilizable method of Nafion pretreatment for the nitrogen reduction reaction (NRR) is proposed. This method rules out a critical source of false positive results in NRR experiments. Failing to follow these steps can introduce variable

amounts of atmospheric ammonia to the setup, which may be interpreted falsely as catalysis product. This observation questions previous results reported in this field.

## Supporting Information

### **Preparation of Nafion Membranes for Reproducible Ammonia Quantification in Nitrogen Reduction Reaction Experiments**

*Fatemeh Hanifpour, Arnar Sveinbjörnsson, Camila Pía Canales, Egill Skúlason, and Helga Dögg Flosadóttir\**

ange\_202007998\_sm\_miscellaneous\_information.pdf

## Table of Contents

1. Chemicals and Reagents .....	S1
2. Experimental Procedures .....	S1
2.1 Ammonia detection method .....	S1
2.2 Analysis of organic content.....	S2
2.3 Analysis of metallic impurities .....	S3
3. References.....	S4
Author Contributions.....	S4

### 1. Chemicals and Reagents

Nafion® 211 and 117 were purchased as sheets of 30 × 30 cm<sup>2</sup> from FuelCellStore, Texas, USA. Sulfuric acid (H<sub>2</sub>SO<sub>4</sub>, Honeywell FlukaTM, 97.0%) was diluted in ultrapure water (milliQ Quantum TEX) to obtain the desired concentrations. Hydrogen peroxide (H<sub>2</sub>O<sub>2</sub>, Sigma-Aldrich, ≥30%) was diluted in milliQ water to make the 5% solution needed in the pretreatment sequence.

Materials required for ammonia determination and quantification include: sodium hydroxide (NaOH, Sigma-Aldrich, ≥98%), ortho-phthalaldehyde (OPA, Sigma-Aldrich, ≥99%), disodium tetra borate decahydrate (Na<sub>2</sub>B<sub>4</sub>O<sub>7</sub>·10H<sub>2</sub>O, Merck, 99.5%), sodium sulfite (Na<sub>2</sub>O<sub>3</sub>S, Sigma-Aldrich, 98-100%) and triton X-100 ((C<sub>2</sub>H<sub>4</sub>O)<sub>n</sub>C<sub>14</sub>H<sub>22</sub>O, Sigma-Aldrich).

### 2. Experimental Procedures

#### 2.1 Ammonia detection method

Flow Injection Analysis® (FIALab-3500b, FIALab Instruments Inc. Bellevue, WA 98007 USA) is used to detect and quantify ammonia using the fluorescent method, as previously described by FIALab, with slight changes discussed below (see schematic in Fig. S1).<sup>[1]</sup> In this setup, a peristaltic pump was used to control the flowrate of all solutions required for ammonia detection. These include: (i) Carrier stream of 0.05 M H<sub>2</sub>SO<sub>4</sub>, (ii) Carrier stream of milliQ water, (iii) Reagent number 1: 2 M NaOH, prepared within the same day, and (iv) Reagent number 2: 150 g disodium tetraborate decahydrate, 4 g OPA dissolved in 100 mL ethanol, 0.08 g sodium sulfite and 5 g Triton-X soap in 5 L solution, pH: 9.4, prepared 7-10 days prior to use and kept in amber bottles. For quantitative calibration, an autosampler was used to collect ammonia standards from vials into the sample loop. A two-way valve was used to load/inject ammonia standards/samples in/from a 200 µL sample loop. A carrier stream was used to push the sample inside the sample loop forward to be mixed with reagent 1, converting the NH<sub>4</sub><sup>+</sup><sub>(aq)</sub> to NH<sub>3(g)</sub>. At this point, a gas diffusion cell was used to separate the gaseous ammonia from the liquid stream through a Teflon membrane and collect it in a clean, degassed, milliQ water stream. This water carrying ammonia was later mixed with reagent 2 and heated to 70 °C using a heating coil to promote a reaction between NH<sub>3</sub> and OPA to form a fluorescent compound. Then the sample was chilled in a cooling bath at 20 °C prior to entering the photo multiplier tube (PMT) cuvette. The fluorescent excitation wavelength used was 370 nm. The emission of 425 nm was then amplified by the PMT providing the final reading and a detection limit of as low as 1 ppb for ammonia in aqueous solutions was acquired.

## SUPPORTING INFORMATION

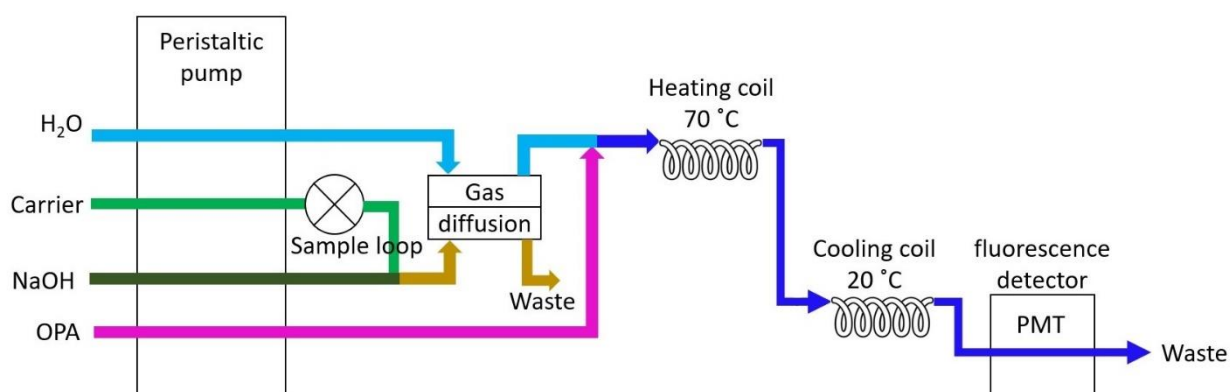


**Figure S1.** Schematic drawing of the fluorometric quantitative ammonia detection method used in the present study. OPA stands for ortho-phthalaldehyde and when combined with ammonia becomes fluorescent (see text).

A set of standards were prepared by diluting as purchased ammonium standard solution of 1000 ppm (Merck) with the electrolyte to the desired concentrations. Standards were collected in the sample loop using the device's auto sampler and analyzed through a FIA method defined specifically for calibration. A typical calibration curve is presented in Fig. S2. All samples measured fall within the calibrated range.

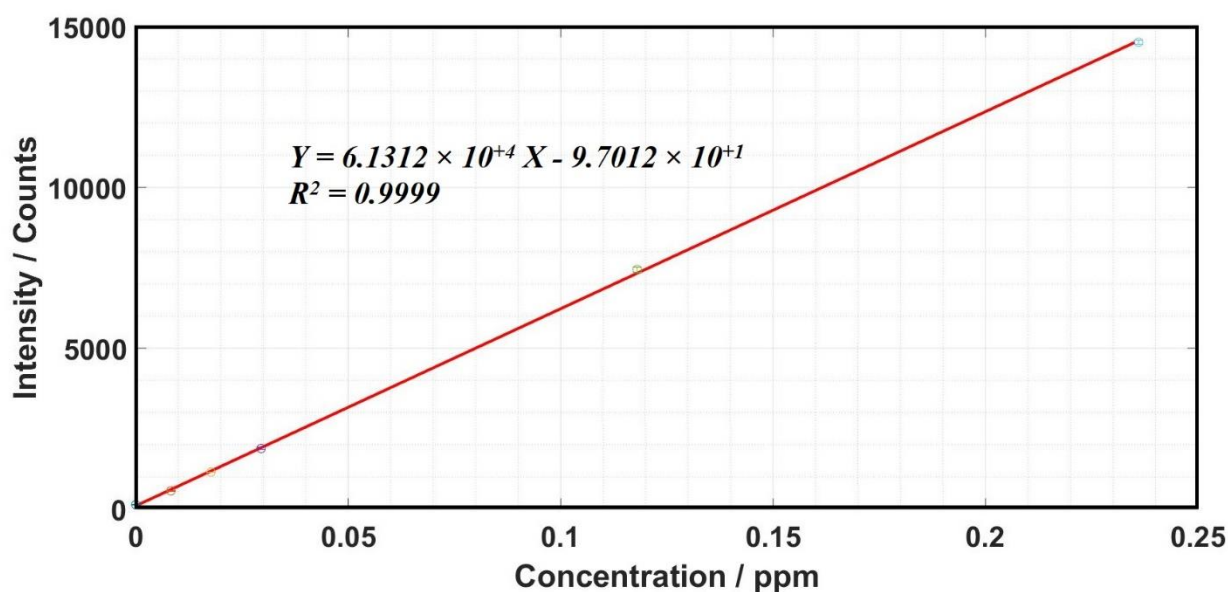


**Figure S2.** Ammonia calibration curve.

## 2.2 Analysis of organic content

In order to confirm the efficiency of the modified method in removing organic impurities from Nafion® membrane, the comparison between the conventional method and Method 5 was performed. The common procedure for this aim is to heat the membrane to 80 °C in 3-5 % H<sub>2</sub>O<sub>2</sub> solution for 1 hour. Since, Method 5 suggests 20 minutes of sonication at room temperature (RT) for this step, here we tested if the result of these two approaches would in fact be comparable, i.e. the modified method is efficient enough in this regard.

Two sets of tests using 4.5 cm<sup>2</sup> Nafion® 211 were designed for this aim. The first Nafion® went through 1 hour of heating at 80 °C in 10 mL of 5% H<sub>2</sub>O<sub>2</sub> in a glass beaker covered with Al foil, whereas, the second piece went through 20 minutes of sonication in 10

## SUPPORTING INFORMATION

mL of 5% H<sub>2</sub>O<sub>2</sub> at room temperature in a glass beaker covered with Al foil. The 10 mL of H<sub>2</sub>O<sub>2</sub> from both tests were collected and diluted 3 times and stored at 4 °C for later analysis (Sample 1). 10 mL of fresh solution of 5% H<sub>2</sub>O<sub>2</sub> was added to the membranes in both tests and the same procedure was repeated for a second time and samples were collected for analysis (Sample 2). In both cases, blanks were taken in the same manner as samples were taken, i.e. for the heating bath test, the blank sample was 10 mL of 5% H<sub>2</sub>O<sub>2</sub> in a glass beaker covered with Al foil which was heated at 80 °C for 1 hour, and for the ultrasonic bath test, the blank sample was 10 mL of 5% H<sub>2</sub>O<sub>2</sub> in a glass beaker covered with Al foil which was sonicated for 20 minutes at room temperature.

The result of analysis using Vario TOC cube (Elementar Analysensysteme GmbH, 63505 Langenselbold, Germany) is given in the Table S1. The limit of detection for this method is 30 µg/L. It is obvious that both approaches have similar yield of removing organic impurities, as the membranes in both methods are left with 570 µg/L of TOC in the second step. Thus, the modified method proves to be efficient in this regard.

**Table S1.** Total organic content (TOC) of Nafion® 211 undergone two different approaches to remove organic impurities.

Samples	20 min in ultrasonic bath at RT	1 h in heating bath at 80 °C
1	9.36 mg/L	10.23 mg/L
2	2.37 mg/L	2.16 mg/L
Blank	1.80 mg/L	1.59 mg/L

### 2.3 Analysis of metallic impurities

In order to confirm the efficiency of the modified method in removing metallic impurities from Nafion® membrane, the comparison between the conventional method and Method 5 was carried out. The common procedure for this aim is to heat the membrane to 80 °C in 0.5 M H<sub>2</sub>SO<sub>4</sub> solution for 3 hours. Since, Method 5 suggests 20 minutes of sonication at room temperature (RT) for this step, here we tested if the result of these two approaches would in fact be comparable, i.e. the modified method is efficient enough in this regard.

Two sets of tests using 4.5 cm<sup>2</sup> Nafion® 211 were designed for this aim. The first Nafion® went through 3 hours of heating at 80 °C in 10 mL of 0.5 M H<sub>2</sub>SO<sub>4</sub> in a glass beaker covered with Al foil, whereas, the second piece went through 20 minutes of sonication in 10 mL of 0.5 M H<sub>2</sub>SO<sub>4</sub> at room temperature in a glass beaker covered with Al foil. The H<sub>2</sub>SO<sub>4</sub> from both tests were collected and stored at 4 °C for later analysis (Sample 1). 10 mL of fresh solution of 0.5 M H<sub>2</sub>SO<sub>4</sub> was added to the membranes in both tests and the same procedure was repeated for a second time and samples were collected for analysis (Sample 2). In both cases, blanks were taken in the same manner as samples were taken, i.e. for the heating bath test, the blank sample was 10 mL of 0.5 M H<sub>2</sub>SO<sub>4</sub> in a glass beaker covered with Al foil which was heated at 80 °C for 3 hour, and for the ultrasonic bath test, the blank sample was 10 mL of 0.5 M H<sub>2</sub>SO<sub>4</sub> in a glass beaker covered with Al foil which was sonicated for 20 minutes at room temperature.

Elemental analysis was carried out using Agilent Technologies 7800 ICP-MS and the result is given in Table S2. Looking at the data, it is apparent that 20 minutes of sonication at room temperature can remove metallic impurities efficiently, since Sample 2 does not contain significantly higher metallic impurities than the collected blank for this procedure. On the other hand, excluding B, Si and Na which are the main components of borosilicate glasses, using high temperature results in lower metallic content in the samples (compared to the samples in the other method). High temperature gives higher metallic contents in the blank (compared to the blank in the other method) which could mean that (i) the sonication method is more efficient in removing the metallic contents, and (ii) the membrane could even capture the metallic impurities at high temperature, thereby, reducing its functionality in the NRR experiments.

Furthermore, the result of the elemental analysis for B, Si and Na is reported separately in Table S3. The numbers show the drastic difference between the two methods with regards to leaching out these elements from the beakers into the acid media. Thus, the membrane is even more contaminated with these elements at high temperatures which can affect its conductivity for application in NRR experiments.

**Table S2.** Metallic content of Nafion® 211 (except for B, Si and Na) undergone two different approaches to remove metallic impurities.

Samples	20 min in ultrasonic bath at RT	3 h in heating bath at 80 °C
1	939 ng	795 ng
2	374 ng	287 ng
Blank	346 ng	647 ng

## SUPPORTING INFORMATION

**Table S3.** B, Si and Na content of Nafion® 211 undergone two different approaches to remove metallic impurities.

Elements	Samples	Ultrasonic Bath at RT	Heating Bath at 80 °C
B	1	50 ng	755 ng
	2	34 ng	436 ng
	Blank	6 ng	117 ng
Si	1	--	1402 ng
	2	130 ng	798 ng
	Blank	--	302 ng
Na	1	443 ng	1331 ng
	2	153 ng	1154 ng
	Blank	75 ng	363 ng

### 3. References

- [1] FIALab Instruments Inc. Gas Diffusion Ammonia Method (Water Based Samples) and Various Extracts. Seattle, WA, 2013.

### Author Contributions

FH conceived the idea, designed the experiments, and carried out the experiments and data analysis. AS and HDF developed the setup and the method for ammonia detection and quantification. HDF and ES supervised overall project. FH, HDF, ES and CPC co-wrote the manuscript. All authors commented on the manuscript.



# Paper II

**In-line quantification of ammonia produced from theoretically derived transition metal nitrides electro-catalysts**

Hanifpour, F., Canales, C. P., Fridriksson, E. G., Sveinbjörnsson, A., Tryggvason, T. K., Yang, J., von Fieandt, K., Arthur, C., Jónsdóttir, S., Garden, A. L., Ólafsson, S., Leósson, K., Árnadóttir, L., Lewin, E., Abghoui, Y., Ingason, Á. S., Magnus, F., Flosadóttir, H. D., & Skúlason, E.

**In preparation**



# In-line quantification of ammonia produced from theoretically derived transition metal nitrides electro-catalysts

*Fatemeh Hanifpour<sup>a</sup>, Camila P. Canales<sup>a</sup>, Emil G. Fridriksson<sup>b</sup>, Arnar Sveinbjörnsson<sup>c</sup>, Tryggvi K. Tryggvason<sup>b</sup>, Jian Yang<sup>a</sup>, Kristina von Fieandt<sup>d</sup>, Connel Arthur<sup>a</sup>, Sigríður Jónsdóttir<sup>a</sup>, Anna L. Garden<sup>e</sup>, Sveinn Ólafsson<sup>a</sup>, Kristján Leósson<sup>f</sup>, Liney Árnadóttir<sup>g</sup>, Erik Lewin<sup>d</sup>, Younes Abghoui<sup>a</sup>, Árni S. Ingason<sup>b</sup>, Fridrik Magnus<sup>a,b</sup>, Helga D. Flosadóttir<sup>\*a,b</sup>, and Egill Skúlason<sup>\*a,b,h</sup>*

- a. Science Institute, University of Iceland, VR-III, 107 Reykjavík, Iceland.
- b. Grein Research ehf., Dunhagi 5, 107 Reykjavík, Iceland.
- c. Atmonia ehf., Keldnaholt, 112 Reykjavík, Iceland.
- d. Inorganic Research Programme, Department of Chemistry – Ångström Laboratory, Uppsala University, Box 538, SE-751 21 Uppsala, Sweden.
- e. Department of Chemistry and MacDiarmid Institute for Advanced Materials and nanotechnology, University of Otago, P.O. Box 56, Dunedin 9054, New Zealand.
- f. DT-Equipment, Keldnaholt, 112 Reykjavík, Iceland.
- g. School of Chemical, Biological and Environmental Engineering, Oregon State University, Corvallis, OR, 97331, United States.
- h. Faculty of Industrial Engineering, Mechanical Engineering and Computer Science, University of Iceland, VR-III, 107 Reykjavík, Iceland.

\* [egillsk@hi.is](mailto:egillsk@hi.is) , [helgadogg@atmonia.com](mailto:helgadogg@atmonia.com)

## Abstract

Electrochemical reduction of dinitrogen to ammonia at ambient conditions is investigated in a three-electrode setup, two-compartment micro-reactor flow-cell using thin film surfaces of polycrystalline VN, CrN, NbN, and ZrN. Electrochemical techniques are used to characterize the surfaces and study the favorable nitrogen reduction reaction and the competing hydrogen evolution reaction. Chronoamperometry loops are used for ammonia production analysis. Accurate and automated quantification of ammonia with the most sensitive limit of detection currently practiced for the nitrogen reduction reaction is accomplished in a flow injection analyzer in-line with the micro-reactor. The results show the effect of availability of  $N_2(g)$  within both the electrochemical characterization and ammonia production for ZrN. However, no ammonia is detected from studies on CrN in  $N_2(g)$  medium. VN and NbN are inactivated upon reacting their inherent N atoms of the surface top layer(s). The overall analyses of the results obtained from ammonia measurements, electrochemical impedance spectroscopy analysis, surface stability checks within the experiments, and surface characterization after the experiments using X-ray reflectivity, reveal certain trends indicating catalytic behavior for ZrN. However, the concentration of produced ammonia is below the limit of detection of the methods devised to analyze the samples from isotope labeling experiments. The onset of ammonia production on ZrN appears to be in close agreement with that obtained previously by computational studies.

**KEYWORDS:** Nitrogen reduction reaction, ammonia electrosynthesis, transition metal nitride thin films, ambient condition, aqueous electrolyte solution.

## 1. Introduction

The world's ammonia production relies completely on the Haber-Bosch process, which has been revolutionary for the progress of humankind. Nonetheless, the process suffers from several disadvantages such as harsh operating conditions, high  $CO_2$  emissions, and the necessity for large-scale implementation which has led to the existence of only a few operating plants around the globe. In order to eliminate these obstacles and allow for a distributed and sustainable ammonia production at a small scale under ambient conditions, researchers started to explore the electrochemical conversion of di-nitrogen to ammonia as one of the viable alternatives [1–5]. Electrocatalysis facilitates electron transfer to the adsorbed  $N_2$  reactant in the catalysts' active sites and in this way, enables chemical reactions through direct use of electrons [6]. The choice of electrolyte and electrocatalyst, thus, directly affects the outcome of this reaction. The electrode materials that have been studied the most, both theoretically and experimentally, are metals [7–13], metal compounds [14–16], single-atom catalysts [17–19], and metal-free materials [20,21]. At ambient conditions, the choice of electrolytes is limited to aqueous electrolytes, non-aqueous electrolytes, ion-conductive membranes, and ionic liquids, each with some advantages and disadvantages [1–3], [22–24]. As the final goal of nitrogen reduction reaction (NRR) studies is to design a catalyst that can produce ammonia electrochemically from air and water, investigations using aqueous electrolytes are generally more appealing.

Transition metal nitrides (TMNs) have been shown to be promising for various electrochemical reactions such as oxygen reduction reaction (ORR) and hydrogen evolution

reaction (HER) [25–29]. Furthermore, Zeinalipour-Yazdi et al. have shown high catalytic activities for TMNs in a Haber-Bosch ammonia synthesis process under less severe operating conditions, notably due to the facile formation of nitrogen vacancies on their surfaces [30]. In electrochemical synthesis route, TMNs may, as well, outperform pure transition metals in favoring NRR over HER by stabilizing surface N-vacancies and destabilizing H or O surface species. The N-vacancies in these surfaces which push forward NRR through the Mars Van Krevelen (MvK) mechanism instead of associative or dissociative mechanisms, makes these surfaces unique in their application [16,31]. Comprehensive density functional theory (DFT) calculations by Abghoui et al. on TMNs have furthermore predicted some of these nitrides to be selective to catalyze NRR via a MvK mechanism, where the surface N atom is protonated, releasing one  $\text{NH}_3$  molecule and leaving behind a N-vacancy. The formation of the initial ammonia molecules from the surface nitride layer is hereafter referred to the initiation of the MvK mechanism. In the next step, an  $\text{N}_2$  molecule is adsorbed into the surface N-vacancy which weakens and dissociates the  $\text{N}\equiv\text{N}$  triple bond [32,33]. The nitrides that were found to follow this mechanism are in particular the (100) facets of VN, ZrN, NbN and CrN in the rocksalt (RS) which are predicted to be stable against poisoning and decomposition according to the assumptions made in the calculations [34,35].

There have been several reports on the experimental aspects of the electrochemical NRR and the applications of TMNs as electrocatalysts for ammonia synthesis in aqueous media at ambient conditions. However, accurate ammonia measurement in NRR experiments is challenging because detection of low concentrations of aqueous ammonia is prone to false positives. Lately, several studies have shown the importance of applying strict protocols to NRR experiments [10, 36–40]. To conduct a reliable NRR study, sensitive quantification methods must be used, and rigorous control experiments must be performed.  $\text{Ar(g)}$  should be used as a blank media deprived of all reactive  $\text{N}_2(\text{g})$  in the solution, and  $^{15}\text{N}_2$  isotope labeling experiments should precisely determine the source of ammonia. All the gases used in these experiments need to be scrubbed of  $\text{NO}_x$ ,  $\text{CO}_2$ , and  $\text{NH}_3$  before entering the electrolyte environment. This is particularly important for performing an accurate isotope labeling experiment as there can be traces of  $^{15}\text{NH}_3$  and  $^{15}\text{NO}_x$  in  $^{15}\text{N}_2$  tanks. This was conveyed in a study by Dabundo et al. who analyzed the contamination of  $^{15}\text{NH}_4^+$ ,  $^{15}\text{NO}_3^-$ ,  $^{15}\text{NO}_2^-$  and  $^{15}\text{N}_2\text{O}$  in different commercial  $^{15}\text{N}_2$  gas stocks from three suppliers. The authors reported the presence of up to  $1900 \mu\text{mol}$  of  $^{15}\text{N}$ -ammonium per mole of  $^{15}\text{N}_2$  gas in one of Sigma-Aldrich stocks [41]. This external source of labelled ammonia can readily buildup in the volume of electrolyte under study and generate false positives. Therefore, it is imperative to remove all contaminants from the gas before introducing it into the electrolyte chamber and collect blank samples to make sure there are no contaminants from the gas, forming false positives in the experiments; a fact that is, in most cases, ignored by researchers. Correct pretreatment of Nafion, the commonly used membrane in NRR experiments, is equally important. Poor treatment processes can easily introduce ammonia from the atmosphere into the Nafion, which can be released to the media during NRR experiments [42].

Unfortunately, out of all experimental reports on TMNs, none with positive results meet all the criteria mentioned above and are therefore not discussed further in this paper. On the other hand, Manjunatha et al. reported the instability of VN nanoparticles, and chemical and electrochemical leaching of vanadium and nitrogen out of the catalyst structure into the acidic, neutral, and alkaline electrolytes [43]. Hu et al. reported negative results when using  $\text{Mo}_2\text{N}$  nanoparticles in their experiments. Of specific importance is that they found no  $^{15}\text{NH}_4^+$  formation, and thus, no catalysis when they purified their  $^{15}\text{N}_2$  gas using 50 mM sulfuric acid [44]. Du et al.

investigated into the performances of rocksalt cubic VN and NbN as well as tetragonal Nb<sub>4</sub>N<sub>5</sub> in aqueous electrolytes with different pH values. By ensuring strict experimental conditions such as using a sealed electrochemical setup, purification of gas through an acid-trap, and measuring background contamination and subtracting that amount from all the subsequent samples, no catalytic activity was reported for VN and NbN. Furthermore, VN synthesized at 600 °C in alkaline media and Nb<sub>4</sub>N<sub>5</sub> in all pH ranges were found to be unstable and produced ammonia through leaching of inherent nitrogen atoms in the catalyst structure [45].

Although there have been numerous experimental studies on electrochemical NRR on TMNs, a comprehensive electrochemical study on the mechanisms of this reaction is still missing. In the present work, we utilize different electrochemical techniques to unravel the possible underlying mechanisms for NRR in an aqueous electrolyte at ambient conditions using four polycrystalline TMNs in their rocksalt structure: VN, CrN, NbN, and ZrN produced as thin films on conductive substrates. The thin films are characterized before and after each experiment via X-ray diffraction (XRD) and X-ray reflectivity (XRR). A flow-injection analysis method is used for ammonia detection, with a detection limit of as low as 1 ppb for a sample size of 200  $\mu$ L (over an order of magnitude more sensitive than the conventional method of Nessler's reagent [46]), and rigorous controls and analyses are performed to ensure robustness of results.

Out of the four TMNs tested under the experimental conditions in this study, CrN does not produce ammonia under any circumstances. VN and NbN produce ammonia through the reaction of nitrides of their topmost layers and thereafter undergo an inactivation phase where both the MvK mechanism and the nitride leaching from subsurface layers stop. ZrN is shown to be the only surface that not only does not go through inactivation but also produces ammonia with higher reaction rates and current efficiencies at low overpotentials in N<sub>2</sub>(g) compared to Ar(g). Compared to VN and NbN, ZrN is shown to be a more stable surface demonstrated by cyclic voltammograms recorded at fixed intervals throughout the experiments. However, since ammonia concentrations are below the detection limit of <sup>1</sup>H-NMR (ca. 30 ppb), <sup>15</sup>N<sub>2</sub> isotope labeling experiments are not performed to confirm the ammonia source. All surfaces, on the other hand, demonstrate distinctly different behavior in N<sub>2</sub> environment when compared with the Ar blank environment where a larger double layer capacitance is observed in all cases at selected potentials demonstrating a stronger adsorption of the species that can be explained by N<sub>2</sub> adsorption to the surfaces. Moreover, these experimental results are compared with our previously published DFT results. Further analysis of the theoretical results done in this study explains why CrN does not produce ammonia and why ZrN shows the best performance among other catalysts. The onset of ammonia production on ZrN is also in close agreement with theoretical predictions. This study, therefore, sheds more light on the catalytic behavior of the TMN surfaces studied, and can be used for further surface and environment engineering and development towards a stable and active catalytic reactor system.

## 2. Experimental

### 2.1. Deposition of thin film surfaces and characterization

Thin films of CrN, VN, NbN and ZrN are deposited using reactive dc magnetron sputtering in a modified high-vacuum Polytechnic Discovery E500 deposition system. 4" diameter targets of Cr (99.95%), V (99.9%), Nb (99.95%) and Zr (99.7%) are used, and the substrates are 4" (100 mm) diameter, low-resistivity Si wafers (< 0.02 Ohm cm). The target-substrate distance is approximately 11 cm and the angle between the target and substrate normals is

60°. The substrate temperature is 200 °C and controlled using a radiative heater and an Omega OS100 series IR temperature sensor which is calibrated with a K-type thermocouple prior to deposition. The total pressure during deposition is in the range  $3.2 \times 10^{-3}$  mbar to  $3.7 \times 10^{-3}$  mbar with a 99.999% purity Ar flow of 17-25 sccm and 99.999% pure N<sub>2</sub> flow in the range 2.0-10.0 sccm, depending on the nitride system. The reader is referred to Table S4 in the SI for the details of the growth process for each surface. The base pressure of the system prior to deposition is below  $2 \times 10^{-5}$  mbar. After deposition, the wafers are diced to appropriate sizes using a diamond cutting saw. The film thickness, density and roughness is characterized after growth by X-ray reflectivity (XRR) and the crystal structure and morphology are studied using grazing incidence X-ray diffraction (GIXRD), both using a Panalytical X'Pert MRD system. XRR is carried out with a Goebel mirror on the incident side (1/32° slit and a Soller slit) and a 0.27° collimator and a collimator slit on the diffracted side. XRD measurements are carried out in a grazing incidence geometry with a fixed incident angle of  $\omega = 1^\circ$ , an incident slit of  $\frac{1}{4}^\circ$  and the collimator slit is removed. XRR shows that the films are relatively smooth (rms surface roughnesses of 1.3-2.2 nm) and exhibit densities close to the expected bulk densities of the respective nitride, as found by fitting the data using the GenX software for reflectivity [47]. A representative XRR curve including the fit is shown in the inset of Figure S11(a) in the SI. The fitting results for all of the samples are summarized in Table 1. The structure is in all cases polycrystalline, as revealed by the grazing incidence XRD measurements shown in Figure 1. All allowed diffraction peaks are observed, with positions matching their rocksalt structure as given by the following ICDD Reference Patterns, CrN(00-011-0065), VN(00-035-0768), NbN(01-089-5007), and ZrN(00-035-0753).

Table 1. Density, thickness and root mean squared surface roughness, as determined by fitting XRR data, as well as the observed lattice parameter based on the XRD measurements for the pristine TMN films.

TMN Films	Density / g cm <sup>-3</sup>	Thickness / nm	Roughness / nm	2 $\theta$ - (111) peak / °	2 $\theta$ - (200) peak / °	2 $\theta$ - (220) peak / °	a / Å
CrN	6.2	55	1.3	38.75	44.10	64.80	4.06396
VN	5.7	67	1.5	37.86	43.98	63.95	4.11354
NbN	8.1	100	1.3	35.65	40.86	59.96	4.37731
ZrN	7.1	83	1.7	33.87	39.36	56.85	4.57733

X-ray photoelectron spectroscopy (XPS) is used to study chemical bonding and the film composition of ZrN coatings prior to and after electrochemical testing. The measurements are conducted using an Ulvac-Phi Quantera II XPS microprobe (USA, Chanhassen Minnesota) with monochromatic Al *K* $\alpha$  radiation. Measurements are conducted using a spot size of 100  $\mu$ m and settings giving a line width of 0.7 eV. Sputter depth profiles are obtained using 500 eV Ar<sup>+</sup> ions rastered on an area of  $1 \times 1$  mm<sup>2</sup>, in 30 steps of 1 min. Calibration of etch rate with a sample of known thickness gives a rate of 1.6 nm/min and thus a total depth for the profiles of 48 nm. Chemical composition is obtained using custom sensitivity factors derived from reference measurements using Elastic Recoil Detection Analysis (ERDA). Selected Zr 3d spectra are analyzed with peak fitting using the software XPS peak, to separate different chemical states of Zr [48]. Contributions are fitted with Voight functions (20% Lorentzian), symmetric for oxide contributions and asymmetric (fixed parameters) for nitride and oxynitride contributions. A representative depth profile

and peak fittings at the surface and below the surface oxide is given in Figure S11(a) in the SI.

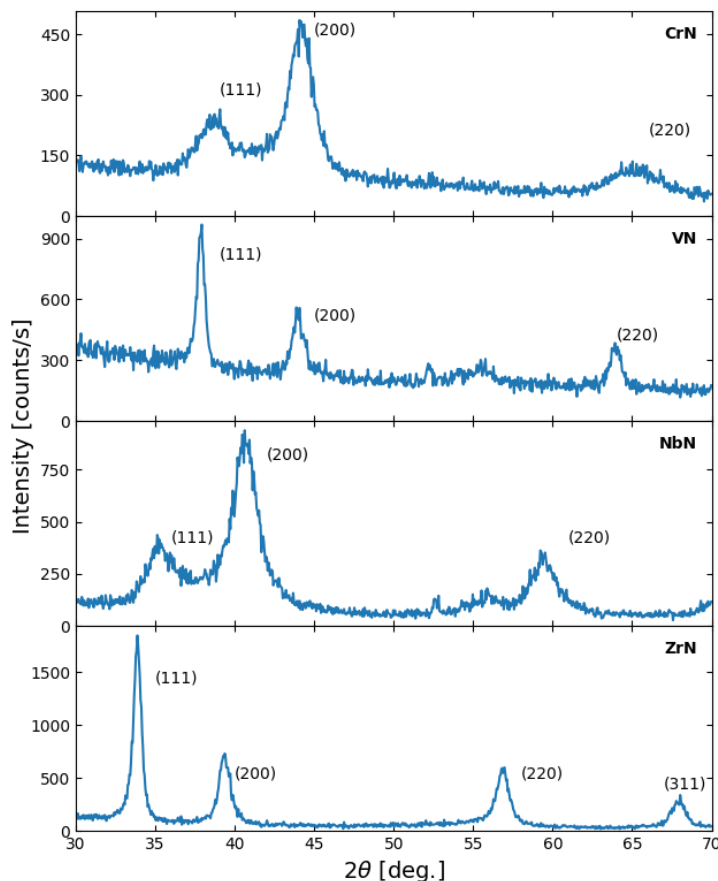


Figure 1. Grazing incidence X-ray diffraction (GIXRD) measurements on the pristine TMN films. All films are polycrystalline with a rocksalt crystal structure.

## 2.2. Electrochemical procedure

All electrochemical studies are performed according to the protocol illustrated in Figure 2. The experiments are performed in a setup in-line with ammonia measurement unit without any manual handling of the samples. This combination of electrochemical experiments and analysis method significantly reduces any type of possible external contamination to the samples (Figure S2). The electrolyte used in the study is 0.1 M potassium hydroxide (KOH, Merck,  $\geq 85\%$ ). Before starting any electrochemical experiments, the electrolyte is deprived of solvated gases such as oxygen and nitrogen by purging with Ar(g) (HiQ<sup>®</sup> Argon 5.0, Linde) for 1 h. Prior to entering the electrolyte container, the gas is first passed through a container of 0.05 M H<sub>2</sub>SO<sub>4</sub> and next ultrapure water (MilliQ<sup>®</sup>, Grade 1) to remove any possible traces of NO<sub>x</sub>, CO<sub>2</sub>, and NH<sub>3</sub>. The Ar saturated electrolyte is collected into two 50 mL gas-tight syringes (Model 1050 TLL, Hamilton<sup>®</sup>, USA) which are used to feed the electrochemical system. The thin-film catalysts are used in a three-electrode electrochemical flow-cell reactor ( $\mu$ -PrepCell<sup>TM</sup>, Antec Scientific, Netherlands, Zoeterwoude). The commercial reactor is a one-compartment design. However, for the specific

aim of this study, the design is modified to allow for two compartments for the working and the counter electrode separated by a Nafion membrane. The commercial counter electrode,  $Ti_{(s)}$  is coated with Pt on top of a Ta adhesive layer. The commercial Pd/H<sub>2</sub> reference electrode is not used since it is a pH dependent electrode. Instead, a holder is designed to allow for Ag/AgCl (3 M KCl) reference electrode to be mounted on the counter electrode block. All potentials in this work are referenced against the reversible hydrogen electrode (RHE). The experimental potential values are converted from Ag/AgCl to RHE scale using the formula:  $E(\text{RHE}) = E(\text{Ag/AgCl}) + 0.059 \times \text{pH} + 0.21$ . Nafion 211 is used as the proton exchange membrane separating the working and the counter compartment. The pretreatment of Nafion 211 is carried out using a modified method [42]. The procedure involves i) 10 minutes of sonication of Nafion in 5% H<sub>2</sub>O<sub>2</sub> to remove the organic impurities, ii) 10 minutes of sonication in DI-water, iii) 10 minutes of sonication in 0.5 M H<sub>2</sub>SO<sub>4</sub> to remove the metallic impurities, iv) 10 minutes of sonication in DI-water, v) more than 12 h in DI-water at 80 °C for expansion, and vi) sonication in 0.05 M H<sub>2</sub>SO<sub>4</sub> and DI-water right before application in the electrochemical setup. The electrochemical flow-cell design is described in detail in Figure S1 in the Supplementary Information (SI). The catalysts are the working electrodes in the electrochemical system whose potentials are controlled using a Gamry potentiostat, Reference 1010E (Gamry Instruments, Warminster, PA 18974 USA).

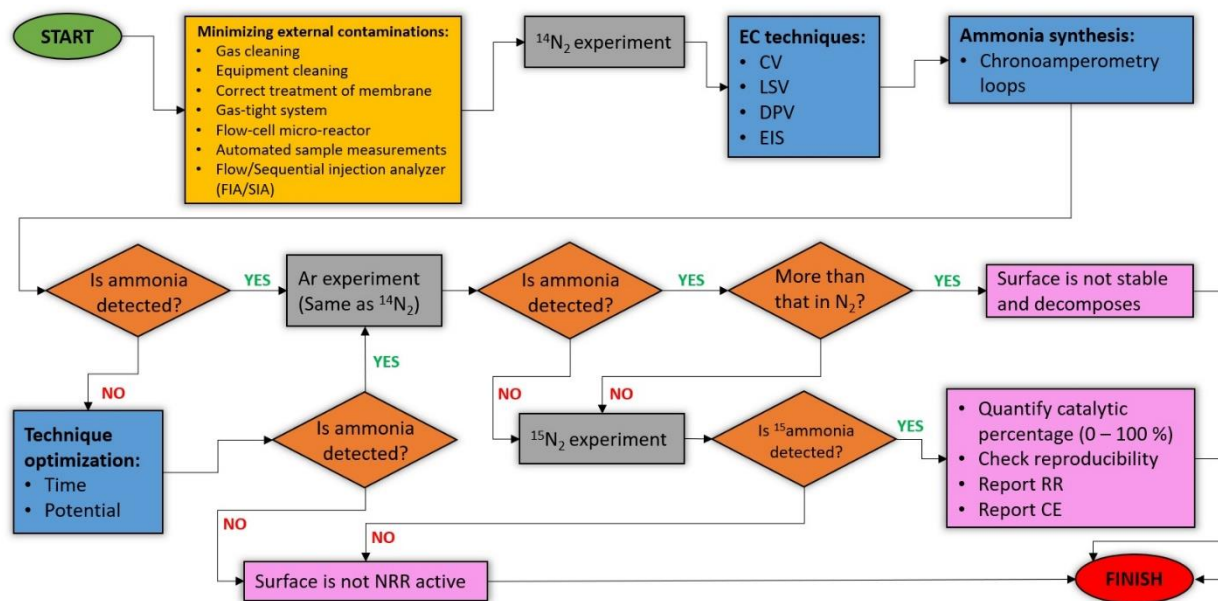


Figure 2. Procedures pursued for the NRR studies in this work which ensures reliable and reproducible data.

Once the setup is assembled, a constant flow of electrolyte (20  $\mu\text{L}/\text{min}$ ) is sent through each compartment using a dual syringe pump (KD Scientific, Inc., Legato 100, Massachusetts 01746-1388 USA). In the experiments where the aim is to quantify ammonia, the gas of interest, either N<sub>2</sub> (HiQ<sup>®</sup> Nitrogen 5.0, Linde) or Ar, is introduced to the working compartment after passing through two scrubbing units and a “T” junction where it is mixed with the electrolyte. The fluid (gas and electrolyte combined) leaving the working compartment of the cell is collected in 100  $\mu\text{l}$  of 0.5 M H<sub>2</sub>SO<sub>4</sub> used as an acid-trap and the resulting solution is collected, using a syringe pump, in a 200

$\mu\text{L}$  sample loop to be analyzed in the ammonia measurement unit. In the experiments where the aim is to study the electrical behavior of the catalyst using dynamic electrochemical impedance spectroscopy (DEIS), the electrolyte is saturated with the gas of interest and sent through the electrochemical system without the introduction of gas directly over the working electrode. This is done due to the large perturbation caused by the gas flow which would disrupt data interpretation. We show in the SI a comparison between Nyquist plots with and without gas bubbles in the system, demonstrating that the same trend is maintained, and the resistances and capacitances are measured within the same order of magnitude (Figure S7).

At the beginning of all experiments, background ammonia is measured until low and equal-sized peaks emerge. This is taken as the background level and consequently subtracted from all the rest of the peaks measured during the electrochemical sequence. In the beginning of the sequence, the open circuit potential (OCP) is recorded until reaching a stable value. Cyclic voltammetry (CV) with a scan rate of 100 mV/s and linear sweep voltammetry (LSV) with a scan rate of 10 mV/s are recorded in the potential window between OCP and a negative applied potential in the faradaic zone for all the surfaces. Figure 3 shows the overlay of LSV in Ar and  $\text{N}_2$  media. To quantify ammonia and calculate the reaction rate (RR) and current efficiency (CE), the chronoamperometry technique is utilized. Based on the LSV profiles on each surface, four different potentials (E1, E2, E3, and E4) are selected to be used in a chronoamperometry loop. The loop consists of 10 s of applied potential and 10 s of resting potential (recording the OCP). The loop is maintained for 2100 s which is the duration needed to measure three consecutive samples in the in-line ammonia measurement unit. Since the OCP values in all the systems are positive values ranging from 0.6 – 0.8 V, these values are used in the chronoamperometry loop to desorb the adsorbed cation species which could possibly block the active sites on the catalyst and hinder  $\text{N}_2$  adsorption (Figure S16). The effectiveness of this method has been shown for ZrN as an example (Figure S17) where the ammonia production is maintained for 2 hours when the potential is cycled in a loop compared to when the same potential is held constant. In the latter case, ammonia production has a decreasing trend with time and comes to a complete halt after around 40 minutes. The reader can refer to Figure S18 for an example of a potential and current density graphs as a function of time recorded in a chronoamperometry loop for ZrN. Once the study at each potential is completed and before the next potential is applied on the same surface, two CV cycles are collected to monitor the status of the catalyst after going through each specific applied potential. These CV cycles are also used to study the stability of the catalyst during the whole electrochemical study in both  $\text{N}_2$  and Ar environment. The samples collected into the acid trap are then sent for ammonia analysis as described in the next section and schematically shown in Figure S2. The whole process from ammonia production inside the micro-reactor to ammonia measurement is conducted in a closed, in-line system.

For a more detailed study of the electrical behavior of the surfaces in different gas environments, DEIS is carried out on each surface in Ar and  $\text{N}_2$  at four potential ranges: (1) at OCP, (2) in the capacitive zone, (3) at onset potential (OP), and (4) in the faradaic zone. The amplitude is set at 10 mV rms and 10 points are collected per decade in a frequency range of 100,000 Hz to 0.1 Hz. The DEIS spectra are fitted using the Z-View® Software (Scribner Associates) and equivalent electrical circuits are fitted to determine the corresponding resistances, capacitances, inductors, etc. Each fitting is done by starting with a typical Randles circuit which is then modified to obtain the best fit to the data.

### 2.3. Ammonia Quantification

Ammonia quantification is done using a method described in our previous work [42]. The fluid leaving the working compartment of the cell is collected into an acid trap, a vial containing 100  $\mu\text{l}$  of 0.5 M  $\text{H}_2\text{SO}_4$ , and the resulting solution is collected, using an automated syringe pump, and inserted into a 200  $\mu\text{L}$  sample loop in the Flow Injection Analysis® system (FIALab-3500b, FIALab Instruments Inc. Bellevue, WA 98007 USA) [49]. The sample is reacted with Ortho-phthalaldehyde (OPA) to make an  $\text{NH}_3$ -OPA fluorescent product to be detected in a photomultiplier tube (PMT) with a fluorometric detection (excitation at 370 nm, detection at 425 nm). This method has the most sensitive limit of detection (down to 1 ppb) compared to the commonly used methods. The electrolyte is always contained in a gas tight environment, never exposed to atmosphere, or handled in any manner. This minimizes any external sources of contamination to the samples. A full description of the method is included in the SI.

## 3. Results

### 3.1. Electrochemical characterization

Figure 3 shows the linear sweep voltammograms of the four TMNs in Ar vs.  $\text{N}_2$  media. CrN is removed from all the comparisons here since it does not produce ammonia in the  $\text{N}_2$  reactive gas media. The reader is referred to Figures S4 and S5 regarding the CV and ammonia measurements for CrN. As discussed in section 2.2, gas is introduced into the working compartment of the micro-reactor with the electrolyte. This is done to assure sufficient access of the N-vacancies to  $\text{N}_2$  for a higher chance of regeneration. The gas flow over the surface of the catalyst causes a perturbation in the system which generates noise in the current-potential curves. However, the general trend of these curves is not lost, and it is possible to observe the system response differences with and without the reactive gas ( $\text{N}_2$  and Ar, respectively). Figure S6 shows the comparison of LSV curves in both cases of introducing the gas directly over the surfaces on one hand and using electrolyte saturated with the gas on the other hand. Current density is generally higher when the electrolyte is saturated with the gas. We explain this by the fact that when the surface is exposed to gas saturated electrolyte, the full area of the electrode is in contact with the electrolyte, while the gaseous environment reduces the exposed surface area at each moment as bubbles are partially filling the cathodic chamber. Furthermore, when electrolytes are saturated with gas, LSV in Ar(aq) and  $\text{N}_2$ (aq) are almost overlapped with a slight shift in the OCP and OP in all the cases. NbN shows a less negative OP in  $\text{N}_2$ (aq) vs Ar(aq), while VN and ZrN show a more negative OP in  $\text{N}_2$ (aq) (Figure S6). On the other hand, when gases are introduced directly over the surfaces, VN does not show any outstanding difference in the two media. The OP is not shifted and the current density vs. applied potential does not change drastically between Ar(g) and  $\text{N}_2$ (g). However, NbN and ZrN show an evident difference between  $\text{N}_2$  and Ar. The differences when comparing Ar(g) over  $\text{N}_2$ (g) environment are observed in i) more positive OCP, ii) more negative OP, and iii) lower current density.

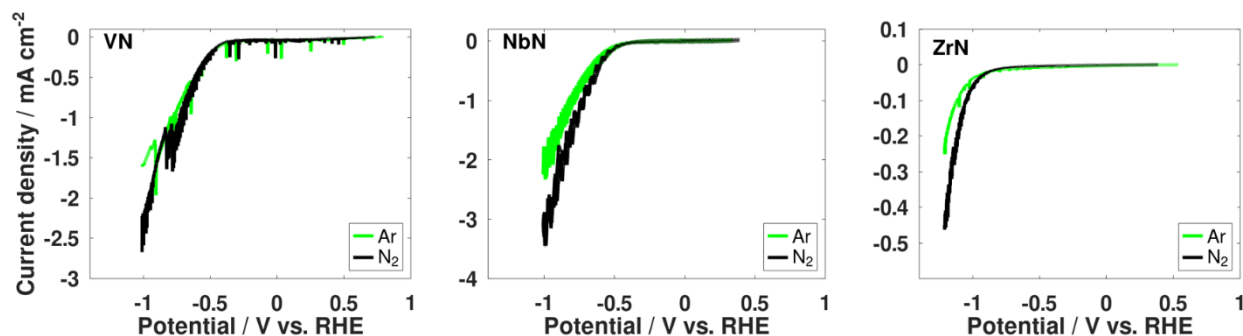


Figure 3. Comparison of linear sweep voltammetry (LSV) in Ar vs. N<sub>2</sub> on TiN, VN, NbN, and ZrN starting from the measured OCP in each case. Note that the noise on these curves is due to the perturbation caused by the introduction of the gas together with the electrolyte directly over the surfaces. Figure S6 shows a comparison of the LSV curves with and without direct bubbling of Ar and N<sub>2</sub> gasses over the surfaces.

Table 2 presents the Tafel slope values for each catalyst both in Ar(aq) and N<sub>2</sub>(aq), and in Ar(g) and N<sub>2</sub>(g). The catalysts under study all present a higher Tafel slope value in Ar(aq) vs. N<sub>2</sub>(aq) environment. Considering the physical-chemical meaning of the Tafel slopes, as the energy required (potential) to increase the current by a factor of 10 and initiate the faradaic process, the larger this value, the more difficult it is to initiate this process [50]. As the predominant electrochemical reaction occurring in Ar is HER after the formation of the initial ammonia molecules from the surface nitride layer, it is possible to infer that the decrease in the Tafel slope when N<sub>2</sub> is added to the system is due to an additional available reaction (NRR). The fact that N<sub>2</sub> molecules can inhibit the HER can also be attributed to the diffusional mass transport and adsorption of N<sub>2</sub> onto the surface. This selectivity towards NRR over HER is clearly seen for ZrN, but the similarity of the slope values for VN and NbN (difference of around 10-20 mV/decade) shows less of a competition between HER and NRR. VN presents the lowest Tafel slope in Ar(aq) of the four nitrides (ca. 139 mV per decade). This value indicates a common Volmer rate-determining step in such conditions [51]. The other two nitrides presented here, have a Tafel slope over 200 mV per decade in Ar(aq), demonstrating a greater energy demand for HER on these surfaces in comparison with the VN surface.

Table 2. Tafel slopes in Ar and N<sub>2</sub> environments. The slopes are calculated based on LSV curves collected for electrolyte saturated with Ar and N<sub>2</sub> gas, denoted as Ar(aq) and N<sub>2</sub>(aq) and for electrolyte directly bubbled with the gasses, denoted as Ar(g) and N<sub>2</sub>(g).

Surfaces	Tafel slopes $\pm 2$ / mV decade <sup>-1</sup>			
	Ar(aq)	Ar(g)	N <sub>2</sub> (aq)	N <sub>2</sub> (g)
VN	139	324	129	248
NbN	208	227	189	302
ZrN	271	310	193	232

The trend in the Tafel slopes changes when the access to the gas is increased, i.e., Ar(g) and N<sub>2</sub>(g). The general trend is that these values are larger compared to those recorded in aqueous media which is an indication of the difficulty of initiating the faradaic processes when gasses are directly bubbled over the surfaces. This might be due to turbulence imposed on the system which affects the availability of the reactants close to the electrode surface, thus, not allowing the effective electron transfer to occur, as well as less surface area active at each moment. We will not quantitatively compare the values between the two environments (aq) vs. (g) for this reason but focus on different trends observed in Ar vs. N<sub>2</sub>, that is Ar(g) vs. N<sub>2</sub>(g) or Ar(aq) vs. N<sub>2</sub>(aq).

In Ar(g) media, where HER is the predominant reaction to take place, NbN has the lowest Tafel slope, meaning that this reaction is more favored on this surface compared to the rest of the surfaces. In N<sub>2</sub>(g), however, where there is the possibility of NRR in addition to HER, NbN shows the highest Tafel slope of all, meaning that these two faradaic processes are less favored on NbN compared to the rest of the surfaces. Thus, addition of N<sub>2</sub>(g) to the system seems to inhibit the HER process to a great extent as the Tafel slope in N<sub>2</sub>(g) is higher than that of Ar(g). However, the less negative OP in N<sub>2</sub>(g) vs. Ar(g) on this surface might as well indicate that NRR is still competitive within the potential range between OP in N<sub>2</sub>(g) and OP in Ar(g). In Ar(g), the other two nitrides are equally bad for HER as they have relatively high Tafel slopes in this medium. However, the decreased value of the Tafel slope in N<sub>2</sub>(g) compared to Ar(g) indicates an increasing current density due to NRR on ZrN and VN. Qualitatively, these two surfaces are the only surfaces that yield lower Tafel slopes in both N<sub>2</sub>(g) vs. Ar(g) and N<sub>2</sub>(aq) vs. Ar(aq).

### 3.2. Ammonia synthesis and measurement

Based on the LSVs, four potentials are individually selected for each surface to be applied in chronoamperometry loops for ammonia catalysis studies. These potentials cover a range from the capacitive region to the faradaic zone. The exact procedure of the chronoamperometric technique is provided in the experimental section. Table 3 shows the selected potentials for each surface.

Table 3. Potentials used in the chronoamperometry loop for ammonia quantification. Chronoamperometry loop consists of two steps: (1) applying cathodic potential (E1, E2, E3, or E4) for 10 s, and (2) recording OCP for 10 s. The loop is programmed to continue for as long as three consecutive peaks are measured using the in-line ammonia quantification method.

Surfaces	E1 (V)	E2 (V)	E3 (V)	E4 (V)
CrN	-0.5	-0.6	-0.7	-0.8
VN	-0.2	-0.4	-0.6	-0.8
NbN	-0.2	-0.4	-0.6	-0.8
ZrN	-0.6	-0.8	-1	-1.2

Figure 4a shows the ammonia production on all the surfaces during the whole electrochemical (EC) studies. Initial EC characterizations of each surface include CV recorded in various potential windows from OCP to the faradaic region, LSV, differential pulse voltammetry (DPV), and EIS. E1 to E4 refers to the chronoamperometry loops recorded at potentials E1 to E4 according to Table 3. The data used to generate this figure is available in Table S1. For all the surfaces, the experiments in N<sub>2</sub>(g) and Ar(g) are repeated at least three times. Results reveal that CrN does not produce ammonia at any stage of the electrochemical characterization and chronoamperometry loops. The surface is regarded as being quite stable under the operating conditions of the study and therefore, not undergoing the initial stage of the MvK mechanism, which is the reacting of the surface nitrides to produce ammonia. Due to this fact, no Ar blank test is performed on this surface. VN produces equal amounts of ammonia in N<sub>2</sub>(g) and Ar(g) within the measurement error during the initial electrochemical characterization, and does not produce ammonia at E1, E2, E3, and E4. This is as explained more in the discussion section, due to surface inactivation for NRR upon reacting the N atoms in the surface top layer(s). NbN also produces same amounts of ammonia in Ar(g) and N<sub>2</sub>(g) within the error range during the initial characterization phase and in the chronoamperometry loops at E1-E4 potentials. The low amounts of ammonia production at E1-E4 potentials indicates a slight leaching of the surface-bound nitride in cases where it was not formed during the initial

characterization step. In the case of ZrN, equal amounts of ammonia are produced within the initial electrochemical characterization which is, as for the cases of VN and NbN, due to reacting the N atoms in the first 2 – 3 monolayers of the catalyst. Monolayer calculations are provided in section 4 of the SI. Thereafter, ammonia is detected at all the tested potentials of the chronoamperometry loops under N<sub>2</sub>(g) environment. Ammonia formation under the same conditions in Ar(g) is missing at potentials E1 and E2 which indicates that NRR is being catalyzed at low applied potentials in the N<sub>2</sub>(g) environment. However, due to surface decomposition at E3 and E4, ammonia starts to form.

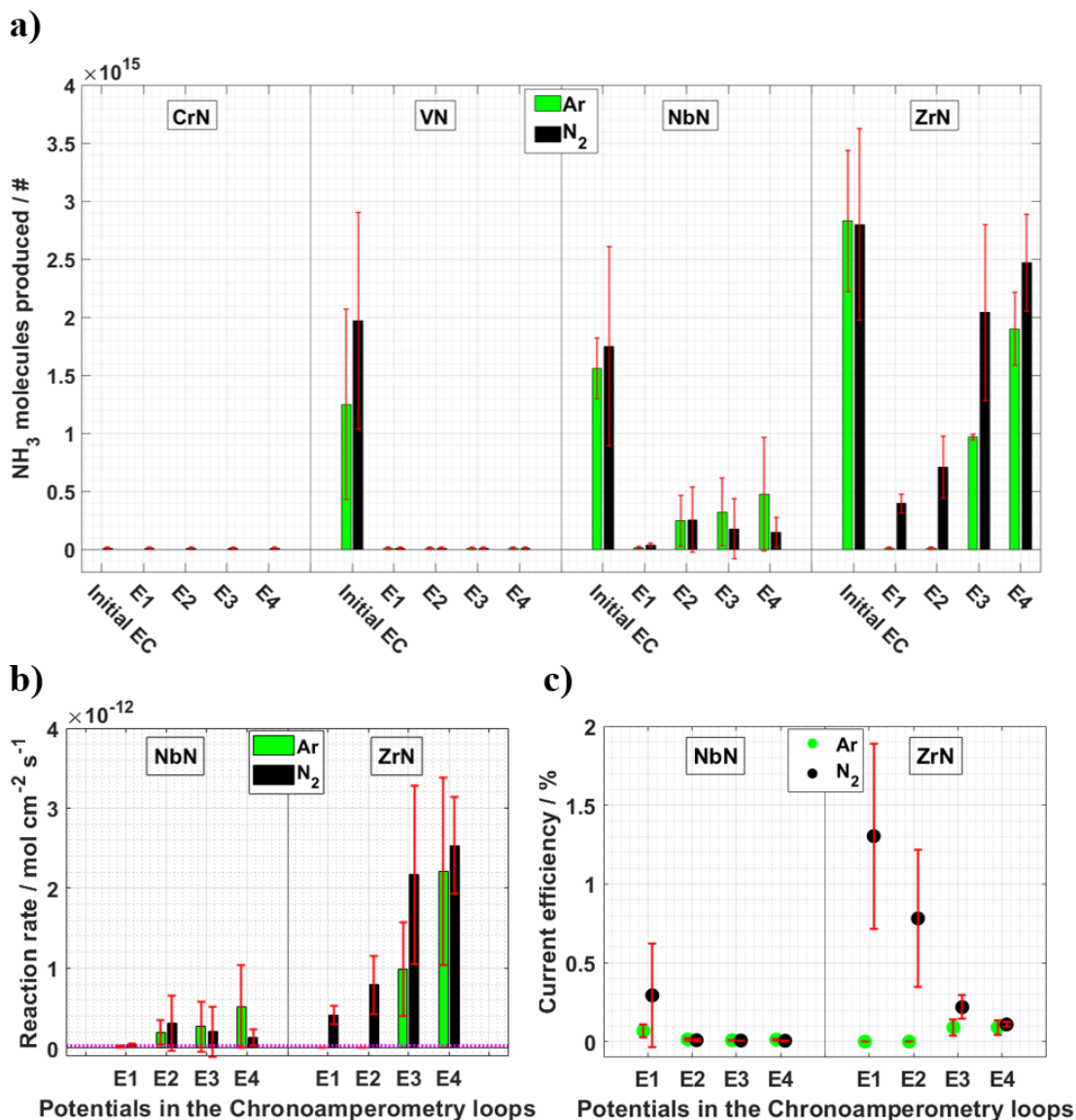


Figure 4. Comparison of (a) ammonia molecules production in the whole electrochemical (EC) studies, (b) reaction rate (RR) of ammonia formation on NbN and ZrN, and (c) current efficiency (CE) towards ammonia on NbN and ZrN as a function of applied potential in the chronoamperometry loops (see Table 3) in both N<sub>2</sub>(g) reactive medium (black columns) and Ar(g) blank medium (green columns). Limit of detection for the reaction rate is plotted in dotted magenta line.

Figures 4b and 4c demonstrate RR and CE for NbN and ZrN in the chronoamperometry loops. The reader is referred to the SI, section 3, for details of the calculations. Although NbN produces ammonia in the loops, the RR and CE associated to these productions are not significantly higher than zero, accounting for the error bars. Therefore, the only surface to produce ammonia in this study is considered to be ZrN. The maximum RR is  $2.53 \times 10^{-12} \pm 0.6 \times 10^{-12}$  mol cm<sup>-2</sup> s<sup>-1</sup> for ZrN at E4 (-1.2 V) corresponding to a concentration of  $114 \pm 43$  ppb in a 200  $\mu$ L sample volume, while the maximum CE is  $1.30 \pm 0.59$  % at E1 (-0.6 V) corresponding to a concentration of  $20 \pm 5$  ppb in a 200  $\mu$ L sample volume. On ZrN, increasing the cathodic potential from E1 to E4 in N<sub>2</sub> environment increases the RR towards NRR but reduces the CE. We attribute that to the increasing charge transfers towards HER which predominates the increasing charge transfer towards NRR. The rate of CE decrease in N<sub>2</sub> is more drastic than the rate of CE increase in Ar (from 1.30% to 0.11% in N<sub>2</sub> vs. 0% to 0.09% in Ar). In the Ar(g) environment, CE towards NRR increases at E3, and at E4 it is similar to the CE in N<sub>2</sub>(g) environment. It is therefore clear that ammonia production at these two potentials in N<sub>2</sub> is partially (E3) and completely (E4) non-catalytic, whereas, at E1 and E2 the production appears to be catalytic. Again, as we discuss further below, the concentration of the produced ammonia at these two potentials is not high enough to be detected in the isotope labeling experiment.

### 3.3. Dynamic electrochemical impedance spectroscopy

DEIS analysis is performed on all the surfaces in Ar vs. N<sub>2</sub> to study the electrical behavior of the catalysts more profoundly according to their individual voltammetric responses as observed from their respective LSVs. As discussed in section 2.2, this study is conducted by saturating the electrolyte with the selected gases, N<sub>2</sub> or Ar. When comparing the LSVs in Figures 3 and 5 (also shown in Figure S6 for comparison), VN shows no significant difference between Ar and N<sub>2</sub>, independent of the availability of N<sub>2</sub>(g) reactant (saturated electrolyte vs. gas introduction). NbN and ZrN show a relatively overlapping LSVs for Ar(aq) and N<sub>2</sub>(aq) saturated electrolytes, while the behavior when exposed to excessive N<sub>2</sub>(g) shows an earlier onset in N<sub>2</sub>(g). Since there is no way to interpret DEIS data due to the perturbation caused by bubbling the gas directly into the working compartment, gas saturated electrolytes are used. The reader is referred to Figure S7 to observe the trends in the Nyquist plots with and without the direct bubbling over the surfaces.

The Nyquist plots in Figure 5 demonstrate that the TMN surfaces tend to have lower impedance values when exposed to Ar environment. This can be inferred through the semicircles that close at lower Z-real values in most cases in Ar compared to that in N<sub>2</sub>. This effect can be observed more clearly at more negative potentials due to the high polarization of the electrocatalysts which forces the diffusion of electroactive species present in the solution, and, for instance, the redox reactions to occur. Semicircles in the Nyquist plots indicate a contribution from the parallel combination of charge transfer resistance (R<sub>ct</sub>) and the frequency independent capacitance (C), or in this case, constant phase element (CPE) for a more accurate fitting. CPEs convey the formation of the electrical double layer (EDL) at the surface that is related to the adsorption phenomena. Therefore, it is expected that at more negative potentials, protons are easily adsorbed in the EDL and reduced to hydrogen gas, generating a first lower R<sub>ct</sub> value, as observed in Figure 5. From both Bode plots (Figures S8 and S9) and Nyquist plots (Figure 5), we conclude that CPE is due to interfacial capacitance and R is a result of the charge movement through junctions between the atoms of the catalysts.

The Nyquist plots for VN in  $N_2(aq)$  show a more pronounced larger semi-circle, and thus, larger capacitance and resistance, when compared to  $Ar(aq)$  moving to more negative potentials ( $R_{ct1}$  and  $CPE_1$  T values for VN in Tables S2 and S3). As this is a direct outcome of accumulating more species in the EDL, it is inferred that  $N_2$  is indeed adsorbed to the surface when it is saturated in the electrolyte [52]. At E3 and E4 in  $N_2(aq)$  vs.  $Ar(aq)$ , the phase shift diagram (Figure S9) shows a shift to lower angles at low frequencies. We attribute this to an increase in the capacitance which could be due to the adsorption of  $N_2$  in the electrochemical double layer region.

In the case of NbN, negative phase shift responses at the highest frequencies with lower impedance than that of the electrolyte are observed indicating surface instability (Figure S9) [53,54]. The Nyquist in  $Ar(aq)$  at E3 and E4 shows a coil, and the best equivalent circuit includes an inductor in parallel to a resistor which is an indication of the HER. A shift in the phase difference towards a lower angle in the phase angle plot (Figure S9) is observed at OP in  $N_2$  environment. This is an indication of an increase in the capacitive behavior which might be attributed to the existence of  $N_2$  molecules adsorbed in the double layer.

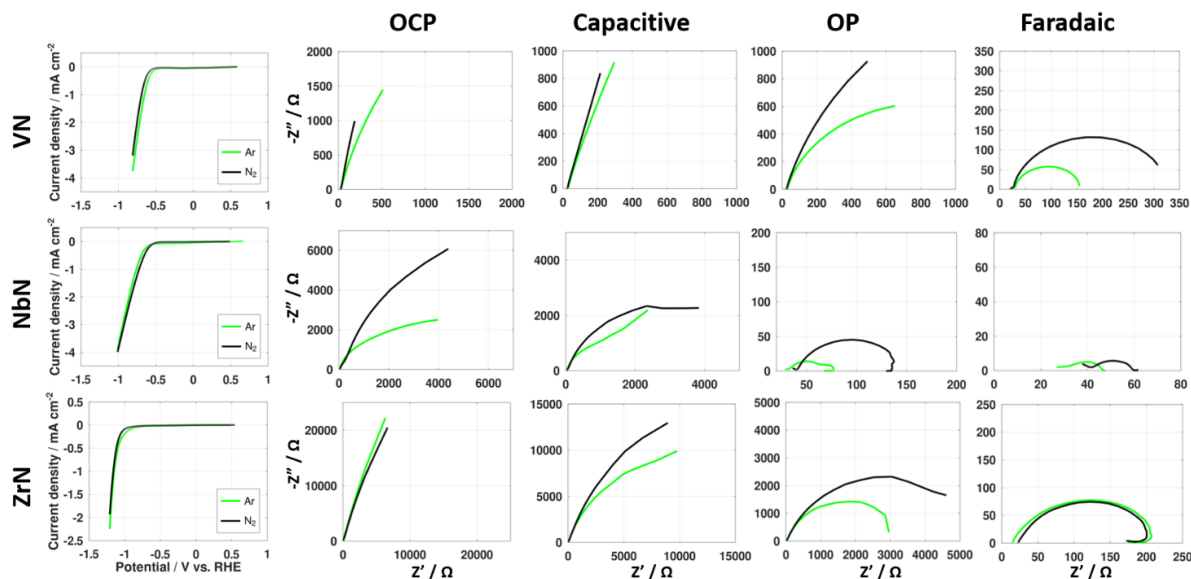


Figure 5. LSV and Nyquist plots for VN, NbN, and ZrN. The Nyquist plots are the result of the DEIS study performed at open circuit potential (OCP), capacitive zone, onset potential (OP), and faradaic zone.

ZrN shows a distinct difference between  $Ar(aq)$  and  $N_2(aq)$  media in the capacitive zone and at OP. In these two regions it is believed that nitrogen is being adsorbed to the surface. In the faradaic zone, a coil is observed in the Nyquist plot in both environments. This is a feature attributed to the HER and the formation of an inductor in parallel to a resistor is confirmed by the circuit model accurate fit (Figure S10 and Tables S2 and S3). Considering these observations, it is clear that the Tafel slopes presented in Table 2 in  $Ar(aq)$  and  $N_2(aq)$  are in agreement with the DEIS results for all three TMN surfaces.

Finally, to compare the  $N_2(g)$  and  $N_2(aq)$  environments (Figure S7), it is clear that for NbN no difference is observed between minimal and excess of the reactant gas, while for VN, both the resistivity and capacitance of the first charge transfer closest to the surface is substantially decreased, indicating that a reaction occurs more easily. This is in agreement with the difference in LSV where an earlier onset potential is observed, even though the Tafel slope is higher with the  $N_2(g)$  environment. For ZrN on the other hand the resistivity and capacitance of the comparable charge transfer are significantly increased in  $N_2(g)$  media, indicating that the reaction is inhibited. This is again in agreement with the LSV, where a later OP is observed. The system impedance does not drastically change upon introduction of gaseous  $N_2$  and the agreement with the LSVs demonstrates that this can be used as a reference point on the system differences between dissolved or gaseous reactants.

### 3.4. Catalyst stability check

As mentioned in the experimental section, stability of the surfaces during each experiment is studied by collecting two CV curves in a fixed potential range. Hereafter, we call these “CV checks”. CV checks are run after each chronoamperometry loop, before starting the next loop, to observe the possible changes enforced on the surface. Figure 6a shows the overlay of these CV checks for the surfaces in Ar(g) and  $N_2(g)$ . In order to make it easier for the reader to follow these changes, the total charge associated with each CV was calculated by integrating the surface area under the forward and the backward scan. This is shown in Figure 6b.

In Figure 6a, VN appears to have a relatively stable CV after application of E1 and E2 (CV check 2 and 3) in Ar(g). After E3, a drastic decrease in current density and capacitance is observed. At this point, surface reconstruction during HER may have slowed down the HER on the surface. The same behavior is observed in  $N_2(g)$  environment, however, reduced current density only happens after application of E4. Although no ammonia is detected at any of these applied potentials, the CV cycles indicate a better stability of the surface in the presence of  $N_2(g)$ .

In the case of NbN in both Ar and  $N_2$  media, there is a decreasing trend in the maximum current densities achieved in the CV checks throughout the experiments. The CVs in Ar show a sudden decrease in total charge after application of E1, whereas, in  $N_2$  medium, this drastic change is observed after application of E3. Therefore, it is possible to presume that surface stability is improved when  $N_2(g)$  is present in the environment. After application of E3 and E4, the surfaces end up showing similar CVs with relatively the same total charges independent of the gas environment.

ZrN in Ar shows a slight decrease in current density after applying E1 and E2. As seen in Figure 4, there is also no ammonia production at these two potentials. After application of faradaic potentials of E3 and E4, a significant increase and a subsequent decrease in the faradaic current density is observed, respectively. The changes observed in the CVs in  $N_2$  have a similar trend while being less significant when compared with the observed changes in Ar, with the only difference being that the current density slightly increases after E1 and E2.

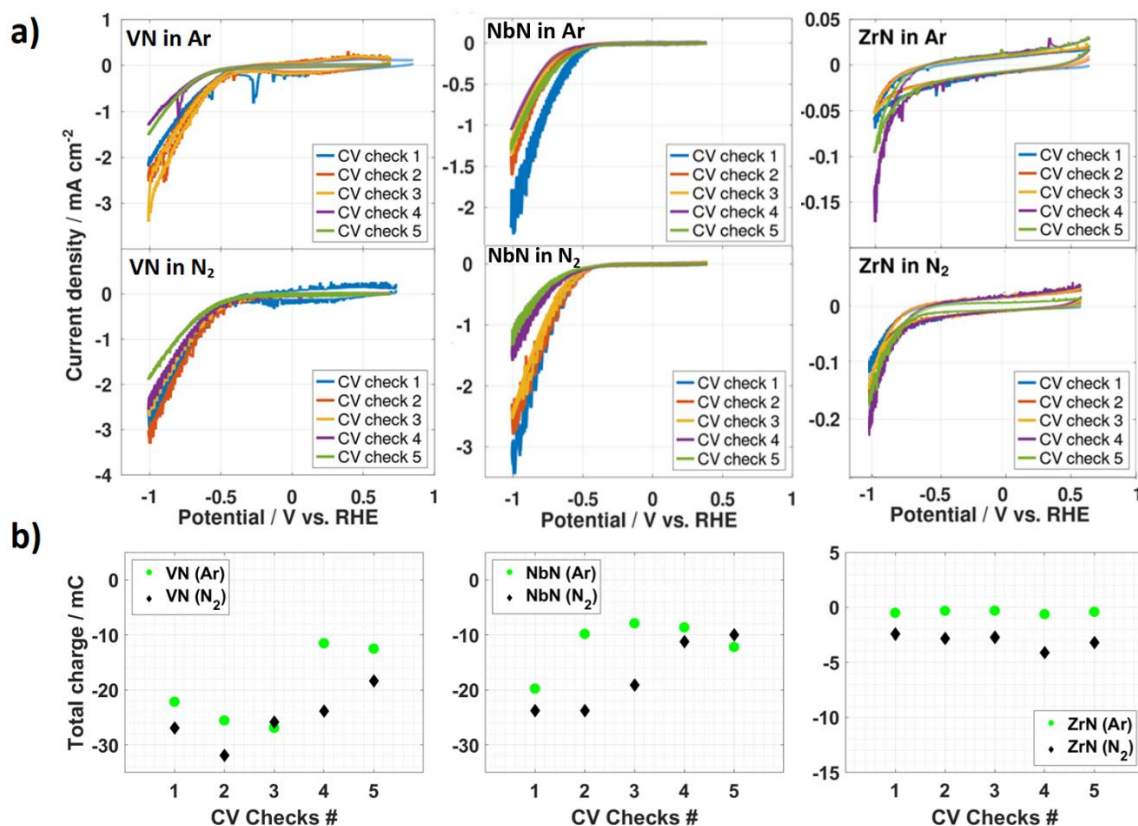


Figure 6. (a) Stability check throughout the experiments by means of cyclic voltammograms taken within fixed intervals between the chronoamperometry loops. The first cycle in each case, CV check 1, is taken before starting the first chronoamperometry loop at E1, and CV check 5 is taken after the last chronoamperometry loop at E4. (b) Total charge in the CVs shown in (a) for each surface in Ar (green circles) vs. N<sub>2</sub> (black diamonds).

The surfaces after the experiments are studied in more detail by XRD and XRR analysis (Figure S13). In all cases, the XRD measurements show no significant change in the crystal structure of the films compared to their pristine form. XRR is used to probe changes in the density profile of the films, from which we can extract the total film thickness, the thickness of possible surface (oxide) layers as well as the surface roughness. This data which is summarized in Table S5 shows no changes in the total film thicknesses within the experimental and equipment errors. XPS depth profiles were collected on a ZrN film for comparison with the XRR results, as shown in Figure S12 of the SI. Good agreement was found between the surface oxide thickness measured from both methods which allows us to rely on only XRR analysis for the surface characterization of all the nitrides.

#### 4. Discussion; DFT vs. Experiment

From kinetics perspective, Abghoui et al. predicted that the first step associated with decomposition of transition metal nitride surfaces should benefit from higher activation free energies of a surface vacancy migration into the bulk than for N<sub>2</sub> adsorption to the N-vacancy that can slow this process

down at ambient conditions in a way that catalyst regeneration occur faster than decomposition [34]. There it was concluded that the RS(100) surfaces of ZrN, NbN, VN and CrN should all be able to regenerate the N-vacancies rather than decomposing. However, for the RS(111) facets, ZrN and NbN were predicted to regenerate the N-vacancies whereas VN and CrN were predicted to decompose, and the RS(110) facets of all these TMNs turned out to be not promising for NRR with regards to activity, selectivity, and stability [55]. This of course depends to great extent on the accessibility of the surface to nitrogen for fast enough regeneration, a phenomenon that can be under influence of the lack of N<sub>2</sub> availability in the electrolyte and probable reorientation of the surface structure causing special hindrance for N<sub>2</sub> to approach the vacant site. These two limitations can be solved by engineering the surface (to be more stable under operating conditions) and the setup (to provide more N<sub>2</sub> access to the surface), and they are the scope of our future work. In the following discussion we will connect the predicted OP and stability from DFT simulations with the observed trends in the experiments.

According to the prediction by Abghoui et al., all facets of VN except RS(100) were predicted to show a faster migration than replenishment of the N-vacancies, i.e. decomposing [34,55]. Furthermore, production of ammonia with high CE over this facet was predicted to only need a bias of -0.5 V. However, between -0.67 to -0.85 V, both the RS(111) and RS(110) facets were predicted unstable and to decompose [55,56]. It was further suggested that in order for a polycrystalline surface not to decompose, the bias should not exceed -0.5 V [34]. However, ammonia production in practice is only observed during the initial electrochemical characterization of the films independent of the presence or absence of the reactive gas, N<sub>2</sub>(g), in the environment. The total ammonia obtained using VN surfaces is in all cases equivalent to a case wherein the inherent nitrides in the 2-3 top layers of the catalyst surface leach out of their structure and react to form ammonia. This scenario may indicate either an initiation of a MvK mechanism or an onset of surface decomposition. However, neither of these two are observed during the chronoamperometry loops. Therefore, ammonia production on VN seems to be sourced from the surface nitride layer after which point the surface becomes inactive and ammonia synthesis comes to a halt. This result is in-line with the previous experimental results wherein polycrystalline VN was found to be electrochemically inactive towards NRR in aqueous media [45].

DFT calculations for NbN showed that both RS(100) and RS(111) facets were stable against decomposition, predicting a well-maintained ammonia production cycle. However, the activation energy of regeneration process (1.7 eV) for the RS(110) of NbN was found to be higher than activation energy of decomposition (0.8 eV). This means that decomposition happens at much higher rate compared to regeneration, and thus this facet might contribute to some instabilities observed in the experiments. It was predicted that the RS(100) and (111) facets of NbN would catalyze the NRR with high CE at -0.65 V and -1.12 V, respectively [34], but the RS(110) at relatively higher potential of -1.5 V but with lower CE as this facet is expected to contribute to both ammonia and hydrogen synthesis [55]. Experiments on this film cannot define a clear OP as ammonia production in N<sub>2</sub>(g) environment is on the verge of falling below the limit of detection. Moreover, the total ammonia production in the whole electrochemical experiments equals to ammonia production from the 2 – 3 top layers of this surface. The same performance of the surface in Ar(g) environment indicates an open pathway for surface decomposition through N-leaching at all tested potentials which is independent of the presence of N<sub>2</sub>(g) in the gas environment. Like VN surface, NbN also renders inactive upon releasing the N atoms in its first monolayers in which case even leaching of surface bound nitrides is prevented. This result is again in agreement with previous

experimental results of Du et al. where polycrystalline NbN was proved to be inactive towards NRR in aqueous media [45].

Polycrystalline ZrN was shown theoretically to be one of the most stable candidates against decomposition. Rocksalt (100), (111), and (110) of ZrN were predicted theoretically to catalyze ammonia production with high to medium CE at -0.76 V, -1.42 V, and -1.45 V, respectively [34,55]. The fact that the total film thickness during Ar and N<sub>2</sub> experiments is not changed (Table S5) shows that ZrN has acceptable stability. At -0.6 V and -0.8 V, ammonia production is only seen in N<sub>2</sub>(g) but not in Ar(g) with a maximum current efficiency of 1.30% ± 0.59% at the OP (-0.6 V) which means that no decomposition takes place at these potentials. Unfortunately, as it is discussed above and in section 9 of the SI, the concentrations of ammonia produced at these potentials (-0.6 V and -0.8 V) are too low to be detectable with our current isotope labeling experiment measurement setup.

Furthermore, analysis of experimental thermochemical data done by Abghoui et al. shows that VN, NbN, and CrN may thermodynamically decompose to their parent metal because their decomposition potential is less negative than their NRR onset potential [32]. However, ZrN was the only nitride that not only had the decomposition potential more negative than its NRR onset potential but also its vacancy migration barrier was much higher than that of CrN, VN, and NbN and thus should be stable enough under operating conditions. This prediction is now observed in this experimental study where ZrN is the only surface demonstrating stability in both Ar and N<sub>2</sub> solutions at the NRR active potentials.

In the theoretical studies as shown in Figure S16, the free energies of adsorbing H<sup>+</sup>, OH<sup>-</sup> and O<sup>2-</sup> are calculated and demonstrated relative to N, showing that there is no potential window for CrN at which the active site becomes available for N<sub>2</sub> adsorption and surface regeneration. This can suggest the observed experimental results of no NH<sub>3</sub> formation on CrN. For other nitrides, there is a potential window for both the (100) and the (111) facets where none of those species are present, and this determines the importance of resting potential in order to regenerate the active sites. This is further observed in the experiments demonstrating higher capacitance in the N<sub>2</sub> environment, due to more adsorbed species, and an earlier onset potential for HER in the Ar environment as observed from LSV, both for NbN and ZrN but not for VN. Based on the theoretical OP values on Figure S16, one could presume that the initial ammonia formation on ZrN and NbN is due to the release of N atoms from the (100) facet. VN, on the other hand, has all three facets available.

In the end of these discussions, we summarize the results obtained in the overall work in Table 5. Interestingly, it is seen that it is not enough to rely on a single analysis to draw conclusions about the performance of the surfaces as the positive or negative results from each of these analyses do not always agree with each other. Rather, it is wise to make use of various techniques to gain insight into the catalytic behavior of the surfaces.

Table 4. Summary of the results obtained in this study. The overall performance of the surfaces is compared in Ar vs. N<sub>2</sub> media. The green boxes show a favorable performance achieved in the specific category by the specific surface. OCP stands for open circuit potential, OP, onset potential, j is the current density.

	VN	NbN	ZrN
<b>LSV – Figure 3</b>	Ar(g) ~ N <sub>2</sub> (g)	OCP: Ar(g) >> N <sub>2</sub> (g) OP: Ar(g) < N <sub>2</sub> (g) j: Ar(g) < N <sub>2</sub> (g)	OCP: Ar(g) > N <sub>2</sub> (g) OP: Ar(g) < N <sub>2</sub> (g) j: Ar(g) << N <sub>2</sub> (g)
<b>Tafel Slopes – Table 2</b>	Ar(g) >> N <sub>2</sub> (g)	Ar(g) <<< N <sub>2</sub> (g)	Ar(g) >> N <sub>2</sub> (g)
<b>Ammonia production in chronoamperometry loops – Figure 4a</b>	Ar(g) = N <sub>2</sub> (g)	Ar(g) > N <sub>2</sub> (g)	Ar(g) << N <sub>2</sub> (g)
<b>DEIS analysis – Figures 5, S8, and S9</b>	Capacitance: Ar(g) < N <sub>2</sub> (g) at OP and in the faradaic zone	Capacitance: Ar(g) < N <sub>2</sub> (g) in the capacitive zone and at OP	Capacitance: Ar(g) < N <sub>2</sub> (g) at OP
<b>Stability check by DEIS analysis – Figures 5, S8, and S9</b>	N <sub>2</sub> (aq): X Ar(aq): X	N <sub>2</sub> (aq): X Ar(aq): X	N <sub>2</sub> (aq): ✓ Ar(aq): ✓
<b>Stability within experiments – Figure 6</b>	N <sub>2</sub> (g): X Ar(g): X	N <sub>2</sub> (g): X Ar(g): X	N <sub>2</sub> (g): ✓ Ar(g): ✓

## 5. Conclusions

In this study, transition metal nitrides that had previously been nominated by DFT calculations as promising catalysts for NRR, are tested in an electrochemical setup to investigate their performance in ammonia synthesis at ambient conditions using 0.1 M KOH(aq) electrolyte solution. Considering the differences in theory and experiments regarding specific surface facets studied in DFT vs. polycrystalline surfaces used in experiments, a full agreement in results is not anticipated. Despite that, some agreement is found between theoretical and the experimental observed OP values for NRR, in particular for ZrN. Different approaches of data acquisition and analysis are presented. The combined data from ammonia measurements, impedance analysis, and stability checks within experiments are used to conclude whether ammonia production is catalytic or not. From this study it is concluded that the nitrides demonstrate distinct electrochemical behavior when exposed to N<sub>2</sub>(g) compared with Ar(g) that can only be attributed to electrochemical interaction with nitrogen. The difference between linear sweep voltammograms in Ar and N<sub>2</sub> media is increased when surfaces are directly exposed to gasses rather than the electrolyte saturation of Ar/N<sub>2</sub>. Overall, CrN is shown to be completely inactive for NRR. VN and NbN both produce ammonia by releasing their inherent N atoms in the beginning of electrochemical experiments. Based on theoretical onset potential determinations from DFT data, it is believed that ammonia production on NbN is dominantly from the RS(100) facet while VN has all its three facets actively involved. Both these surfaces become inactive upon reacting their N atoms of the topmost layers and thus, no further ammonia is produced detected. ZrN is the most promising precursor for an active NRR catalyst. However, the concentration of the produced ammonia at the first two applied potentials (-0.6 V and -0.8 V) is not sufficient to prove catalysis by means of an isotope labeling experiment. Apart from this, the stability of all surfaces is not optimal in the environment used in this study and the conclusion is therefore that despite electrochemical data that indicate catalysis, inactivation/decomposition appears to be the limitations of working with these TMNs. This can possibly be solved by further increasing access to N<sub>2</sub>(g) and/or engineering surface stability to prevent vacancies from becoming inactive before new N<sub>2</sub>(g) molecule is available. While none of the surfaces here are demonstrated to be catalysts that are good for scale up and industrial commercialization, their electrochemical behavior

provides important insight for further optimization of catalysts chemical composition and catalysis environment.

## Funding

This work was supported by the Icelandic Research Fund [grant numbers 152619-051, 185051-051, 185404-051 and 196437-051]; the Icelandic Technology Development Fund [grant number 175350-0611]; and the Research Fund of the University of Iceland.

## Data availability

The data that support the findings of this study are available upon reasonable request to the corresponding author.

## References

- [1] J. Hou, M. Yang, J. Zhang, Recent advances in catalysts, electrolytes and electrode engineering for the nitrogen reduction reaction under ambient conditions, *Nanoscale*. 12 (2020) 6900–6920. <https://doi.org/10.1039/d0nr00412j>.
- [2] H. Xu, K. Ithisuphalap, Y. Li, S. Mukherjee, J. Lattimer, G. Soloveichik, G. Wu, Electrochemical ammonia synthesis through N<sub>2</sub> and H<sub>2</sub>O under ambient conditions: Theory, practices, and challenges for catalysts and electrolytes, *Nano Energy*. 69 (2020). <https://doi.org/10.1016/j.nanoen.2020.104469>.
- [3] Y. Yao, J. Wang, U. bin Shahid, M. Gu, H. Wang, H. Li, M. Shao, Electrochemical Synthesis of Ammonia from Nitrogen Under Mild Conditions: Current Status and Challenges, *Electrochemical Energy Reviews*. 3 (2020) 239–270. <https://doi.org/10.1007/s41918-019-00061-3>.
- [4] J.S.J. Hargreaves, Y.M. Chung, W.S. Ahn, T. Hisatomi, K. Domen, M.C. Kung, H.H. Kung, Minimizing energy demand and environmental impact for sustainable NH<sub>3</sub> and H<sub>2</sub>O<sub>2</sub> production—A perspective on contributions from thermal, electro-, and photo-catalysis, *Applied Catalysis A: General*. 594 (2020). <https://doi.org/10.1016/j.apcata.2020.117419>.
- [5] B.M. Comer, P. Fuentes, C.O. Dimkpa, Y.H. Liu, C.A. Fernandez, P. Arora, M. Realff, U. Singh, M.C. Hatzell, A.J. Medford, Prospects and Challenges for Solar Fertilizers, *Joule*. 3 (2019) 1578–1605. <https://doi.org/10.1016/j.joule.2019.05.001>.
- [6] A. Yazdani, G.G. Botte, Perspectives of electrocatalysis in the chemical industry: a platform for energy storage, *Current Opinion in Chemical Engineering*. 29 (2020) 89–95. <https://doi.org/10.1016/j.coche.2020.07.003>.
- [7] E. Skúlason, T. Bligaard, S. Gudmundsdóttir, F. Studt, J. Rossmeisl, F. Abild-Pedersen, T. Vegge, H. Jónsson, J.K. Nørskov, A theoretical evaluation of possible transition metal electro-catalysts for N<sub>2</sub> reduction, *Physical Chemistry Chemical Physics*. 14 (2012) 1235–1245. <https://doi.org/10.1039/c1cp22271f>.
- [8] J.G. Howalt, T. Bligaard, J. Rossmeisl, T. Vegge, DFT based study of transition metal nano-clusters for electrochemical NH<sub>3</sub> production, *Physical Chemistry Chemical Physics*. 15 (2013) 7785–7795. <https://doi.org/10.1039/c3cp44641g>.

- [9] E. Tayyebi, Y. Abghoui, E. Skúlason, Elucidating the Mechanism of Electrochemical N<sub>2</sub> Reduction at the Ru(0001) Electrode, *ACS Catalysis*. 9 (2019) 11137–11145. <https://doi.org/10.1021/acscatal.9b03903>.
- [10] S.Z. Andersen, V. Čolić, S. Yang, J.A. Schwalbe, A.C. Nielander, J.M. McEnaney, K. Enemark-Rasmussen, J.G. Baker, A.R. Singh, B.A. Rohr, M.J. Statt, S.J. Blair, S. Mezzavilla, J. Kibsgaard, P.C.K. Vesborg, M. Cargnello, S.F. Bent, T.F. Jaramillo, I.E.L. Stephens, J.K. Nørskov, I. Chorkendorff, A rigorous electrochemical ammonia synthesis protocol with quantitative isotope measurements, *Nature*. 570 (2019) 504–508. <https://doi.org/10.1038/s41586-019-1260-x>.
- [11] E. Dražević, E. Skúlason, Are There Any Overlooked Catalysts for Electrochemical NH<sub>3</sub> Synthesis—New Insights from Analysis of Thermochemical Data, *IScience*. 23 (2020). <https://doi.org/10.1016/j.isci.2020.101803>.
- [12] J.M. Ontoya, C. Ts, A. Vojvodic, J.K.N. Ørskov, The Challenge of Electrochemical Ammonia Synthesis: A New Perspective on the Role of Nitrogen Scaling Relations, n.d. [www.chemsuschem.org](http://www.chemsuschem.org).
- [13] L.Y. Chen, T.C. Kuo, Z.S. Hong, M.J. Cheng, W.A. Goddard, Mechanism and kinetics for both thermal and electrochemical reduction of N<sub>2</sub> catalysed by Ru(0001) based on quantum mechanics, *Physical Chemistry Chemical Physics*. 21 (2019) 17605–17612. <https://doi.org/10.1039/c9cp03187a>.
- [14] Á.B. Höskuldsson, Y. Abghoui, A.B. Gunnarsdóttir, E. Skúlason, Computational Screening of Rutile Oxides for Electrochemical Ammonia Formation, *ACS Sustainable Chemistry and Engineering*. 5 (2017) 10327–10333. <https://doi.org/10.1021/acssuschemeng.7b02379>.
- [15] J. Pan, H.A. Hansen, T. Vegge, Vanadium oxynitrides as stable catalysts for electrochemical reduction of nitrogen to ammonia: The role of oxygen, *Journal of Materials Chemistry A*. 8 (2020) 24098–24107. <https://doi.org/10.1039/d0ta08313e>.
- [16] B.M. Ceballos, G. Pilania, K.P. Ramaiyan, A. Banerjee, C. Kreller, R. Mukundan, Roads less traveled: Nitrogen reduction reaction catalyst design strategies for improved selectivity, *Current Opinion in Electrochemistry*. 28 (2021). <https://doi.org/10.1016/j.coelec.2021.100723>.
- [17] J. Li, S. Chen, F. Quan, G. Zhan, F. Jia, Z. Ai, L. Zhang, Accelerated Dinitrogen Electroreduction to Ammonia via Interfacial Polarization Triggered by Single-Atom Protrusions, *Chem*. 6 (2020) 885–901. <https://doi.org/10.1016/j.chempr.2020.01.013>.
- [18] L. Yang, C. Choi, S. Hong, Z. Liu, Z. Zhao, M. Yang, H. Shen, A.W. Robertson, H. Zhang, T.W.B. Lo, Y. Jung, Z. Sun, Single yttrium sites on carbon-coated TiO<sub>2</sub> for efficient electrocatalytic N<sub>2</sub> reduction, *Chemical Communications*. 56 (2020) 10910–10913. <https://doi.org/10.1039/d0cc01136c>.
- [19] C. Liu, Q. Li, C. Wu, J. Zhang, Y. Jin, D.R. Macfarlane, C. Sun, Single-Boron Catalysts for Nitrogen Reduction Reaction, *Journal of the American Chemical Society*. 141 (2019) 2884–2888. <https://doi.org/10.1021/jacs.8b13165>.
- [20] G. Peng, J. Wu, M. Wang, J. Niklas, H. Zhou, C. Liu, Nitrogen-Defective Polymeric Carbon Nitride Nanolayer Enabled Efficient Electrocatalytic Nitrogen Reduction with High Faradaic Efficiency, *Nano Letters*. 20 (2020) 2879–2885. <https://doi.org/10.1021/acs.nanolett.0c00698>.
- [21] Y. Song, D. Johnson, R. Peng, D.K. Hensley, P. v Bonnesen, L. Liang, J. Huang, F. Yang, F. Zhang, R. Qiao, A.P. Baddorf, T.J. Tschaplinski, N.L. Engle, M.C. Hatzell, Z. Wu, D.A. Cullen, H.M.M. Iii, B.G.

- Sumpter, A.J. Rondinone, A physical catalyst for the electrolysis of nitrogen to ammonia, 2018. <http://advances.sciencemag.org/>.
- [22] A.R. Singh, B.A. Rohr, M.J. Statt, J.A. Schwalbe, M. Cargnello, J.K. Nørskov, Strategies toward Selective Electrochemical Ammonia Synthesis, *ACS Catalysis*. 9 (2019) 8316–8324. <https://doi.org/10.1021/acscatal.9b02245>.
- [23] J. Nash, X. Yang, J. Anibal, J. Wang, Y. Yan, B. Xu, Electrochemical Nitrogen Reduction Reaction on Noble Metal Catalysts in Proton and Hydroxide Exchange Membrane Electrolyzers, *Journal of The Electrochemical Society*. 164 (2017) F1712–F1716. <https://doi.org/10.1149/2.0071802jes>.
- [24] B.H.R. Suryanto, C.S.M. Kang, D. Wang, C. Xiao, F. Zhou, L.M. Azofra, L. Cavallo, X. Zhang, D.R. Macfarlane, Rational Electrode-Electrolyte Design for Efficient Ammonia Electrosynthesis under Ambient Conditions, *ACS Energy Letters*. 3 (2018) 1219–1224. <https://doi.org/10.1021/acseenergylett.8b00487>.
- [25] H. Abroshan, P. Bothra, S. Back, A. Kulkarni, J.K. Nørskov, S. Siahrostami, Ultrathin Cobalt Oxide Overlayer Promotes Catalytic Activity of Cobalt Nitride for the Oxygen Reduction Reaction, *Journal of Physical Chemistry C*. 122 (2018) 4783–4791. <https://doi.org/10.1021/acs.jpcc.7b12643>.
- [26] M.E. Kreider, M.B. Stevens, Y. Liu, A.M. Patel, M.J. Statt, B.M. Gibbons, A. Gallo, M. Ben-Naim, A. Mehta, R.C. Davis, A. v. Ilevlev, J.K. Nørskov, R. Sinclair, L.A. King, T.F. Jaramillo, Nitride or Oxynitride? Elucidating the Composition-Activity Relationships in Molybdenum Nitride Electrocatalysts for the Oxygen Reduction Reaction, *Chemistry of Materials*. (2020). <https://doi.org/10.1021/acs.chemmater.9b05212>.
- [27] M.B. Stevens, M.E. Kreider, A.M. Patel, Z. Wang, Y. Liu, B.M. Gibbons, M.J. Statt, A. v. Ilevlev, R. Sinclair, A. Mehta, R.C. Davis, J.K. Nørskov, A. Gallo, L.A. King, T.F. Jaramillo, Identifying and Tuning the in Situ Oxygen-Rich Surface of Molybdenum Nitride Electrocatalysts for Oxygen Reduction, *ACS Applied Energy Materials*. 3 (2020) 12433–12446. <https://doi.org/10.1021/acsaem.0c02423>.
- [28] Y. Yuan, J. Wang, S. Adimi, H. Shen, T. Thomas, R. Ma, J.P. Attfield, M. Yang, Zirconium nitride catalysts surpass platinum for oxygen reduction, *Nature Materials*. (2019). <https://doi.org/10.1038/s41563-019-0535-9>.
- [29] A. Garden, Y. Abghoui, E. Skúlason, Applications of Metal Nitrides as Electrocatalysts, in: J. Hargreaves, A. McFarlane, S. Laassiri (Eds.), *Alternative Catalytic Materials*, Royal Society of Chemistry, Croydon, 2018.
- [30] C.D. Zeinalipour-Yazdi, J.S.J. Hargreaves, S. Laassiri, C.R.A. Catlow, The integration of experiment and computational modelling in heterogeneously catalysed ammonia synthesis over metal nitrides, *Physical Chemistry Chemical Physics*. 20 (2018) 21803–21808. <https://doi.org/10.1039/c8cp04216k>.
- [31] Y. Abghoui, E. Skúlason, Onset potentials for different reaction mechanisms of nitrogen activation to ammonia on transition metal nitride electro-catalysts, *Catalysis Today*. 286 (2017) 69–77. <https://doi.org/10.1016/j.cattod.2016.11.047>.
- [32] Y. Abghoui, A.L. Garden, V.F. Hlynsson, S. Björgvinsdóttir, H. Ólafsdóttir, E. Skúlason, Enabling electrochemical reduction of nitrogen to ammonia at ambient conditions through rational

- catalyst design, *Physical Chemistry Chemical Physics*. 17 (2015) 4909–4918.  
<https://doi.org/10.1039/c4cp04838e>.
- [33] E. Skúlason, Electrolytic Production of Ammonia, WO 2015/189865 A1, 2015.
- [34] Y. Abghoui, A.L. Garden, J.G. Howalt, T. Vegge, E. Skúlason, Electroreduction of N<sub>2</sub> to Ammonia at Ambient Conditions on Mononitrides of Zr, Nb, Cr, and V: A DFT Guide for Experiments, *ACS Catalysis*. 6 (2016) 635–646. <https://doi.org/10.1021/acscatal.5b01918>.
- [35] Y. Abghoui, E. Skúlason, Computational Predictions of Catalytic Activity of Zincblende (110) Surfaces of Metal Nitrides for Electrochemical Ammonia Synthesis, *The Journal of Physical Chemistry C*. 121 (2017) 6141–6151. <https://doi.org/10.1021/acs.jpcc.7b00196>.
- [36] G.F. Chen, S. Ren, L. Zhang, H. Cheng, Y. Luo, K. Zhu, L.X. Ding, H. Wang, Advances in Electrocatalytic N<sub>2</sub> Reduction—Strategies to Tackle the Selectivity Challenge, *Small Methods*. 3 (2019). <https://doi.org/10.1002/smt.201800337>.
- [37] C. Tang, S.Z. Qiao, How to explore ambient electrocatalytic nitrogen reduction reliably and insightfully, *Chemical Society Reviews*. 48 (2019) 3166–3180.  
<https://doi.org/10.1039/c9cs00280d>.
- [38] B.H.R. Suryanto, H.L. Du, D. Wang, J. Chen, A.N. Simonov, D.R. MacFarlane, Challenges and prospects in the catalysis of electroreduction of nitrogen to ammonia, *Nature Catalysis*. 2 (2019) 290–296. <https://doi.org/10.1038/s41929-019-0252-4>.
- [39] J. Choi, B.H.R. Suryanto, D. Wang, H.L. Du, R.Y. Hodgetts, F.M. Ferrero Vallana, D.R. MacFarlane, A.N. Simonov, Identification and elimination of false positives in electrochemical nitrogen reduction studies, *Nature Communications*. 11 (2020). <https://doi.org/10.1038/s41467-020-19130-z>.
- [40] S.L. Foster, S.I.P. Bakovic, R.D. Duda, S. Maheshwari, R.D. Milton, S.D. Minter, M.J. Janik, J.N. Renner, L.F. Greenlee, Catalysts for nitrogen reduction to ammonia, *Nature Catalysis*. 1 (2018) 490–500. <https://doi.org/10.1038/s41929-018-0092-7>.
- [41] R. Dabundo, M.F. Lehmann, L. Treibergs, C.R. Tobias, M.A. Altabet, P.H. Moisaner, J. Granger, The contamination of commercial <sup>15</sup>N<sub>2</sub> gas stocks with <sup>15</sup>N-labeled nitrate and ammonium and consequences for nitrogen fixation measurements, *PLoS ONE*. 9 (2014).  
<https://doi.org/10.1371/journal.pone.0110335>.
- [42] F. Hanifpour, A. Sveinbjörnsson, C.P. Canales, E. Skúlason, H.D. Flosadóttir, Preparation of Nafion Membranes for Reproducible Ammonia Quantification in Nitrogen Reduction Reaction Experiments, *Angewandte Chemie - International Edition*. 59 (2020) 22938–22942.  
<https://doi.org/10.1002/anie.202007998>.
- [43] R. Manjunatha, A. Karajić, H. Teller, K. Nicoara, A. Schechter, Electrochemical and Chemical Instability of Vanadium Nitride in the Synthesis of Ammonia Directly from Nitrogen, *ChemCatChem*. 12 (2020) 438–443. <https://doi.org/10.1002/cctc.201901558>.
- [44] B. Hu, M. Hu, L. Seefeldt, T.L. Liu, Electrochemical Dinitrogen Reduction to Ammonia by Mo<sub>2</sub>N: Catalysis or Decomposition?, *ACS Energy Letters*. 4 (2019) 1053–1054.  
<https://doi.org/10.1021/acsenergylett.9b00648>.

- [45] H.L. Du, T.R. Gengenbach, R. Hodgetts, D.R. Macfarlane, A.N. Simonov, Critical Assessment of the Electrocatalytic Activity of Vanadium and Niobium Nitrides toward Dinitrogen Reduction to Ammonia, *ACS Sustainable Chemistry and Engineering*. 7 (2019) 6839–6850. <https://doi.org/10.1021/acssuschemeng.8b06163>.
- [46] Y.G. Zeng, L. Chen, H.X. Li, J. Huang, B. Yu, Comparison study on measuring ammonia and nitrogen in surface water by flow injection and Nessler's reagent, in: *Advanced Materials Research*, 2014: pp. 46–50. <https://doi.org/10.4028/www.scientific.net/AMR.884-885.46>.
- [47] M. Björck, G. Andersson, *GenX* : an extensible X-ray reflectivity refinement program utilizing differential evolution, *Journal of Applied Crystallography*. 40 (2007). <https://doi.org/10.1107/S0021889807045086>.
- [48] R.W.M. Kwok, XPS PEAK Program, version 4.1. The Chinese University of Hong Kong: Shatin, New Territories, Hong Kong SAR, 1999.
- [49] FIALab Instruments Inc., Gas Diffusion Ammonia Method (Water Based Samples) and Various Extracts, Seattle, WA, 2013.
- [50] S. Fletcher, Tafel slopes from first principles, *Journal of Solid State Electrochemistry*. 13 (2009) 537–549. <https://doi.org/10.1007/s10008-008-0670-8>.
- [51] A. Morozan, V. Goellner, Y. Nedellec, J. Hannauer, F. Jaouen, Effect of the Transition Metal on Metal–Nitrogen–Carbon Catalysts for the Hydrogen Evolution Reaction, *Journal of The Electrochemical Society*. 162 (2015) H719–H726. <https://doi.org/10.1149/2.0051511jes>.
- [52] A.R.C. Bredar, A.L. Chown, A.R. Burton, B.H. Farnum, Electrochemical Impedance Spectroscopy of Metal Oxide Electrodes for Energy Applications, *ACS Applied Energy Materials*. 3 (2020) 66–98. <https://doi.org/10.1021/acsaem.9b01965>.
- [53] S. Touzain, Some comments on the use of the EIS phase angle to evaluate organic coating degradation, *Electrochimica Acta*. 55 (2010) 6190–6194. <https://doi.org/10.1016/j.electacta.2009.09.045>.
- [54] R.S. Melo, S. Brasil, A.L. Filho, R. de Siqueira Melo, S. Louise, D. Cezar Brasil, L. José De Carvalho, A. Maia, L. Filho, C. Pereira, Assessment of the Antifouling Effect of Exopolysaccharides Incorporated into Copper Oxide-Based Organic Paint Using the technique of infrared spectroscopy for evaluation of paints with anti-fouling characteristics View project Biocorrosion View project Assessment of the Antifouling Effect of Exopolysaccharides Incorporated into Copper Oxide-Based Organic Paint, *Article in International Journal of Electrochemical Science*. 11 (2016) 7750–7763. <https://doi.org/10.20064/2016.09.37>.
- [55] M. Gudmundsson, V. Ellingsson, E. Skúlason, Y. Abghoui, Optimizing Nitrogen Reduction Reaction on Nitrides: A Computational Study on Crystallographic Orientation, *Topics in Catalysis*. (2021) 1–10. <https://doi.org/10.1007/s11244-021-01485-2>.
- [56] Y. Abghoui, E. Skúlason, Electrochemical synthesis of ammonia via Mars-van Krevelen mechanism on the (111) facets of group III–VII transition metal mononitrides, *Catalysis Today*, 286 (2017) 78–84. <http://dx.doi.org/10.1016/j.cattod.2016.06.009>.

## Supplementary Information

# In-line quantification of ammonia produced from theoretically derived transition metal nitrides electro-catalysts

Fatemeh Hanifpour<sup>a</sup>, Camila P. Canales<sup>a</sup>, Emil G. Fridriksson<sup>b</sup>, Arnar Sveinbjörnsson<sup>c</sup>, Tryggvi K. Tryggvason<sup>b</sup>, Jian Yang<sup>a</sup>, Kristin<sup>a</sup> von Fieandt<sup>d</sup>, Connel Arthur<sup>a</sup>, Sigríður Jónsdóttir<sup>a</sup>, Anna L. Garden<sup>e</sup>, Sveinn Ólafsson<sup>a</sup>, Kristján Leósson<sup>f</sup>, Liney Árnadóttir<sup>g</sup>, Erik Lewin<sup>d</sup>, Younes Abghoui<sup>a</sup>, Árni S. Ingason<sup>b</sup>, Fridrik Magnus<sup>a,b</sup>, Helga D. Flosadóttir<sup>\*a,b</sup>, and Egill Skúlason<sup>\*a,b,h</sup>

---

<sup>a</sup> Science Institute, University of Iceland, VR-III, 107 Reykjavík, Iceland.

<sup>b</sup> Grein Research ehf., Dunhagi 5, 107 Reykjavík, Iceland.

<sup>c</sup> Atmonia ehf., Keldnaholt, 112 Reykjavík, Iceland.

<sup>d</sup> Inorganic Research Programme, Department of Chemistry – Ångström Laboratory, Uppsala University, Box 538, SE-751 21 Uppsala, Sweden.

<sup>e</sup> Department of Chemistry and MacDiarmid Institute for Advanced Materials and nanotechnology, University of Otago, P.O. Box 56, Dunedin 9054, New Zealand.

<sup>f</sup> DT-Equipment, Keldnaholt, 112 Reykjavík, Iceland.

<sup>g</sup> School of Chemical, Biological and Environmental Engineering, Oregon State University, Corvallis, OR, 97331, United States.

<sup>h</sup> Faculty of Industrial Engineering, Mechanical Engineering and Computer Science, University of Iceland, VR-III, 107 Reykjavík, Iceland.

\* [egillsk@hi.is](mailto:egillsk@hi.is), [helgadogg@atmonia.com](mailto:helgadogg@atmonia.com)

---

## 1- Materials for electrochemical experiments and product detection

The electrolyte used in all the experiments was 0.1 M potassium hydroxide (KOH, Merck, ≥85%) in ultrapure water (MilliQ®, Grade 1).

Sodium hydroxide (NaOH, Fluka, ≥98%), Sulfuric acid (H<sub>2</sub>SO<sub>4</sub>, Merck, 95-97%), ortho-phthalaldehyde (OPA, Sigma-Aldrich, ≥99%), ethanol (C<sub>2</sub>H<sub>6</sub>O, Riedel-de Haën, ≥99.8%), disodium tetra borate decahydrate (Na<sub>2</sub>B<sub>4</sub>O<sub>7</sub>·10H<sub>2</sub>O, Merck, 99.5%), sodium sulfite (Na<sub>2</sub>O<sub>3</sub>S, Sigma-Aldrich, 98-100%), and triton X-100 ((C<sub>2</sub>H<sub>4</sub>O)<sub>n</sub>C<sub>14</sub>H<sub>22</sub>O, Sigma-Aldrich) were required for ammonia determination and quantification.

Ammonium chloride (NH<sub>4</sub>Cl, Merck, 1000 mg/l NH<sub>4</sub> in H<sub>2</sub>O), ammonia-<sup>15</sup>N solution (Sigma-Aldrich, 98 atom % <sup>15</sup>N, 2 M in methanol), dimethyl sulfoxide-d<sub>6</sub> (DMSO-d<sub>6</sub>, Merck, 99.9 atom % D) was used for <sup>14</sup>NH<sub>3</sub> and <sup>15</sup>NH<sub>3</sub> calibration standards preparation for <sup>1</sup>H-NMR method.

## 2- Micro-reactor flow-cell and flow injection analyzer (FIA)

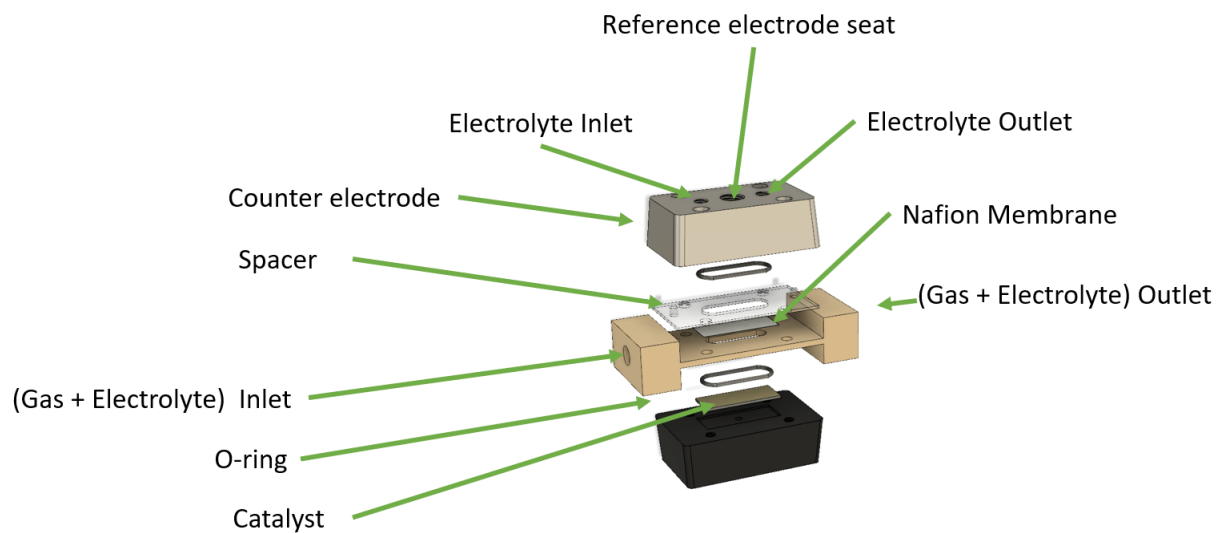


*Figure S1. Exploded view of an upgraded commercial Antec micro-reactor modified with a PEEK spacer to separate the working and the counter compartment by means of Nafion membrane.*

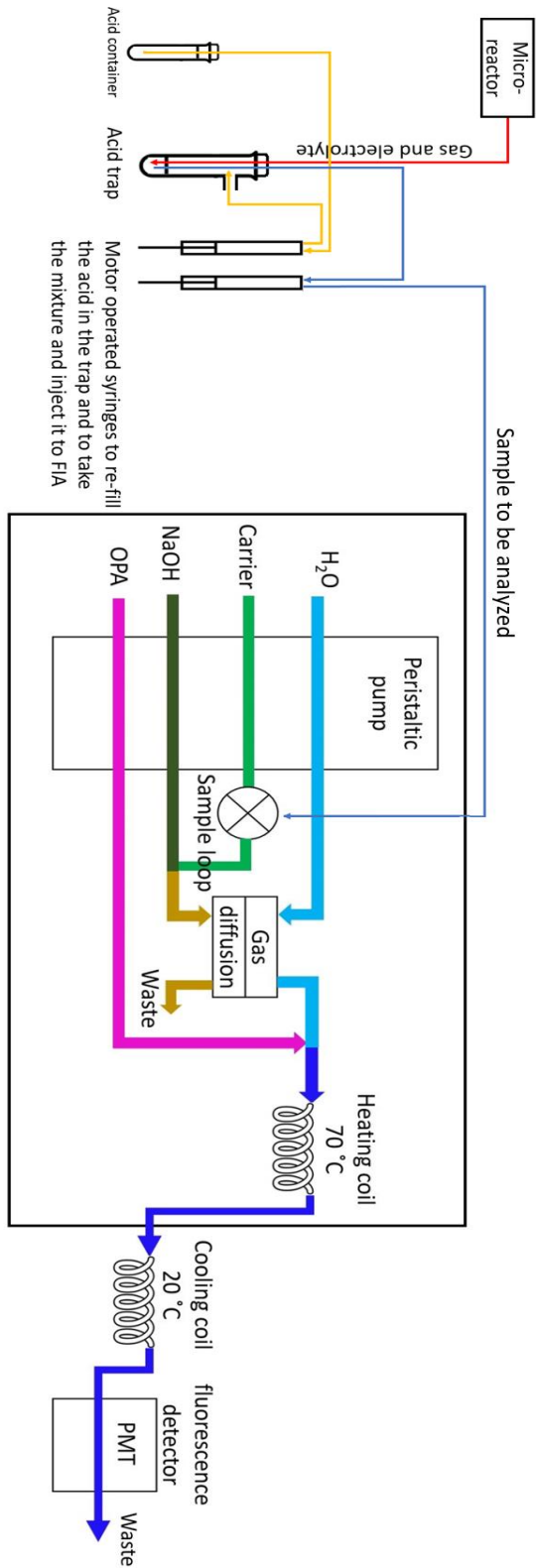


Figure S2. The illustration of the setup used for NRR in-line with ammonia measurement unit. The outlet of the working compartment of the micro-reactor is collected in an acid trap and the mixture is sent for analysis to the flow injection analyzer (FIA).

### 3- Ammonia measurement calculations

Quantification of ammonia contained in the samples was performed based on two sets of calibration in the beginning and at the end of each electrochemical experiment. The standards were prepared in a mixture of 2:1 (v/v) of 0.1 M KOH and 0.5 M H<sub>2</sub>SO<sub>4</sub> (matrix matched with the samples from the experiment) and sent to the FIA using an autosampler. A linear regression was the best fit to the calibration data, correlating ammonia concentration to the intensity of the fluorescence emission. Figure S3 shows a typical calibration curve in the FIA.

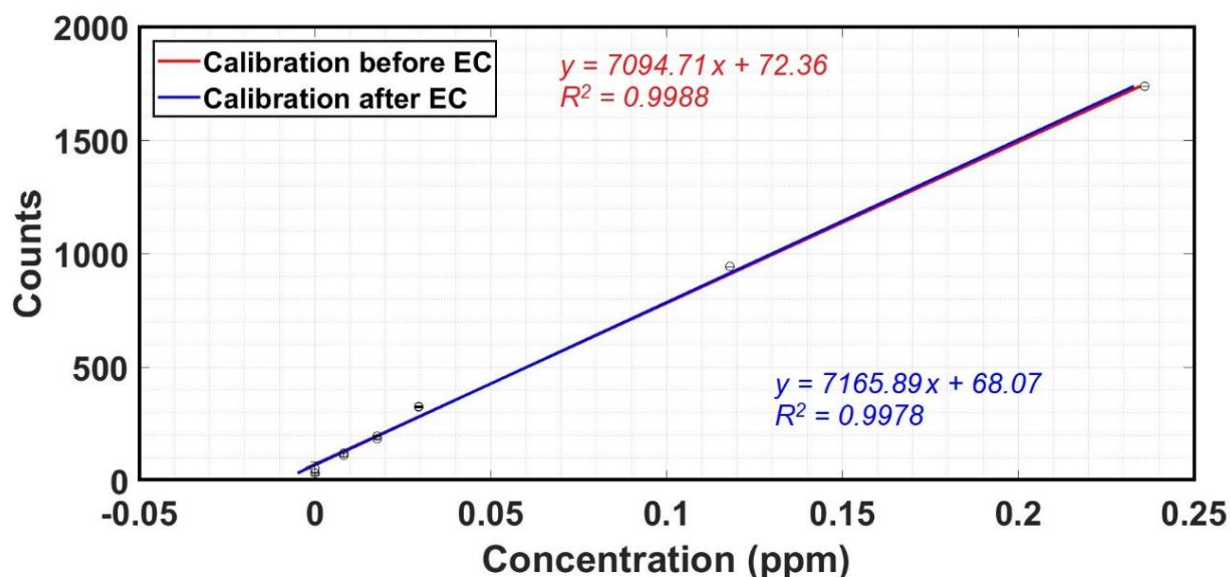


Figure S3. Ammonia calibration curve before and after an electrochemical experiment.

Based on the calibration curve, the ammonia concentration in the electrolyte was known in ppm after correcting for the dilution caused by the acid trap. This value was converted to N-atoms considering the volume of 200  $\mu$ L for the sample loop. The background N-atoms was subtracted from the N-atoms produced in each step. The total N-atom produced for each chronoamperometry combination was calculated by summing up the 3 subsequent N-atoms (since for each combination 3 measurements were done). This value was converted to moles of ammonia. Reaction rate in mol/cm<sup>2</sup>/s was calculated from the total moles of ammonia divided by the active working electrode area (1.9 cm<sup>2</sup>) and the reaction time (the total time of applying potential). Current efficiency was accordingly calculated accounting for 3 electrons per molecule of NH<sub>3</sub> produced.

$$\text{mol NH}_3 = \frac{x \times 10^{-3} \frac{\text{g}}{\text{L}} \times \frac{\text{electrolyte volume} + \text{acid trap volume}}{\text{electrolyte volume}} \times 200 \times 10^{-6} \text{L}}{17.03 \frac{\text{g}}{\text{mol}}}$$

$$\text{Reaction Rate (mol/cm}^2 \cdot \text{s)} = \frac{\text{mol NH}_3}{1.9 \text{ cm}^2 \times t \text{ (s)}}$$

$$\text{Current efficiency (\%)} = \frac{\text{mol NH}_3 \times 3 \left( \frac{\text{mol e}^-}{\text{mol NH}_3} \right) \times F \left( \frac{\text{C}}{\text{mol e}^-} \right)}{\text{Integrated Charge (C)}} \times 100$$

Table S1. Ammonia production in the electrochemical (EC) studies using CrN, VN, NbN, and ZrN. The data reported here is based on the average of three independent experiments performed in each case. Error bars are the standard deviation calculated from the experimental repetitions. Initial characterizations of each surface include cyclic voltammetry recorded in various potential windows from OCP to the faradaic region, linear sweep voltammetry, differential pulse voltammetry, and electrochemical impedance spectroscopy. E1 to E4 (which are specified for each surface in Table 3) refer to chronoamperometry loops, run for 10 s at E1 and 10 s of recording OCP, repeated for 2100 s at each potential.

Films	Gas environment	Number of NH <sub>3</sub> molecules produced				
		Initial characterization	E1	E2	E3	E4
CrN	N <sub>2</sub>	< LOD (1.1×10 <sup>13</sup> )	< LOD (1.1×10 <sup>13</sup> )	< LOD (1.1×10 <sup>13</sup> )	< LOD (1.1×10 <sup>13</sup> )	< LOD (1.1×10 <sup>13</sup> )
	Ar	-	-	-	-	-
VN	N <sub>2</sub>	2.0×10 <sup>15</sup> ±0.9×10 <sup>15</sup>	< LOD (1.0×10 <sup>13</sup> )	< LOD (1.0×10 <sup>13</sup> )	< LOD (1.0×10 <sup>13</sup> )	< LOD (1.0×10 <sup>13</sup> )
	Ar	1.2×10 <sup>15</sup> ±0.8×10 <sup>15</sup>	< LOD (1.0×10 <sup>13</sup> )	< LOD (1.0×10 <sup>13</sup> )	< LOD (1.0×10 <sup>13</sup> )	< LOD (1.0×10 <sup>13</sup> )
NbN	N <sub>2</sub>	1.7×10 <sup>15</sup> ±0.9×10 <sup>15</sup>	3.5×10 <sup>13</sup> ±1.6×10 <sup>13</sup>	2.5×10 <sup>14</sup> ±2.8×10 <sup>14</sup>	1.8×10 <sup>14</sup> ±2.6×10 <sup>14</sup>	1.5×10 <sup>14</sup> ±1.3×10 <sup>14</sup>
	Ar	1.6×10 <sup>15</sup> ±0.3×10 <sup>15</sup>	1.3×10 <sup>13</sup> ±1.3×10 <sup>13</sup>	2.45×10 <sup>14</sup> ±2.2×10 <sup>14</sup>	3.2×10 <sup>14</sup> ±2.9×10 <sup>14</sup>	4.8×10 <sup>14</sup> ±4.9×10 <sup>14</sup>
ZrN	N <sub>2</sub>	2.8×10 <sup>15</sup> ±0.8×10 <sup>15</sup>	4.0×10 <sup>14</sup> ±0.8×10 <sup>14</sup>	7.1×10 <sup>14</sup> ±2.6×10 <sup>14</sup>	2.0×10 <sup>15</sup> ±7.6×10 <sup>14</sup>	2.5×10 <sup>15</sup> ±4.2×10 <sup>14</sup>
	Ar	2.8×10 <sup>15</sup> ±0.6×10 <sup>15</sup>	< LOD (1.5×10 <sup>13</sup> )	< LOD (1.5×10 <sup>13</sup> )	9.7×10 <sup>14</sup> ±0.2×10 <sup>14</sup>	1.9×10 <sup>15</sup> ±3.1×10 <sup>14</sup>

\* LOD: Limit of detection

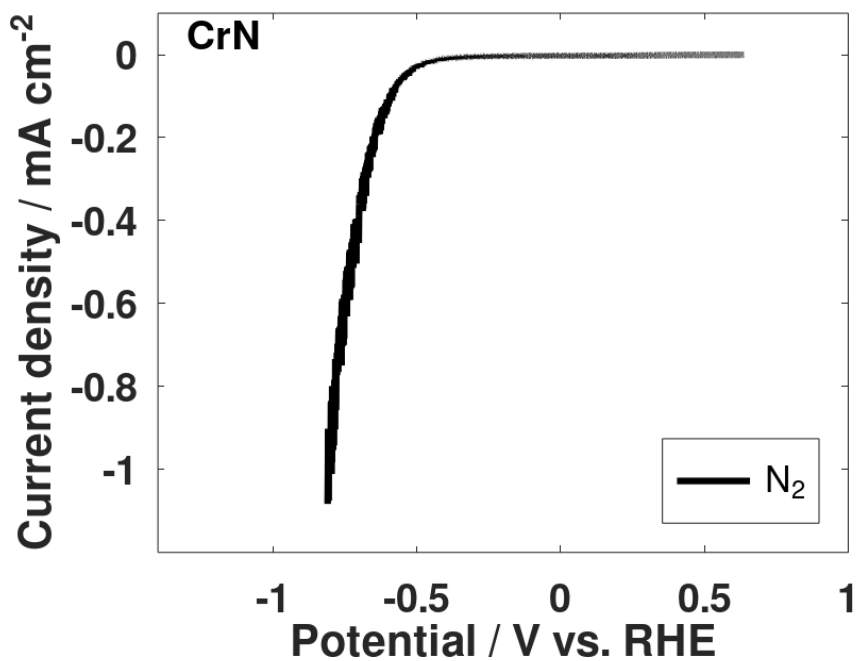


Figure S4. LSV in N<sub>2</sub> media on CrN. The starting potential is the open circuit potential.

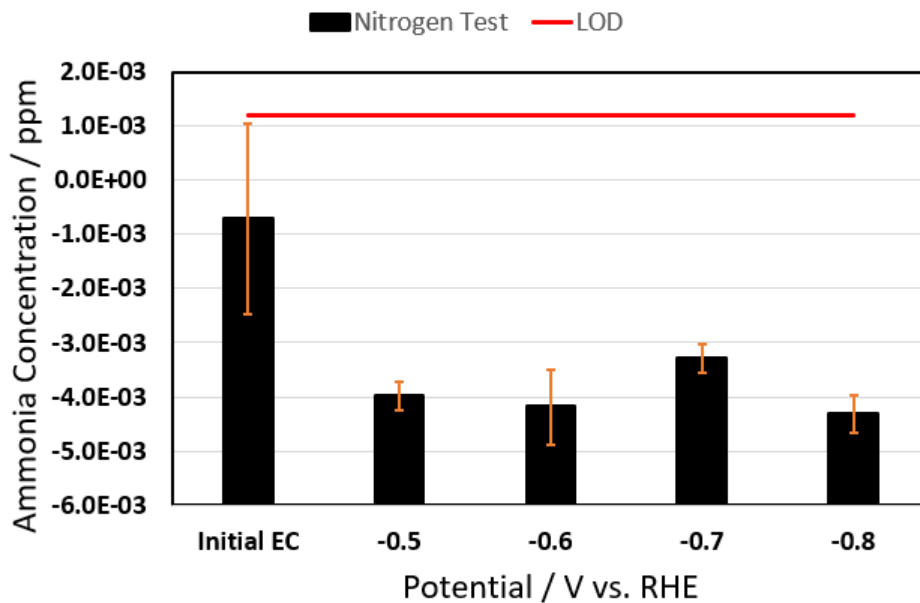
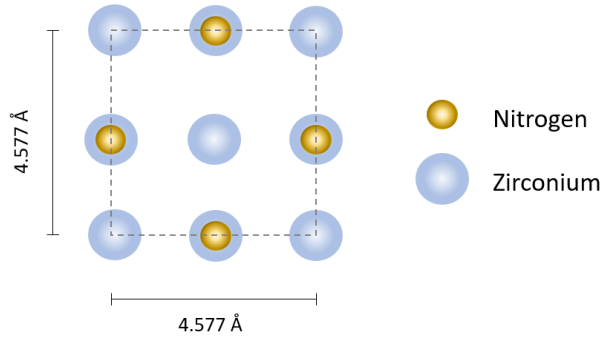


Figure S5. Ammonia measurement for different samples taken during the experiment in N<sub>2</sub> media on CrN. As it is seen, all the intensities fall below the background level; thus, no ammonia concentration is reported for this catalyst. This result has been reproducibly repeated.

## 4- Monolayer calculations

Due to the complexity of the calculation of monolayers (ML) for a polycrystalline catalyst, the calculation is done with a simplifying assumption that the structure of the catalyst is rocksalt (100). The calculation here is done for ZrN as an example. Figure below shows the (100) plane in a FCC cubic unit cell.



$$\text{Area of the plane} = (4.577 \times 10^{-8} \text{ cm})^2 = 2.095 \times 10^{-15} \text{ cm}^2$$

$$\text{Number of nitrogen atoms in one plane} = 4 \times \frac{1}{2} = 2 \text{ atoms}$$

$$\text{Number of nitrogen atoms per plane area} = \frac{2 \text{ N atoms}}{2.095 \times 10^{-15} \text{ cm}^2} = 9.546 \times 10^{14} \text{ N atoms/cm}^2$$

The geometric active area of the catalyst in our setup is 1.9 cm<sup>2</sup>. So, the number of nitrogen atoms in one monolayer is:

$$9.546 \times 10^{14} \text{ N atoms/cm}^2 \times 1.9 \text{ cm}^2/\text{monolayer} = 1.814 \times 10^{15} \text{ N atoms/monolayer}$$

The total number of monolayers present in a ZrN film with thickness of 83 nm is:

$$\frac{83 \text{ nm} \times 10}{4.577 \text{ Å}/2} = 363 \text{ monolayers in a pristine ZrN catalyst}$$

From Section 3, we know how to calculate the moles of ammonia produced. Accordingly, it is possible to calculate the total atoms of ammonia produced in a whole experiment simply by multiplying it by Avogadro's number. So, dividing this number by  $1.814 \times 10^{15} \text{ N atoms/monolayer}$  would result in the equivalent total monolayers produced. In the case of ZrN experiment in N<sub>2</sub>(g), for example, a total of  $8.42 \times 10^{15}$  N atoms were measured in the samples. This equals to 4.81 (~ 5) monolayers produced and 358 monolayers left in the film.

## 5- Comparison of system responses with and without the gas flow

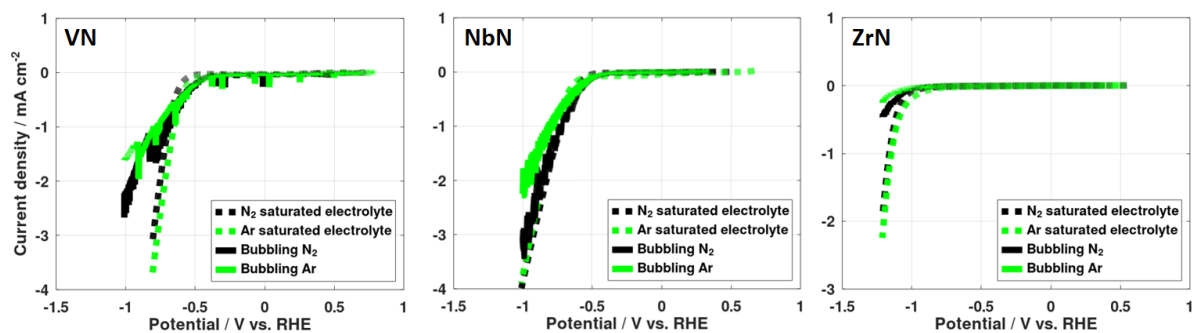


Figure S6. Comparison of LSV curves with and without direct bubbling of the gas inside the working electrode compartment.

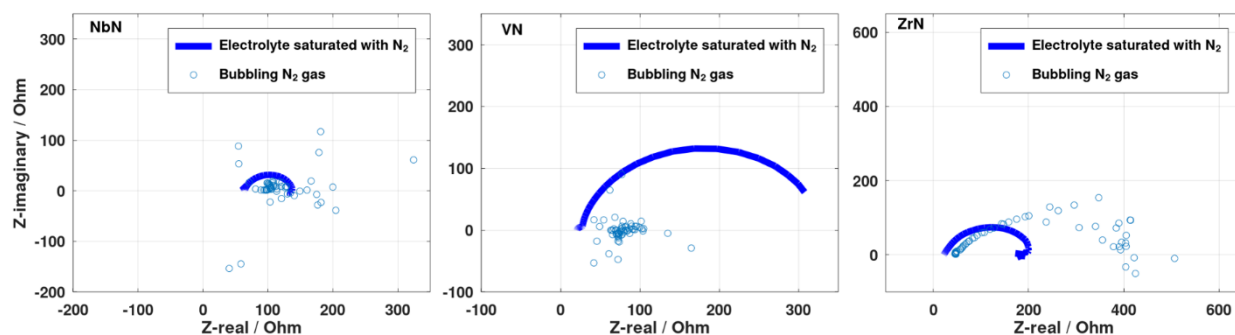


Figure S7. Comparison of the Nyquist plots in the faradaic zone with and without direct bubbling of the gas inside the working electrode compartment.

## 6- Bode plots and model fitting parameters

The Bode plots show, in general, that the impedance modulus ( $|Z|$ ) decreases at higher frequency values meaning that the TMNs catalysts under study show a mixed capacitive and resistive behavior. The charge carriers or electrons involved in the reduction mechanism of  $N_2(g)$  to produce ammonia must have sufficient energy to bypass the impedances of two main regions: the bulk (TMN electrodes) and the boundaries between atomic interfaces. At high frequencies, charges are effectively displaced due to a fast-alternating current. This includes the initial leaching of the surfaces observed in the EIS data. But at the low frequencies, the movement of charge carriers becomes harder at the interfaces including the catalysts junctions (Metal – Nitrides). It is further seen from all the Bode plots that the behavior shifts from resistive to capacitive by moving from lower frequencies to higher frequencies. Thus, at lower frequencies, the impedance of the capacitor increases due to its inverse dependence on frequency and the current flows through the resistor or junctions between the metal and nitride ions. On the other hand, at high frequencies, the impedance to current in the capacitor is smaller than the impedance of a resistor (which is constant at all frequencies), so the capacitive behavior is enhanced as it is observed in the Nyquist plots and the height of the semicircles<sup>1</sup>.

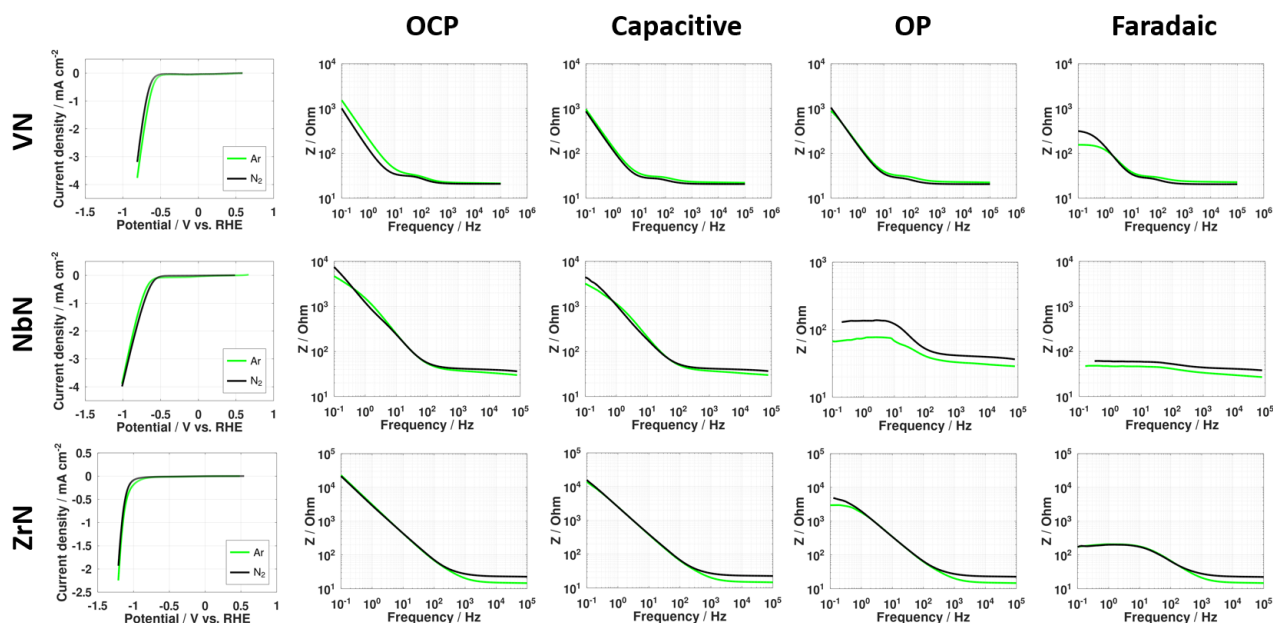


Figure S8. Bode plots recorded for the four TMNs at open circuit potential (OCP), capacitive zone, onset potential (OP), and faradaic zone.

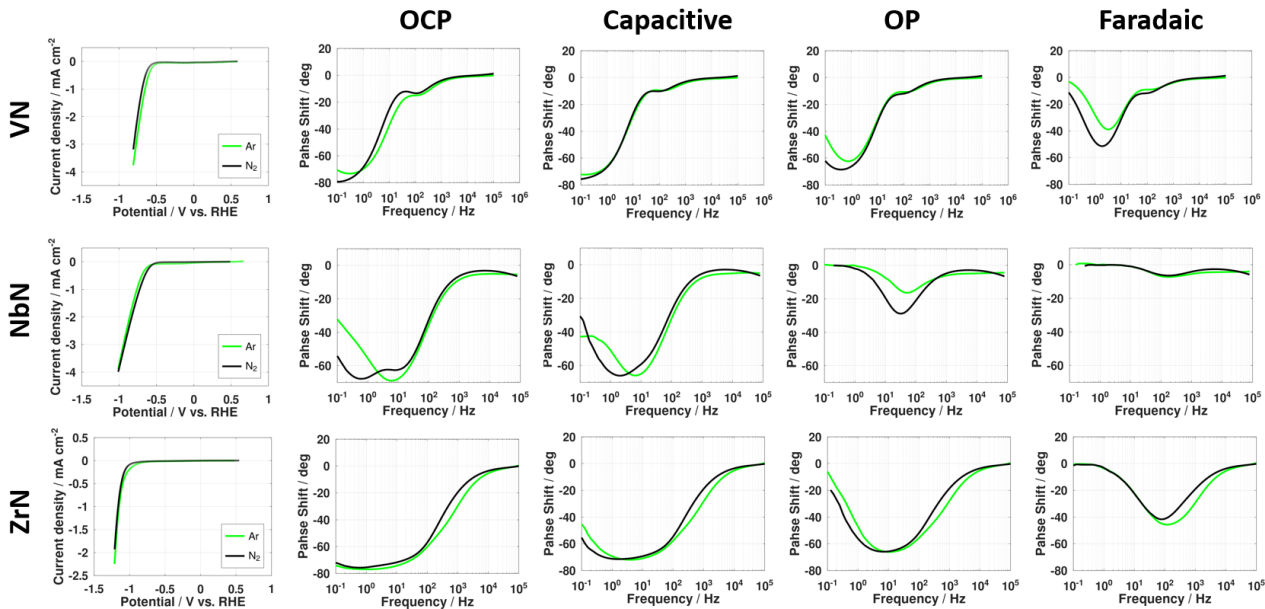


Figure S9. Phase shift diagram recorded for the four TMNs at open circuit potential (OCP), capacitive zone, onset potential (OP), and faradaic zone.

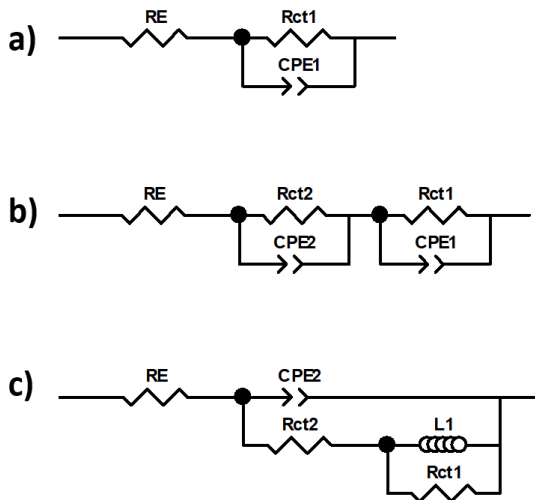


Figure S10. Equivalent circuits used to model the four systems in N<sub>2</sub> and Ar media. (a) for ZrN at E1, E2, and E3 in Ar and N<sub>2</sub>, (b) for VN at all potentials and for NbN at all potentials in N<sub>2</sub> and at E1 and E2 in Ar, (c) for ZrN at E4 and NbN at E3 and E4 in Ar

Table S2. Equivalent circuit and fit parameters in Ar(aq)

	Model	Parameters	Unit	E1	E2	E3	E4
VN	b	R <sub>E</sub>	Ω	21.78	22.51	22.58	23.07
		R <sub>ct1</sub>	Ω	1.09E4	8.89E3	1.43E3	1.38E2
		CPE <sub>1</sub> T	μF/cm <sup>2</sup>	9.51E-4	1.51E-3	1.26E-3	1.09E-3
		CPE <sub>1</sub> P	-	0.88	0.87	0.88	0.94
		R <sub>ct2</sub>	Ω	9.94	6.25	7.07	6.95
		CPE <sub>2</sub> T	μF/cm <sup>2</sup>	1.51E-4	1.22E-4	1.45E-4	2.59E-4
		CPE <sub>2</sub> P	-	0.94	0.98	0.95	0.87
		χ <sup>2</sup>	-	3.46E-5	9.83E-5	9.84E-5	4.37E-5
NbN	b @ E1, E2 c @ E3, E4	R <sub>E</sub>	Ω	35.09	34.59	30.14	27.12
		R <sub>ct1</sub>	Ω	3.32E3	2.03E3	16	6.45
		L1	H	-	-	1.2	0.079
		CPE <sub>1</sub> T	μF/cm <sup>2</sup>	1.26E-4	1.65E-4	-	-
		CPE <sub>1</sub> P	-	0.85	0.84	-	-
		R <sub>ct2</sub>	Ω	3.03E3	6.42E3	40.99	21.3
		CPE <sub>2</sub> T	μF/cm <sup>2</sup>	7.07E-4	7.94E-4	8.20E-4	2.12E-3
		CPE <sub>2</sub> P	-	1	1	0.65	0.44
χ <sup>2</sup>	-	1.08-3	1.027E-3	1.15E-3	1.48E-4		
ZrN	a @ E1 – E3 c @ E4	R <sub>E</sub>	Ω	17.76	15.07	14.91	14.51
		R <sub>ct1</sub>	Ω	3.44E5	2.94E4	3.97E3	28.2
		L1	H	-	-	-	9.92
		CPE <sub>1</sub> T	μF/cm <sup>2</sup>	6.00E-5	8.61E-5	1.02E-4	-
		CPE <sub>1</sub> P	-	0.82	0.82	0.80	-
		R <sub>ct2</sub>	Ω	-	-	-	178.7
		CPE <sub>2</sub> T	μF/cm <sup>2</sup>	-	-	-	9.73E-5
		CPE <sub>2</sub> P	-	-	-	-	0.78
χ <sup>2</sup>	-	2.49E-4	8.70E-4	8.45E-4	5.02E-4		

Table S3. Equivalent circuit and fit parameters in  $N_2(aq)$

	Model	Parameters	Unit	E1	E2	E3	E4
VN	b	$R_E$	$\Omega$	20.96	20.75	20.64	20.54
		$R_{ct1}$	$\Omega$	2.71E4	1.21E4	3.49E3	3.03E2
		CPE <sub>1</sub> T	$\mu\text{F}/\text{cm}^2$	1.53E-3	1.72E-3	1.34E-3	1.23E-3
		CPE <sub>1</sub> P	-	0.92	0.89	0.88	0.92
		$R_{ct2}$	$\Omega$	9.04	5.11	5.54	6.23
		CPE <sub>2</sub> T	$\mu\text{F}/\text{cm}^2$	1.17E-4	1.21E-4	1.41E-4	1.66E-41
		CPE <sub>2</sub> P	-	1	1	1	1
		$\chi^2$	-	5.31E-5	1.20E-4	9.95E-4	5.33E-5
NbN	b	$R_E$	$\Omega$	34.87	39.74	28.3	27.35
		$R_{ct1}$	$\Omega$	2.33E4	1.47E2	93.5	16.5
		CPE <sub>1</sub> T	$\mu\text{F}/\text{cm}^2$	1.75E-4	1.03E-3	1.14E-4	2.88E-4
		CPE <sub>1</sub> P	-	0.82	0.70	0.95	0.80
		$R_{ct2}$	$\Omega$	38.84	5.43E3	16.92	16.18
		CPE <sub>2</sub> T	$\mu\text{F}/\text{cm}^2$	1.80E-4	1.88E-4	1.61E-3	1.08E-4
		CPE <sub>2</sub> P	-	1	0.90	0.30	0.43
		$\chi^2$	-	3.87E-4	2.45E-4	1.88E-4	6.15E-5
ZrN	a @ E1 – E3 c @ E4	$R_E$	$\Omega$	23.32	23.07	23.2	22.47
		$R_{ct1}$	$\Omega$	6.04E5	5.31E4	6.21E3	28.19
		L1	H	-	-	-	5.6
		CPE <sub>1</sub> T	$\mu\text{F}/\text{cm}^2$	7.15E-5	8.55E-5	1.01E-4	-
		CPE <sub>1</sub> P	-	0.84	0.82	0.81	-
		$R_{ct2}$	$\Omega$	-	-	-	167.8
		CPE <sub>2</sub> T	$\mu\text{F}/\text{cm}^2$	-	-	-	1.15E-4
		CPE <sub>2</sub> P	-	-	-	-	0.78
		$\chi^2$	-	2.31E-4	1.76E-3	3.13E-4	5.92E-4

## 7- XRD, XRR, and XPS analysis of the pristine film of ZrN

Figure S11(a) shows the grazing incidence x-ray diffraction (GIXRD) and XRR measurements of a pristine test sample of ZrN. The GIXRD reveals a polycrystalline structure matching the rocksalt structure of ZrN. The grain size is determined as 15.5 nm from the full width at half maximum of the [111] peak, using the Scherrer formula. The XRR yields a density of  $6.85 \text{ g/cm}^3$  which is close to the bulk density of ZrN ( $7.1 \text{ g/cm}^3$ ). However, XRR is not very sensitive to small changes in stoichiometry due to the much higher weight of Zr compared to N. The thickness is 65 nm and the rms surface roughness approximately 2.2 nm, as determined by fitting using the GenX software (red line).

Figure S11(b) shows the result of XPS analysis of a pristine sample. As can be seen oxygen is only present in the outermost part of the coating, and a stable bulk composition is observed below a sputtering depth of 3 nm. The average bulk composition from XPS of the pristine film is 58.4 at.% Zr, 41.0 at.% N, and  $\leq 0.6$  at.% O, with a standard deviation of 0.6 at.%, i.e.  $\text{ZrN}_{0.7}$ . The Zr 3d spectra from bulk and surface (right panel, bottom) show that the bulk is practically pure ZrN with the main contributions (dashed yellow lines) matching the literature for ZrN with peaks at 179.7 eV ( $3d_{5/2}$ ) and 182.0 eV ( $3d_{3/2}$ )<sup>2</sup>. The small high binding energy contributions (at 183.4 eV for  $3d_{5/2}$  and 185.7 eV for  $3d_{3/2}$ , dashed red lines) are consistent with Zr bonded to oxygen<sup>2</sup> and are either caused by small amounts of oxygen in the film, or by knock-in of oxygen atoms from the oxidized surface during sputter-etching. Also, the N 1s peak (not shown) which is observed at 397.3 eV is consistent with ZrN.

The surface spectra are consistent with literature of native oxides formed in air.<sup>2</sup> The spectra contain contributions both from Zr in a nitride environment and mixed oxygen/nitrogen environment where the latter dominates. Oxynitride contributions are mainly found at 182.4 eV ( $3d_{5/2}$ ) and 184.8 eV ( $3d_{3/2}$ ) (purple dashed lines). To attain a satisfactory fit to the surface spectra, however, an additional component with a binding energy of 181.0 eV ( $3d_{5/2}$ ) and 183.5 eV ( $3d_{3/2}$ ) was needed (dashed blue lines). This contribution is also consistent with Zr in a mixed oxygen/nitrogen environment and has been described for native oxides of  $\text{ZrN}^3$ .

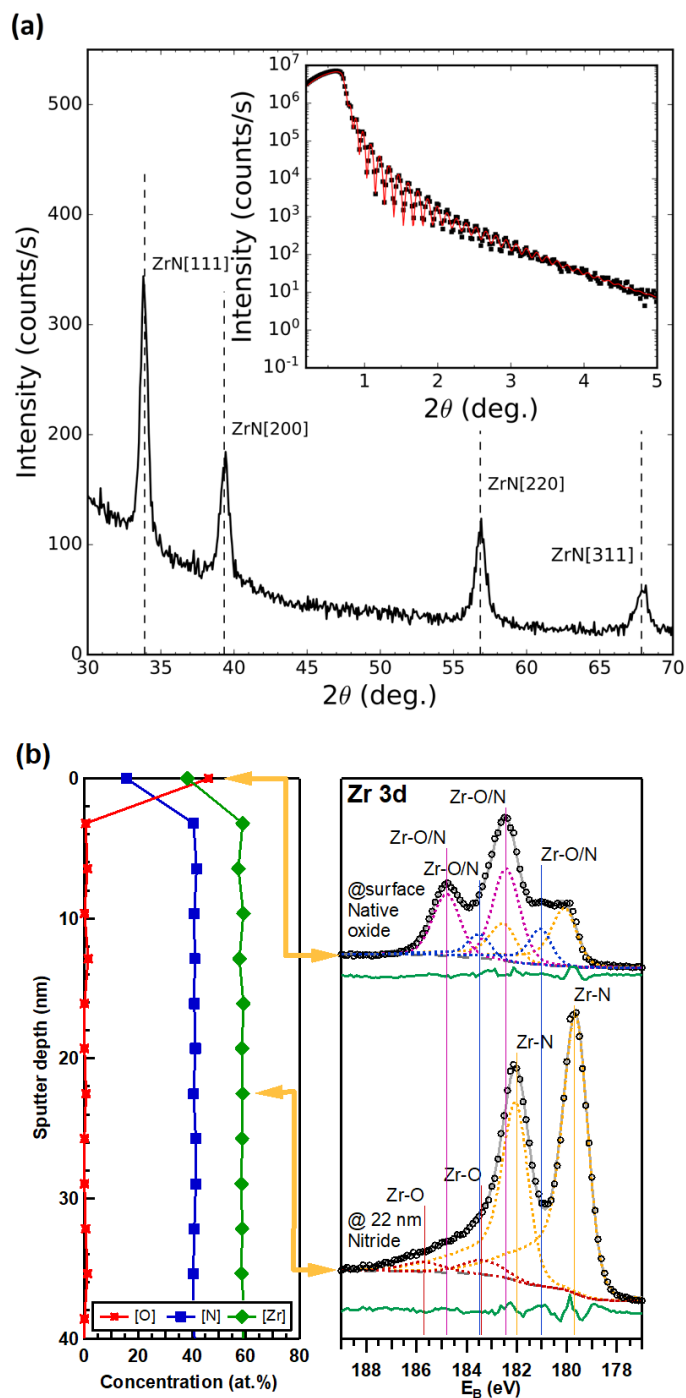


Figure S11. (a) GIXRD of the pristine film confirming a NaCl-type ZrN phase with a polycrystalline microstructure. Inset: XRR data (black squares) and including fit (red line) showing a smooth (rms roughness approx. 2.2 nm) film with 65 nm thickness. (b) XPS of the pristine film. The XRR (inset) shows a smooth (rms roughness approx. 2.2 nm) film with 64 nm thickness. The XPS sputter depth profiles show a thin native oxide and a stable bulk composition. The right panel shows fitted Zr 3d spectra from the surface and bulk of the pristine sample.

The ZrN test samples were tested in the electrochemical setup in N<sub>2</sub> media at different applied potentials for 240 min and in N<sub>2</sub> and at a fixed potential of -0.88 V vs. RHE for different time durations of 35, 70, 120, and 240 min. Figure S12(a) and (b) shows the resulting oxide layer thicknesses derived from the XRR and the XPS analysis. The XRR results show slightly thicker oxide layers compared to the XPS results, as different reference cut-off criteria were used for each method, but both series follow the same trend. However, the proximity of the results allows us to use the XRR analysis for the surface characterization.

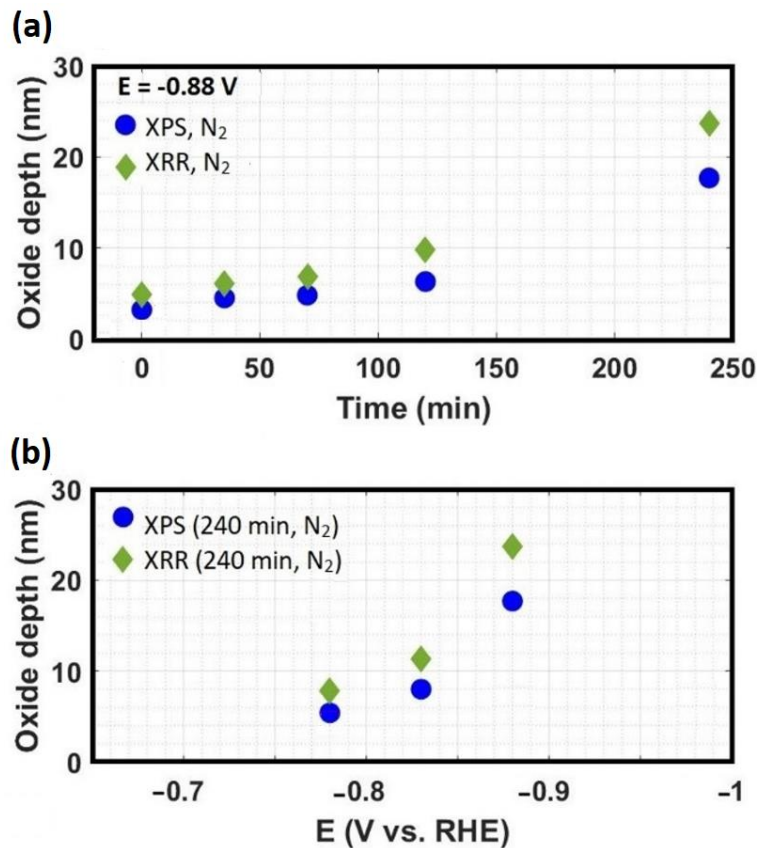


Figure S12. Oxide layer thickness (depth) obtained using both XPS and XRR measurements as a function of (a) total time and (b) applied potential, respectively.

## 8- Growth parameters and surface characterization before and after electrochemical experiments

The general growing procedure for the thin-film surfaces is described in the experimental section of the article. The specific parameters to get the desired final structure for each TMN was followed based on the parameter listed in Table S4.

Table S4. Parameters applied in the growing procedure of the TMN surfaces.

TMNs	N <sub>2</sub> / sccm	Ar / sccm	P / W	V / V	I / mA	Growth pressure / mbar
CrN	10	17	400	440	910	$3.50 \times 10^{-3}$
VN	3.6	25	400	363	1102	$3.20 \times 10^{-3}$
NbN	3.5	25	400	376	1064	$3.70 \times 10^{-3}$
ZrN	2	25	200	327	612	$3.30 \times 10^{-3}$

Figure S13 shows the XRD measurements on the TMN surfaces after going through full electrochemical experiments in N<sub>2</sub>(g) and Ar(g) media. The XRD spectra for each surface are overlaid on the spectra from the respective pristine surface. The results do not present significant differences between N<sub>2</sub>(g) and Ar(g). However, only VN and ZrN seem to be not changed compared to their pristine forms.

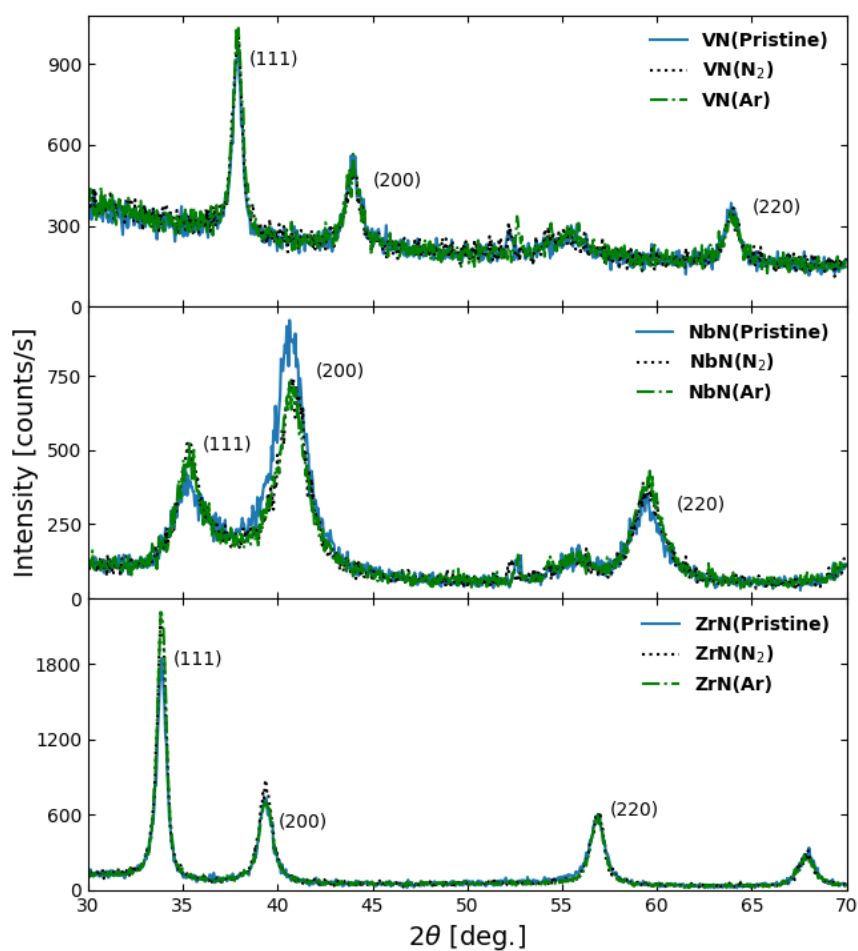


Figure S13. Grazing incidence x-ray diffraction (GIXRD) measurements on the TMN surfaces after experiments in Ar (green dashed lines) and  $N_2$  (black dotted lines) overlaid on the pristine measurements before experiments (blue solid lines).

Table S5. Information derived from the XRR measurements of the pristine and used surfaces.

	Total film thickness / nm			Oxide layer thickness / nm			Main film density / g cm <sup>-3</sup>		
	Pristine	Ar	N <sub>2</sub>	Pristine	Ar	N <sub>2</sub>	Pristine	Ar	N <sub>2</sub>
<b>VN</b>	66.6 ± 1.3	63.5 ± 2.1	65.0 ± 2.1	3.5 ± 0.5	2 ± 1	3 ± 1	5.85 ± 0.1	5.67 ± 0.20	5.67 ± 0.20
<b>NbN</b>	100.3 ± 0.1	101.5 ± 1.2	100.9 ± 0.7	3.7 ± 0.1	2 ± 1	2.1 ± 0.5	8.24 ± 0.01	8 ± 1	8.27 ± 0.01
<b>ZrN</b>	83 ± 2	82 ± 2	82 ± 2	7 ± 1	9 ± 1	10.0 ± 1	7.09 ± 0.01	6.73 ± 0.01	6.66 ± 0.01

## 9- $^{14}\text{NH}_3$ and $^{15}\text{NH}_3$ Standard preparation for analysis using $^1\text{H}$ -NMR

$^1\text{H}$  nuclear magnetic resonance (NMR) was also used to analyze the calibration standards. Calibration standards of  $^{14}\text{NH}_3$  and  $^{15}\text{NH}_3$  were diluted using 2:1 (v/v) of 0.1 M KOH and 0.5 M  $\text{H}_2\text{SO}_4$  to each get to a final concentration of 2 ppm. The  $^{14}\text{NH}_3$  and  $^{15}\text{NH}_3$  standards were then mixed to get a range of 0, 0.2, 0.4, 0.6, 0.8, and 1 for the volume ratio of  $^{15}\text{NH}_3$  to  $^{14}\text{NH}_3$ . 110  $\mu\text{L}$  of each standard was transferred to the NMR tubes and 440  $\mu\text{L}$  of dimethyl sulfoxide- $d_6$  ( $\text{DMSO-}d_6$ ) was added to all the tubes and mixed thoroughly.  $^1\text{H}$ -NMR was carried out with 3000 scans. Figure S14 shows the gradual shift in the calibration standards in terms of the normalized NMR peak integration. The red arrow marks the point where signals of  $^{15}\text{NH}_3$  start to appear in the response. This point is equivalent to 0.8 ppm and thus,  $8.8 \times 10^{-5}$  mg is the lowest amount that can be detected.

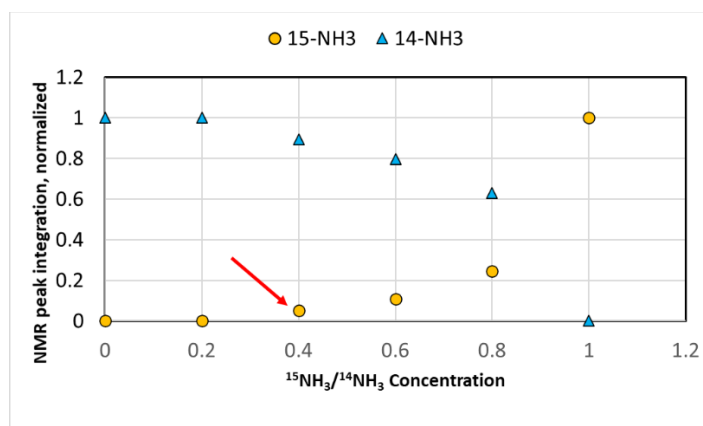


Figure S14. A 2-ppm mixture of  $^{14}\text{NH}_3$  and  $^{15}\text{NH}_3$  with varying ratios are analyzed using  $^1\text{H}$ -NMR. The graph shows the trend of the normalized peak integration when moving from a pure  $^{14}\text{NH}_3$  standard to a pure  $^{15}\text{NH}_3$  standard. The arrow marks the point where it is possible to see the doublet peak signals from  $^{15}\text{NH}_3$  in the full spectrum.

However, this amount is far higher than the ranges that usually emerge out of electrochemical experiments (ca. 0.05 ppm). In order to be able to detect lower concentrations of  $^{15}\text{NH}_3$ , the standards were concentrated prior to preparation for the  $^1\text{H}$ -NMR analysis by means of micro-diffusion ( $\mu\text{D}$ ) method. In this method, the standards were poured into acid washed Petri dishes (55 mm diameter). 110  $\mu\text{L}$  of 1 M  $\text{H}_2\text{SO}_4(\text{aq})$  were pipetted into 12 mL Sarstedt tube screw caps and centered on the Petri dishes. A 2-mm diameter hole was drilled on the petri dish lids. The lids were sealed on top of the dishes using Vaseline. 1 mL 10 M  $\text{NaOH}(\text{aq})$  was pipetted into the petri dishes through the holes, and the holes were immediately sealed with Vaseline. The standards were left standing on a shaker for 15 h. The ion equilibrium was thus shifted to favor  $\text{NH}_3$  which readily evaporates and is then slowly dissolved and captured as ammonium sulfate in the acidic solution. The caps were, then, taken out after 15 h and the acid was pipetted into the NMR tubes. Next,  $\text{DMSO-}d_6$  was added to the tubes and mixed completely and analyzed in NMR. Method blanks proved to be totally free of external contamination. Depending on the initial volume of the standards poured into the Petri dishes (i.e., the initial mols of  $^{15}\text{NH}_3$ ), the fixed volume of the acid

inside the caps ends up being concentrated to different levels. Accounting for the maximum experimental duration to collect real samples, and doing a back of the envelope calculation, it turned out that ca. 0.03 ppm was the minimum concentration able to be detected using this method. ZrN, that shows catalytic behavior at -0.6 V and -0.8 V vs. RHE, yields ammonia concentrations of  $0.02 \pm 0.005$  ppm which falls below this sensitivity level, thus making isotope labeling experiment not worth the attempt.

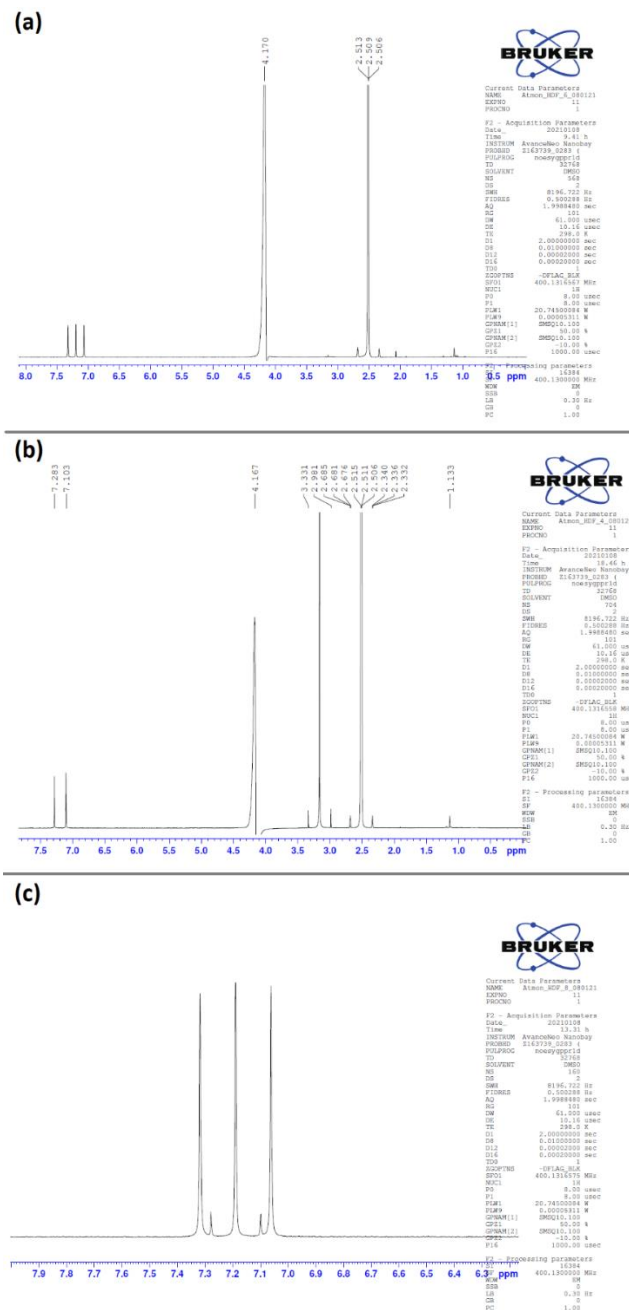
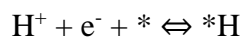


Figure S15. <sup>1</sup>H-NMR spectra for (a) 100% <sup>14</sup>NH<sub>3</sub> standard, (b) 100% <sup>15</sup>NH<sub>3</sub> standard, and (c) 60% <sup>14</sup>NH<sub>3</sub> / 40% <sup>15</sup>NH<sub>3</sub> standard (where the red arrow marks on Figure S14).

## 10- DFT calculations

Density functional theory (DFT) calculations were used to obtain the energetics of adsorbed species ( $\text{H}^+$ ,  $\text{OH}^-$  and  $\text{O}^{2-}$ ) from an aqueous electrolyte solution into the N-vacancies generated during the Mars-van Krevelen mechanism of the NRR<sup>4</sup>.

The applied potential affects the adsorption energies of the positively charged  $\text{H}^+$  species and the negatively charged  $\text{OH}^-$  and  $\text{O}^{2-}$  species in an opposite way where the  $\text{H}^+$  species adsorb stronger when the applied potential becomes more negative:



while the  $\text{OH}^-$  and  $\text{O}^{2-}$  species adsorb stronger when the applied potential becomes more positive:



Figure S16 shows three different facets of VN, CrN, NbN, and ZrN (rocksalt (100), (110), and (111)) where the most stable species ( $\text{H}^+$ ,  $\text{OH}^-$  and  $\text{O}^{2-}$ ) is shown as a function of the applied potential (referenced against the RHE). For VN, NbN, and ZrN there is a certain potential window where none of those species are adsorbed. Since the onset potential for NRR is at more negative potential, where the N-vacancies will be occupied with  $\text{H}^+$ , one needs to switch the applied potential to the resting potential window (i.e., white space in Figure S16) where the adsorbed protons will be transferred back to the aqueous solution and where water molecules will not oxidize to  $\text{OH}^-$  and  $\text{O}^{2-}$  species adsorbed at the N-vacant site. For CrN, however, these species are predicted to be adsorbed at all potential values. Thus, the N-vacant active sites are predicted to be poisoned by those species and therefore the MvK mechanism cannot take place. This is possibly the reason why no ammonia is produced on CrN in  $\text{N}_2(\text{g})$  (see Figure S5).

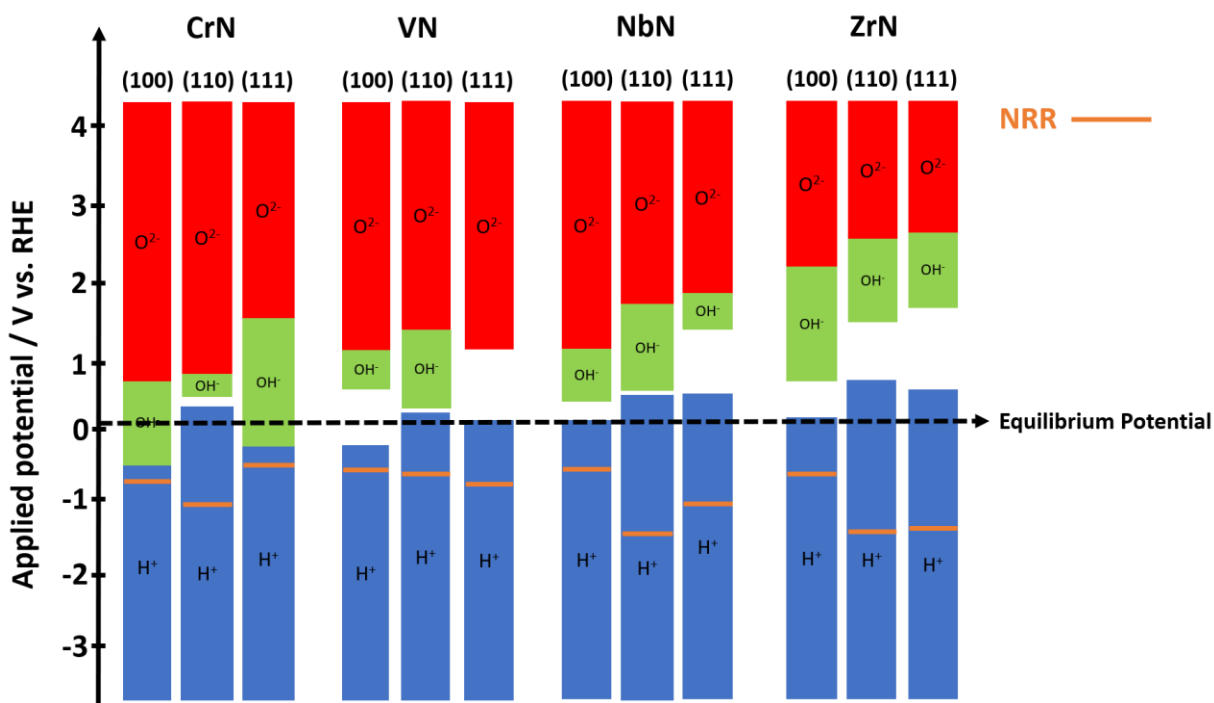


Figure S16. The most stable species ( $H^+$ ,  $OH^-$  or  $O^{2-}$ ) from an aqueous solution that could be adsorbed into the nitrogen vacancies on CrN, VN, NbN, and ZrN with three different crystal structures and facets (RS(100), RS(110), and RS(111)), obtained using density functional theory (DFT) calculations. Predicted onset potentials for nitrogen reduction reaction (NRR) is also indicated on the figure. In all cases except for CrN, there is a potential window where none of those species are present, which determines the resting potential needed in order to regenerate active sites. Only ZrN shows reasonably wide potential windows for all three facets. The DFT data is extracted from References 4 and 5.

## 11- Effect of chronoamperometry loop

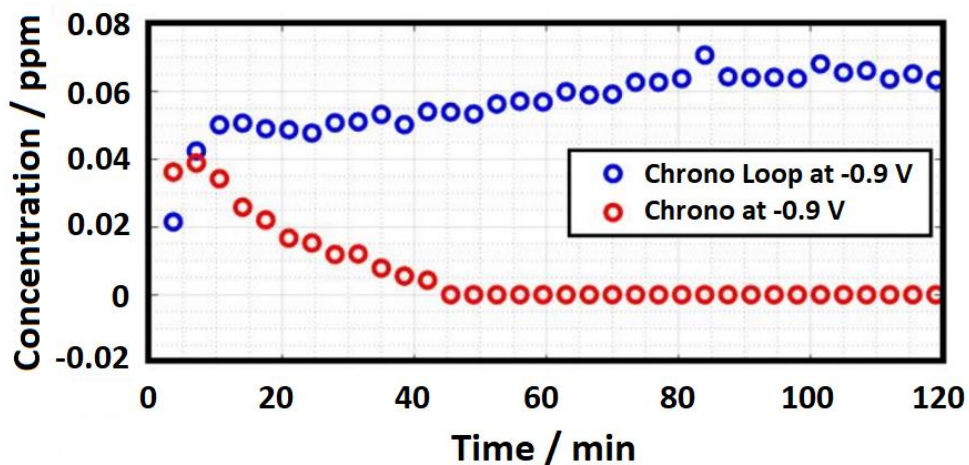


Figure S17. Comparison between ammonia measurements on ZrN when a potential of -0.9 V vs RHE is applied in chronoamperometry loop compared to when the same potential is held constant.

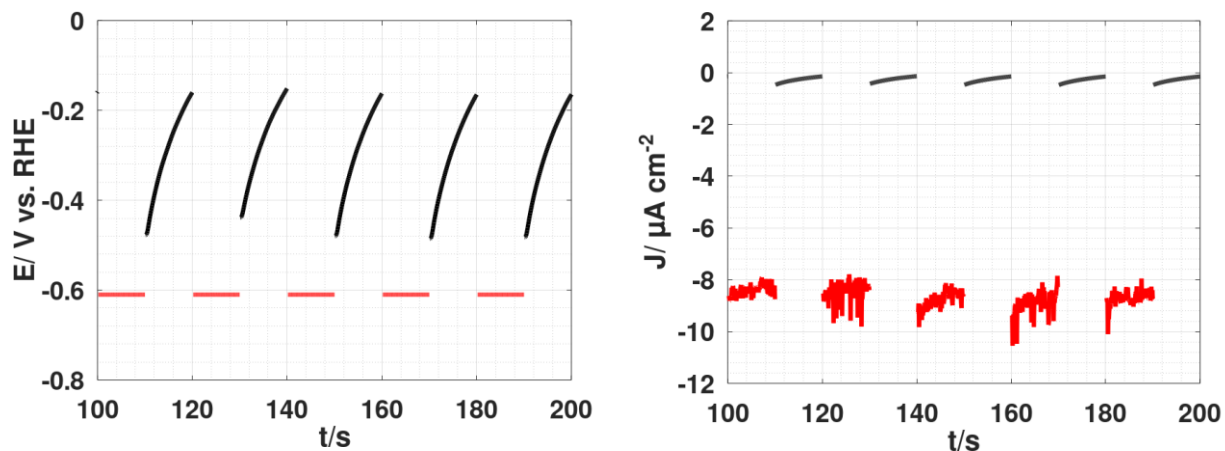


Figure S18. Applied potential and current density as a function of time for 5 cycles of a chronoamperometry loop recorded at -0.6 V vs. RHE (red) and OCP (black) on ZrN.

## 12- References

- (1) Mohammadi, M.; Fardindoost, S.; Almasi-Kashi, M. Room temperature selective sensing of aligned Ni nanowires using impedance spectroscopy. *Materials Research Express* **2020**, *7* (2), 025044.
- (2) Milošev, I.; Strehblow, H. H.; Gaberšček, M.; Navinšek, B. Electrochemical Oxidation of ZrN Hard (PVD) Coatings Studied by XPS. *Surf. Interface. Anal.* **1996**, *24*, 448-458.
- (3) Muneshwar, T.; Cadien, K. Comparing XPS on Bare and Capped ZrN Films Grown by Plasma Enhanced ALD: Effect of Ambient Oxidation. *Appl. Surf. Sci.* **2018**, *435*, 367-376.
- (4) Abghoui, Y.; Garden, A. L.; Howalt, J. G.; Vegge, T.; Skulason, E. Electroreduction of N<sub>2</sub> to Ammonia at Ambient Conditions on Mononitrides of Zr, Nb, Cr, and V: A DFT Guide for Experiments. *ACS Catal.* **2016**, *6*, 635-646.
- (5) Gudmundsson, M.; Ellingsson, V.; Skúlason, E.; Abghoui, Y. Optimizing Nitrogen Reduction Reaction on Nitrides: A Computational Study on Crystallographic Orientation. *Top Catal.* **2021**, 1-10.



# **Paper III**

**Investigation into the Mechanism of Electrochemical Nitrogen Reduction Reaction to Ammonia using Niobium Oxynitride Catalysts**

Hanifpour, F., Canales, C. P., Fridriksson, E. G., Sveinbjörnsson, A., Tryggvason, T. K., Lewin, E., Magnus. F., Ingason, Á. S., Skúlason, E., & Flosadóttir, H. D.

**Submitted**



# Investigation into the mechanism of electrochemical nitrogen reduction reaction to ammonia using niobium oxynitride thin-film catalysts

Fatemeh Hanifpour<sup>a</sup>, Camila P. Canales<sup>a</sup>, Emil G. Fridriksson<sup>b</sup>, Arnar Sveinbjörnsson<sup>c</sup>, Tryggvi K. Tryggvason<sup>b</sup>, Erik Lewin<sup>d</sup>, Fridrik Magnus<sup>a,b</sup>, Árni S. Ingason<sup>b</sup>, Egill Skúlason<sup>\*a,c,e</sup>, and Helga D. Flosadóttir<sup>\*c,e</sup>

- a. Science Institute, University of Iceland, VR-III, 107 Reykjavík, Iceland.
- b. Grein Research ehf., Dunhagi 5, 107 Reykjavík, Iceland.
- c. Atmonia ehf., Keldnaholt, 112 Reykjavík, Iceland.
- d. Inorganic Research Programme, Department of Chemistry – Ångström Laboratory, Uppsala University, Box 538, SE-751 21 Uppsala, Sweden.
- e. Faculty of Industrial Engineering, Mechanical Engineering and Computer Science, University of Iceland, VR-III, 107 Reykjavík, Iceland.

\* [helgadogg@atmonia.com](mailto:helgadogg@atmonia.com), [egillsk@hi.is](mailto:egillsk@hi.is)

## Abstract

Niobium oxynitride ( $\text{NbO}_x\text{N}_y$ ) thin films with varying combined non-metal vs. metal stoichiometries ( $x+y$ ) and N/O stoichiometric ratios ( $y/x$ ) are investigated for their ability to catalyze the nitrogen reduction reaction and ammonia synthesis at ambient conditions. Electrochemical impedance spectroscopy and ammonia measurements show stark differences both in nitrogen vs. argon media on each surface and on the surfaces in the series when the combined stoichiometry of N+O vs. Nb increases. Surface stability checks at fixed intervals during the experiments and surface characterization after the experiments using X-ray diffraction reveal the least changes occurred to the surface with the highest N+O stoichiometry. Based on these observations, an ammonia synthesis mechanism is proposed. Isotope labeling experiments on the most promising surface of the series, however, show no sign of catalytically produced ammonia, possibly due to the lack of stability of the surface to endure through the ammonia production cycle.

**KEYWORDS:** Ammonia electrosynthesis, transition metal oxynitride, thin films, ambient condition, aqueous electrolyte solution.

## 1. Introduction

The Haber-Bosch (HB) process has been used over the past century to produce ammonia ( $\text{NH}_3$ ) with the main aim of providing fertilizers [1]. The limitations associated with this process, namely the harsh operating conditions and the release of carbon dioxide ( $\text{CO}_2$ ) as a side-product to the environment, have made scientists look for more sustainable means of ammonia synthesis [2,3]. With this aim, various alternatives have been proposed including electrocatalysis, photocatalysis, plasma catalysis, plasma electrolysis, homogeneous catalysis, and electrochemical lithium cycling [4-12]. Given the advantages and disadvantages associated with each alternative, electrocatalysis seems to be the most appealing option to be developed for the future of sustainable ammonia synthesis.

Many theoretical studies have been carried out on viable catalysts and mechanisms for the nitrogen reduction reaction (NRR) [2,13,14]. Abghoui et al. have conducted thorough density functional theory (DFT) calculations on transition metal nitrides (TMNs) [15-19]. In their first work, the authors studied the Mars Van Krevelen (MvK) mechanism of  $\text{NH}_3$  synthesis on all the mono-nitrides of naturally occurring transition metals in rocksalt (RS) and zincblende (ZB) structures. There, niobium nitride ( $\text{NbN}$ ) was predicted to be a good candidate for NRR being catalytically active towards ammonia formation, stable towards poisoning of surface vacancies and relatively stable towards decomposition upon polarization [15,16]. Similarly, a thorough screening of transition metal oxides (TMOs) was carried out by Höskuldsson et al. in which the (110) facets of 11 TMOs in their rutile structure were investigated with respect to ammonia electrosynthesis.  $\text{NbO}_2$  was among the most promising candidates that demonstrated a stable facet plus catalytic activity towards ammonia formation while catalysing the unfavourable hydrogen evolution reaction (HER) at the same time [20].

Implementing the promising theoretical results into practice and validating those results through experiments is a challenging task. So far, several reports have stressed the importance of

following strict protocols in NRR experiments [21-26]. These include sensitive quantification methods, rigorous control experiments, removing all sorts of contamination from the catalyst, electrochemical setup, and the gas. There is also evidence of contamination of  $^{15}\text{N}_2$  gas stocks with  $^{15}\text{NH}_4^+$ ,  $^{15}\text{NO}_3^-$ ,  $^{15}\text{NO}_2^-$  and  $^{15}\text{N}_2\text{O}$  which should be eliminated and accounted for in the experiments [27]. Choi et al. have demonstrated in a recent study that the reduction of  $\text{NO}_2^-$ ,  $\text{NO}_3^-$ ,  $\text{NO}$ , and  $\text{NO}_2$  to ammonium could be catalysed more easily over Bi or Au nanoparticles, while the conversion of  $\text{N}_2$  to  $\text{NH}_4^+$  was highly unlikely [28]. As these contaminants are present as traces in even the highest purity  $^{14}\text{N}_2$  and much more in the  $^{15}\text{N}_2$  gas tanks, extra care must be taken before introducing the gas into the electrochemical systems. Moreover, researchers need to consider the possibility of introducing external ammonia contamination into their setup by using membranes that have undergone insufficient pretreatment [29]. Thus, it is important that all studies on NRR include blank tests in  $\text{Ar(g)}$ , isotope labeling control experiment, purification of all gases before introduction into the electrochemical setup, and make sure to use the acceptable pretreatment of the Nafion membrane.

Numerous experimental studies have been conducted to date on the oxide and nitride form of niobium. Cubic and tetragonal niobium nitride ( $\text{NbN}$  and  $\text{Nb}_4\text{N}_5$ ) were reported by Du et al. as not suitable for NRR. In 0.05 M  $\text{H}_2\text{SO}_4$ ,  $\text{NbN}$  was too stable to initiate the MvK mechanism and  $\text{Nb}_4\text{N}_5$  produced ammonia via leaching of inherent N atoms. Furthermore,  $\text{Nb}_4\text{N}_5$  was found to decompose and thus proved to be unstable in alkaline electrolytes [30]. The authors have check-marked all the necessary experimental NRR criteria and therefore, the results are reliable. Han et al. claimed high selectivity and excellent stability of  $\text{Nb}_2\text{O}_5$  nanofibers in 0.1 M  $\text{HCl}$  and reported an ammonia production yield of  $43.6 \mu\text{g h}^{-1} \text{mg}^{-1}_{\text{cat}}$  and 9.26% current efficiency at -0.55 V vs. reversible hydrogen electrode (RHE) [31]. The authors confirmed the source of the ammonia by conducting both a blank experiment in  $\text{Ar}$  and an isotope labeling experiment (i.e., a control experiment in  $^{15}\text{N}_2$  gas). However, the gases used in the working compartment of their two-compartment batch-cell were used without a purification step and no information was given on the type of the membrane used in their system, both important sources of ammonia contamination. Huang et al. presented encouraging results on  $\text{NbO}_2$  nanoparticles and less promising results on  $\text{Nb}_2\text{O}_5$  nanorods [32]. When using high purity  $\text{N}_2$  gas but with no further purification, the authors reported a high current efficiency of 32% at -0.6 V vs. RHE in 0.05 M  $\text{H}_2\text{SO}_4$  and attributed the outstanding performance to the partially occupied d-orbitals of  $\text{Nb}^{4+}$  which formed  $\pi$  back-bonding with  $\text{N}_2$ . No ammonia was detected in the  $\text{Ar}$  blank test and no further isotope labeling experiment was performed to verify the source of the ammonia product. No information regarding the preparation of the Nafion 212 membrane was provided in this study. Kong et al. reported high ammonia production rate of  $1.58 \times 10^{-10} \text{ mol s}^{-1} \text{ cm}^{-2}$  and 2.26% current efficiency for  $\text{Nb}_2\text{O}_5$  nanowires at -0.6 V vs RHE in 0.1 M  $\text{Na}_2\text{SO}_4$  [33]. Their DFT calculations showed that NRR would take place via a distal associative route over the  $\text{Nb}_2\text{O}_5$  (001) facet. The  $\text{Ar}$  blank test showed no ammonia production, and the authors did not perform any isotope labeling test to verify the source of ammonia. Nafion used in their experiments was pretreated using the common pretreatment method which is boiling in water,  $\text{H}_2\text{O}_2$ , and water each for 1h, followed by 3 h in 0.5 M  $\text{H}_2\text{SO}_4$  and finally for 6 h in water. Our previous studies have demonstrated that this pretreatment method is prone to increasing the  $\text{NH}_3(\text{aq})$  contamination in this membrane [29]. Hu et al. reported porous  $\text{Ce}_{1/3}\text{NbO}_3$  to be active towards the NRR and catalyse the ammonia synthesis at -0.8 V vs. RHE in 0.1 M  $\text{Na}_2\text{SO}_4$  with a rate of  $10.34 \mu\text{g h}^{-1} \text{ cm}^{-2}$  ( $1.69 \times 10^{-10} \text{ mol s}^{-1} \text{ cm}^{-2}$ ) and a current efficiency of 6.87 % [34]. The authors claimed that the catalyst benefitted from the synergistic effect of Nb atoms as active centres for NRR and Ce atoms in boosting the charge transfer within the process.

Transition metal oxynitrides have recently been suggested as potential candidates towards ammonia electrosynthesis [35-37]. A theoretical study by Pan et al. investigated various oxygen contents in vanadium oxynitride (VON) and reported the effect of specific low and high oxygen contents on enhanced selectivity and improved nitrogen adsorption and dissociation, respectively [38]. A DFT and experimental study by Wu et al. showed that nanoparticles of  $\text{Nb}_3\text{O}_7(\text{OH})$  would electrochemically form NbO during NRR which according to the authors was the catalytically active phase, but the NbON, which was formed by further continuation of the experiment, was claimed to have drastically decreased the NRR yield and efficiency [39]. Bimetallic vanadium-nickel oxynitride (VNiON) over VNiO nanosheet was shown to possess promising electrochemical performance and catalytic activity for ammonia synthesis in 0.05 M  $\text{Na}_2\text{SO}_4$  with 5.57 % current efficiency [40]. The NRR process was proposed to proceed via MvK mechanism, and the stability of the oxide was shown to have improved by introduction of the oxynitride layer. However, no gas cleaning and isotope labeling control experiment was reported by the authors.

As promising as all these experimental reports are, care must be taken while reporting such results. The importance of accurate ammonia analysis in NRR studies must be considered to prevent false positive results. Although these studies do not all follow the strict protocol necessary to prove ammonia electrosynthesis, oxynitrides are still considered promising candidates towards NRR and a more careful examination is necessary to investigate this further. In this study we assess the electrocatalytic properties of thin films of  $\text{NbO}_x\text{N}_y$  with different N+O vs. Nb stoichiometries by employing several electrochemical techniques together with an accurate ammonia quantification.

## 2. Experimental section

### 2.1. Surface deposition and characterization methods

Thin films of  $\text{NbO}_x\text{N}_y$  are grown by reactive dc magnetron sputtering from a 4" diameter Nb target (99.95%) in a high vacuum chamber with a base pressure of  $(4\pm 1)\times 10^{-5}$  mbar. The films are deposited on conductive highly p-doped Si(001) substrates, with a native oxide layer, without substrate heating. A constant Ar (99.999%) gas flow of 25 sccm is used whereas the  $\text{N}_2$  and  $\text{O}_2$  flows (both 99.999%) are varied individually in the range 1.0-3.0 sccm to obtain different oxynitride stoichiometries. This results in a total pressure of  $(3.2\pm 0.1)\times 10^{-3}$  mbar during growth. The flow rates for each film are presented in

Table 2. The films are post-annealed ex-situ in vacuum in a Jipelec JetFirst 100C rapid thermal annealing (RTA) system for 20 minutes at a temperature of 800 °C to induce crystallization of the oxynitride phase. The base pressure of the RTA system is  $(2.4\pm 0.5)\times 10^{-5}$  mbar.

All films are characterized structurally by x-ray diffraction (XRD) and x-ray reflectivity (XRR), both after annealing (denoted by pristine) and after electrochemical testing (Figures S11 and S12). A Panalytical X'Pert MRD system is used, equipped with a Goebel mirror on the incident side (for a parallel beam) and a  $0.27^\circ$  collimator on the diffracted side. The XRD measurements are carried out in a grazing incidence geometry with the incident angle fixed at  $\omega = 1^\circ$ . XRR scans are fitted using the GenX software [41] package to extract the film density, thickness, and roughness.

The oxynitride films are measured using X-ray photoelectron spectroscopy (XPS) to determine the film composition. The measurements are conducted in an Ulvac-Phi Quantera II XPS microprobe (USA, Chanhassen Minnesota) employing monochromatic Al K $\alpha$  radiation. Sputter depth profiles are acquired to map the depth-dependent composition, 500 eV Ar<sup>+</sup> ions rastered over an area of 1  $\times$  1 mm<sup>2</sup>, and 10 steps of 2 minutes, giving a total depth in the order of 30 nm. Composition was determined using custom sensitivity factors determined using reference films with compositions determined by a combination of Elastic Recoil Detection Analysis (ERDA) and Rutherford Backscattering (RBS). Presented stoichiometries in Table 2 are averages from sub-surface part of the sputter depth profiles.

## 2.2. Electrochemical setup and techniques

All electrochemical studies are performed according to the protocol illustrated in Figure 1. The experiments are carried out in a setup in-line with ammonia measurement unit without any manual handling of the samples. This combination of electrochemical experiments and analysis method significantly reduces any sorts of possible external contamination to the samples (Figure S2). The electrolyte of choice is 0.1 M potassium hydroxide (KOH, Merck,  $\geq$ 85%) which is bubbled with Ar (HiQ<sup>®</sup> Argon 5.0, Linde) for 1 h before experiments. The gas is scrubbed of any possible traces of NO<sub>x</sub>, CO<sub>2</sub> or NH<sub>3</sub> using first, 0.05 M H<sub>2</sub>SO<sub>4</sub> and second, ultrapure water (MilliQ<sup>®</sup>, Grade 1), prior to entering the electrolyte. Then the Ar saturated electrolyte is transferred to two 50 mL gas-tight syringes. A three-electrode electrochemical flow cell ( $\mu$ -PrepCell<sup>TM</sup>, Antec Scientific, Netherlands) is used for this study. The commercial flow-cell is modified to allow for two spacers and a Nafion membrane in between the working and the counter electrode, ensuring two separate chambers for the working and the counter electrodes. The pretreatment of Nafion 211 is carried out using a previously reported method [29] consisting of i) 10 minutes of sonication of Nafion in 5% H<sub>2</sub>O<sub>2</sub> to remove the organic impurities, ii) 10 minutes of sonication in DI-water, iii) 10 minutes of sonication in 0.5 M H<sub>2</sub>SO<sub>4</sub> to remove the metallic impurities, iv) 10 minutes of sonication in DI-water, v) more than 12 h in DI-water at 80 °C for expansion, and vi) sonication in 0.05 M H<sub>2</sub>SO<sub>4</sub> and DI-water right before application in the electrochemical setup. The Ti(s) counter electrode is coated with 100 nm of Pt on top of a 10-nm thick Ta adhesion layer in a magnetron sputtering chamber. Ag/AgCl is used as the reference electrode. The backside and the edges of the Si substrates together with the corners of the thin film oxynitride catalysts are silver-painted to ensure sufficient electrical connection to the potentiostat. For more information regarding the electrochemical flow-cell, refer to Figure S1 in the Supplementary Information (SI). The catalyst surface acts as the working electrode within the flow-cell. The potential of the working electrode surface is controlled with a Gamry potentiostat, Reference 600<sup>TM</sup> (Gamry Instruments, Warminster, PA 18974 USA). Constant flow of the electrolyte from two gas-tight syringes (Model 1050 TLL, Hamilton<sup>®</sup>, USA) is maintained and sent through the working and the counter compartment of the  $\mu$ -PrepCell at a flow rate of 20  $\mu$ L/min using a dual syringe pump (KD Scientific, Inc., Legato 100, Massachusetts 01746-1388 USA). Depending on the requirements of the experiment, Ar or N<sub>2</sub> (HiQ<sup>®</sup> Nitrogen 5.0, Linde) gas is introduced to the working compartment with a flow rate of 50 mL/min after passing through two scrubbing units and a T junction where it is mixed with the electrolyte. The fluid (gas and electrolyte combined) leaving the working compartment of the cell is collected in 100  $\mu$ L of 0.5 M H<sub>2</sub>SO<sub>4</sub> used as acid-trap and the resulting solution is collected, using an automated syringe, in a 200  $\mu$ L sample loop to be analyzed in the

ammonia measurement unit described in section 2.3. Figure S1 illustrates the electrochemical workstation connected in-line to the ammonia quantification unit.

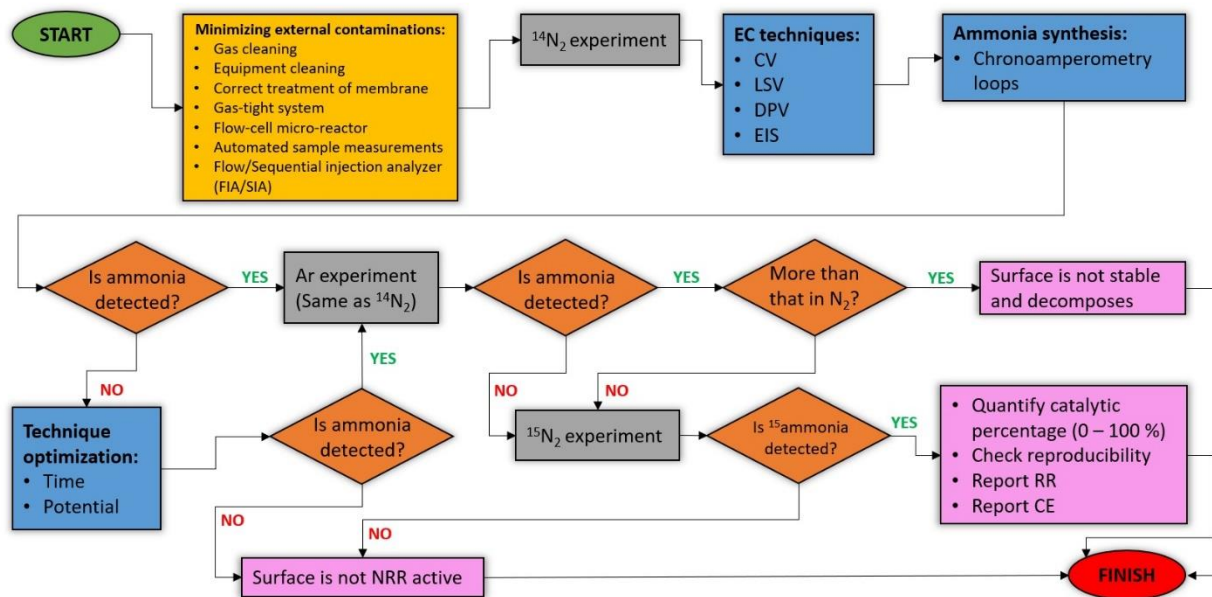


Figure 1. Procedures pursued for the NRR studies in this work which ensures reliable and reproducible data.

At the beginning of all electrochemical experiments, open circuit potential (OCP) is recorded until reaching stability. Then, 0 V vs. RHE is applied until ammonia from any source of contamination within the closed system is removed. The background ammonia in the system is subtracted from all subsequent samples measured during electrochemical procedures. The reader is referred to section 2.3 for the details of the ammonia measurement method. Cyclic voltammetry (CV) with a scan rate of 100 mV/s and linear sweep voltammetry (LSV) with a scan rate of 10 mV/s are recorded in the potential window between OCP and HER potential for each surface. CV comparison in Ar vs. N<sub>2</sub> for all surfaces in the same potential range is shown in Figure 3. Dynamic electrochemical impedance spectroscopy (DEIS) at four different potentials namely at OCP, in the capacitive zone (0 V vs. RHE), at the onset potential (OP; -0.5 V vs. RHE), and in the faradaic zone (-0.7 V vs. RHE) is carried out to investigate the electrical behavior of each surface more thoroughly (Figure 3). An amplitude of 10 mV rms and 10 points per decade in a frequency range of 100,000 Hz to 0.1 Hz are used in this study. The DEIS spectra are fitted using the Z-View® Software (Scribner Associates) [42]. Due to the large perturbation in the system and the difficulty to interpret the DEIS data while gas is bubbled over the surface, this study is done using Ar/N<sub>2</sub> saturated electrolyte. DEIS data shows to follow the same trend with and without gas bubbling inside the micro-reactor, with the only observable difference being larger impedances while bubbling the gas directly over the surface. The reader is referred to section 4 in the SI for some examples of this comparison (Figure S5).

To study the electrochemical ammonia synthesis and calculate NRR reaction rate (RR) and current efficiency (CE), chronoamperometry technique is utilized, both in Ar and N<sub>2</sub> environments. Based on the CV profiles, chronoamperometry loops are designed where one selected negative potential and one selected positive potential are applied intermittently for 10 s each and the loop

is repeated for 30 min, long enough to collect three samples for in-line ammonia quantification corresponding to each loop. The positive potential is applied to desorb the cation species in the electrolyte (such as  $K^+$  and  $H^+$ ) which could block the active sites on the catalyst and hinder  $N_2$  adsorption on these sites [43]. Eight combinations of three positive potentials (OCP, OCP + 0.2 V, and OCP + 0.4 V), and three negative potentials (-0.2 V, -0.4 V, and -0.6 V vs. RHE) are tested for the chronoamperometry loop as put forward in Table 1.

Table 1. Chronoamperometry potentials applied for 10 s in a loop which is maintained long enough to give three consecutive ammonia measurements for each combination.

Upper limits (A)	Lower limits (B)		
	-0.2 V vs. RHE	-0.4 V vs. RHE	-0.6 V vs. RHE
OCP	✓	✓	✓
OCP+200 mV	✓	✓	✓
OCP+400 mV	✓	✓	

The samples collected into the acid trap are then sent for ammonia analysis. The whole process from ammonia production inside the micro-reactor to ammonia measurement takes place in a closed, in-line system.

### 2.3. Ammonia measurement method

Ammonia quantification is done using a method described in our previous work [20]. In short, the output line from the micro-reactor carrying the produced ammonia is connected to the specialized Sequential Injection Analysis® system (OminSIA, FIALab Instruments Inc. Bellevue, WA 98103 USA) with gas tight PEEK tubing. The sample is reacted with Ortho-phthalaldehyde (OPA) to make an  $NH_3$ -OPA fluorescent product to be detected in a photomultiplier tube (PMT) with a fluorometric detection (excitation at 370 nm, detection at 425 nm) [44]. This method has a very sensitive limit of detection (ca. 0.5 ppb of ammonia) compared to the commonly used methods and only demands 200  $\mu$ L volume of each sample. The electrolyte is always contained in a gas tight environment, never exposed to atmosphere, or handled in any manner. This minimizes the external sources of contamination to the samples. A full description of the method is included in the SI, section 3.

### 2.4. Isotope labeling experiment

Due to ammonia's adventitious contamination, isotope labeling experiment is a criterion for scientific proof of catalysis in the field of electrochemical NRR. Furthermore, potential N leaching of catalysts provides a new source of  $NH_3$  contamination from materials that have N atoms inherent within their structures.  $^{15}N$  isotope labeling, therefore, serves as a key to investigate the source of ammonia detected in the experiments here.

In isotope labeling experiments,  $^{15}N_2$  is purified by passing through 0.05 M  $H_2SO_4$  and ultrapure water before being introduced in the micro-reactor set-up. The electrochemical procedure is limited to: (i) recording the OCP value and collecting one sample as the background; (ii) recording CV, and (iii) chronoamperometry loops in the optimized range of potentials. All samples plus calibration standards are then concentrated by means of micro-diffusion ( $\mu$ D) method and

ammonia is derivatized from the concentrated samples to be measured using gas chromatography-mass spectroscopy (GC-MS, Trace<sup>TM</sup> 1300, ISQ LT, Thermo Scientific). In the  $\mu$ D method, the samples are poured into acid washed Petri dishes (55 mm diameter). 100  $\mu$ L of 1 M  $\text{H}_2\text{SO}_4(\text{aq})$  are pipetted into 12 mL Sarstedt tube screw caps and centered on the Petri dishes. A 2-mm diameter hole is drilled on the petri dish lids. The lids are sealed on top of the dishes using Vaseline. 1 mL 10 M  $\text{NaOH}(\text{aq})$  is pipetted into the petri dishes through the holes, and the holes are immediately sealed with Vaseline. The samples are left standing on a shaker for 15 h. The ion equilibrium is thus shifted to favor  $\text{NH}_3$  which readily evaporates and is then slowly dissolved and captured as ammonium sulfate in the acidic solution. Then, caps are taken out and the acid is diluted in 450  $\mu$ L of milliQ water. In order to accurately detect  $\text{NH}_3$  (17 amu) and  $^{15}\text{NH}_3$  (18 amu), and reliably distinguish between ammonia and water, an organic ammonia derivative is produced through a simple organic reaction. The 550  $\mu$ L of samples are transferred to the 9MM AVCS KIT, clear vials with PTFE/silicone caps from Thermo Scientific. Following the addition of 20  $\mu$ L of 10 M  $\text{NaOH}$ , 100  $\mu$ L of internal standard (p-toluenesulfonamide), 1 mL of dioxane, 2.5% of  $\text{Na}_2\text{CO}_3$  and 50  $\mu$ L of benzenesulfonyl chloride, as suggested by Kataoka et al., the vials are shaken vigorously up and down for at least 15 min. To remove the unreacted benzenesulfonyl chloride, two times extraction with 3 mL of Hexane is performed after adjusting the pH to  $\sim 14$  using 1.6 mL of 10 M  $\text{NaOH}$ . The aqueous phase from the Hexane extraction is separated and mixed with 1 mL of 2 M  $\text{HCl}$ . Having reached a pH of  $\sim 1$ , two times extraction with 3 mL of diethyl ether is performed to extract the ammonia in the liquid samples as a benzenesulfonamide derivative. The organic phase from this extraction is evaporated on a heating block and the residue is dissolved in 200  $\mu$ L of ethyl acetate. This sample is then analyzed using GC-MS [45]. The limit of detection of  $^{15}\text{NH}_3$  using this method is 20 ppb. In all experiments, standard samples and two blanks are prepared and exposed to the same method of isolation and derivatization.

### 3. Results and discussion

#### 3.1. Surface characterization

The stoichiometry of four thin-film coatings prepared in different gas environment is determined by XPS sputter depth profiles (shown in Figure S10), and the bulk averages are presented in Table 2, where the total non-metal constituents of the  $\text{NbO}_x\text{N}_y$  ( $x+y$ , also denoted as  $\text{N}+\text{O}$ ) are also presented together with the  $\text{N}/\text{O}$  ratio. These two parameters will henceforth be used to describe the stoichiometry of the films. As can be seen, films #1 and #2 have a higher nitrogen content with  $\text{N}/\text{O}$  ratios of 0.53-0.49 and lower total non-metal content ( $\text{N}+\text{O} = 1.22\text{-}1.28$ ). films #3 and #4 which are deposited with a higher oxygen flow have lower  $\text{N}/\text{O}$  ratios (both 0.19) and a higher total non-metal content with  $\text{N}+\text{O}$  at 1.43-1.52, compared to #1 and #2.

The Nb 3d spectra from the bulk of the pristine coatings (attained after 8 min sputter etching using 500 eV  $\text{Ar}^+$ , at approximately 13 nm) is also presented in Figure 2. To fit each spectra using the XPS peak software [46] two (doublet) contributions are required: One with the Nb  $3d_{5/2}$  peak at 203.8-203.9 eV and Nb  $3d_{3/2}$  at 206.5-206.6 eV, which is in good agreement with both NbN and NbO phases and is thus consistent with an oxynitride phase [47]. films #3 and #4 exhibit slightly higher binding energies for the primary peak, which is consistent with a higher oxygen content. These contributions have been fitted with an asymmetric peak shape, which is required to explain the asymmetry of the Nb  $3d_{5/2}$  peak and fits well with the fact that the films are electrically conductive. For all the films, this oxynitride contribution makes out 88~89% of the total intensity.

An additional, smaller, contribution (11~12% of the intensity) is found at higher binding energies with Nb 3d<sub>5/2</sub> at 207.5~207.7 eV. This matches what is expected from Nb<sub>2</sub>O<sub>5</sub> [47], and also the oxide found on the surface of the air-exposed films.

Table 2. Flow rates of O<sub>2</sub> and N<sub>2</sub> gas during the deposition process and resulting stoichiometries of the NbO<sub>x</sub>N<sub>y</sub> films, determined by XPS depth profile measurements.

Surfaces	O <sub>2</sub> / sccm	N <sub>2</sub> / sccm	Average bulk composition / at.%			Stoichiometry NbO <sub>x</sub> N <sub>y</sub>			
			Nb	O	N	x	y	x+y	y/x
#1	2.0	1.5	45%	36%	19%	0.80	0.42	1.22	0.53
#2	2.5	1.5	44%	38%	18%	0.86	0.42	1.28	0.49
#3	3.0	1.0	41%	49%	9%	1.20	0.23	1.43	0.19
#4	3.0	1.5	40%	51%	10%	1.28	0.24	1.52	0.19

Diffraction patterns from the pristine films are shown in Figure 2. All films are polycrystalline and show clear characteristic diffraction peaks corresponding to the tetragonal (rutile) Nb(O,N)<sub>2</sub>-type structure but in addition, films #1 and #2 show peaks belonging to the cubic rocksalt Nb(O,N) phase. Diffraction peaks are representative of the crystal structure of the film and as such do not give direct evidence of chemical composition. The XRD measurements can therefore only confirm the presence/absence of the rutile and rocksalt structures but the precise stoichiometry of each phase cannot be determined from this data. However, substitution of O for N and vice versa will result in an expansion or contraction of the crystal lattice with an associated shift in diffraction peak positions relative to the pure nitride or oxide phases. Indeed, we observe such a shift for both phases, indicating that both the rutile and rocksalt phases are oxynitrides. To highlight that peak positions can be expected over a range of angles due to the varied O/N ratio we label peaks with shaded areas in Figure 2.

### 3.2. Electrochemical analysis

The surfaces' electrochemical behavior is observed to be highly dependent on both the N+O stoichiometry and the N/O ratio. Figure 3 shows the voltametric profiles at a scan rate of 100 mV/s from OCP towards negative potentials, and the dynamic electrochemical impedance spectra at four DC potentials for each surface, in both Ar and N<sub>2</sub> environment. For the three surfaces with lowest N+O stoichiometries, NbON#1, NbON#2 and NbON#3 the CVs collected in Ar saturated electrolyte demonstrate less negative onset potentials (OP) and higher current than the ones collected in N<sub>2</sub> saturated electrolyte, meaning that HER is delayed on these three systems due to the presence of N<sub>2</sub> in the electrochemical environment. For NbON#4, on the other hand, the Ar and N<sub>2</sub> CVs are close to being overlapped and the system clearly demonstrates lower capacitive and faradaic current in both environments.

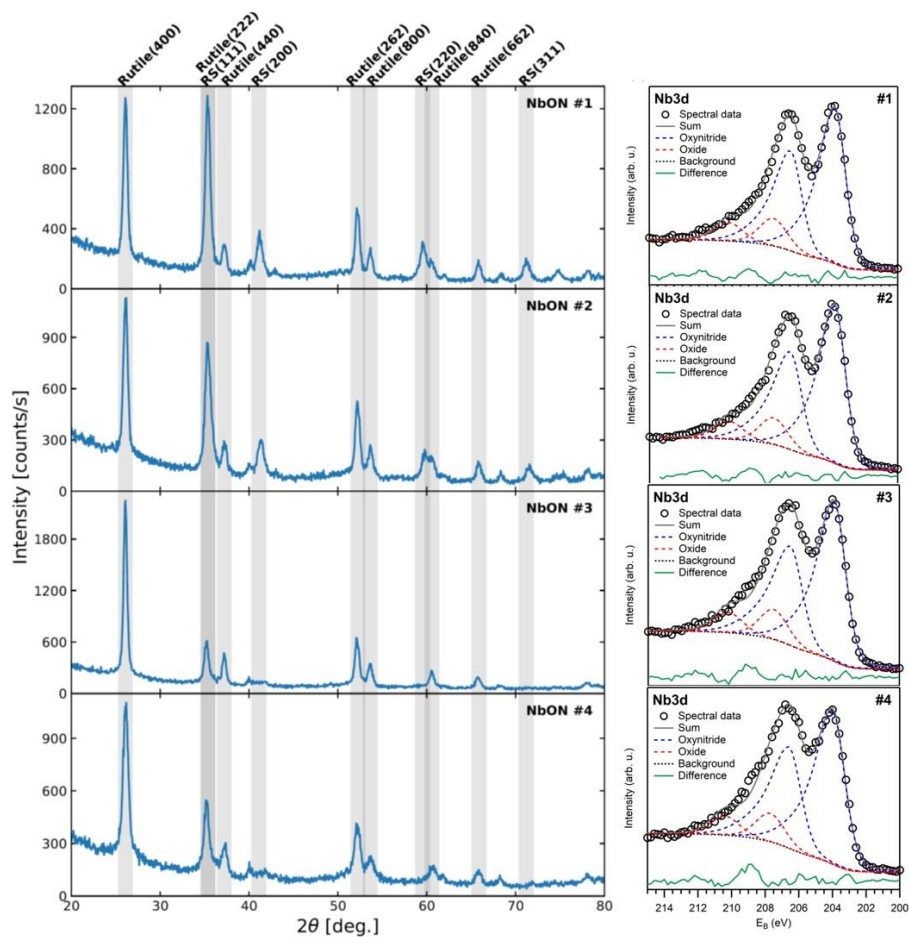


Figure 2. Diffractograms from the pristine surfaces of  $\text{NbO}_x\text{N}_y$  obtained by grazing incidence XRD (left) and Nb 3d spectra from XPS attained after sputter etching (right).

The results of the DEIS study are shown in the form of Nyquist plots in Figure 3. NbON#1 ( $\text{N}+\text{O} = 1.22$ ) and NbON#2 ( $\text{N}+\text{O} = 1.28$ ), demonstrate no significant difference between Ar and  $\text{N}_2$  environment for E1 and E2. Reaching E3, a lower charge transfer resistance ( $R_{ct}$ ) is observed in Ar environment compared to  $\text{N}_2$ . This can be attributed to the later OP in  $\text{N}_2$ , that is just reached at E4. This indicates that  $\text{N}_2$  gas acts as an inhibitor for HER on these surfaces. At this potential, a larger semicircle is observed for these two surfaces, meaning a higher adsorption of species  $\text{N}_2$  environment as also demonstrated by larger double layer capacitance [48] ( $2.0 \times 10^{-4}$  and  $5.9 \times 10^{-4} \mu\text{F cm}^{-2}$  in  $\text{N}_2$  vs.  $8.4 \times 10^{-5}$  and  $5.4 \times 10^{-6} \mu\text{F cm}^{-2}$  in Ar for NbON#1 and NbON#2, respectively).

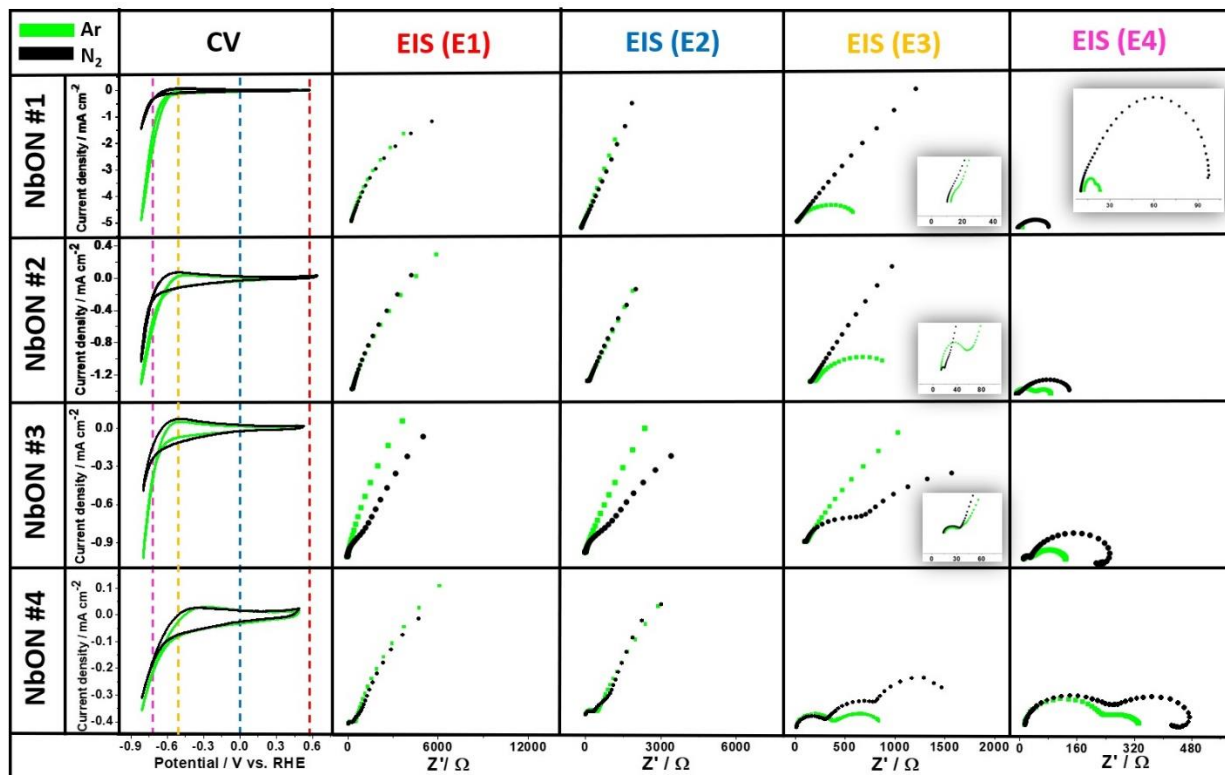


Figure 3. Cyclic voltammetry (CV) and electrochemical impedance spectroscopy (EIS) study of all surfaces in Ar (green) and N<sub>2</sub> (black) gas. E1, E2, E3, and E4 in the Nyquist plots are equivalent to open circuit potential (case sensitive), 0 V, -0.5 V, and -0.7 V vs. RHE, respectively. All Nyquist plots are plotted on square axes. The y axes of these plots ( $Z''/\Omega$ ) are not displayed to make the figure less crowded.

When the N+O stoichiometry increases from 1.22 and 1.28 in NbON#1 and NbON#2 to 1.43 and 1.52 in NbON#3 and NbON#4 which is closer to the rutile structure (NbO<sub>2</sub>), a third charge transfer resistance is observed in the Nyquist plots collected in N<sub>2</sub> environment, which is absent in Ar. This is demonstrated at potentials E1-E3 (Figure 3). The presence of the third charge transfer at E1 and E2 is best seen in the Bode plot and phase shift diagram (Figures S6 and S7 in the SI). We attribute this to an additional reaction that is dependent upon the presence of N<sub>2</sub> which leads to a change in the reduction process. For NbON#3 at potentials E1 and E2 lower impedance is observed in the N<sub>2</sub> environment, while NbON#4 demonstrates a similar impedance in both N<sub>2</sub> and Ar, despite the difference caused by the third charge transfer.

An important observation out of these plots is that at E3 for all the surfaces, the first charge transfer ( $R_{ct}$ ) that occurs at high frequency ranges ( $10^2 - 10^5$  Hz) and results in low impedance values (real component as shown in the x-axis which is denoted as  $R_{ct2}$  values in Tables S1 and S2) overlaps in most cases (Except for NbON#2) in Ar and N<sub>2</sub> media. We suggest this to be a result of the generation of vacancies from the reduction of oxides in the structure, which is well-known to have a favorable kinetics at these potential ranges [49,50]. This is further justified by the XPS analysis of the films after electrochemical experiments

(Figure S13 and Table S5). In all cases except for NbON#2, the stoichiometries of O in the bulk of the films are decreased after experiments compared to their initial states. The study of oxide reduction is not within the scope of this paper and is therefore not further addressed. No diffusion component (Warburg element) is observed in any surface, which is an indication of the negligible effect of mass transport from the surface to the bulk of the solution and conveys that the adsorption of species takes place. This effect is further enhanced in the N<sub>2</sub> environment at E4 for NbON#3 and NbON#4, where an inductor is formed. This effect is not observed in Ar environment. According to Bai et al., inductive behavior appears at faradaic potentials in systems containing at least one adsorbed intermediate when the surface coverage of the intermediate decreases with increased potential [51]. Based on this fact, the inductive behavior at E4 in NbON#3 and NbON#4 is attributed to the initial coverage of surface by N species followed by subsequent release of ammonia product. HER in both cases of Ar(g) and N<sub>2</sub>(g) in alkaline media takes place by the adsorption of water molecules, leading to water reduction (HER, 2H<sub>2</sub>O + 2e<sup>-</sup> → H<sub>2</sub> + 2OH<sup>-</sup>).

Bode plots (Figure S6) present the stark difference in Ar vs. N<sub>2</sub> media for each surface at E3 and E4, and a total impedance ( $|Z|$ ) in the same order of magnitude at E1 and E2. Furthermore, the phase shift diagram (Figure S7) clearly shows the existence of an electrical double layer, which is accounted for in the equivalent circuit as a capacitor in parallel with a resistor. We consider the Double Layer Capacitor (Cdl) component as a Constant Phase Element (CPE) in the model circuit.

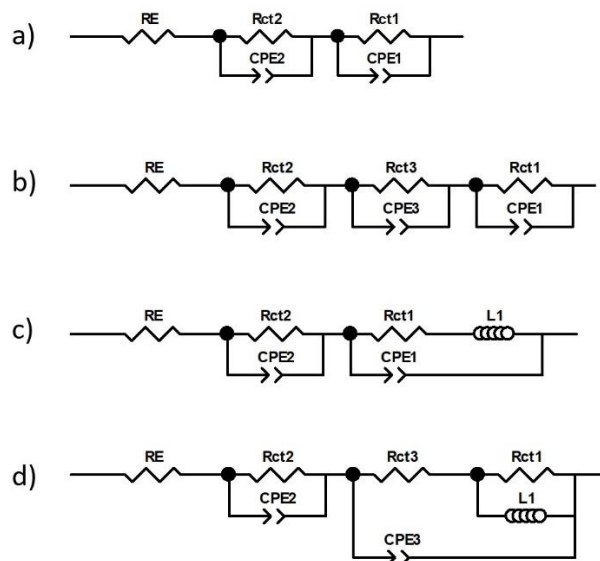


Figure 4. Models used for NbON systems; a) NbON#1 and NbON#2 in N<sub>2</sub> and Ar; NbON#3 and NbON#4 in Ar b) NbON#3 and NbON#4 in N<sub>2</sub> at E1-E3, c) NbON#4 in N<sub>2</sub> at E4; and d) NbON#3 in N<sub>2</sub> at E4

Figure 4 demonstrates the circuits that were used to describe the DEIS data. Based on the observations from the Nyquist (Figure 3) and Bode plots (Figure S6), all the curves were both fitted to two charge transfer/ constant phase elements (R<sub>ct</sub>/CPE) as well as three R<sub>ct</sub>/CPE for comparison. It was observed that the two (R<sub>ct</sub>/CPE) was the best fit for all the

Ar data. This circuit was also the best representative model for the surfaces with higher N/O ratios (NbON#1 and NbON#2) in N<sub>2</sub> media. For the other two surfaces in the series (NbON#3 and NbON#4), the three (R<sub>ct</sub>/CPE) in the model resulted in better fits (lower  $\chi^2$  value) in N<sub>2</sub> media. Adding an inductor to the model for NbON#3 and NbON#4 in N<sub>2</sub> environment at E4, also resulted in more accuracy in the fitting. As mentioned earlier this inductive behavior is only observed on these two surfaces in N<sub>2</sub>(g) at E4 which is attributed to a reduced coverage of adsorbed N intermediate at this potential.

### 3.3. Catalysis study and ammonia quantification

Figure 5 shows the total ammonia reaction rate and current efficiency measured from electrocatalysis studies using our in-line quantification as described in section 2.3. The data is also presented in Tables S3 and S4. For the catalysis, selected chronoamperometry loops are carried out at (A) a potential close to OCP to allow the access of N<sub>2</sub> to the surface and facilitate the replenishment of the vacancies and NH<sub>3</sub> desorption, and (B) a potential close to the OP for catalysis. The reader is referred to the SI, Figure S8 and Section 3, for an example of potential vs. time and current density vs. time graphs in a chronoamperometry loop and details of the reaction rate and current efficiency calculations, respectively. Generally, reaction rates are not high in this system for any of the surfaces under study compared to systems where high surface area catalysts with nanostructures are incorporated. In the case of thin film catalysts, the physical and electrochemical active surface area are closely the same, and we correlate directly with surface area but not catalyst mass.

The study reveals more ammonia production in Ar vs. N<sub>2</sub> in NbON#1 and NbON#2 at most of the potential combinations. We attribute this to surface instability, a circumstance that may be prevented or decelerated through N<sub>2</sub> adsorption when there is sufficient access to this gas in the media. Moving on to the higher N+O stoichiometries, in all cases, considerably lower reaction rates are observed from NbON#3 compared to NbON#4. However, NbON#4 demonstrates significantly greater ammonia production rates in N<sub>2</sub> media compared to that in Ar at A = OCP and OCP+0.2 V, and B = -0.2 V and -0.4 V.

For NbON#1, potential at B = -0.2 V, changing A does not drastically change the production rate in N<sub>2</sub> media. This is not the case at B = -0.4 V and -0.6 V where reaction rate substantially increases when going from A = OCP to OCP+0.2 V. For NbON#2, at B = -0.2 V, reaction rate in N<sub>2</sub> is increased when moving from A = OCP to OCP+0.2V and further to OCP+0.4V. For NbON#1 and NbON#2 however, at a fixed value of A, increasing the negative potential reduces the reaction rate in N<sub>2</sub>(g) environment. Increasing the negative potential at fixed A in Ar(g) media, does not yield a general trend for the reaction rate. It is clear however that at A = OCP+ 0.2 V, most nitrogen is leached from NbON#1 and NbON#2 in the form of NH<sub>3</sub>. Only at A = OCP + 0.4 V and B = -0.2 V does NbON#2 show a higher reaction rate in N<sub>2</sub> compared to that in Ar.

In NbON#3, the reaction rate does not follow a pattern as a function of the applied potentials, neither in N<sub>2</sub> nor in Ar. It is furthermore evident that the reaction rates are quite low in both media. At B = -0.4 V the lowest ammonia production rate is observed. This surface composition appears to completely quench the leaching of surface nitride.

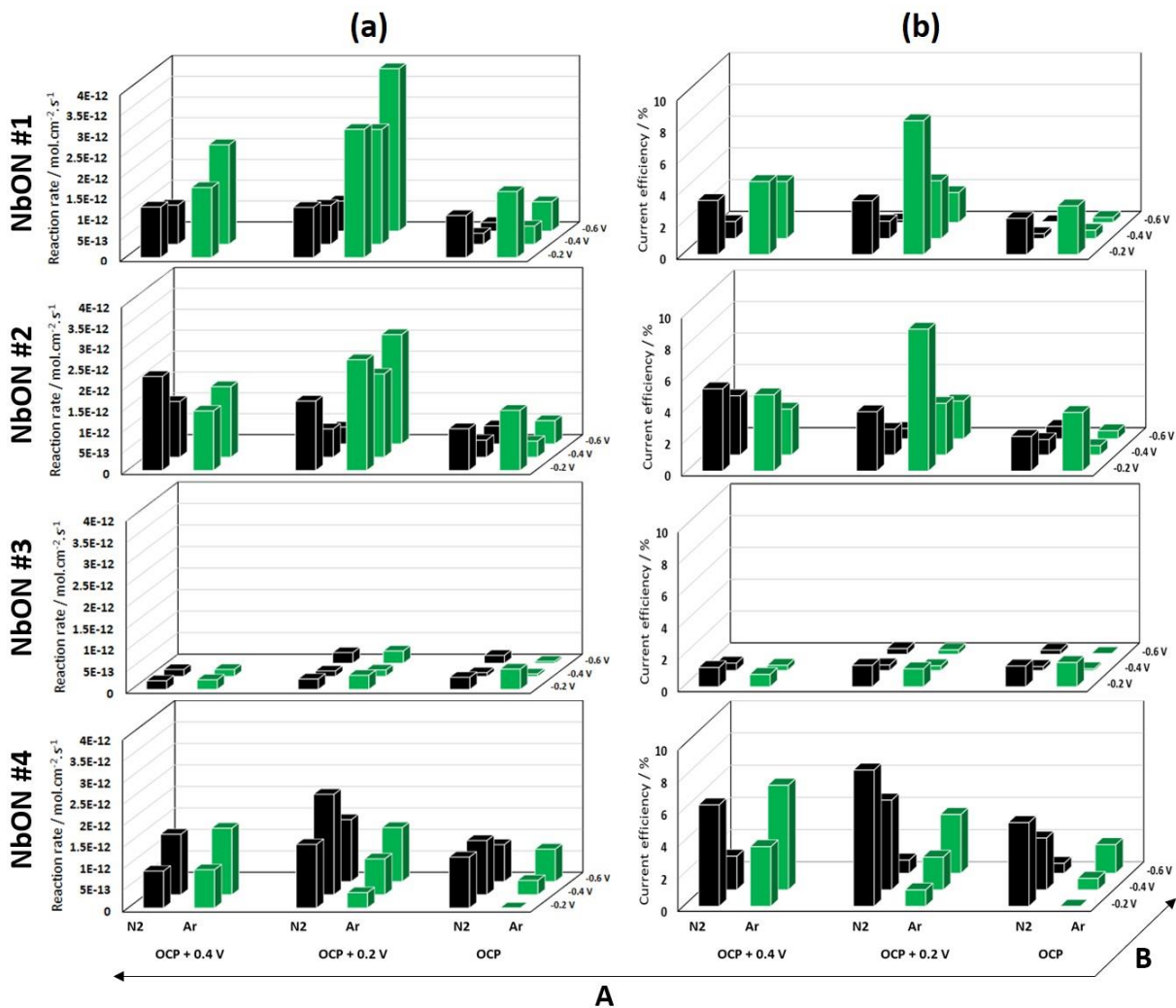


Figure 5. Comparison of (a) reaction rate and (b) current efficiency in Ar (green) and  $N_2$  (black) environments. Chronoamperometry was done in a loop for 10 s at a positive potential (A) and 10 s at a negative potential (B). The loop was repeated long enough to get three consecutive ammonia measurements at each potential combination. Standard deviations of three measurements at each potential combination are provided in Tables S3 and S4.

For NbON#4, the same N/O ratio is kept as for NbON#3 but the stoichiometry N+O vs Nb is increased. This is the only surface that repeatedly produces ammonia to a greater extent in  $N_2$  than in Ar environment. In  $N_2$ , A = OCP+0.2V and B = -0.4 V yields the highest reaction rate in the chronoamperometry loop combinations. In Ar, the reaction rate increases with more negative B, and with more positive A. It is only at B = OCP + 0.4 V when Ar starts to show comparable and even higher reaction rates compared to that in  $N_2$ .

Current efficiency for NbON#1, NbON#2, and NbON#3 decreases when moving to more negative B potentials both in Ar and  $N_2$ . In most of the potential combinations higher current efficiency is observed in Ar rather than in  $N_2$  medium. We conclude that all the ammonia produced

from those surfaces is produced through surface nitride leaching. The evident decrease of leaching when comparing NbON#1 and NbON#2 with NbON#3 can be attributed to the increased stability of the surface with higher N+O stoichiometry, which is closer to the rutile stoichiometry of NbO<sub>2</sub>. In the case of NbON#4, ammonia production is observed with an opposite trend compared to the other three surfaces, the efficiency increases as more negative potentials are applied, suggesting a new mechanism. The observed trend in Ar environment for NbON#4 when compared with the other three surfaces demonstrates an increased surface stability, and that for NbON#4, surface bound nitride is significantly less leached at less negative potentials. The trend of decreasing current efficiencies is visible when more negative potentials are applied in N<sub>2</sub> environment, suggesting a competition between NRR and HER. This is further elaborated in section 3.4.

Overall, from Figure 5 it is clear that the two chronoamperometry loops of A = OCP+0.2V and B = -0.2 V on one hand, and A = OCP+0.2V and B = -0.4 V on the other demonstrate the highest current efficiency and reaction rate for NbON#4 ( $1.5 \times 10^{-12} \pm 7.9 \times 10^{-14}$  mol cm<sup>-2</sup> s<sup>-1</sup>,  $8.47 \pm 0.45$  % and  $2.3 \times 10^{-12} \pm 3.5 \times 10^{-13}$  mol cm<sup>-2</sup> s<sup>-1</sup>,  $5.57 \pm 0.82$  %, respectively). For these potentials the greatest difference is also observed for NH<sub>3</sub> production between N<sub>2</sub> and Ar environment, in favor of N<sub>2</sub>.

Isotope labeling experiment, using <sup>15</sup>N<sub>2</sub> reactant gas, was carried out on NbON#4 by conducting chronoamperometry loops at potential combinations of -0.2 V / OCP + 0.2 V, and -0.4 V / OCP + 0.2 V. No <sup>15</sup>NH<sub>3</sub> ammonia was detected, and the conclusion is that within experimental error, no electrocatalysis was observed. The produced ammonia is thus fully attributed to nitrogen leaching from the catalyst. The reader is referred to the SI, section 10, Figures S14 and S15, for the details of these experiments and the negative outcome.

### 3.4. The role of stoichiometries on ammonia synthesis mechanism

The N+O stoichiometry within NbON has a strong effect on the electrochemical reactions and charge transfers occurring at the surface. As discussed in section 3.2, within Figure 3, all surfaces show a sign of HER inhibition in N<sub>2</sub> environment where more negative OP is observed. However, from the lower to higher N+O stoichiometries, the surfaces move from only inhibiting the HER to inhibiting HER plus an added third charge transfer observed in DEIS when exposed to N<sub>2</sub>.

Nitrogen leaching of the NbON surfaces is further studied, by quantifying the ammonia released in N<sub>2</sub> containing electrolyte for an extended period at the OCP. As shown in Figure S4, a continuous release of ammonia is observed with no current involved, as the lattice bound nitride has the oxidation state of -3. By applying 0 V vs RHE, the ammonia release starts to decline and reaches a background level. We therefore suggest a decoupled MvK mechanism where the first ammonia is produced from protonation of the lattice bound N<sup>3-</sup> (i.e. surface nitride) without any electron transfer, following that, a nitrogen molecule is adsorbed and the first electron transfer step is the reduction of the adsorbed N≡N.

The proposed reaction steps are thus as follows: three protons are adsorbed to the lattice N (Eq. 1). Then, the first ammonia is desorbed, forming an N vacancy on the surface (Eq. 2). Nitrogen is next adsorbed on the N vacancy and reduced. The first N atom replenishes the vacancy while the second N atom sits on top of the surface (Eq. 3). Following this step, three protons are adsorbed to the surface N (Eq. 4). Finally, the second ammonia is desorbed, and surface is replenished (Eq. 5).



The overall cathode reaction is then:



At the anode we anticipate water to split according to alkaline environment:



Providing the overall cell reaction:



The competing reaction mechanism is the production of H<sub>2</sub> upon proton adsorption through the Volmer step. This can happen through the adsorption of a proton to one Nb site as in equation 9a, or the adsorption of a proton to a surface nitride (N) as in equation 9b, primarily following a Heyrovsky proton combination and desorption, as deduced from the EIS data. In either case, hydrogen is released according to equations 10a and 10b.



Hydrogen evolution reaction depends upon proton adsorption to the surface. The competing adsorption of N<sub>2</sub> to the surface (reaction 3) may therefore lower the surface proton coverage and slow down HER.

A reliable assessment of an electrocatalyst can only be based on the complete electrochemical dataset as collected in this work. From the NRR studies for ammonia production and the DEIS data we have demonstrated the following difference between the N+O stoichiometries in the NbON series. For NbON#1 and NbON#2, the higher ammonia production in Ar media is attributed to the inherent surface N atoms leaching out of the structure as the only source of ammonia. Here we propose that nitrogen adsorption may inhibit the nitrogen leaching and slow down HER. This is reflected in lower current and later OP observed for HER, the higher charge transfer resistance and a higher double layer capacitance in N<sub>2</sub> vs. Ar environment (Figure 3). The surfaces are however too unstable to be considered catalysts. This is clearly observed from change of CV throughout the experiments (Figure S9). The XRD measurements of the surfaces

after electrochemical experiments (see Figure S11 in the SI) do not show a drastic change in crystal structure compared to their pristine forms. However, the XRR analysis of used surfaces (Figure S12) shows a significant increase in surface roughness which prevents the evaluation of layer thicknesses and density profiles. Furthermore, XPS measurements of the films after electrochemical experiments in  $N_2(g)$  (Figure S13) reveal different profiles compared to the pristine films. Table S5 provides the stoichiometries of the pristine and used films in the bulk and the top layer of the surface. Bulk and top stoichiometries are considered as the average of atom concentrations from 4 – 16 min and from 2 – 4 min of sputtering time, respectively. All catalyst films develop more oxygen into their composition in the top layer compared to their pristine state while either maintaining the nitrogen composition in cases of NbON#1 and NbON#2 or increasing the nitrogen composition in cases of NbON#3 and NbON#4. In this sense, used NbON#4 is the only surface with a top layer non-metal stoichiometry ( $x+y = 1.98$ ) closest to a perfect rutile structure of  $NbO_2$ . We attribute this to immediate oxidation of vacant sites when exposed to air after electrochemical studies. The bulk composition, on the other hand, shows an increase in nitrogen stoichiometry for all the films with the most significant increase being that of NbON#4. Oxygen stoichiometry in bulk decreases in all cases except for NbON#2 and again the most pronounced decrease is that of NbON#4. This decrease in oxygen stoichiometry is attributed to lattice oxide reduction under experimental overpotentials. The vacancies left from this step seem to be refilled with N. As we have observed significant changes in electrochemical behavior between  $NbO_xN_y$  thin films, such a change in chemical composition during electrocatalysis may result in a severe change in the catalytic efficiency.

As the N content decreases and N+O stoichiometries increase in the series of films, the surface stability increases. NbON#3 demonstrates the least activity towards ammonia production, but at the same time, we observe that this production is not the result of  $N_2$  reduction (Figure 5). This surface still demonstrates three charge transfers in  $N_2$  while only two in Ar (Figure 3), indicating that this surface may facilitate NRR.

Moving to the highest N+O stoichiometries, while maintaining a similar N/O proportion, NbON#4 demonstrates higher reaction rates for ammonia production in  $N_2$  compared to Ar. This surface has a more pronounced third charge transfer in  $N_2$  environment, but not in Ar as demonstrated in the DEIS data. Furthermore, NbON#4 has the highest reaction rate and current efficiency in  $N_2$  environment, when compared with all the other surfaces.

We suggest three different electrochemical reactions facilitated by charge transfers within this system 1) NRR (reaction 3), 2) HER (reactions 9 and 10), and 3) oxide reduction from lattice oxide. In  $Ar(g)$  environment we can anticipate observing charge transfer for HER (2) and ORR (3), but charge transfer (1) can only be observed in  $N_2$  environment that allows for  $N_2$  adsorption and reduction thereof. The protonation of surface N does not involve an electron transfer, but a combination of charged species, and can therefore be available at OCP. The negative reduction potentials are however needed for reducing the nitrogen molecule upon adsorption and prepare it for further protonation (Eq. 3).

NbON#3 and NbON#4 are therefore likely to undergo similar reaction pathway but with different impedances. The presence of the third charge transfer is observed with decreasing N/O ratio, and its physical parameters appear to depend upon the N+O stoichiometry. The stoichiometry, furthermore, is an important factor for the surface stability. The combination of increased N+O stoichiometry and decreased N/O ratio (while still maintaining some N) appears to be a two-dimensional optimization path that is needed for a stable NbON catalyst for nitrogen

reduction. The electrochemical environment is a third but no less important factor. A faster removal of surface N for  $\text{NH}_3$  production (reaction 1) than adsorption and reduction of  $\text{N}_2$  (reaction 3) can result in the surface N/O ratio falling, drastically increasing the surface impedance, and therefore changing its electrochemical behavior. The reaction rate and current efficiency of the catalysis therefore comes to a sudden halt.

#### 4. Conclusions

In this study we explore whether niobium oxynitrides are catalytically active, selective, and stable towards electrochemical reduction of dinitrogen to ammonia in an aqueous electrolyte at ambient conditions. We utilize several electrochemical approaches to understand the underlying mechanism for NRR. These include cyclic voltammetry and electrochemical impedance spectroscopy together with chronoamperometry measurements combined with an accurate ammonia quantification in  $\text{N}_2$  and Ar media. Thin films of rutile  $\text{NbO}_x\text{N}_y$  were synthesized with different  $x+y$  stoichiometries and the effects of the stoichiometric ratios on the NRR performance were investigated. The impedance spectroscopy shows significant differences and signs of catalytic ammonia formation with the initiation of an  $\text{N}_2$  dependent charge transfer as  $x+y$  stoichiometries increase from 1.22 in  $\text{NbO}_{0.80}\text{N}_{0.42}$  to 1.52 in  $\text{NbO}_{1.28}\text{N}_{0.24}$ . Furthermore,  $\text{NbO}_{1.28}\text{N}_{0.24}$  demonstrates higher ammonia production rate and current efficiency in  $\text{N}_2$  vs. Ar. Therefore, our results have shown the effect of stoichiometric ratios of  $y/x$  and  $x+y$  in the  $\text{NbO}_x\text{N}_y$  catalyst on the nitrogen reduction reaction. Despite these promising results,  $^{15}\text{N}_2$  isotope labeling demonstrates that the catalyst system is not stable enough to maintain ammonia production throughout the experiment to produce sufficient quantities of  $^{15}\text{NH}_3$  for detection, as determined by detection of only  $^{14}\text{NH}_3$  with GC-MS while supplying  $^{15}\text{N}_2$  to the reactor as feed gas. We attribute this to low reaction rates and lack of surface stability, resulting in higher concentrations of  $^{14}\text{NH}_3$  ( $^{14}\text{N}$  derived from surface, the first steps of the MvK mechanism) but too low proportion of  $^{15}\text{NH}_3/^{14}\text{NH}_3$  for detection. This can be a result of insufficient access of  $\text{N}_2(\text{g})$  to the electrode, slowing down the refurbishment of surface vacancies for continued catalysis. The results, however, provide guidelines for further research regarding surface engineering. Stability of the catalyst and the electrochemical reaction environment can be improved via various routes that are currently being studied in our research group. This study, moreover, demonstrates that following strict experimental protocols is essential to prevent the report of misleading results and false positives.

#### Acknowledgements

The authors would like to acknowledge the Icelandic Research Fund (grants 152619-051, 185404-051 and 196437-051), the Icelandic Technology Development Fund (grant 175350-0611) and the Research Fund of the University of Iceland for the financial support of this work.

The authors acknowledge Dr. Guðjón A. Auðunsson and Dr. Kristmann Gíslason, project managers at the Innovation Centre Iceland, for their valuable input for SIA and GC-MS method optimization. The authors would also like to thank Dr. Anna Bergljót Gunnarsdóttir, post-doctoral researcher at the University of Iceland, for helpful discussions and comments over the manuscript.

## Data availability

The data that support the findings of this study are available upon a reasonable request from the corresponding author.

## References

- [1] C. Smith, A.K. Hill, L. Torrente-Murciano, Current and future role of Haber–Bosch ammonia in a carbon-free energy landscape, *Energy Environ. Sci.* 13 (2020), 331–344. <https://doi.org/10.1039/C9EE02873K>.
- [2] B.M. Ceballos, G. Pilania, K.P. Ramaiyan, A. Banerjee, C. Kreller, R. Mukundan, Roads Less Traveled: Nitrogen Reduction Reaction (NRR) Catalyst Design Strategies for Improved Selectivity, *Curr. Opin. Electrochem.* (2021) 100723. <https://doi.org/10.1016/j.coelec.2021.100723>.
- [3] B.M. Comer, P. Fuentes, C.O. Dimkpa, Y.H. Liu, C.A. Fernandez, P. Arora, M. Realff, U. Singh, M.C. Hazell, A.J. Medford, Prospects and challenges for solar fertilizers, *Joule*, 3 (2019), 1578–1605. <https://doi.org/10.1016/j.joule.2019.05.001>.
- [4] Z. Wang, X. Hu, Z. Liu, G. Zou, G. Wang, K. Zhang, Recent developments in polymeric carbon nitride-derived photocatalysts and electrocatalysts for nitrogen fixation, *ACS Catal.* 9 (2019), 10260–10278. <https://doi.org/10.1021/acscatal.9b03015>.
- [5] K. Ithisuphalap, H. Zhang, L. Guo, Q. Yang, H. Yang, G. Wu, Photocatalysis and photoelectrocatalysis methods of nitrogen reduction for sustainable ammonia synthesis, *Small Methods* 3 (2019), 1800352. <https://doi.org/10.1002/smtd.201800352>.
- [6] B.S. Patil, Q. Wang, V. Hessel, J. Lang, Plasma N<sub>2</sub>-fixation: 1900–2014, *Catal. Today* 256 (2015), 49–66. <https://doi.org/10.1016/j.cattod.2015.05.005>.
- [7] J. Hong, S. Praver, A.B. Murphy, Plasma catalysis as an alternative route for ammonia production: status, mechanisms, and prospects for progress, *ACS Sustain. Chem. Eng.* 6 (2018) 15–31. <https://doi.org/10.1021/acssuschemeng.7b02381>.
- [8] M.B. Yaala, A. Saeedi, D.F. Scherrer, L. Moser, R. Steiner, M. Zutter, M. Oberkofler, G.D. Temmerman, L. Marot, E. Meyer, Plasma-assisted catalytic formation of ammonia in N<sub>2</sub>–H<sub>2</sub> plasma on a tungsten surface, *Phys. Chem. Chem. Phys.* 21 (2019), 16623–16633. <https://doi.org/10.1039/C9CP01139K>.
- [9] R. Hawtof, S. Ghosh, E. Guarr, C. Xu, R.M. Sankaran, J.N. Renner, 2019. Catalyst-free, highly selective synthesis of ammonia from nitrogen and water by a plasma electrolytic system. *Sci. adv.* 5, eaat5778. <https://doi.org/10.1126/sciadv.aat5778>.
- [10] K.C. MacLeod, P.L. Holland, Recent developments in the homogeneous reduction of dinitrogen by molybdenum and iron, *Nat. Chem.* 5 (2013) 559–565. <https://doi.org/10.1038/nchem.1620>.

- [11] H.P. Jia, E.A. Quadrelli, Mechanistic aspects of dinitrogen cleavage and hydrogenation to produce ammonia in catalysis and organometallic chemistry: relevance of metal hydride bonds and dihydrogen, *Chem. Soc. Rev.* 43 (2014) 547-564. <https://doi.org/10.1039/C3CS60206K>.
- [12] J.M. McEnaney, A.R. Singh, J.A. Schwalbe, J. Kibsgaard, J.C. Lin, M. Cargnello, T.F. Jaramillo, J.K. Nørskov, Ammonia synthesis from N<sub>2</sub> and H<sub>2</sub>O using a lithium cycling electrification strategy at atmospheric pressure, *Energy Environ. Sci.* 10 (2017) 1621-1630. <https://doi.org/10.1039/C7EE01126A>.
- [13] B. Yang, W. Ding, H. Zhang, S. Zhang, Recent progress in electrochemical synthesis of ammonia from nitrogen: strategies to improve the catalytic activity and selectivity, *Energy Environ. Sci.* 14 (2021), 672-687. <https://doi.org/10.1039/D0EE02263B>.
- [14] Z. Qiao, D. Johnson, A. Djire, Challenges and opportunities for nitrogen reduction to ammonia on transitional metal nitrides via Mars-van Krevelen mechanism, *Cell Rep. Phys. Sci.* 2 (2021), 100438. <https://doi.org/10.1016/j.xcrp.2021.100438>.
- [15] Y. Abghoui, A.L. Garden, V.F. Hlynsson, S. Björgvinsdóttir, H. Ólafsdóttir, E. Skúlason, Enabling electrochemical reduction of nitrogen to ammonia at ambient conditions through rational catalyst design, *Phys. Chem. Chem. Phys.*, 17 (2015) 4909-4918. <https://doi.org/10.1039/C4CP04838E>.
- [16] Y. Abghoui, A.L. Garden, J.G. Howalt, T. Vegge, E. Skúlason, Electroreduction of N<sub>2</sub> to ammonia at ambient conditions on mononitrides of Zr, Nb, Cr, and V: A DFT guide for experiments, *ACS Catal.* 6 (2016) 635-646. <https://doi.org/10.1021/acscatal.5b01918>.
- [17] Y. Abghoui, E. Skúlason, Computational predictions of catalytic activity of zincblende (110) surfaces of metal nitrides for electrochemical ammonia synthesis, *J. Phys. Chem. C.* 121 (2017) 6141-6151. <https://doi.org/10.1021/acs.jpcc.7b00196>.
- [18] Y. Abghoui, E. Skúlason, Onset potentials for different reaction mechanisms of nitrogen activation to ammonia on transition metal nitride electro-catalysts, *Catal. Today.* 286 (2017) 69-77. <https://doi.org/10.1016/j.cattod.2016.11.047>.
- [19] M. Gudmundsson, V. Ellingsson, E. Skúlason, Y. Abghoui, Optimizing Nitrogen Reduction Reaction on Nitrides: A Computational Study on Crystallographic Orientation, *Top. Catal.* (2021) 1-10. <https://doi.org/10.1007/s11244-021-01485-2>.
- [20] A.B. Höskuldsson, Y. Abghoui, A.B. Gunnarsdóttir, E. Skúlason, Computational screening of rutile oxides for electrochemical ammonia formation, *ACS Sustain. Chem. Eng.* 5 (2017) 10327-10333. <https://doi.org/10.1021/acssuschemeng.7b02379>.
- [21] S.L. Foster, S.I.P. Bakovic, R.D. Duda, S. Maheshwari, R.D. Milton, S.D. Minter, M.J. Janik, J.N. Renner, L.F. Greenlee, Catalysts for nitrogen reduction to ammonia, *Nat. Catal.* 1 (2018) 490-500. <https://doi.org/10.1038/s41929-018-0092-7>.
- [22] G.F. Chen, S. Ren, L. Zhang, H. Cheng, Y. Luo, K. Zhu, L. Ding, H. Wang, Advances in electrocatalytic N<sub>2</sub> reduction—strategies to tackle the selectivity challenge, *Small Methods*, 3 (2019) 1800337. <https://doi.org/10.1002/smt.201800337>.
- [23] C. Tang, S.Z. Qiao, How to explore ambient electrocatalytic nitrogen reduction reliably and insightfully, *Chem. Soc. Rev.* 48 (2019) 3166-3180. <https://doi.org/10.1039/C9CS00280D>.

- [24] B.H. Suryanto, H.L. Du, D. Wang, J. Chen, A.N. Simonov, D.R. MacFarlane, Challenges and prospects in the catalysis of electroreduction of nitrogen to ammonia, *Nat. Catal.* 2 (2019) 290-296. <https://doi.org/10.1038/s41929-019-0252-4>.
- [25] J. Choi, B.H. Suryanto, D. Wang, H.L. Du, R.Y. Hodgetts, F.M.F. Vallana, D.R. MacFarlane, A.N. Simonov, Identification and elimination of false positives in electrochemical nitrogen reduction studies, *Nat. Commun.* 11 (2020) 1-10. <https://doi.org/10.1038/s41467-020-19130-z>.
- [26] S.Z. Andersen, V. Čolić, S. Yang, J.A. Schwalbe, A.C. Nielander, J.M. McEnaney, K. Enemark-Rasmussen, J.G. Baker, A.R. Singh, B.A. Rohr, M.J. Statt, S.J. Blair, S. Mezzavilla, J. Kibsgaard, P.C.K. Vesborg, M. Cargnello, S.F. Bent, T.F. Jaramillo, I.E.L. Stephens, J.K. Nørskov, I. Chorkendorff, A rigorous electrochemical ammonia synthesis protocol with quantitative isotope measurements, *Nature* 570 (2019) 504-508. <https://doi.org/10.1038/s41586-019-1260-x>.
- [27] R. Dabundo, M.F. Lehmann, L. Treibergs, C.R. Tobias, M.A. Altabet, P.H. Moisaner, J. Granger, The contamination of commercial  $^{15}\text{N}_2$  gas stocks with  $^{15}\text{N}$ -labeled nitrate and ammonium and consequences for nitrogen fixation measurements, *PloS one.* 9 (2014) e110335. <https://doi.org/10.1371/journal.pone.0110335>.
- [28] J. Choi, H.L. Du, C.K. Nguyen, B.H. Suryanto, A.N. Simonov, D.R. MacFarlane, Electroreduction of nitrates, nitrites, and gaseous nitrogen oxides: A potential source of ammonia in dinitrogen reduction studies, *ACS Energy Lett.* 5 (2020) 2095-2097. <https://doi.org/10.1021/acseenergylett.0c00924>.
- [29] F. Hanifpour, A. Sveinbjörnsson, C.P. Canales, E. Skúlason, H.D. Flosadóttir, Preparation of Nafion membranes for reproducible ammonia quantification in nitrogen reduction reaction experiments, *Angew. Chem.* 132 (2020) 23138-23142. <https://doi.org/10.1002/ange.202007998>.
- [30] H.L. Du, T.R. Gengenbach, R. Hodgetts, D.R. MacFarlane, A.N. Simonov, Critical assessment of the electrocatalytic activity of vanadium and niobium nitrides toward dinitrogen reduction to ammonia, *ACS Sustain. Chem. Eng.* 7 (2019) 6839-6850. <https://doi.org/10.1021/acssuschemeng.8b06163>.
- [31] J. Han, Z. Liu, Y. Ma, G. Cui, F. Xie, F. Wang, Y. Wu, S. Gao, Y. Xu, X. Sun, Ambient  $\text{N}_2$  fixation to  $\text{NH}_3$  at ambient conditions: Using  $\text{Nb}_2\text{O}_5$  nanofiber as a high-performance electrocatalyst, *Nano Energy*, 52 (2018) 264-270. <https://doi.org/10.1016/j.nanoen.2018.07.045>.
- [32] L. Huang, J. Wu, P. Han, A.M. Al-Enizi, T.M. Almutairi, L. Zhang, G. Zheng,  $\text{NbO}_2$  electrocatalyst toward 32% Faradaic efficiency for  $\text{N}_2$  fixation, *Small Methods*, 3 (2019) 1800386. <https://doi.org/10.1002/smt.201800386>.
- [33] W. Kong, Z. Liu, J. Han, L. Xia, Y. Wang, Q. Liu, X. Shi, Y. Wu, Y. Xu, X. Sun, Ambient electrochemical  $\text{N}_2$ -to- $\text{NH}_3$  fixation enabled by  $\text{Nb}_2\text{O}_5$  nanowire array, *Inorg. Chem. Front.* 6 (2019) 423-427. <https://doi.org/10.1039/C8QI01049H>.
- [34] X. Hu, Y. Sun, S. Guo, J. Sun, Y. Fu, S. Chen, S. Zhang, J. Zhu, Identifying electrocatalytic activity and mechanism of  $\text{Ce}_{1/3}\text{NbO}_3$  perovskite for nitrogen reduction to ammonia at ambient conditions, *Appl. Catal. B Environ.* 280 (2021) 119419. <https://doi.org/10.1016/j.apcatb.2020.119419>.

- [35] X. Yang, J. Nash, J. Anibal, M. Dunwell, S. Kattel, E. Stavitski, K. Attenkofer, J.G. Chen, Y. Yan, B. Xu, Mechanistic insights into electrochemical nitrogen reduction reaction on vanadium nitride nanoparticles, *J. Am. Chem. Soc.* 140 (2018) 13387-13391. <https://doi.org/10.1021/jacs.8b08379>.
- [36] Y. Yao, Q. Feng, S. Zhu, J. Li, Y. Yao, Y. Wang, Q. Wang, M. Gu, H. Wang, H. Li, X. Yuan, M. Shao, Chromium oxynitride electrocatalysts for electrochemical synthesis of ammonia under ambient conditions, *Small Methods*, 3 (2019) 1800324. <https://doi.org/10.1002/smt.201800324>.
- [37] S. Kang, J. Wang, S. Zhang, C. Zhao, G. Wang, W. Cai, H. Zhang, Plasma-etching enhanced titanium oxynitride active phase with high oxygen content for ambient electrosynthesis of ammonia, *Electrochem. Commun.* 100 (2019) 90-95. <https://doi.org/10.1016/j.elecom.2019.01.028>.
- [38] J. Pan, H.A. Hansen, T. Vegge, Vanadium oxynitrides as stable catalysts for electrochemical reduction of nitrogen to ammonia: the role of oxygen, *J. Mater. Chem. A*. 8 (2020) 24098-24107. <https://doi.org/10.1039/D0TA08313E>.
- [39] T. Wu, M. Han, X. Zhu, G. Wang, Y. Zhang, H. Zhang, H. Zhao, Experimental and theoretical understanding on electrochemical activation and inactivation processes of Nb<sub>3</sub>O<sub>7</sub>(OH) for ambient electrosynthesis of NH<sub>3</sub>, *J. Mat. Chem. A*. 7 (2019) 16969-16978. <https://doi.org/10.1039/C9TA05155D>.
- [40] B. Chang, L. Deng, S. Wang, D. Shi, Z. Ai, H. Jiang, Y. Shao, L. Zhang, J. Shen, Y. Wu, X. Hao, A vanadium–nickel oxynitride layer for enhanced electrocatalytic nitrogen fixation in neutral media, *J. Mater. Chem. A* 8 (2020), 91-96. <https://doi.org/10.1039/C9TA11378A>.
- [41] M. Björck, G. Andersson, GenX: An extensible X-ray reflectivity refinement program utilizing differential evolution, *J. Appl. Cryst.* 40 (2007) 1174-1178. <https://doi.org/10.1107/S0021889807045086>.
- [42] Scribner Associates Inc, Impedance / Gain Phase Graphing and Analysis Software (Version 3.5), Southern Pines, March 5, 2020.
- [43] K. W. Kimura, K. E. Fritz, J. Kim, J. Suntivich, H. D. Abruña, T. Hanrath, Controlled selectivity of CO<sub>2</sub> reduction on copper by pulsing the electrochemical potential, *ChemSusChem*. 11 (2018) 1781-1786. <http://hvar.is/upload/4/SFX/sfx.gif>.
- [44] FIALab Instruments Inc. Gas Diffusion Ammonia Method (Water Based Samples) and Various Extracts. Seattle, 2013.
- [45] H. Kataoka, S. Ohrui, A. Kanemoto, M. Makita, Determination of ammonia as its benzenesulphonyldimethylaminomethylene derivative in environmental water samples by gas chromatography with flame photometric detection, *J. Chromatogr. A*. 633 (1993) 311-314. [https://doi.org/10.1016/0021-9673\(93\)83169-S](https://doi.org/10.1016/0021-9673(93)83169-S).
- [46] R.W.M. Kwok, XPS Peak Program (Version 4.0), November 2000.
- [47] J.F. Moulder, W.F. Stickle, P.E. Sobol, K.D. Bomben, Handbook of X-ray Photoelectron Spectroscopy, ed., J. Chastain and R.C.J. King, Minnesota, 1995.

- [48] W. Guo, X. Tan, J. Bi, L. Xu, D. Yang, C. Chen, Q. Zhu, J. Ma, A. Tayal, J. Ma, Y. Huang, X. Sun, S. Liu, B. Han, Atomic indium catalysts for switching CO<sub>2</sub> electroreduction products from formate to CO, *JACS*. 143 (2021) 6877-6885. <https://doi.org/10.1021/jacs.1c00151>.
- [49] Y. Shao, J. Wang, M. Engelhard, C. Wang, Y. Lin, Facile and controllable electrochemical reduction of graphene oxide and its applications, *J. Mat. Chem.* 20 (2010) 743-748. <https://doi.org/10.1039/B917975E>.
- [50] G.Z. Chen, D.L. Fray, T.W. Farthing, Direct electrochemical reduction of titanium dioxide to titanium in molten calcium chloride, *Nature* 407 (2000) 361-364. <https://doi.org/10.1038/35030069>.
- [51] L. Bai, B.E. Conway, AC Impedance of faradaic reactions involving electrosorbed intermediates: Examination of conditions leading to pseudoinductive behavior represented in three-dimensional impedance spectroscopy diagrams, *J. Electrochem. Soc.* 138 (1991) 2897. <https://doi.org/10.1149/1.2085336>.

## Supplementary Information

### Investigation into the mechanism of electrochemical nitrogen reduction reaction to ammonia using niobium oxynitride thin-film catalysts

Fatemeh Hanifpour<sup>a</sup>, Camila P. Canales<sup>a</sup>, Emil G. Fridriksson<sup>b</sup>, Arnar Sveinbjörnsson<sup>c</sup>, Tryggvi K. Tryggvason<sup>b</sup>, Erik Lewin<sup>d</sup>, Fridrik Magnus<sup>a,b</sup>, Árni S. Ingason<sup>b</sup>, Egill Skúlason<sup>\*a,c,e</sup>, and Helga D. Flosadóttir<sup>\*c,e</sup>

<sup>a.</sup> Science Institute, University of Iceland, VR-III, 107 Reykjavík, Iceland.

<sup>b.</sup> Grein Research ehf., Dunhagi 5, 107 Reykjavík, Iceland.

<sup>c.</sup> Atmonia ehf., Keldnaholt, 112 Reykjavík, Iceland.

<sup>d.</sup> Inorganic Research Programme, Department of Chemistry – Ångström Laboratory, Uppsala University, Box 538, SE-751 21 Uppsala, Sweden.

<sup>e.</sup> Faculty of Industrial Engineering, Mechanical Engineering and Computer Science, University of Iceland, VR-III, 107 Reykjavík, Iceland.

\* [helgadogg@atmonia.com](mailto:helgadogg@atmonia.com), [egillsk@hi.is](mailto:egillsk@hi.is)

#### 1- Materials for electrochemical experiments and product detection

The electrolyte used in all the experiments was 0.1 M potassium hydroxide (KOH, Merck, ≥85%) in ultrapure water (MilliQ®, Grade 1).

Sodium hydroxide (NaOH, Fluka, ≥98%), Sulfuric acid (H<sub>2</sub>SO<sub>4</sub>, Merck, 95-97%), ortho-phthalaldehyde (OPA, Sigma-Aldrich, ≥99%), ethanol (C<sub>2</sub>H<sub>6</sub>O, Riedel-de Haën, ≥99.8%), disodium tetra borate decahydrate (Na<sub>2</sub>B<sub>4</sub>O<sub>7</sub>·10H<sub>2</sub>O, Merck, 99.5%), sodium sulfite (Na<sub>2</sub>O<sub>3</sub>S, Sigma-Aldrich, 98-100%), and triton X-100 ((C<sub>2</sub>H<sub>4</sub>O)<sub>n</sub>C<sub>14</sub>H<sub>22</sub>O, Sigma-Aldrich) were required for ammonia determination and quantification.

Ammonium chloride (NH<sub>4</sub>Cl, Merck, 1000 mg/l NH<sub>4</sub> in H<sub>2</sub>O), hydrochloric acid (HCl, Fluka, ≥37%), benzenesulfonyl chloride (C<sub>6</sub>H<sub>5</sub>SO<sub>2</sub>Cl, Sigma-Aldrich, 99%), sodium carbonate (Na<sub>2</sub>CO<sub>3</sub>, Fluka, ≥99.5%), 1,4-Dioxan (C<sub>4</sub>H<sub>8</sub>O<sub>2</sub>, Merck, 99.5%), p-toluenesulfonamide (C<sub>7</sub>H<sub>9</sub>NO<sub>2</sub>S, Sigma-Aldrich, ≥99%), n-hexane (C<sub>6</sub>H<sub>14</sub>, Riedel-de Haën, ≥99%), diethyl ether (C<sub>4</sub>H<sub>10</sub>O, Riedel-de Haën, ≥99.8%), and ethyl acetate (C<sub>4</sub>H<sub>8</sub>O<sub>2</sub>, Riedel-de Haën, ≥99.7%) were the chemicals used for ammonia derivatization.

## 2- Micro-reactor flow-cell and sequential injection analyzer (SIA)

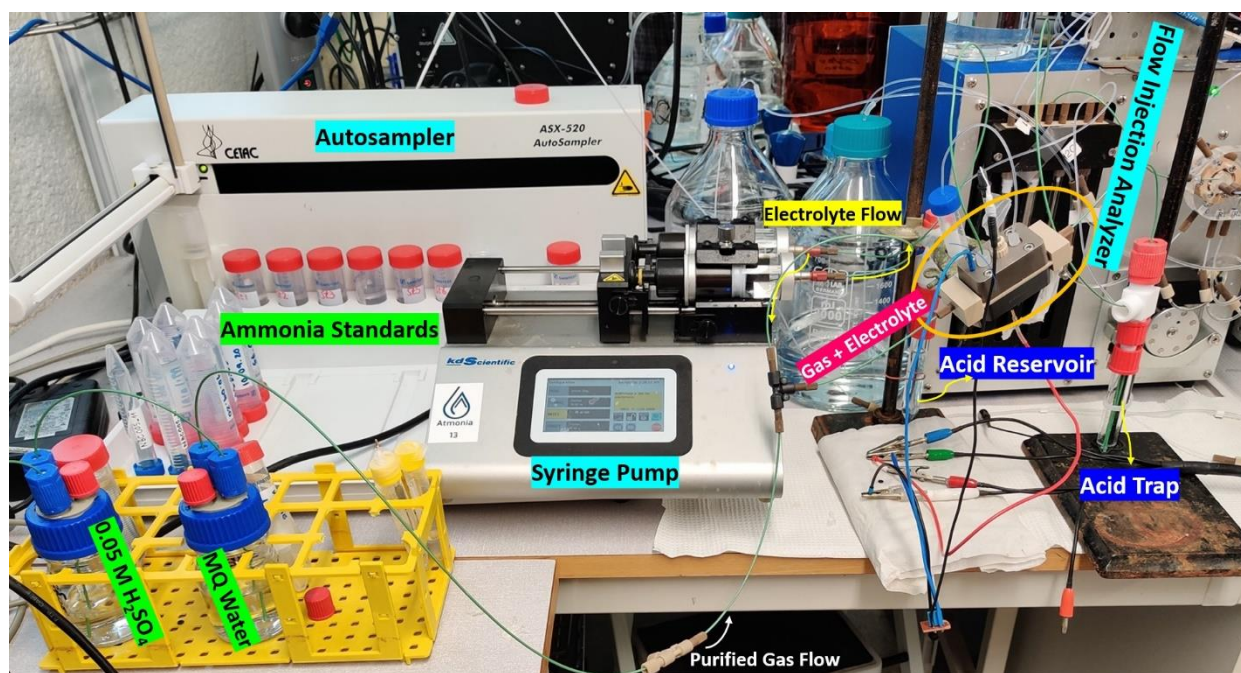
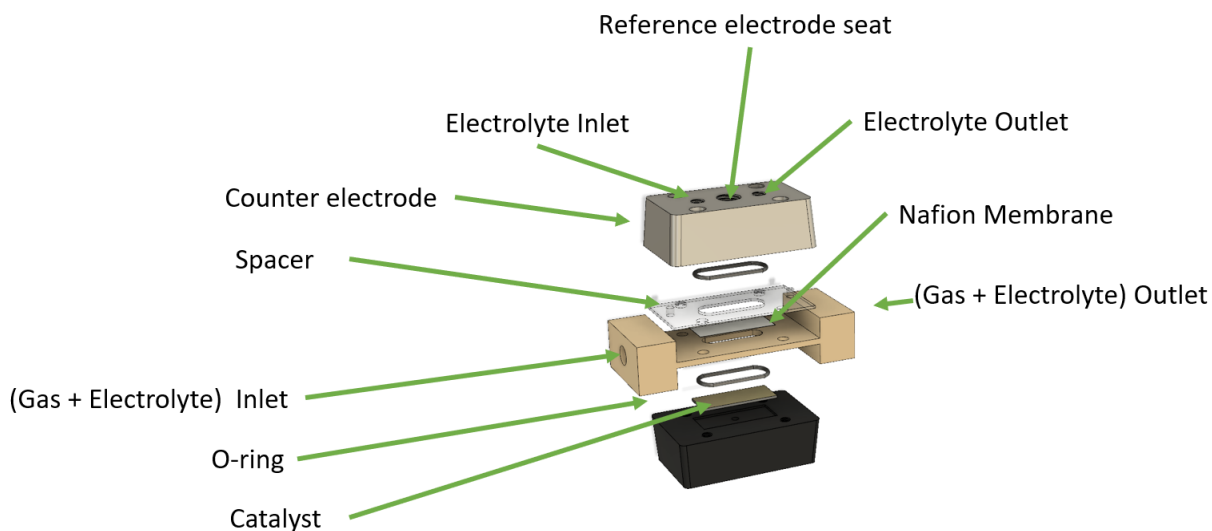


Figure S1. (Top) Exploded view of an upgraded commercial Antec micro-reactor modified with a PEEK spacer to separate the working and the counter compartment by means of Nafion membrane. (Bottom) Electrochemical micro-reactor flow-cell setup in-line with the ammonia measurement unit.

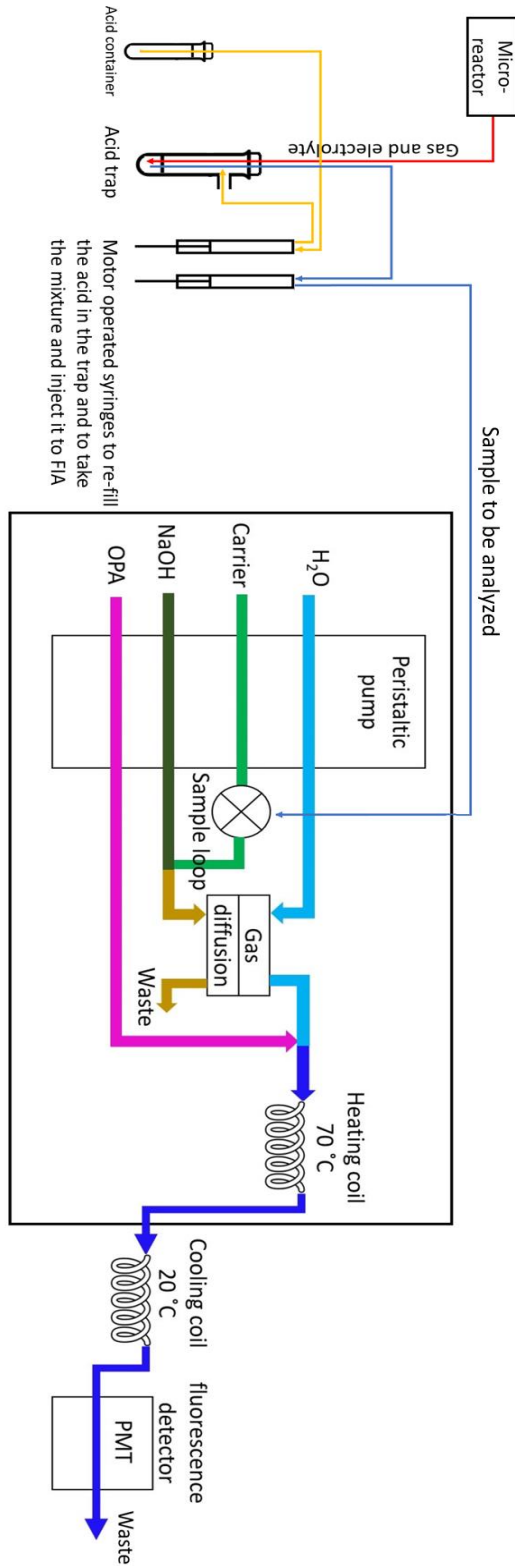


Figure S2. The illustration of the setup used for NRR in-line with ammonia measurement unit. The outlet of the working compartment of the micro-reactor is collected in an acid trap and the mixture is sent for analysis to the sequential injection analyzer (SIA).

### 3- Ammonia measurement calculations

Quantification of ammonia contained in the samples was performed based on two sets of calibration in the beginning and at the end of each electrochemical experiment. The standards were prepared in a mixture of 2:1 (v/v) of 0.1 M KOH and 0.5 M H<sub>2</sub>SO<sub>4</sub> (matrix matched with the samples from the experiment) and sent to the SIA using an autosampler. A linear regression was the best fit to the calibration data, correlating ammonia concentration to the intensity of the fluorescence emission. Figure S3 shows a typical calibration curve in the SIA.

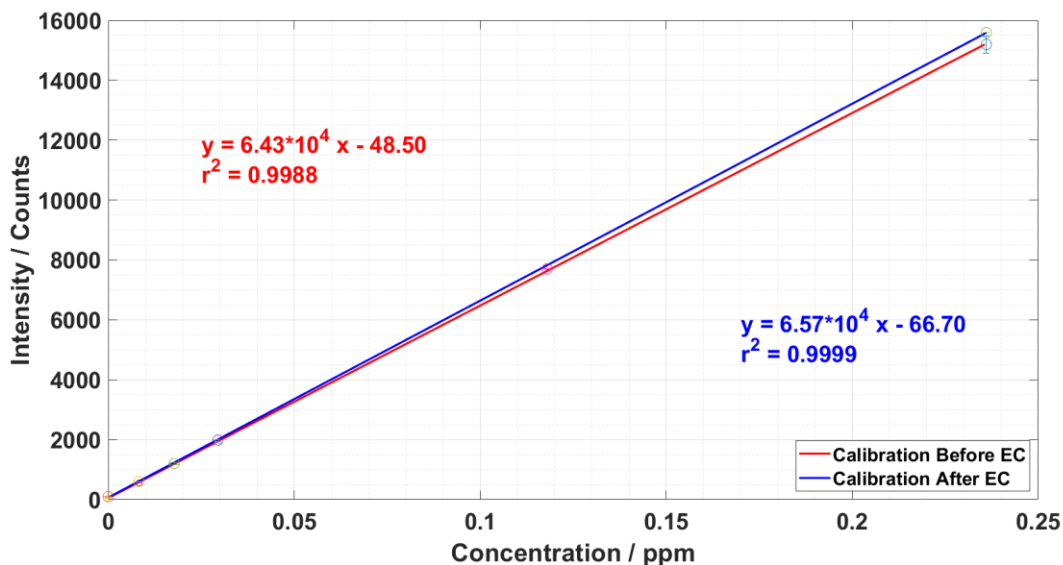


Figure S3. Ammonia calibration curve before and after an electrochemical experiment.

Based on the calibration curve, the ammonia concentration in the electrolyte was known in ppm after correcting for the dilution caused by the acid trap. This value was converted to N-atoms considering the volume of 200  $\mu$ L for the sample loop. The background N-atoms was subtracted from the N-atoms produced in each step. The total N-atom produced for each chronoamperometry combination was calculated by summing up the 3 subsequent N-atoms (since for each combination 3 measurements were done). This value was converted to moles of ammonia. Reaction rate in mol/cm<sup>2</sup>/s was calculated from the total moles of ammonia divided by the active working electrode area (1.9 cm<sup>2</sup>) and the reaction time (the total time of applying potential). Current efficiency was accordingly calculated accounting for 3 electrons per molecule of NH<sub>3</sub> produced.

$$\text{mol NH}_3 = \frac{x \times 10^{-3} \frac{\text{g}}{\text{L}} \times \frac{\text{electrolyte volume} + \text{acid trap volume}}{\text{electrolyte volume}} \times 200 \times 10^{-6} \text{L}}{17.03 \frac{\text{g}}{\text{mol}}}$$

$$\text{Reaction Rate (mol/cm}^2 \cdot \text{s)} = \frac{\text{mol NH}_3}{1.9 \text{ cm}^2 \times t \text{ (s)}}$$

$$\text{Current efficiency (\%)} = \frac{\text{mol NH}_3 \times 3 \left( \frac{\text{mol e}^-}{\text{mol NH}_3} \right) \times F \left( \frac{\text{C}}{\text{mol e}^-} \right)}{\text{Integrated Charge (C)}} \times 100$$

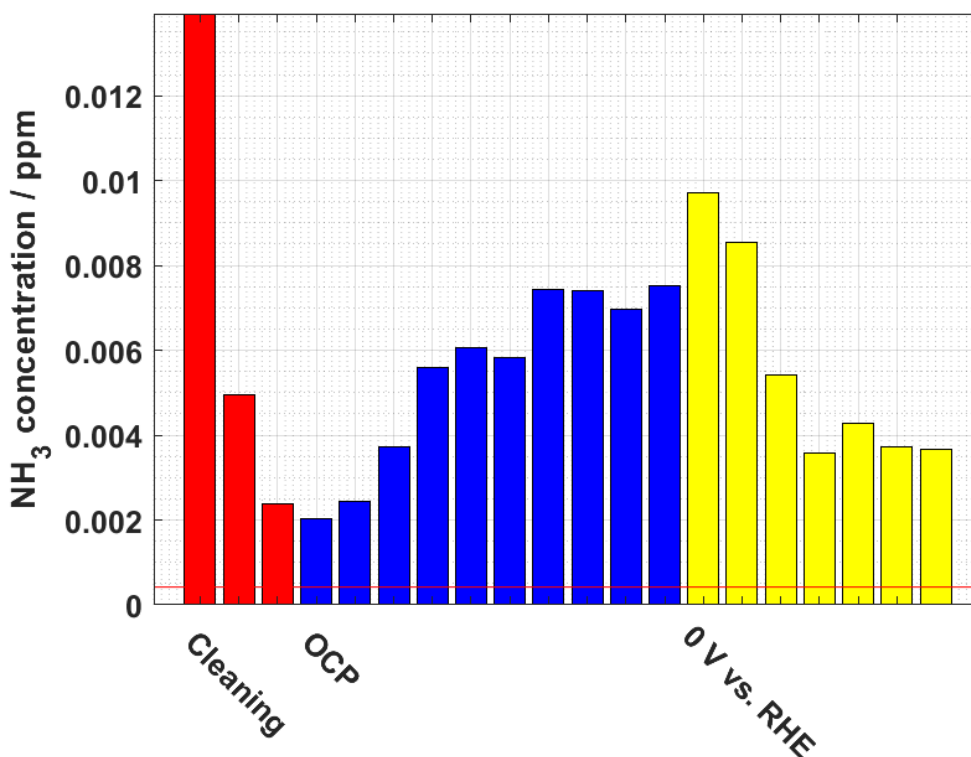


Figure S4. Ammonia intensities and concentrations in N<sub>2</sub> environment. Red columns show the cleaning peaks right after assembling the reactor there is inevitably some environmental contamination that is washed of by the flow of the electrolyte. Blue columns are the ammonia produced at OCP. Yellow peaks are after applying 0 V vs RHE. The red line represents the limit of detection which is 0.4 ppb.

#### 4- Comparison of system response with and without the gas flow

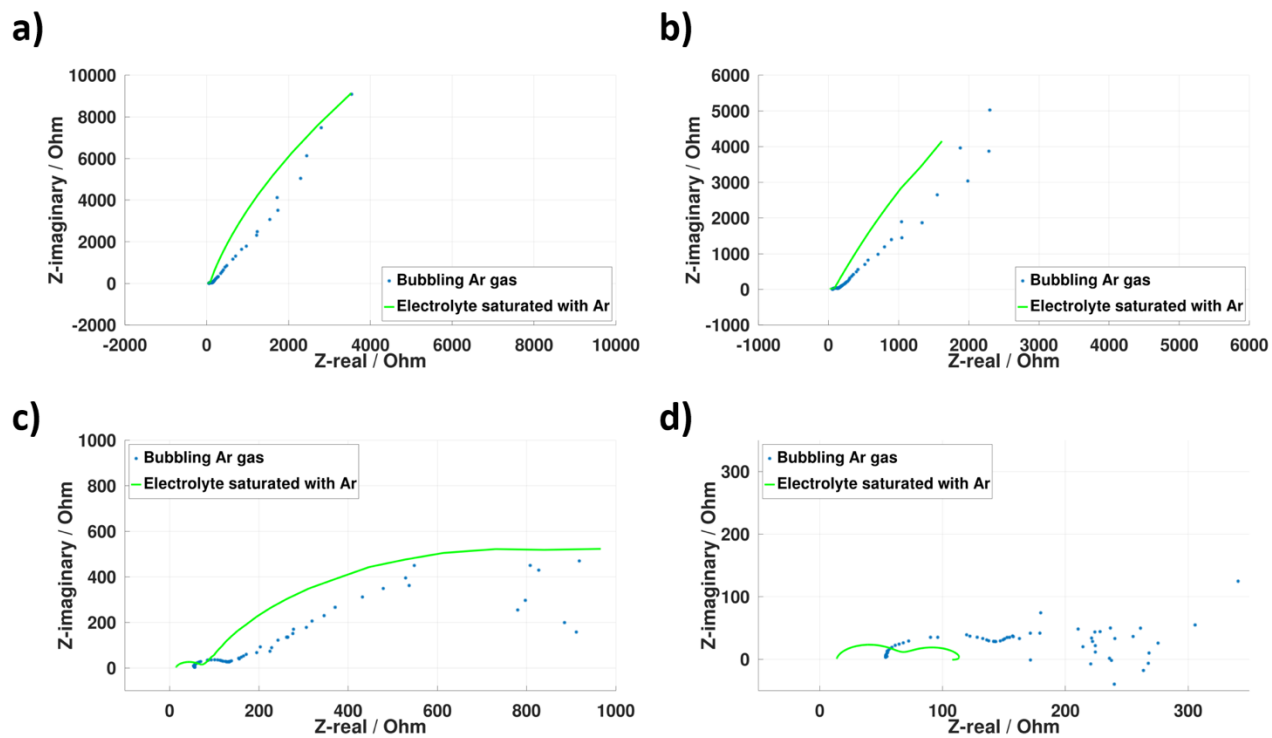


Figure S5. Comparison of the Nyquist plots in NbON#1 (a) at OCP, (b) in the capacitive zone, (c) at OP, and (d) in the faradaic zone with and without direct bubbling of the gas inside the working electrode compartment.

## 5- Equivalent circuits fit parameters

Table S1. Equivalent circuit and fit parameters in Ar

	Model	Parameters	Unit	E1	E2	E3	E4
NbON#1	a	R <sub>E</sub>	Ω	12.01	11.95	12.53	12.5
		R <sub>ct1</sub>	Ω	37690	276610	628.3	2.29
		CPE <sub>1</sub> T	μF/cm <sup>2</sup>	1.48E-4	3.14E-4	7.76E-4	2.72E-3
		CPE <sub>1</sub> P	-	0.89	0.83	0.80	1
		R <sub>ct2</sub>	Ω	3.22	2.5	5.47	8.2
		CPE <sub>2</sub> T	μF/cm <sup>2</sup>	9.50E-5	6.88E-5	2.27E-4	8.70E-5
		CPE <sub>2</sub> P	-	0.87	1	0.91	0.95
		χ <sup>2</sup>	-	8.35E-5	1.32E-4	1.44E-4	6.92E-5
NbON#2	a	R <sub>E</sub>	Ω	12.26	12.28	12.29	13.22
		R <sub>ct1</sub>	Ω	47503	163870	1044	46.98
		CPE <sub>1</sub> T	μF/cm <sup>2</sup>	1.22E-4	3.52E-4	9.56E-4	7.98E-4
		CPE <sub>1</sub> P	-	0.88	0.80	0.74	0.77
		R <sub>ct2</sub>	Ω	50.46	47.5	48.07	47.73
		CPE <sub>2</sub> T	μF/cm <sup>2</sup>	8.54E-6	7.94E-6	8.19E-6	5.40E-6
		CPE <sub>2</sub> P	-	0.87	0.88	0.88	0.91
		χ <sup>2</sup>	-	4.92E-4	4.80E-4	6.32E-4	1.84E-4
NbON#3	a	R <sub>E</sub>	Ω	14.47	14.84	14.26	15.01
		R <sub>ct1</sub>	Ω	105640	56864	23847	103.8
		CPE <sub>1</sub> T	μF/cm <sup>2</sup>	1.20E-4	2.07E-4	5.61E-4	7.37E-4
		CPE <sub>1</sub> P	-	0.90	0.85	0.81	0.72
		R <sub>ct2</sub>	Ω	22.66	20.08	23.57	17.1
		CPE <sub>2</sub> T	μF/cm <sup>2</sup>	3.33E-5	1.62E-5	5.56E-5	1.31E-5
		CPE <sub>2</sub> P	-	0.75	0.82	0.70	0.84
		χ <sup>2</sup>	-	5.68E-4	2.93E-4	8.43E-4	4.23E-4
NbON#4	a	R <sub>E</sub>	Ω	13.59	13.64	13.57	13.69
		R <sub>ct1</sub>	Ω	45597	33375	542.4	109.5
		CPE <sub>1</sub> T	μF/cm <sup>2</sup>	1.09E-4	2.51E-4	6.76E-4	7.57E-4
		CPE <sub>1</sub> P	-	0.88	0.82	0.72	0.76
		R <sub>ct2</sub>	Ω	487.8	461.6	352.7	210.9
		CPE <sub>2</sub> T	μF/cm <sup>2</sup>	3.97E-6	3.95E-6	3.72E-6	3.61E-6
		CPE <sub>2</sub> P	-	0.95	0.95	0.95	0.95
		χ <sup>2</sup>	-	7.00E-5	1.14E-4	6.41E-5	4.78E-5

Table S2. Equivalent circuit and fit parameters in N<sub>2</sub>

	Model	Parameters	Unit	E1	E2	E3	E4
NbON#1	a	R <sub>E</sub>	Ω	9.82	9.94	10.04	10.3
		R <sub>ct1</sub>	Ω	22942	17569	12168	81.8
		CPE <sub>1</sub> T	μF/cm <sup>2</sup>	1.44E-04	3.43E-04	6.60E-04	4.93E-04
		CPE <sub>1</sub> P	-	1	1	0.74	0.82
		R <sub>ct2</sub>	Ω	2693	3594	8.79	9.23
		CPE <sub>2</sub> T	μF/cm <sup>2</sup>	2.77E-04	2.82E-04	1.25E-03	3.37E-04
		CPE <sub>2</sub> P	-	0.77	0.78	0.75	0.85
		χ <sup>2</sup>	-	2.15E-4	2.18E-4	4.79E-4	9.70E-5
NbON#2	a	R <sub>E</sub>	Ω	11.76	12.73	12.1	9.68
		R <sub>ct1</sub>	Ω	66445	25433	28606	129.6
		CPE <sub>1</sub> T	μF/cm <sup>2</sup>	1.51E-04	2.68E-04	8.41E-4	6.47E-4
		CPE <sub>1</sub> P	-	0.87	0.81	0.74	0.25
		R <sub>ct2</sub>	Ω	7.92	5.70	12.73	24.1
		CPE <sub>2</sub> T	μF/cm <sup>2</sup>	1.92E-4	1.01E-05	1.89E-3	6.34E-3
		CPE <sub>2</sub> P	-	0.58	0.86	0.39	0.25
		χ <sup>2</sup>	-	3.84E-4	2.69E-4	8.07E-4	1.15E-3
NbON#3	b @ E1 – E3 d @ E4	R <sub>E</sub>	Ω	13.81	13.85	13.84	14
		R <sub>ct1</sub>	Ω	27944	10725	1977	100.3
		L1	H	N/A	N/A	N/A	18.21
		CPE <sub>1</sub> T	μF/cm <sup>2</sup>	1.47E-04	3.02E-04	9.93E-04	N/A
		CPE <sub>1</sub> P	-	1	1	1	N/A
		R <sub>ct2</sub>	Ω	21.23	21.69	21.92	18.83
		CPE <sub>2</sub> T	μF/cm <sup>2</sup>	4.46E-06	4.37E-06	5.71E-06	3.52E-6
		CPE <sub>2</sub> P	-	0.94	0.95	0.92	0.97
		R <sub>ct3</sub>	Ω	2705	1966	1067	169.1
		CPE <sub>3</sub> T	μF/cm <sup>2</sup>	1.08E-04	1.53E-04	1.82E-04	2.46E-4
		CPE <sub>3</sub> P	-	0.89	0.88	0.90	0.84
		χ <sup>2</sup>	-	2.11E-4	2.31E-4	5.48E-4	1.73E-4
		NbON#4	b @ E1 – E3 c @ E4	R <sub>E</sub>	Ω	15.19	14.94
R <sub>ct1</sub>	Ω			31229	16498	1007	221
L1	H			N/A	N/A	N/A	19.14
CPE <sub>1</sub> T	μF/cm <sup>2</sup>			1.50E-04	2.72E-04	1.11E-03	7.50E-4
CPE <sub>1</sub> P	-			0.95	1	1	0.60
R <sub>ct2</sub>	Ω			291.1	292.6	291.4	223.9
CPE <sub>2</sub> T	μF/cm <sup>2</sup>			4.07E-06	4.03E-06	4.06E-06	3.56E-6
CPE <sub>2</sub> P	-			0.95	0.95	0.94	0.96
R <sub>ct3</sub>	Ω			760.6	920.3	573.1	N/A
CPE <sub>3</sub> T	μF/cm <sup>2</sup>			1.71E-04	1.73E-04	1.46E-04	N/A
CPE <sub>3</sub> P	-			0.80	0.80	0.91	N/A
χ <sup>2</sup>	-			6.07E-5	7.41E-5	2.10E-4	4.98E-4

## 6- Bode plots

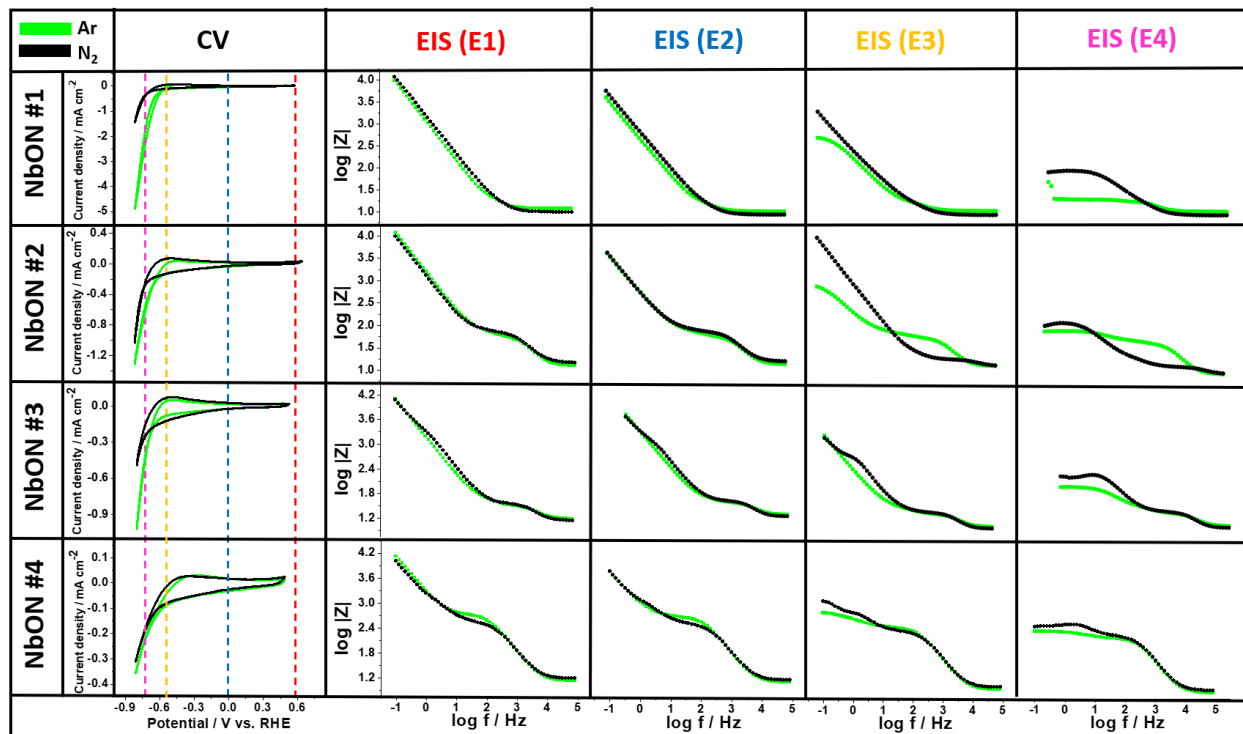


Figure S6. Bode plots recorded for the four series of NbON at open circuit potential (OCP), capacitive zone, onset potential (OP), and faradaic zone. The logarithm of total impedance ( $|Z|$ ) is plotted against the logarithm of the frequency of the applied potential.

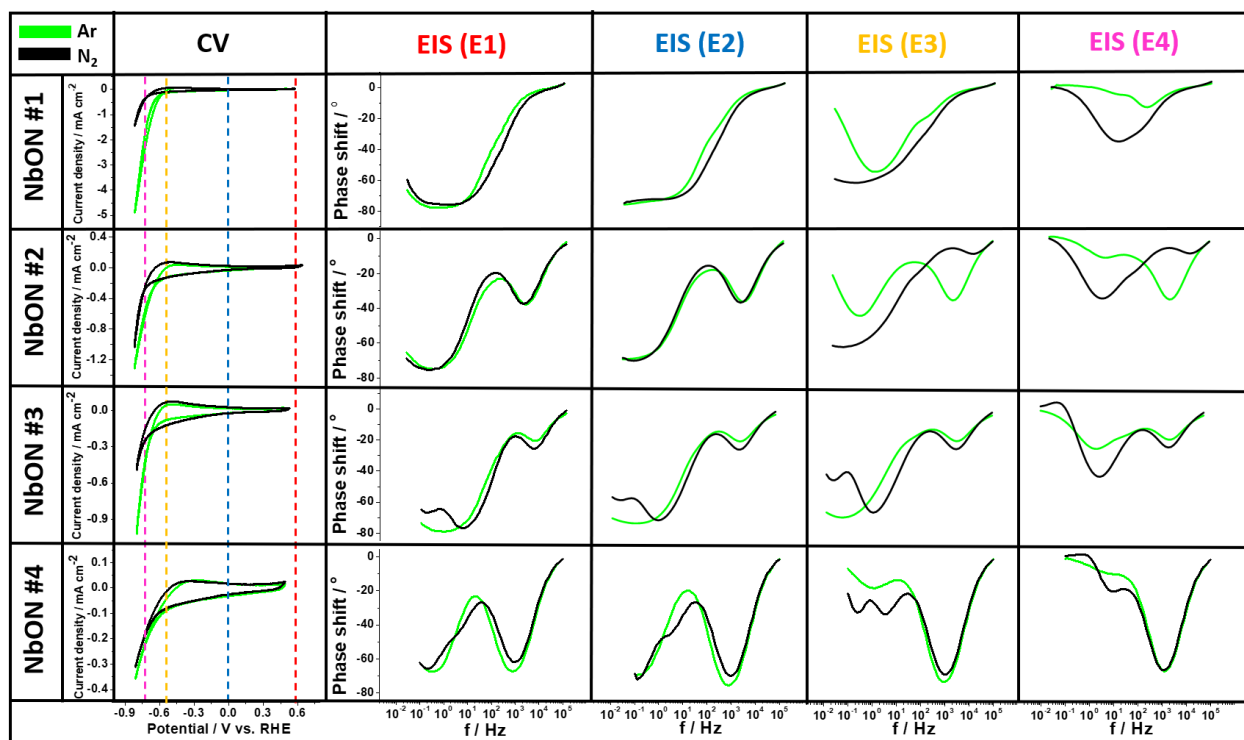


Figure S7. Phase shift diagram recorded for the four TMNs at open circuit potential (OCP), capacitive zone, onset potential (OP), and faradaic zone.

## 7- Data on Reaction rates and current efficiencies

Table S3. Ammonia reaction rates obtained in the chronoamperometry loops at 8 potential combinations. All the numbers are above the limit of detection of the method.

B A		Reaction rate / mol cm <sup>-2</sup> s <sup>-1</sup>					
		Ar(g)			N <sub>2</sub> (g)		
		OCP	OCP + 0.2 V	OCP + 0.4 V	OCP	OCP + 0.2 V	OCP + 0.4 V
NbON #1	-0.2 V	1.59×10 <sup>-12</sup> ± 4×10 <sup>-13</sup>	3.08×10 <sup>-12</sup> ± 2×10 <sup>-13</sup>	1.68×10 <sup>-12</sup> ± 9×10 <sup>-13</sup>	1.01×10 <sup>-12</sup> ± 9×10 <sup>-13</sup>	1.21×10 <sup>-12</sup> ± 1×10 <sup>-12</sup>	1.22×10 <sup>-12</sup> ± 8×10 <sup>-13</sup>
	-0.4 V	4.37×10 <sup>-13</sup> ± 3×10 <sup>-13</sup>	2.76×10 <sup>-12</sup> ± 9×10 <sup>-13</sup>	2.39×10 <sup>-12</sup> ± 1×10 <sup>-12</sup>	2.67×10 <sup>-13</sup> ± 1×10 <sup>-13</sup>	9.4×10 <sup>-13</sup> ± 2×10 <sup>-13</sup>	9.44×10 <sup>-13</sup> ± 4×10 <sup>-13</sup>
	-0.6 V	7.06×10 <sup>-13</sup> ± 5×10 <sup>-13</sup>	3.91×10 <sup>-12</sup> ± 1×10 <sup>-12</sup>	-	2.08×10 <sup>-13</sup> ± 2×10 <sup>-13</sup>	7.22×10 <sup>-13</sup> ± 4×10 <sup>-13</sup>	-
NbON #2	-0.2 V	1.44×10 <sup>-12</sup> ± 4×10 <sup>-13</sup>	2.65×10 <sup>-12</sup> ± 2×10 <sup>-13</sup>	1.43×10 <sup>-12</sup> ± 8×10 <sup>-13</sup>	1×10 <sup>-12</sup> ± 2×10 <sup>-13</sup>	1.66×10 <sup>-12</sup> ± 9×10 <sup>-13</sup>	2.25×10 <sup>-12</sup> ± 9×10 <sup>-13</sup>
	-0.4 V	3.85×10 <sup>-13</sup> ± 1×10 <sup>-13</sup>	1.99×10 <sup>-12</sup> ± 4×10 <sup>-13</sup>	1.69×10 <sup>-12</sup> ± 8×10 <sup>-13</sup>	4.08×10 <sup>-13</sup> ± 4×10 <sup>-14</sup>	6.77×10 <sup>-13</sup> ± 2×10 <sup>-13</sup>	1.33×10 <sup>-12</sup> ± 1×10 <sup>-13</sup>
	-0.6 V	5.57×10 <sup>-13</sup> ± 2×10 <sup>-13</sup>	2.62×10 <sup>-12</sup> ± 5×10 <sup>-13</sup>	-	4.33×10 <sup>-13</sup> ± 7×10 <sup>-14</sup>	4.03×10 <sup>-13</sup> ± 1×10 <sup>-13</sup>	-
NbON #3	-0.2 V	4.74×10 <sup>-13</sup> ± 4×10 <sup>-14</sup>	3.29×10 <sup>-13</sup> ± 7×10 <sup>-14</sup>	2.26×10 <sup>-13</sup> ± 7×10 <sup>-14</sup>	2.83×10 <sup>-13</sup> ± 4×10 <sup>-14</sup>	2.43×10 <sup>-13</sup> ± 8×10 <sup>-14</sup>	2.02×10 <sup>-13</sup> ± 8×10 <sup>-14</sup>
	-0.4 V	5.76×10 <sup>-14</sup> ± 2×10 <sup>-14</sup>	1.50×10 <sup>-13</sup> ± 3×10 <sup>-15</sup>	1.63×10 <sup>-13</sup> ± 1×10 <sup>-13</sup>	8.66×10 <sup>-14</sup> ± 3×10 <sup>-14</sup>	1.26×10 <sup>-13</sup> ± 1×10 <sup>-14</sup>	1.60×10 <sup>-13</sup> ± 4×10 <sup>-14</sup>
	-0.6 V	4.57×10 <sup>-14</sup> ± 8×10 <sup>-14</sup>	2.87×10 <sup>-13</sup> ± 2×10 <sup>-14</sup>	-	1.84×10 <sup>-13</sup> ± 5×10 <sup>-14</sup>	2.49×10 <sup>-13</sup> ± 9×10 <sup>-15</sup>	-
NbON #4	-0.2 V	2.51×10 <sup>-15</sup> ± 4×10 <sup>-15</sup>	3.58×10 <sup>-13</sup> ± 2×10 <sup>-13</sup>	8.91×10 <sup>-13</sup> ± 7×10 <sup>-14</sup>	1.19×10 <sup>-12</sup> ± 6×10 <sup>-13</sup>	1.48×10 <sup>-12</sup> ± 8×10 <sup>-14</sup>	8.59×10 <sup>-13</sup> ± 2×10 <sup>-13</sup>
	-0.4 V	3.36×10 <sup>-13</sup> ± 2×10 <sup>-13</sup>	8.37×10 <sup>-13</sup> ± 2×10 <sup>-13</sup>	1.55×10 <sup>-12</sup> ± 9×10 <sup>-14</sup>	1.26×10 <sup>-12</sup> ± 5×10 <sup>-13</sup>	2.34×10 <sup>-12</sup> ± 3×10 <sup>-13</sup>	1.41×10 <sup>-12</sup> ± 5×10 <sup>-13</sup>
	-0.6 V	7.56×10 <sup>-13</sup> ± 2×10 <sup>-13</sup>	1.26×10 <sup>-12</sup> ± 4×10 <sup>-13</sup>	-	8.61×10 <sup>-13</sup> ± 2×10 <sup>-13</sup>	1.44×10 <sup>-12</sup> ± 3×10 <sup>-13</sup>	-

Table S4. Ammonia current efficiencies obtained in the chronoamperometry loops at 8 potential combinations.

B \ A		Current efficiency / %					
		Ar			N <sub>2</sub>		
		OCP	OCP + 0.2 V	OCP + 0.4 V	OCP	OCP + 0.2 V	OCP + 0.4 V
NbON #1	-0.2 V	3.07 ± 0.84	8.45 ± 0.48	4.61 ± 2.53	2.28 ± 2.00	3.39 ± 3.04	3.41 ± 2.17
	-0.4 V	0.53 ± 0.41	3.65 ± 1.17	3.60 ± 1.92	0.31 ± 0.13	1.09 ± 0.21	1.07 ± 0.44
	-0.6 V	0.32 ± 0.22	1.89 ± 0.51	-	0.05 ± 0.05	0.16 ± 0.11	-
NbON #2	-0.2 V	3.72 ± 0.98	9.00 ± 0.59	4.84 ± 2.60	2.21 ± 0.52	3.77 ± 2.19	5.2 ± 2.12
	-0.4 V	0.59 ± 0.26	3.28 ± 0.67	2.91 ± 1.46	0.98 ± 0.10	1.63 ± 0.46	3.75 ± 0.37
	-0.6 V	0.52 ± 0.20	2.40 ± 0.48	-	0.80 ± 0.13	0.66 ± 0.22	-
NbON #3	-0.2 V	1.52 ± 0.12	1.13 ± 0.23	0.78 ± 0.24	1.31 ± 0.17	1.35 ± 0.44	1.21 ± 0.49
	-0.4 V	0.11 ± 0.04	0.30 ± 0.01	0.33 ± 0.30	0.25 ± 0.10	0.35 ± 0.04	0.46 ± 0.13
	-0.6 V	0.04 ± 0.08	0.27 ± 0.02	-	0.26 ± 0.08	0.36 ± 0.01	-
NbON #4	-0.2 V	0.01 ± 0.01	1.02 ± 0.49	3.71 ± 0.28	5.20 ± 2.87	8.47 ± 0.45	6.31 ± 1.20
	-0.4 V	0.72 ± 0.46	2.04 ± 0.59	6.51 ± 0.39	3.22 ± 1.37	5.57 ± 0.82	2.09 ± 0.68
	-0.6 V	1.7 ± 0.46	3.66 ± 1.13	-	0.62 ± 0.17	0.82 ± 0.17	-

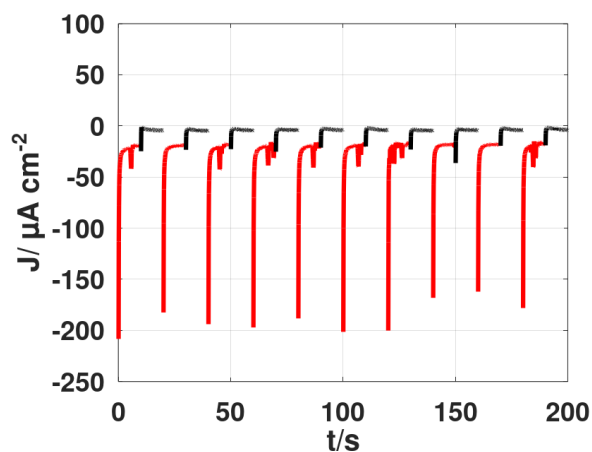
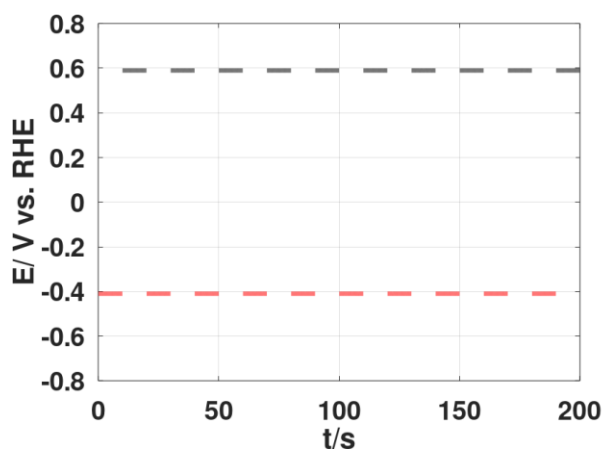


Figure S8. Example of a chronoamperometry loop run between -0.4 V and OCP. A chronoamperometry loop between two fixed potentials is run for 1800 s (3 consecutive ammonia measurements) before switching to the next loop.

## 8- Stability checks during experiments

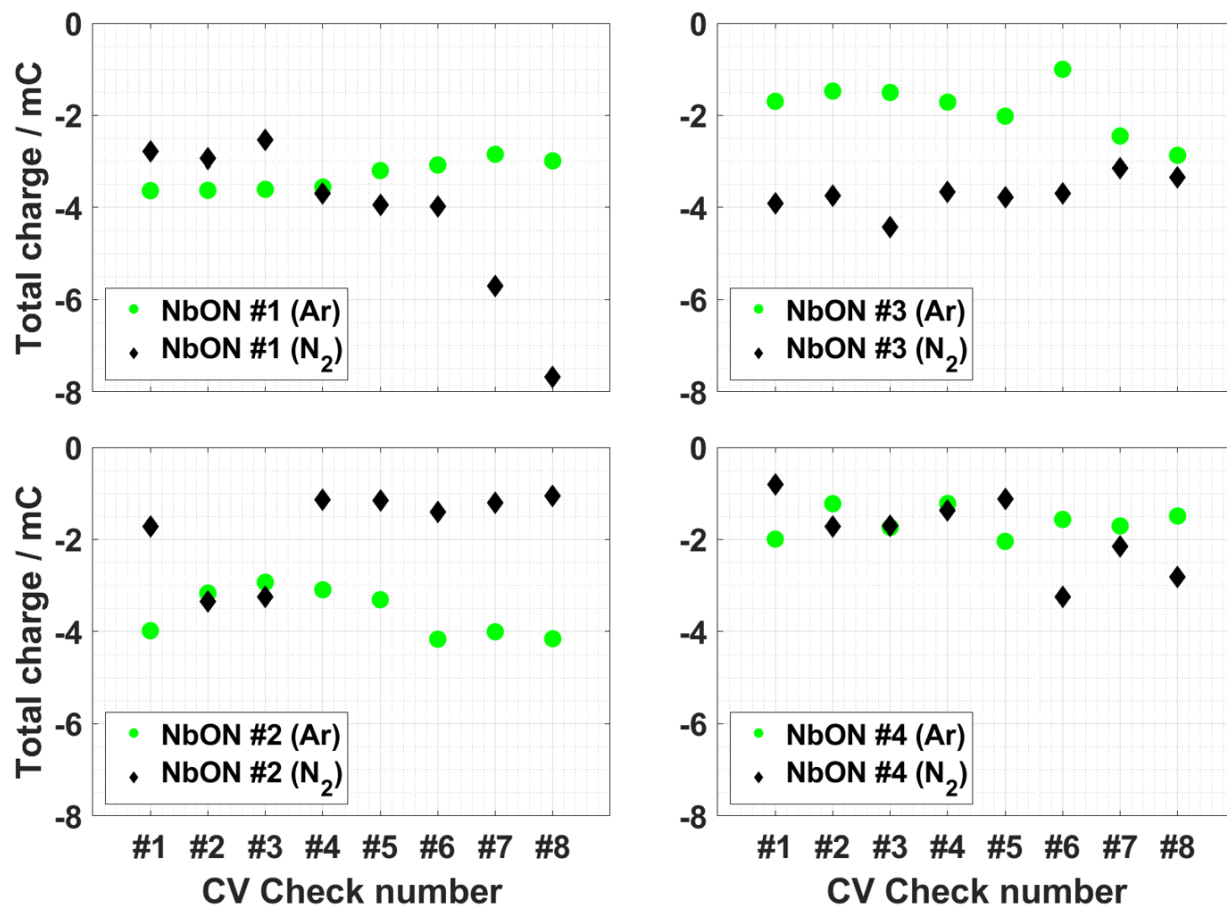


Figure S9. Total charge in the CVs recorded after each chronoamperometry loop for each surface in Ar (green circles) vs. N<sub>2</sub> (black diamonds).

## 9- Surface characterization

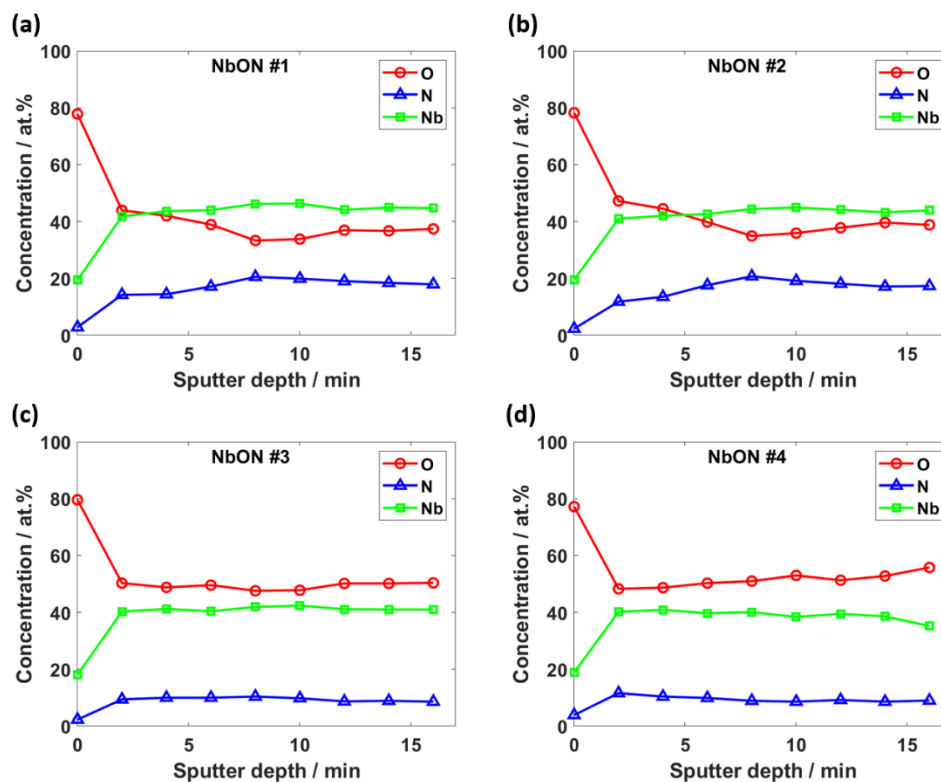


Figure S10. Sputter depth profiles for the pristine NbON surfaces, attained using X-ray photoelectron spectroscopy (XPS) and 500 eV Ar<sup>+</sup> etching. All surfaces demonstrate a uniform bulk chemical composition immediately below the native oxide layer.

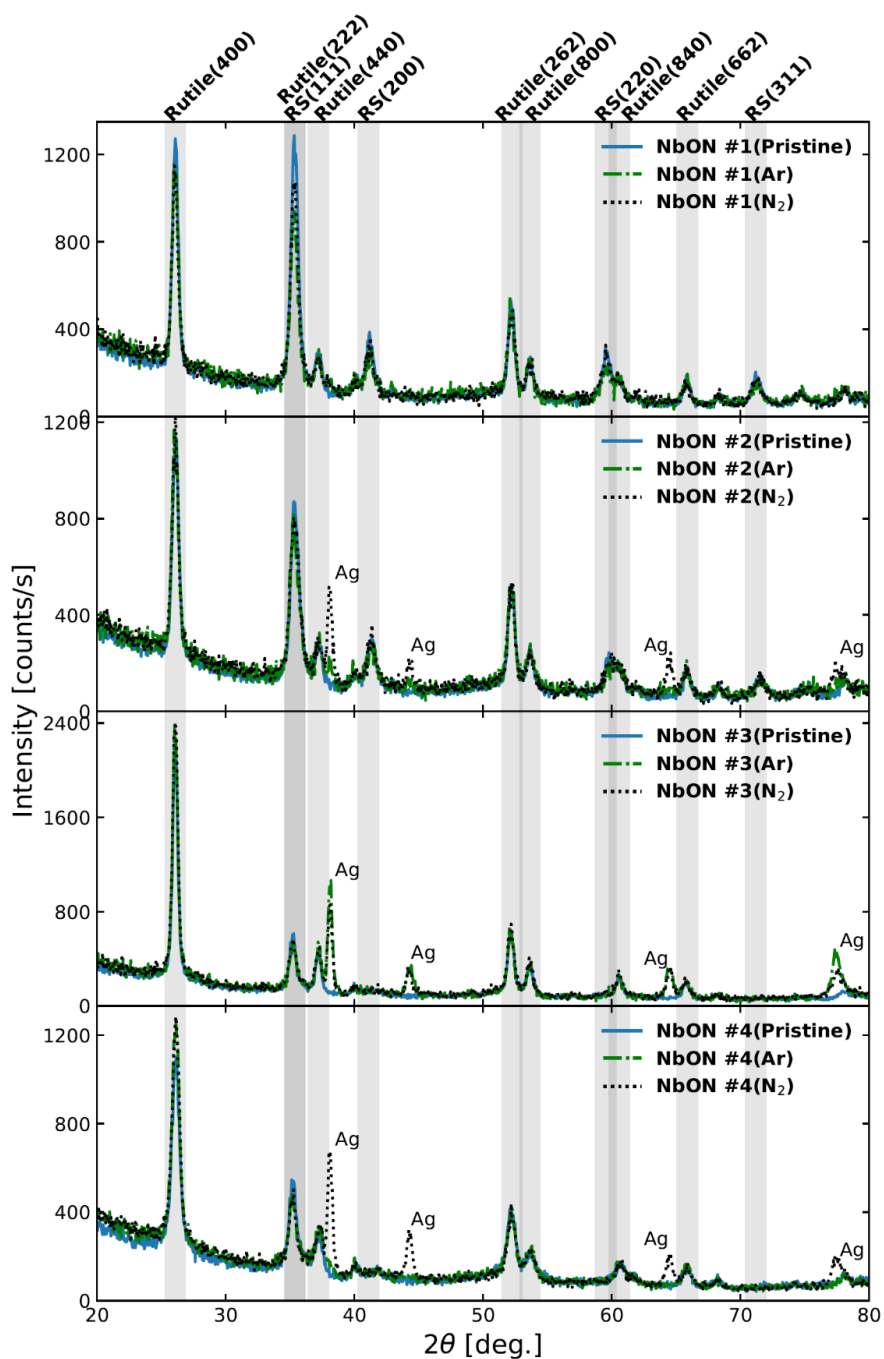


Figure S11. Grazing incidence x-ray diffraction (GIXRD) measurements on the NbON surfaces after experiments in Ar (green dashed lines) and N<sub>2</sub> (black dotted lines) overlaid on the pristine measurements before experiments (blue solid lines). Note that the silver peaks(Ag) in some cases are the result of silver paint application to the edges of the films which was not completely removed before XRD measurements.

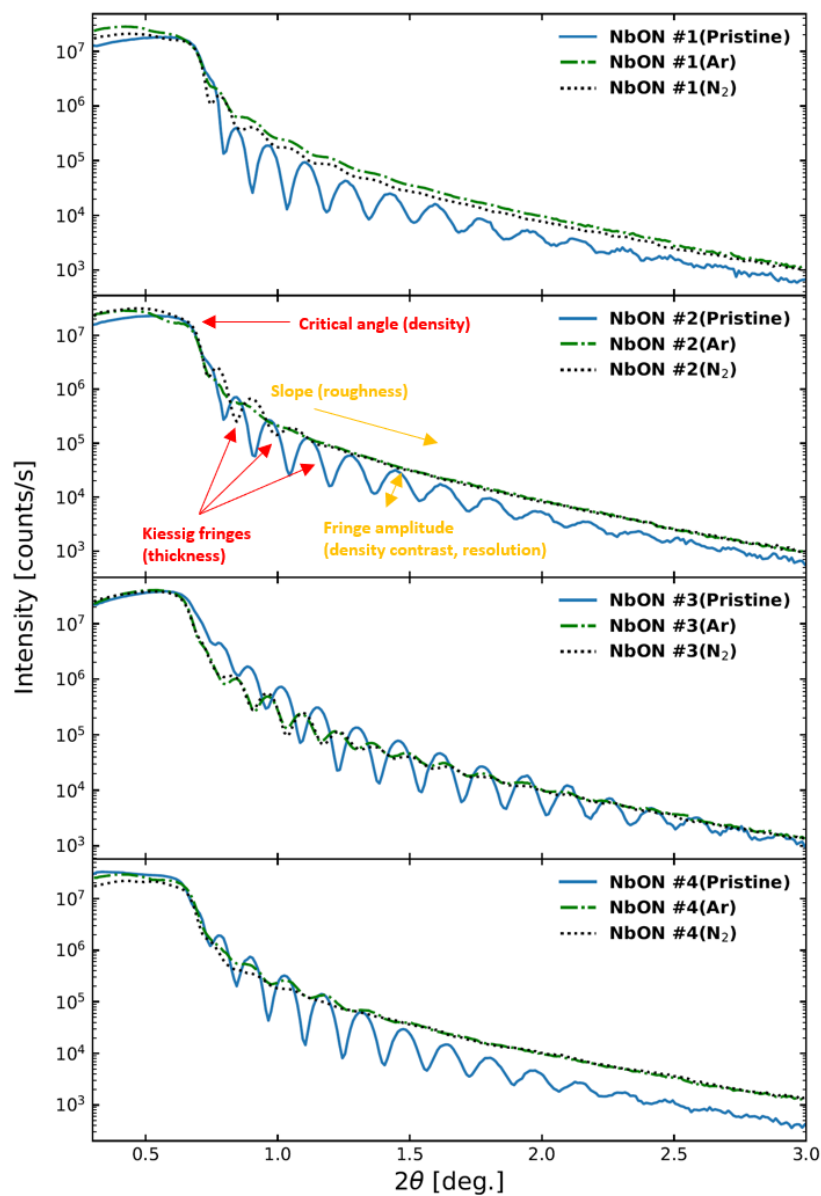


Figure S12. X-ray reflectivity (XRR) measurements on the NbON surfaces after experiments in Ar (dashed green lines) and N<sub>2</sub> (dotted black lines) overlaid on the pristine measurements before experiments (solid blue lines). The sort of information that can be derived from a typical XRR plot is marked on the figure for NbON #2.

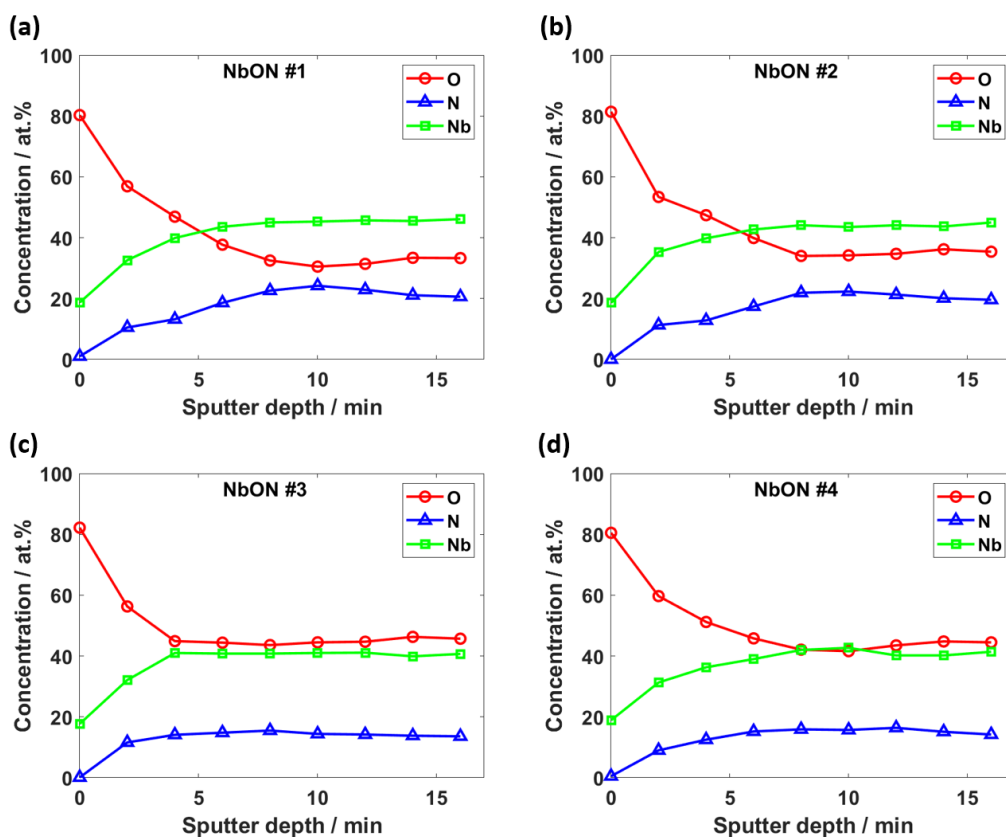


Figure S13. Sputter depth profiles for the NbON surfaces after electrochemical experiments in  $N_2(g)$ , attained using X-ray photoelectron spectroscopy (XPS) and 500 eV  $Ar^+$  etching.

Table S5. Comparison of the stoichiometries of the NbON films in pristine form and after electrochemical experiments in  $N_2(g)$ . Top layer is considered to be the average composition between 2 and 4 minutes of sputtering time. Bulk composition is the average of points between 4 and 16 minutes.

	NbON #1	NbON #2	NbON #3	NbON #4
Pristine film (bulk)	$NbO_{0.80}N_{0.42}$	$NbO_{0.86}N_{0.42}$	$NbO_{1.20}N_{0.23}$	$NbO_{1.28}N_{0.24}$
Used film (bulk)	$NbO_{0.75}N_{0.48}$	$NbO_{0.86}N_{0.47}$	$NbO_{1.10}N_{0.35}$	$NbO_{1.05}N_{0.37}$
Pristine film (top layer)	$NbO_{1.01}N_{0.34}$	$NbO_{1.11}N_{0.30}$	$NbO_{1.22}N_{0.24}$	$NbO_{1.20}N_{0.27}$
Used film (top layer)	$NbO_{1.46}N_{0.33}$	$NbO_{1.35}N_{0.32}$	$NbO_{1.42}N_{0.35}$	$NbO_{1.66}N_{0.32}$

## 10- Isotope labelling experiments

Based on the method described in the experimental section of the article, ammonia is derivatized from the samples in the form of benzenesulfonamide (BSA) prior to injection to the GC-MS. The mass to charge ratios of 157 amu and 158 amu represent  $^{14}\text{NH}_3$  and  $^{15}\text{NH}_3$  BSA derivatives of benzenesulfonyl chloride (BSC), respectively. Figure S11 shows the calibration curve for  $^{14}\text{NH}_3$ . Due to the natural abundance of  $^{13}\text{C}$  in the final product,  $^{157}\text{BSA}$  always contains a natural abundance of  $^{158}\text{BSA}$ . This is also shown on the calibration curve. Figure S14 shows the sample analysis from the isotope labelling experiment. All the samples only contain  $^{157}\text{BSA}$  and  $^{158}\text{BSA}$  is not any higher than the natural abundance of the  $^{157}\text{BSA}$ .

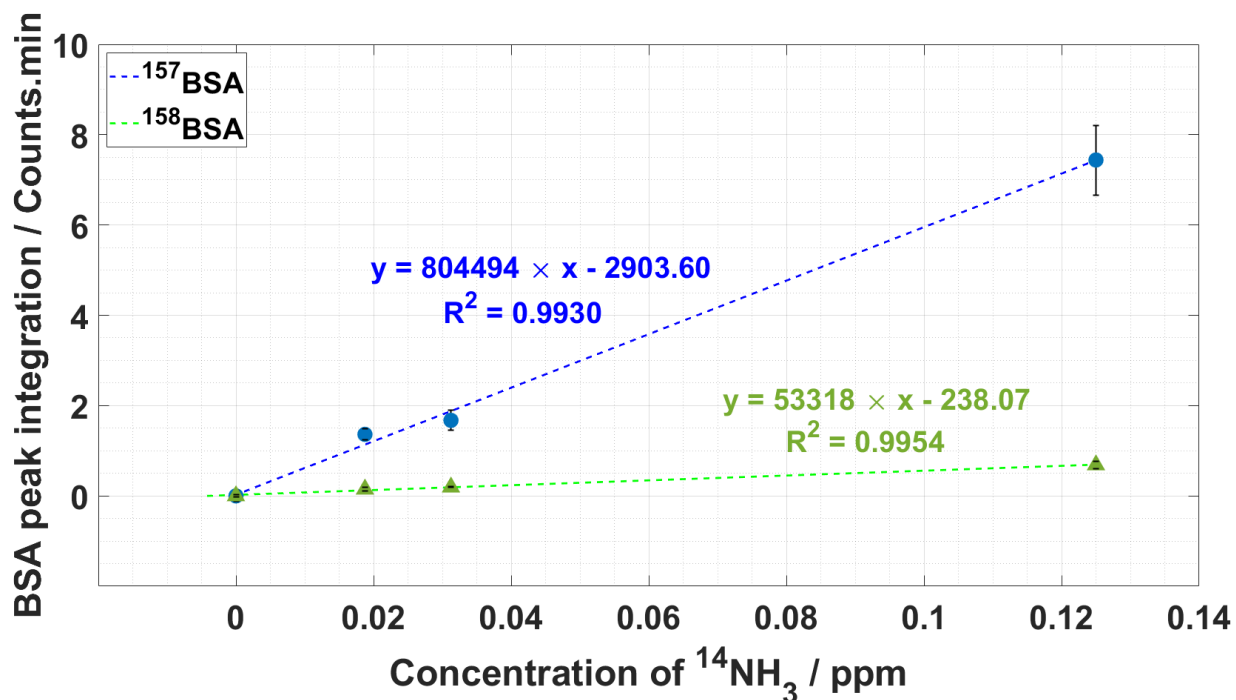


Figure S14. Calibration curve for  $^{14}\text{NH}_3$  which is derivatized in the form of  $^{157}\text{BSA}$ . The natural abundance of  $^{158}\text{BSA}$  is also shown on the graph.

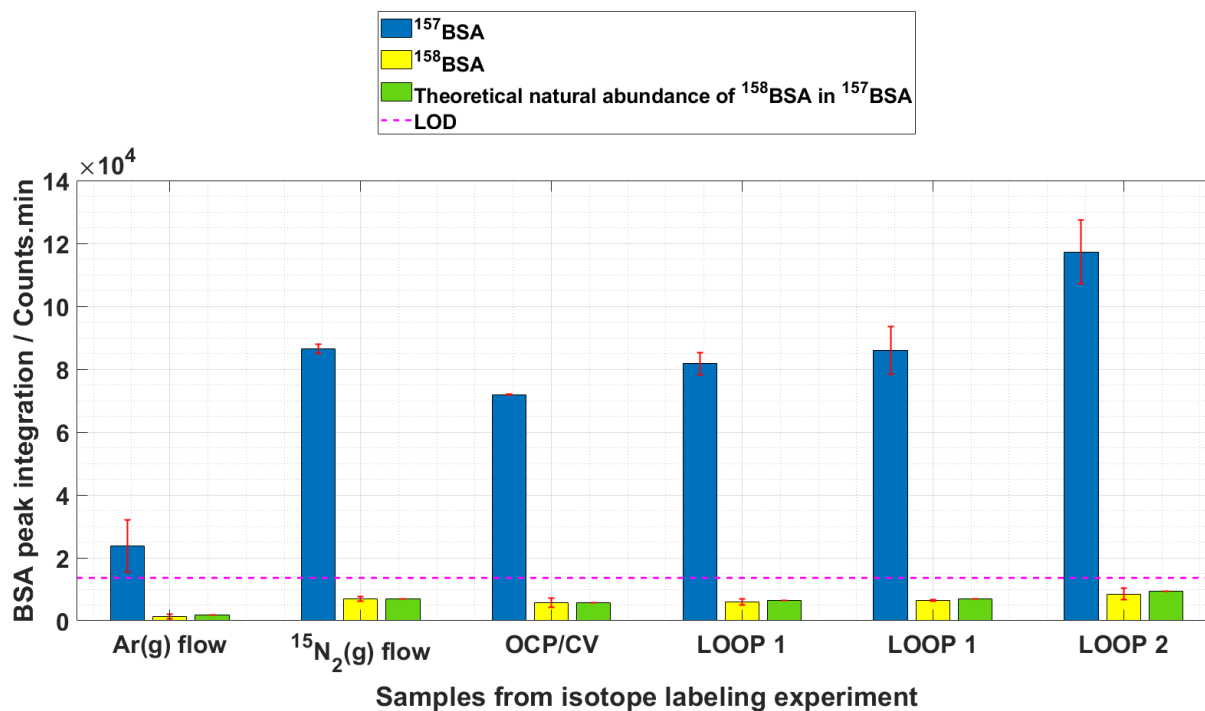


Figure S15. Peak integration of the samples taken from the  $^{15}\text{N}_2$  experiment. The peak integration of the blank sample (electrolyte prior to entering the reactor) is withdrawn from all the samples. The experiment started with the flow of Ar(g) in the system, with no applied potential. Then the gas was shifted to  $^{15}\text{N}_2$ , again no potential application. It is interesting to see that even though the gas is purified prior to entering the reactor, ammonia is detected higher than the background level. This is due to the chemical leaching of the surface bound nitride in 0.1 M KOH electrolyte. Loop 1 and Loop 2 are (-0.2 V / OCP + 0.2 V) and (-0.4 V / OCP + 0.2 V), respectively.